The Reinforcement of Nanocomposites by Boron Nitride Nanosheets and Nanotubes

A thesis submitted to

The University of Manchester

for the degree of

Doctor of Philosophy

in the

Faculty of Science and Engineering

2021

Weimiao Wang

Department of Materials

Contents

Word Count: 57508

List of Tables

List of Figures

Abstract

The project has studied the mechanical reinforcement mechanism in two-dimensional (2D) boron nitride nanosheets (BNNSs) and one-dimensional (1D) boron nitride nanotubes (BNNTs)-based nanocomposites. It has been found that despite the Raman scattering from insulating hexagonal boron nitride-based materials being relatively weak compared with that from their carbon analogues, Raman spectroscopy is still a powerful technique to study both the BNNSs/polymer and BNNTs/polymer nanocomposites. A detailed review of the relevant literature is presented first of all.

Single BNNSs of different thicknesses of up to 100 nm have been deposited upon a polymer substrate and deformed in unixial tension. The in-plane E_{2g} Raman mode (the G band) of the BNNSs has been used to evaluate the stress transfer both between the individual hBN layers in the nanosheets and between the nanosheets and the substrate. The efficiency of internal stress transfer between the different hBN layers has been quantified from the G band shift rate of BNNSs with different thicknesses. The stress transfer between the BNNSs and the polymer substrate has been monitored by mapping the strain along a BNNS flake using Raman spectroscopy. It has been shown that shear-lag theory can be used to evaluate the BNNSs/polymer interfacial stress transfer.

Three types of BNNSs with different geometries have been prepared by liquid-phase exfoliation and used to reinforce poly(vinyl alcohol) (PVA) with different loadings. Raman spectroscopy has been used to both evaluate the distribution of the BNNSs in the nanocomposites and follow stress transfer from the polymer matrix to the BNNSs. The reinforcement of the polymer has then been modelled using a combination of the rule of mixtures and modified shear lag theory. It has been demonstrated that the BNNSs with the larger aspect ratio are needed for realizing high levels of reinforcement.

A detailed study has also been undertaken of the mechanisms of stress transfer in a nanocomposite consisting of BNNTs in a PVA matrix. The structure of the BNNTs has been characterized using transmission electron microscopy (TEM). The dispersion of nanocomposites containing up to 1 wt% of both pristine and hydroxyl-functionalized nanotubes (OH-BNNTs) in PVA have been characterized using a combination of TEM and Raman mapping. Stress transfer from the PVA matrix to both the BNNTs and OH-BNNTs has been evaluated from stress-induced shifts of the hBN Raman G band and larger band shifts have been obtained for the latter. This is in agreement with the mechanical testing results where functionalized nanotubes exhibit better reinforcement. Moreover, it has been found that polarized Raman spectroscopy can be used to characterize of orientation of BNNTs in the nanocomposites.

List of Symbols

c	Speed of light
C_h	Chiral vector
d	Nanotube diameter
$\vec{e_s}$	Tensor for scattered radiation
$\vec{e_I}$	Tensor for incident radiation
E	Oscillating electric field strength
$E_{\|\|}$	Young's modulus of the composite with uniaxially-aligned fillers
E_0	Vibrational amplitude
$E_{\text{2D material}}$	Young's modulus of the 2D material monolayer
$E_{\text{BNNS}}, E_{\text{BNNSs}}$	Young's modulus of the BNNS (or BNNSs)
E_{BNNTs}	Young's modulus of the BNNTs
E_{c}	Young's modulus of the composites
E_{eff}	Effective Young's modulus of the filler
E_{f}	Young's modulus of the filler
E_{m}	Young's modulus of the matrix
E_{r}	Young's modulus of the composite with randomly-distributed fillers
f_c	Degree of crystallinity
G_m	Shear modulus of the matrix
h	Planck's constant
I	Intensity of Raman band
I_{P}	Intensity of the Raman band at peak position
k	Interlayer transfer efficiency
l	Length of the filler along the strain direction

L, t	Length and thickness of Liquid-phase exfoliated BNNSs
l_c	Critical length
N	Number of layers
$P_2(\cos\theta)$	Legendre polynomial of the 2nd degree
q	Nuclear displacement
q_0	Amplitude of molecule nuclear vibration
r	Radius of the 1D filler
s	Aspect ratio of the filler
t	Thickness of filler
T	Total thickness of polymer matrix
T_g	Glass transition temperature
T_m	Melting temperature
v	Poissons ratio
V_{BNNSs}	Volume fraction of the BNNSs
V_{BNNTs}	Volume fraction of the BNNTs
V_f	Volume fraction of the filler
ν_q	Frequency of molecule nuclear vibration
x	Distance along the filler from one end
W_{BNNSs}	Mass fraction of the BNNSs
W_{BNNTs}	Mass fraction of the BNNTs
α	Molecular polarizability or Polarizability tensor
α_0	Equilibrium molecular polarizability
$(\partial\alpha/\partial q)_0$	Change rate of polarizability against the nuclear displacement
ΔH_m	Heat of fusion
$\Delta\nu_0$	Frequency change after scattering
ε_{BNNS}	The variation of strain in the BNNS
ε_m	Strain applied on the matrix

η_a	Agglomeration factor
η_l	Length factor
η_o	Krenchel orientation factor
γ_G	Grüneisen parameter of hBN G band
θ	Chiral angle or Angle between the scattering and incident X-ray
θ,ϕ,ξ	Euler angles
κ	In-plane thermal conductivity
λ	Wavelength
λ_2	Parameter in orientation distribution function
ν_0	Frequency of the light
ρ_{BNNSs}	Density of BNNSs
ρ_{BNNTs}	Density of BNNTs
ρ_{PVA}	Density of PVA
σ_f	Axial stress in the filler
τ	Shear stress
τ_i	Interfacial shear stress
Φ	Angle of incident laser polarization
ω	Raman frequency (wavenumber)
$(d\omega_G/d\varepsilon)$, $(d\omega_{E2g}/d\varepsilon)$	Raman band shift rate of hBN G (E_{2g}) band
$(d\omega_G/d\varepsilon)_{reference}$	Reference Raman band shift rate of hBN G band
$(d\omega_{E2g}/d\varepsilon)(ref)$	Reference Raman band shift rate of hBN E_{2g} band
$\partial\omega_{2D}/\partial\varepsilon$	Band shift rate of graphene 2D band
$\partial\omega_D/\partial\varepsilon$	Band shift rate of graphene D band
Γ	Half width at half maximum of the Raman band

List of Abbreviations

℃	Celsius degree
1D	One-dimensional
1L, 2L, 3L	Monolayer, Bilayer, Trilayer
2D	Two-dimensional
AFM	Atomic Force Microscope
at%	Atomic ratio
$B_3N_3H_6$	Borazine
BN	Boron nitride
BNNRs	Boron nitride nanoribbons
BNNSs	Boron nitride nanosheets
BNNTs	Boron nitride nanotubes
cBN	Cubic boron nitride
CCD	Charge-coupled device
CL	Cathodoluminescence
CNTs	Carbon nanotubes
CVD	Chemical vapor deposition
DFT	Density functional theory
DMF	Dimethyl formamide
DMTA	Dynamic mechanical thermal analysis
DSC	Differential scanning calorimetry
DW	Double-walled or Deionized water
EDS	Energy dispersive X-ray spectroscopy
EELS	Electron energy loss spectroscopy
EPIC	Extended-pressure inductively-coupled plasma
eV	Electronvolt
FTIR	Fourier transform infrared spectra

FWHM	Full width at half maximum
GNPs	Graphite nanoplatelets
GO	Graphene oxide
GPa	GigaPascal
HABS	Hydrogen-assisted BNNT synthesis
hBN	Hexagonal boron nitride
HBP	Hyperbranched aromatic polyamide
HP-HT	High pressure-high temperature
HR	High resolution
HST	Hansen solubility parameter
IPA	Isopropanol
ISM	Interlayer shearing mode
K	Kelvin
kV	Kilovolt
kW	Kilowatt
LE	Liquid-phase exfoliation
MHz	Megahertz
min	Minute
MoS_2	Molybdenum disulfide
MPa	MegaPascal
mV	Millivolt
MW	Multi-walled
NIMS	National institute for materials science
nm	Nanometer
NMP	N-methyl-2-pyrrolidinone
ODA	Octadecylamine
ODF	Orientation distribution function
PA	Polyamide

PAN	Polyacrylonitrile
PC	Polycarbonate
PET	Poly(ethylene terephthalate)
PI	Polyimide
PL	Photoluminescence
PMMA	Polymethyl methacrylate
PmPV	Poly(m-phenylenevinylene-co-2,5-dioctoxy-pphenylenevinylene)
PS	polystyrene
PTFE	Polytetrafluoroethylene
PVA	Poly(vinyl alcohol)
PVB	Polyvinyl butyral
PVC	Poly(vinyl chloride)
PVD	Physical vapor depostion
PVDF	Poly(vinylidene fluoride)
PVF	polyvinyl formal
PVP	Polyvinylpyrrolidone
RBM	Radial breathing mode
rpm	revolutions per minute
SBR	Styrene-butadiene rubber
SEM	Scanning electron microscope
SRS	Stimulated Raman scattering
STEM-ADF	Scanning transmission electron microscopy annular dark field
SU-8	Photoresist
SW	Single-walled
TEM	Transmission electron microscope
TGA	Thermogravimetric analysis
TPa	TeraPascal
TPU	Thermoplastic polyurethane

ULF	Ultra low frequency
UV	Ultraviolet
vol%	Volume fraction
W	Watt
wBN	Wurtzite boron nitride
WS_2	Tungsten disulfide
wt%	Mass fraction
XPS	X-ray photoelectron spectroscopy
XRD	X-ray diffraction
µm	Micrometer

Declaration

No portion of the work referred to in the thesis has been submitted in support of an application for another degree or qualification of this or any other university or other institute of learning.

Copyright Statement

Acknowledgement

First and foremost, I would like to express my most sincere gratitude to Professor Robert Young for the enthusiastic supervision and encouragement throughout this project. Second, my gratitude also goes to Dr. Mark Bissett for his helpful suggestions and kind help during this project.

I would also like to thank Professor. Ian Kinloch for the discussions. My gratitude also goes to Dr. Jonny Blaker for his kind help and guidance on electrospinning and National Research Council Canada for providing the BNNT samples. I would like to thank in particular Mr. Andrij Zadoroshnyj for his kind assistance on Raman spectroscopy and mechanical testing equipments, and Dr. Teruo Hashimoto and Dr. Eric Prestat for their guidance and help on the electron microscope. My thanks also go to the staff in the Departments of Materials, Chemistry and the NGI for their support.

I would also like to express my appreciation to all the colleagues in the group, particularly Dr. Alex Marsden, Dr. Zheling Li, Dr. Dimitrios Papageorgiou, Dr. Jianyun Cao, Dr. Oday Jawad, Dr. Cristina Vallés, Dr. Eunice Cunha, Dr. Mahdi Alqawaz, for their guidance and encouragement through different stages of this project. My gratitude also goes to the colleagues in the Mill G22, friends in the University and visiting scholars from AECC BIAM for their help and friendship.

My gratitude extends to China Scholarship Council (CSC) for their financial support.

Finally, I would like to thank my families and friends, especially my mother for constant support and encouragement. I would also like to thank my dad and two grandfathers who left me several years ago, their glories and expectation for me are endless motivation for my study in the UK.

Chapter 1 BNNSs & BNNTs-Structure, Preparation, Properties

1.1 Introduction

Since the discovery of one-dimensional (1D) carbon nanotubes (CNTs) [1] and two-dimensional (2D) graphene [2], low-dimensional nanomaterials have been regarded some of the most promising materials in 21st century and attracted worldwide attention. Boron nitride nanotubes (BNNTs) and boron nitride nanosheets (BNNSs), were synthesized only 4 years [3] and 1 year [4] after the report of their carbon analogues, respectively. A series of papers in the last decade reported that both BNNTs and BNNSs, with excellent mechanical strength, electrical insulation and thermal conductivity, are ideal nanofillers for polymers.

This chapter reviews the structure, preparation, properties of BNNSs and BNNTs, some recent work on the preparation of BNNTs, measurement of intrinsic mechanical and thermal properties of BNNSs is introduced in detail.

1.2 Structure

1.2.1 Structure of hexagonal boron nitride (hBN)

Typically, boron nitride (BN) is a chemical compound consisting of boron and nitrogen atoms. BN has three different types of crystal structures (Figure 1.1 [5]): cubic boron nitride (cBN), which is analogous to carbon-based diamond, wurtzite boron nitride (wBN) and graphite-like hexagonal BN (hBN) (note that the layered structure can also be stacked in a rhombohedral form). hBN is the most stable crystal

phase among the three structures [6].

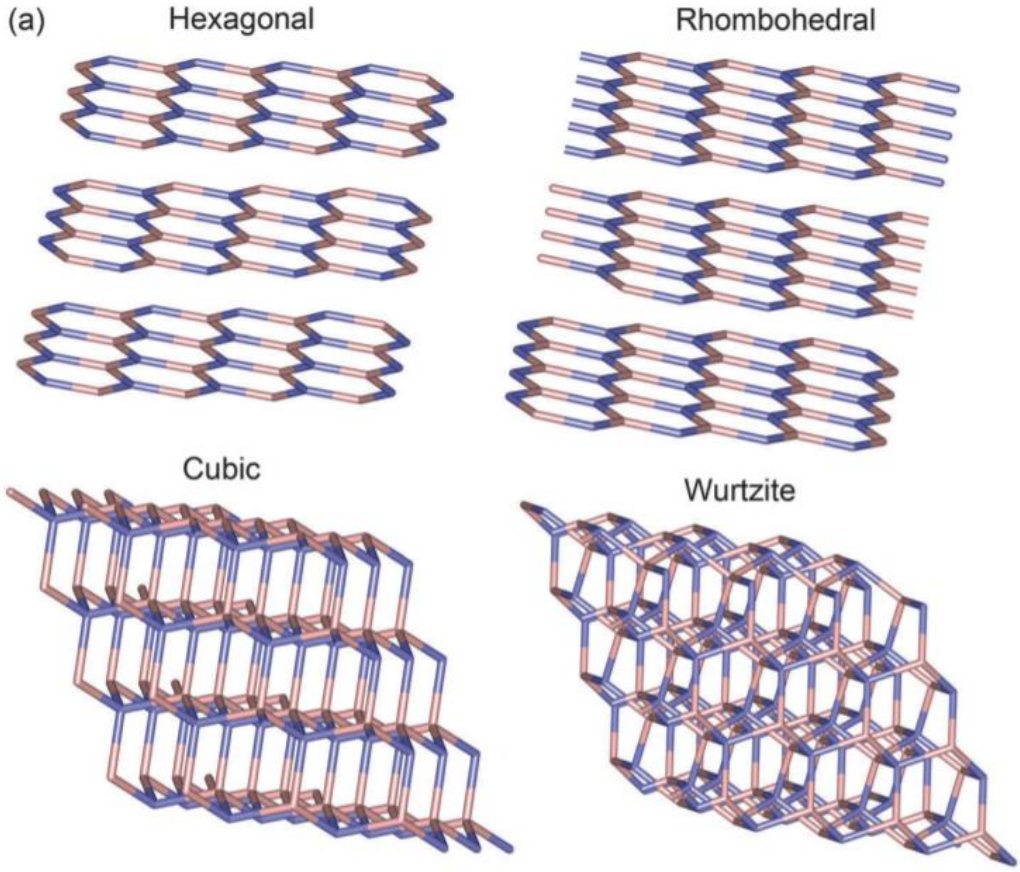

Figure 1.1 Boron nitride with different crystal structures [5].

Layered hBN can be regarded as an analogue of graphite substituting carbon atoms with boron and nitrogen atoms [7]. hBN has a typical layered structure like graphite, alternating boron and nitrogen atoms in a 2D hBN layer are linked by strong covalent bonds, while the neighbouring layers are held by van der Waals forces at a distance of 0.333nm (compared to 0.337 nm for few-layered graphene and graphite) [8-9]. The bond length of B-N is 0.144 nm, which is very close to the value of C-C bond in graphene (0.142 nm) [10], the mismatch between graphite and hBN is only ≈1.6% [11]. Relevant crystallographic information for hBN and graphite has been summarized in a review paper, as shown in Table 1.1 [5]. It can be observed that relevant parameters of hBN and graphite are nearly identical, therefore hBN inherits a series of common properties from graphite, such as high mechanical strength, thermal

conductivity and good lubrication [6].

Table 1.1 [5] Crystallographic parameters of hBN and graphite.

Material	Crystal	Bond length	Lattice parameters (nm)	Interlayer spacing (nm)
hBN	Hexagonal	0.144 nm	*a*: 0.250 *c*: 0.666	0.333
Graphite	Hexagonal	0.142 nm	*a*: 0.246 *c*: 0.670	0.335

However, different from the typical AB stacking of graphite in which each carbon atom is sitting above and below the center of a benzene ring in the neighbouring layers [2], hBN typically demonstrates an AA' stacking order in which B and N atoms are superposed in succession along the *c* axis [12-14], as shown in Figure 1.2 [8, 15]. Due to the difference in electronegativity of B and N, B-N bonding exhibits a partially ionic character. This leads to the favorable electrostatic and polar-polar interactions [16-18]. The so-called "lip-to-lip" interactions between adjacent layers are deduced to be stronger than those between graphene layers, therefore it is more difficult to exfoliate ultrathin hBN nanosheets due to stronger interlayer binding. In addition, detailed DFT calculations about other possible stacking orders of hBN are reported elsewhere [19].

Apart from different layer stacking preference, the electronegativity difference between boron and nitrogen atoms within hBN also leads to the localization of unpaired π electrons around the nitrogen atomic centres, therefore forming a insulating material with wide band gap [9, 20-21]. This special insulating property leads to potential applications of hBN, such as both insulating and thermally conductive fillers [22].

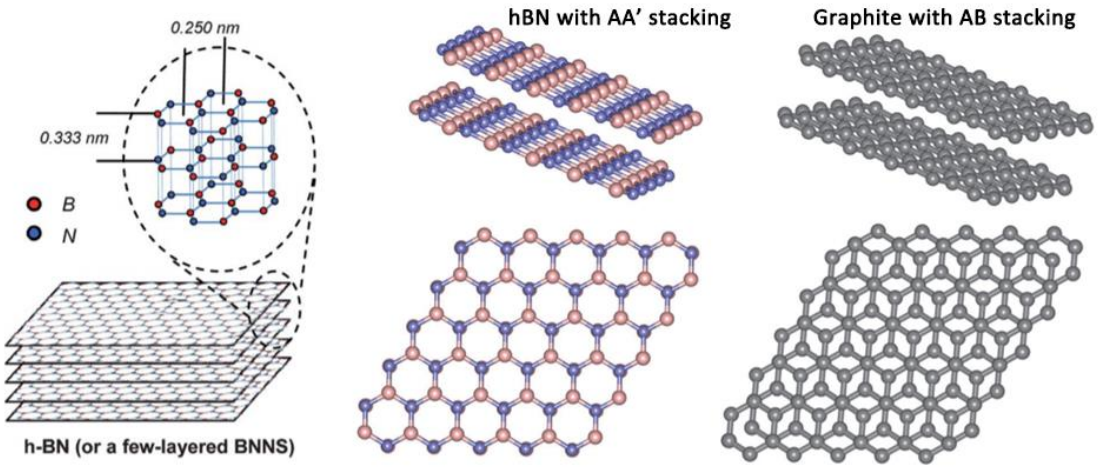

Figure 1.2 Structure of hBN [8] and highly-crystallized hBN with a typical AA' stacking order and graphite with an AB Bernal stacking sequence [15].

1.2.2 Structure of BNNSs

BNNSs refer to the hBN nanostructure constrained to the nanometer scale, for example, an individual hBN layer can be named as "monolayer BNNS", and a thin hBN crystal with several layers is called "few-layered BNNS" [8]. A BNNS monolayer is a honeycomb structure that consists of hexagonal ring units of B_3N_3, analogous to a graphene monolayer which has a carbon skeleton, so BNNSs are also called "white graphene" [23-25]. Similar to bulk hBN, the B-N bonds within BNNSs are partially ionic, and the distance between the centres of adjacent borazine rings is 0.25nm, very close to the value of graphene (0.246 nm). The edge of BNNSs can either be Nitrogen-edged zigzag or Boron-edged zigzag, as well as armchair, as shown in Figure 1.3.

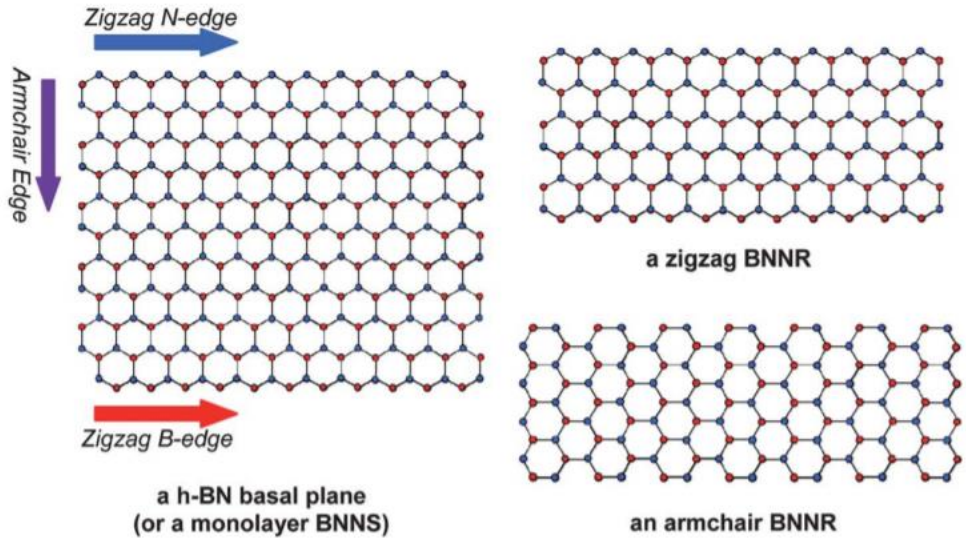

Figure 1.3 Schematic diagram of a monolayer BNNS and hexagonal boron nitride nanoribbons (BNNR) with different edge structures [8].

It has been reported the formation of multilayered BN will stabilize the structure of BNNSs, due to the different electronegativity between B-N atoms and consequent "lip-lip" interlayer interactions (i.e. B-N bonds are partially ionic and chemical bonds form as spot-welds between the atoms of adjacent layers) in the nanosheets [26-28]. In terms of multilayer structure, BNNSs normally exhibit a preference for AA' stacking, but a DFT calculation indicates that it is possible for adjacent hBN layers freely slide from AA' stacking order to AB stacking order along energetically favorable directions despite a band gap reduction of 0.6 eV [29]; experimentally, Warner et al. [30] reported that BNNSs can also have AB stacking. They used continuous electron radiation to generate defects inside a chemically exfoliated BNNS and detected AB stacking in the step edge between a hBN monolayer and hBN bilayer via high resolution transmission electron microscopy (HR-TEM).

In addition to layer stacking, a DFT calculation from Alem et al. [31] suggests covalent B-N bonds are spontaneously formed not only between boron and nitrogen atoms within single layer, but also between adjacent hBN layers. This results in a structure analogous to a folded hBN monolayer, which massively increases the

difficulty for exfoliating hBN monolayer, even though the stronger interlayer interactions in hBN only have a negligible influence upon the interlayer distance [9].

Before 2010, although atomically thin hBN had been prepared [4] and investigated by TEM and AFM [30, 32-34], it was still quite hard to exfoliate hBN monolayer with a large enough flake size due to the lack of suitable hBN crystals for exfoliation. The situation changed after the production of high-quality hBN single crystals [34-37], and it is now possible to isolate BNNSs of several nanometers thickness (even monolayer) with relatively large lateral size (~100 μm). It should be specially noted that although some workers used Momentive crystals [34], the majority of publications concerning mechanical exfoliation of atomically thin BNNSs used high-purity single crystals from Japan's NIMS [38]. Based on AFM measurements of BNNS [39-41], a hBN monolayer has a thickness of ~0.4 nm (including trapped moisture), both for scotch tape exfoliation [42-43] and the CVD grown method [44]. Liquid-exfoliated monolayered hBN exhibits higher AFM-measured thicknesses due to residual solvents between the nanosheet and underlying silicon substrate, with a value of ~ 1 nm [45], similar to the thickness of a graphene oxide monolayer [40].

Several important review papers [5, 8] have discussed defects in BNNSs. First of all, the Stone-Wales defect (pentagon-heptagon fused ring), which is a very common imperfection in sp2 carbon allotropes (such as graphene and carbon nanotubes), are not thermodynamically favorable due to the necessity to form B-B or N-N bonds [46-47]. Although DFT calculations predicted that this structural defect can be stabilized by bond rotation, distortion of the nanosheet planes or the formation of square-octagon (4-8 fused ring) structures [48-49], Stone-Wales defects are rarely observed using HR-TEM [25, 32, 50].

Other two types of defect are grain boundary [51-52] and point defects [30, 32]. Point defects are observed in hBN monolayers and bilayers under electron radiation or ion etching. It is found that boron atoms are removed more easily under electron beam radiation [53] and the same type of vacancy (boron or nitrogen) was not only found within a single hBN layer, but also throughout the entire BNNS structure [8, 32].

All the three types of defect will affect relevant properties of BNNSs, such as band gap reduction [54-56], phonon scattering and consequent thermal conductivity reduction [57] and chemical reactivity (for easier functionalization) [6, 58-59].

1.2.3 Structure of BNNTs

Multi-walled hexagonal boron nitride nanotubes (MW-BNNTs) were first synthesized in 1995 [3] and in 1996, the synthesis of single-walled BNNTs (SW-BNNTs) was also realized [60].

Generally, BNNTs can be imagined as rolled BN sheets, so SW-BNNTs can be regarded as formed by rolling up a hBN monolayer nanosheet. Similar to 2D nanosheets, it is harder to prepare and study SW-BNNTs [61-62] than SW-CNTs due to the partially ionic nature of B-N bonding and so-called “lip-lip” interlayer interactions. The formation of a multiwalled structure is favourable for stabilization. In MW-BNNT structure, the nanotube walls are ordered with a 0.33 – 0.34 nm interlayer distance; this value might be slightly higher than that of bulk hBN (~0.33 nm), resulting from inner stress in the bent walls [63].

As shown in Figure 1.4 [64], there are three types of the tube helicities: “zig-zag” type with a (9, 0) helical structure; “arm-chair” type with a (6, 6) helical structure; and many helical types with varying chiral angles (chiral type). Arenal et al. [65] referred

to the well-established theory of CNTs and introduced a so-called chiral vector C_h = na_1+ ma_2 which is perpendicular to the tube axis direction (where a_1 and a_2 are the lattice vectors, and n and m are two indices for defining C_h) for estimating tube folding direction. The chiral angle (θ), which is the angle between C_h and lattice vectors a_1 and a_2 is used for distinguishing helicity of BNNTs: θ=0 ° (zigzag type), θ=30 ° (armchair type), 0 ≪θ<30 ° (chiral type). Although arm-chair and chiral structures have been observed in BNNTs, the majority of tubes studied by researchers displayed a zigzag configuration, which is quite different from CNTs in which both helicities are equally possible [7].

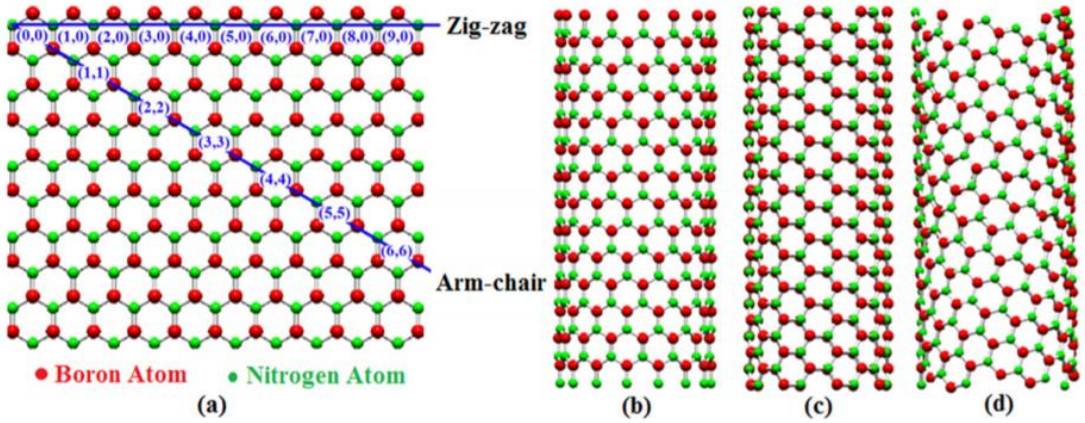

Figure 1.4 (a) Planar hBN single sheet with possible wrapping types and corresponding (n, m) indices. (b) SW-BNNTs with zigzag helicity. (c) SW-BNNTs with armchair helicity. (d) A chiral tube with a 0°<θ<30° [64].

For MW-BNNTs, adjacent layers tend to have a hexagonal or rhombohedral stacking order, that is to say AA' stacking is preferred (same as BNNSs). The AA' stacking order within MW-BNNTs is due to the strong tendency to form atomically perfect B-N stacked adjacent layers. This is quite different from the case of CNTs which allow disordering and interlayer slippage between neighbouring layers.

In consideration of the cross section of MW-BNNTs, a polygonized cross section is favourable rather than a cylindrical section, since the B-N-B-N stacking order across a

tube can be easily maintained and stabilized within a multiple-layered polygonized structure. This type of stacking will easily break a cylindrical MW nanotube due to incremental circumference from the inner BN layer to the outer BN layer [66].

The tip (or end) is another important structural feature of BNNTs. CNTs contain a capped end with six pentagonal C-C rings and these five-membered rings are evenly distributed or not on the surface of the tube [65]. Heptagons can also be introduced with pentagons for closing the tip of CNTs and the shape of these ends should be hemispherical or conical (like a hemisphere of a C_{60} molecule). However, the formation of five-member ring will involve the introduction of B-B and N-N bondings, which are energetically unfavourable. Instead of the odd-numbered rings in CNTs, BNNTs prefer to close the tip by introducing even-numbered rings, especially square rings.

1.3 Preparation

1.3.1 Preparation of bulk hBN

Boron nitride was first prepared by Balman [67] in the 1840's, but the chemical structure was unstable. Afterwards, the synthesis of hBN was limited to the lab scale for a hundred years due to the expensive raw materials and lack of production routes. In the 1950s, boron nitride with a stable crystal structure was first produced on the industrial scale [68].

Recently, different methods have been employed to produce hexagonal boron nitride, such as "classical high-temperature route" [69], "vapor deposition" [70-71], "condensed-phase pyrolysis of molecular reagent" [72-73]. In industry, the most popular route for preparing hBN powders is by heating boric acid/boric oxide and

ammonia/urea/melamine mixture at 900 ℃, followed by a 1500 ℃ annealing under a N_2 flow to increase the crystallinity of the hBN powders [74-75]. Another commercial preparation route is to use calcium hexaboride, boric oxide and nitrogen gas, with a 1500 ℃ reaction temperature [76].

Route 1:

$$B_2O_3 + 2\ NH_3 \rightarrow 2\ BN + 3\ H_2O \quad (T = 900\ ℃)$$

$$B(OH)_3 + NH_3 \rightarrow BN + 3\ H_2O \quad (T = 900\ ℃)$$

$$B_2O_3 + CO(NH_2)_2 \rightarrow 2\ BN + CO_2 + 2\ H_2O \quad (T > 1000\ ℃)$$

Route 2:

$$B_2O_3 + 3\ CaB_6 + 10\ N_2 \rightarrow 20\ BN + CaO \quad (T > 1500\ ℃)$$

In particular, single crystals of hBN with high purity can be prepared by using a so-called temperature gradient method [77]: boron nitride powder is used as raw material, it is heated to a very high temperature (2100 ℃ for 2h) to remove oxygen impurities, the powder is then mixed with a particular metal solvent (catalyst) and put into a modified high pressure-high temperature (HP-HT) apparatus for crystals growth under high temperature (such as 1500 – 1650 ℃ for $Ba_3B_2N_4$ solvent) and high pressure (such as 4-5 GPa for $Ba_3B_2N_4$ solvent) for 20 – 80 hours. Different metal solvent systems have been studied previously, such as: the classical $Ba_3B_2N_4$ (Ba-BN) solvent [36, 38], a Ni-Mo solvent (atmospheric pressure preparation) [37], a Ni-Cr solvent (atmospheric pressure preparation) [78], and a Mg-B (boron powder) solvent [79]. As prepared hBN single crystals can achieve a size of several millimeter and high purity (Figure 1.5(b)). They have been widely used for producing atomically-thin BNNSs by exfoliation.

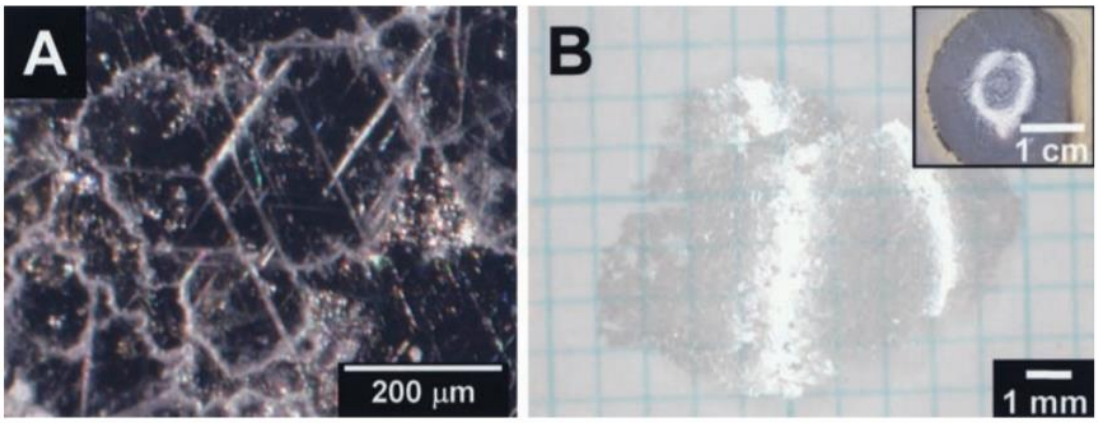

Figure 1.5 (a) Optical graph of recrystallized hBN on solidified Ni-Mo solvent. (b) Optical graph of highly-pure hBN crystals after acid treatment [37].

1.3.2 Preparation of BNNSs

After the first successful exfoliation of BN in 2005 [4], different methods have been employed to prepare BNNSs with atomic thickness, which can be summarized as top-down approach which refers to the exfoliation of bulk hBN; and a bottom-up approach which relates to the synthesis of BNNSs from a boron and nitrogen precursor, such as chemical vapor deposition (CVD), as illustrated in Figure 1.6 [80]. In this review, the top-down method will be the main subject of discussion as it was employed in this present study.

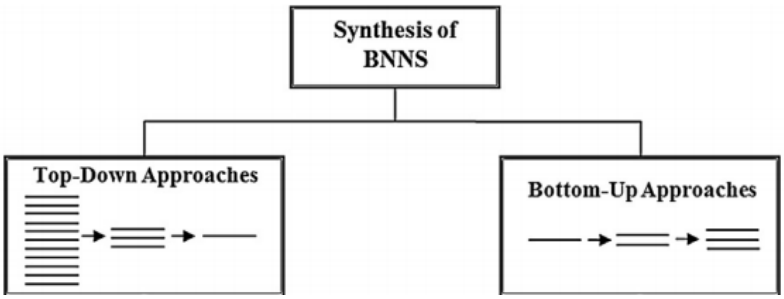

Figure 1.6 Two general routes for the synthesis of boron nitride nanosheets [80].

Mechanical cleavage The initial approach for exfoliating 2D materials, mechanical cleavage is also known as “scotch tape method” [4]. It has been applied for preparing

a series of 2D materials for fundamental studies and BNNSs with different thickness (from monolayer to many layers) and lateral sizes (maximum 100 microns can be achieved) have been successfully prepared by cleaving the adhesive tape [4, 32, 42-43, 81-87]. In brief, a bulk crystal of hBN is placed on the middle of an adhesive tape, another piece of adhesive tape is then used to cleave the bulk crystal by peeling the top tape. The tape is attached and pressed on a substrate (such as SiO_2/Si wafer), thus the exfoliated BNNS is transferred and identified by optical microscopy. BNNSs prepared by this method partially retain the original lateral size and low defect density of bulk hBN. However, there are two challenges for the exfoliation of hBN. First of all, it is hard to exfoliate BNNSs with a sufficiently large flake size, especially monolayer due to the lack of appropriate hBN crystals for scotch tape exfoliation [4]. This problem has been solved with the availability of hBN single crystals [36, 38], which enables the cleavage of BNNS with relatively large sizes (~100 μm) and of atomic thickness. Secondly, the scotch tape method is less effective to exfoliate monolayer and few-layered hBN than graphene. This might be due to the stronger "lip-lip" interaction between adjacent BN planes, i.e., the formation of a multilayer structure can stabilize the BNNSs structure. Although it is more difficult to exfoliate hBN monolayer than graphene, mechanical cleavage is still the optimal method to prepare BNNSs with high quality and large lateral size.

Liquid phase exfoliation The preparation of few-layered BNNSs by a sonication-assisted liquid exfoliation method was initially reported in 2008 [33]. In this pioneering work, 0.2 mg hBN crystals were sonicated in a 5 ml polymer/1, 2-dichloroethane solutions for 1 hour, some few-layered BNNSs were obtained. Afterwards, Zhi et al. [15] successfully fabricated few-layered BNNSs on a large scale by sonicating 1 g hBN powder in 40 ml DMF. As-prepared BNNSs were then incorporated into polymer matrix and achieved a good reinforcement. Spectroscopic work indicated [88] a strong interaction between the oxygen atoms in organic solvent

and boron atoms on BNNSs, which contributed to the sufficient liquid exfoliation. It is also reported that a series of polar organic solvents can be used for solvent exfoliation, while non-polar organic solvents seems to be ineffective for BNNSs preparation, as illustrated on Figure 1.7(a) [8].

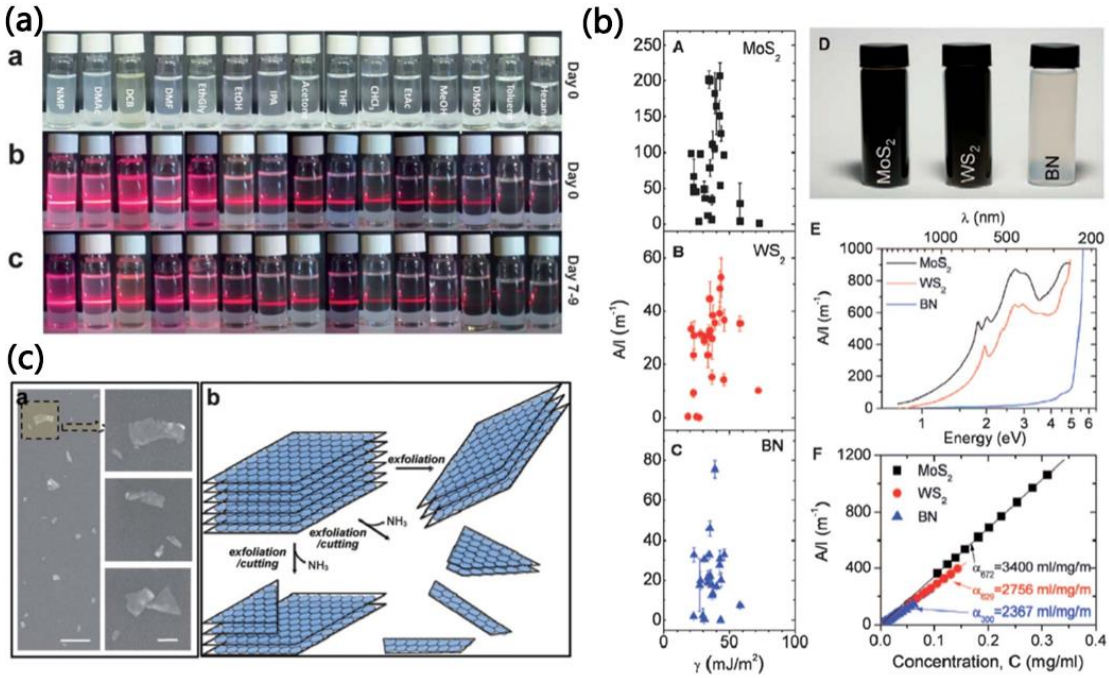

Figure 1.7 (a) a. Photograph of organic dispersions of BNNSs prepared from simple bath sonication. b. Tyndall effect graph of relevant dispersion right after preparation. c. Pictures taken after 1 week [8]. (b) Preparation of organic dispersions of exfoliated hBN using guidance from the Hansen solubility parameter theory (a-c), d. Optical micrographs e. Absorbance spectra and f. Lambert-Beer plots for the dispersions of nanosheets of MoS_2 in NMP, WS_2 in NMP, hBN in IPA [89]. (c) Water-based liquid exfoliation of BNNSs with ~ 100 nm small lateral sizes [45].

To comprehend the efficiency of different solvents used for BNNSs preparation, Coleman et al. [89] used Hansen solubility parameter (HST) theory to explain and optimize the solvents for hBN exfoliation, as well as MoS_2 and WS_2, as shown in Figure 1.7(b). Similar to relevant work of SWCNTs [90] and graphene [91] dispersions, HST theory study suggests that the proper solvents for successful exfoliation should be those that minimize the energy of exfoliation (enthalpy of

mixing). In other words, the solvent should have a similar surface energy to the nanosheets. A systematic survey of different types of organic solvent for dispersing BNNSs was undertaken in this work. The dispersion effect suggested that the optimal solvent for BNNSs exfoliation should have surface energies of around 65 mJ m^{-2}, with IPA (isopropanol) among the best, which achieved a 0.06 mg/ml concentration of BNNSs in dispersions. A recent study [92] using the surface tension component to assess solvents for liquid exfoliation was published. It is suggested that a highly stable dispersion of BNNS is achieved when the surface tension of BNNS matches with solvent, in which the ratio of polar to dispersive component is ~0.45 (theoretical value based on the Owen, Wendt, Rabel, Kaelble theory [93] that the interfacial surface tension can be separated into polar and dispersive contributions) and ~0.6 (UV-absorbance results).

Additionally, some new strategies have been reported to achieve a similar surface tension between BNNSs and solvent. For example, Zhou et al. [94] reported a simple mixed solvent route. They mixed two poor solvents for BNNSs dispersion: ethanol and water with different volume ratios and achieved a mixed solvent with surface energy value close to that of BNNSs. They reported a maximum 0.075 mg/ml concentration of BNNSs in 55 vol% ethanol/water solvent, even higher than the concentration of IPA dispersion. Li et al. [40, 58] initially came up with a "functionalization-sonication" route to prepare thin functionalized hBN. By reacting hBN with octadecylamine (ODA) for 4-6 days at ~180 ℃, the functionalized hBN was then briefly sonication and centrifuged in THF and functionalized BNNSs with 1-7 nm thickness/~1 μm average lateral size was prepared. Different functional groups, such as –OH groups [45], $-NH_2$ group [95], Alkyl group [96] etc. have been successfully grafted on hBN, and the funtionalized hBN can be used for preparing BNNSs using sonication-assisted methods, as summarized in Figure 1.8 [6].

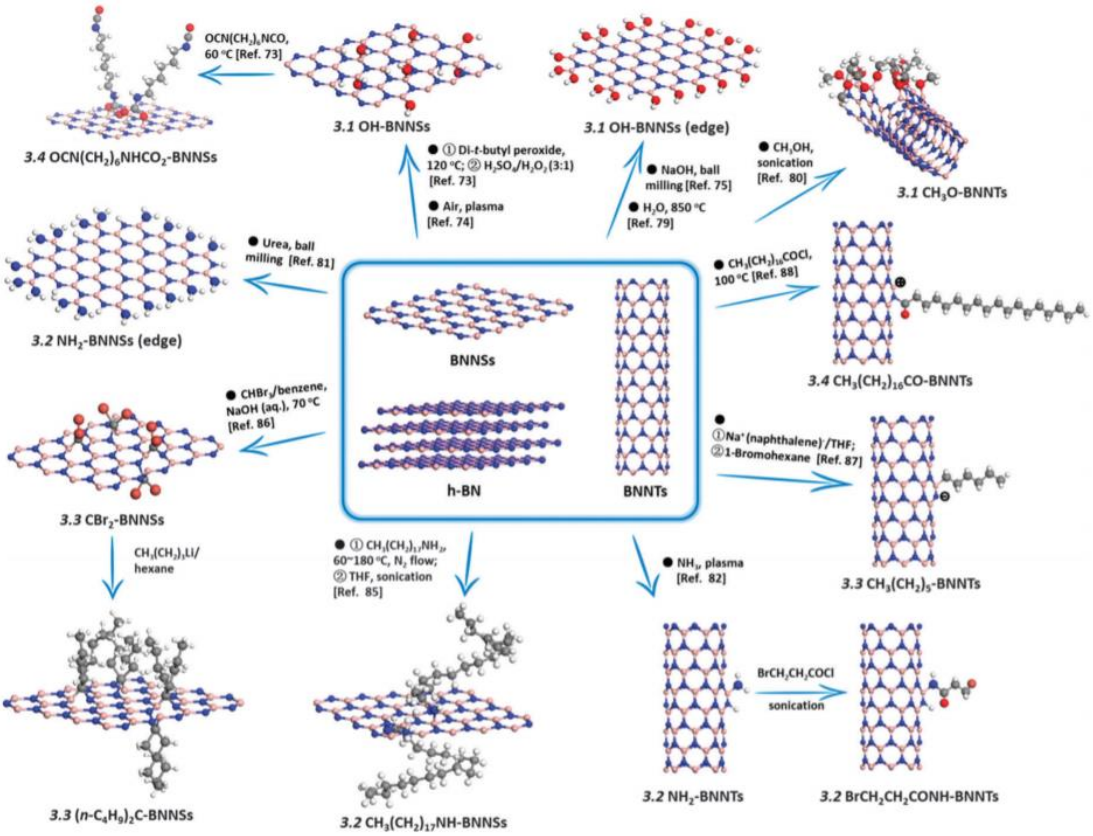

Figure 1.8 Summary of chemical functionalization of BNNSs and BNNTs [6].

In summary, scalable preparation of BNNSs can be achieved by liquid exfoliation and even BNNS monolayers can be prepared. However, it is still a challenge to prepare thin BNNSs with a large enough size using this method (typically < 1 μm when the thickness is very small).

Other approaches Apart from mechanical cleavage and liquid phase exfoliation, other top-down approaches, such as ***Ball-milling*** [95], ***Vortex fluid exfoliation*** [97], ***Electron irradiation*** [98] et al. have been used to exfoliate bulk hBN as BNNSs.

For Bottom-up approaches, first ***Chemical vapor deposition (CVD)*** growth of hBN monolayer was reported in 1990 [99]. In this work, borazine ($B_3N_3H_6$) was decomposed and deposited on Pt(111) and Ru(111) substrates. Later, Oshima et al. [100] successfully prepared hBN single-crystalline monolayer hBN on Ni(111)

substrate using borazine as precursor as well. Until now, hBN monolayer has been successfully grown on a series of transition metal substrate such as Cu(111) [101], Pt(111) [102] etc.. Very recently, Lee et al. [103] reported the wafer-scale preparation of single-crystalline BNNSs monolayer by CVD. This is a milestone work in the CVD preparation of BNNSs. The various CVD preparations of BNNSs have been reviewed in several important papers [5, 8, 80, 104]. Beyond that, ***Physical vapour deposition (PVD)*** [80] can also be used to prepare BNNSs with high quality.

Apart from top-down and bottom-up approaches, BNNSs can be substituted from graphene (***chemical substitution***) [105-107]. Furthermore, some other methods such as ***chemical blowing*** [108], ***B,N-contained compounds prolysis*** [109], ***surface segregation*** [110] etc. were also reported.

1.3.3 Preparation of BNNTs

As summarized in relevant review papers [111], a variety of methods have been used to prepare BNNTs. In brief, an ***arc-discharge method*** (the first method for BNNTs preparation) can be used to fabricate BNNTs via an arc-discharge between a boron compound-packed tungsten rods and electrodes (such as copper [3] for MW-BNNTs or HfB_2 [60] for SW-BNNTs). Arc-discharge prepared BNNTs exhibits good crystallinity due to high reaction temperature, but the reaction generates impurities (e.g. BN onions, cages etc.).

The Laser ablation method was first adopted by Golberg et al. [112] to prepare BNNTs in 1996. Basically, a stable CO_2 laser was focused onto the edge of the BN precursors to heat them up to 5000 ℃. MW-BNNTs were prepared first by using cubic BN single crystals and hBN crystals [113] as a precursor. In 2007, Arenal et al. [61] successfully synthesized SW-BNNTs using this method, by optimizing

synthesis parameters such as nitrogen pressure in reaction chamber, nitrogen flow rate, laser power etc.. Although laser ablation can be carried out without any catalyst [114], the addition of Co or Ni as catalyst can elongate the tube length, meanwhile reducing the number of walls. However, some extra effort has to be made to improve the purity of the final product, such as centrifugation [115].

The hard-template method is also used and can be divided into two routes: the CNT substitution reaction [116] and porous alumina filter template [117]. In the case of CNT substitution (Figure 1.9), CNTs are reacted with B_2O_3 (boron source) under N_2 or NH_3 atmosphere (nitrogen source). Thus a $B_xC_yN_z$ structure is obtained and then oxidized at high temperature to remove extra carbon. However, it is very difficult to completely remove carbon in the product, so the as-prepared BNNTs are generally doped with carbon. The introduction of metal oxide such as MoO_3 [118] can improve the yield of BNNTs. The advantage of CNTs substitution is that the morphology of carbon nanotubes can be inherited well, in other words, SW-BNNTs [119] can be prepared from SW-CNTs by this method. However, it is important to control the reaction temperature and time as overreaction will accelerate the growth of hBN on the tube walls and stick the tubes together. The porous alumina route decomposes 2,4,6-trichloroborazine as hBN at high temperature and fills the inner pores of alumina. The as-prepared product shows a tubular structure, but is likely to have a polycrystalline structure [120].

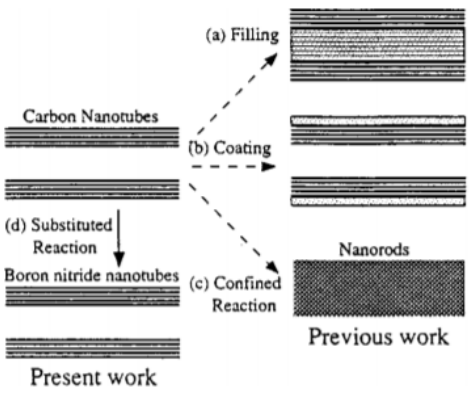

Figure 1.9 Schematic diagram of the CNT substitution reaction for BNNT

preparation [116].

An autoclave can be also used to prepare BNNTs with metals as catalysts (such as Mg, Co, Fe etc.), boron or NH_4BF_4 as the boron source and NH_4Cl or NaN_3 as the nitrogen source [121-122]. However, the as-prepared BNNTs demonstrate thin walls and a large inner space. Additionally, both the quality and yield are not satisfactory.

A ***Ball-milling method*** was first reported by Chen et al. [123]. Bulk hBN powders were ball-milled to generate a highly-disordered nanostructure. The amorphous nano hBN was then annealed at 1300 ℃ for nanotube growth. As-prepared BNNTs may show a special bamboo-like structure. Despite much effort [124-126] being made, such as using boron as the precursor and introducing ammonia gas during ball-milling, the purity of BNNTs still needs to be further improved. The advantage of this method is high yield and no additional catalyst being needed, as the Fe and Cr species that come from the stainless-steel reaction chamber are effective catalysts for BNNT growth.

After the initial reports about the ***chemical vapour deposition (CVD)*** growth of BNNTs [127], this technique has been widely used for BNNTs preparation. In the beginning, borazine ($B_3N_3H_3$) was used as precursor and NiB, Ni_2N, Co, Ni were used as catalysts for CVD growth at 1000 – 1100 ℃. Later on, Wang et al. [128] reported a plasma-enhanced pulsed-laser deposition method at relatively low temperature (600 ℃) and successfully prepared MW-BNNTs with high crystallinity. Other types of CVD precursor such as $B_4N_3O_2H$ [129] and a catalyst such as nickelocene [130] were also reported for preparing MW- and DW-BNNTs. More recently, to meet the demands of large-scale preparation of BNNTs with high purity, Golberg et al. [131] developed a new CVD method using boron powder and metal oxide as reactants (BOCVD). As shown in Figure 1.10(a), the mixture of boron powders and MgO was

placed in a BN crucible and placed at the bottom of a vertical furnace. A protecting argon flow and a reactive ammonia flow were introduced when the furnace was heated to ~1300 ℃. The reaction between boron and MgO happens at this temperature: 2MgO (s) + 2 B (s) → B_2O_2 (g) + 2Mg (g), B_2O_2 will further react with ammonia flow in the low temperature zone (for separating precursor and product) in the furnace and generate BNNTs with high purity due to the absence of carbon impurities, as illustrated in Figure 1.10(b-e). For achieving larger quantities of BNNTs, this method has been further improved by introducing SnO and FeO as melting solvent for reaction [132]. The challenge of this method is how to control the diameter of the tube and reduce the number of walls.

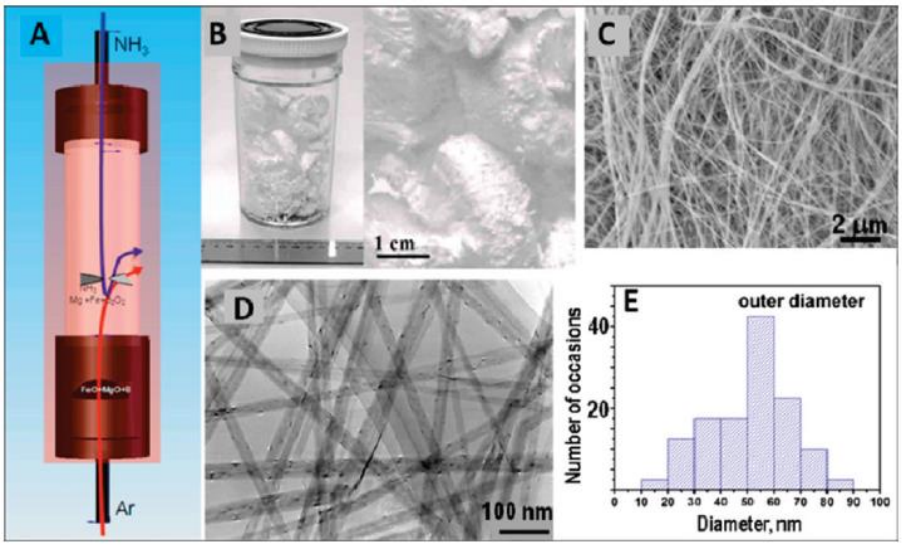

Figure 1.10 (a) Schematic diagram of the BOCVD preparation of highly pure BNNTs. (b-e) Morphologies of as-prepared snow-white BNNTs [131].

More recently, some other methods for scalable production were reported, such as so-called ***pressurized vapor/condenser (PVC) method*** for preparing BNNTs with highly crystallinity and small diameter, large length [133], as well as ***extended-pressure inductively-coupled plasma (EPIC) method*** [134]. Relevant work has been reviewed by Kim et al. [135].

Inspired by previous efforts on using a thermal plasma to prepare BNNTs [136-137], Kim et al. [138] developed a very efficient, rapid and scalable route for synthesizing BNNTs at atmospheric pressure using an induction plasma process. As-prepared BNNTs made by this method were used in this present study. Different from a laser beam with a small size, a thermal plasma offers a much larger thermal treatment volume for vaporizing B at 4000 K. The rapid cooling rate due to the plasma jet expansion is also favorable for BNNTs nucleation. They used an induction plasma system (50 kW, 3 MHz) with much higher power, larger plasma volume and low plasma gas velocity compare to the old DC plasma system [136-137] (8-14 kW). Therefore the residence time of hBN powder precursor in the reaction zone is increased. In addition, 18 vol. % of hydrogen gas (H_2) was injected into the reaction chamber as a reactant, therefore this new method was named as ***hydrogen-assisted BNNT synthesis (HABS)*** process. The introduction of hydrogen is deduced to significantly change the mechanisms of BNNT growth, thus massively improve the yield and quality of BNNTs, compared with the hydrogen-free plasma jet method.

The morphologies of as-prepared BNNTs were shown in Figure 1.11 [138]. From Figure 1.11(d, f), the SEM images of BNNTs show a random orientation of BNNTs, but some nontubular structure can also be observed. These materials are identified to be hBN fragments and the byproduct should be purified for some potential applications. SEM observations also estimate an average length of BNNTs to be a few micrometers. According to TEM, the majority of nanotubes have 2 -5 walls and < 10 nm diameter. A TEM elemental map indicates the uniform distribution of boron and nitrogen along the walls of tube. It is interesting that some carbon element was also detected. The authors attributed [138] this carbon contamination as originating from the adsorption of solvent during TEM sample preparation, as the whole method is a carbon-free process.

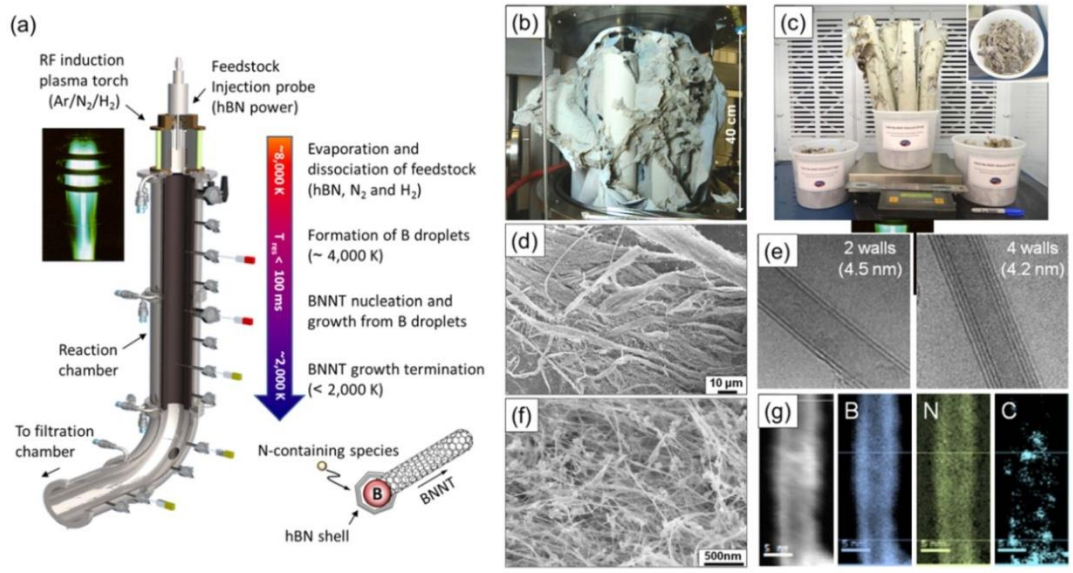

Figure 1.11 (a) Schematic diagram of HABS process for BNNTs preparation. (b-g) Morphologies of BNNTs prepared by the HABS process [138].

1.4 Properties

1.4.1 Physical properties of hBN, BNNSs and BNNTs

Due to its analogous structure but different chemical composition, bulk hBN is usually compared with graphite, as summarized in Table 1.2.

Table 1.2 Properties of bulk hBN and graphite (based on a summary in [22]).

Property	hBN	Graphite
Color	White/near-transparent	Black
Bond length (nm)	0.144	0.142
Bond energy (eV)	4	3.7
Interlayer spacing (nm)	0.333	0.335
Young's modulus (TPa)	0.8-1.3	1.1
Band gap (eV)	5.5 – 6.0	~0

Oxidation resistance (℃)	~840	~600
Breakdown voltage (MV/cm)	~7	Conductor
Charge transferred between neighbours (e)	~0.4	0
In-plane thermal conductivity (W/mK)	400	2600

Analogous to graphite, bulk hBN is mechanically strong, lubricative and highly thermally conductive due to their similar crystal structure and inner bonding. However, insulating, near-transparent, and chemically and thermally stable hBN exhibits many different optical, chemical and electrical properties compared with graphite due to its partially ionic B-N bonding. Both BNNSs and BNNTs inherit these properties from the parental bulk hBN. Relevant properties of BNNSs and BNNTs are summarized in Tables 1.3 and 1.4 and their carbon analogues, graphene and CNTs, are used for comparison.

Table 1.3 Properties of BNNSs and graphene

Property	BNNSs	Graphene
Bond length (nm)	0.142	0.144
Band gap (eV)	~6 [23, 65, 139]	None [2]
Young's modulus (monolayer) (TPa)	0.86±0.07 (measured) [84]	1.0 (measured) [140-141]
Breaking strength (monolayer) (GPa)	70.5±5.5(measured) [84]	130 (measured) [140-141]
Thermal conductivity ($W\ m^{-1}\ K^{-1}$)	>600(Monolayer) [142]*	1800-5400 (Monolayer) [143-144]
Oxygen doping temperature (℃)	>700(Monolayer) [43]	250 [145]
Oxygen etching	> 800(Monolayer) [43]	450 [145]

temperature (℃)		
Specific surface area (m^2g^{-1})	~ 2600 [6] *	2630 [146] *
Luminescence (nm)	Deep UV (217 -232) [147]	No

*Data from theoretical studies.

As shown in Table 1.4, BNNSs (monolayer) exhibit similar mechanical properties to graphene. Meanwhile, the thermal stability of monolayer hBN is superior to graphene. The thermal conductivity of BNNSs was estimated theoretically to be >600W m^{-1} K^{-1} (monolayer) and measured to be 100-270 W m^{-1} K^{-1} (few-layered BNNSs) [148-149] before 2019. More recently, by using an optothermal Raman technique, Cai et al. [150] reported the first measurement of in-plane thermal conductivity (κ) of suspended mechanical exfoliated 1L boron nitride. The value reaches 751 ± 340 W/mK (at room temperature). Moreover the experimental value of κ of 2L and 3L BNNSs were 646 ± 242 W/mK and 602 ± 247 W/mK; A few months later, Ying et al. [151] reported a 545 W/mK (at 315 K temperature) κ of CVD 1L boron nitride. Although the measured κ of BNNSs is lower than the value of graphene with same number of layers (1L graphene: ~ 4000 – 5300 W/mK at room temperature [143, 152]), it is still one of the most thermally conductive electrical insulators. Additionally, BNNSs exhibit much better anti-oxidation properties than graphene. They are considered to be ideal materials for high temperature applications.

Table 1.4 Properties of BNNTs and CNTs (based on a summary in [111]).

Property	BNNTs	CNTs
Color	White	Black
Bond length (nm)	0.1437-0.1454 [153-155]	0.1400–0.1463 [153-155]
Band gap (eV)	5-6, independent of chiralities [156]	Metallic or semiconducting, dependent on chiralities [157]

Young's modulus (TPa)	0.78-0.91 [158]*; 0.71-0.83 [153]*; 0.5-0.7 [66]; 1.22±0.24 [159]	1.09-1.25 [158]*; 0.84-0.99 [153]*; 0.27-0.95 [160-161]
Breaking strength (GPa)	~33 [162]	11-63 [161]
Thermal conductivity (W m^{-1} K^{-1})	>CNTs [163]*; ~180-300 (SW) [164]*; ~180-300 (MW with D~35 nm) [165]	~6000 (SW) [166]*; >3000 (MW with D~14), ~1000 (D~10), ~300 (D~35) [165]
Thermal stability (℃)	>800-900 in air [167-168]	Roughly 500-700 (MW) [169]
Luminescence (nm)	220-460 [170-171]	800-1700 [172-173]

*Data from theoretical studies; D - Tube diameter; MW - Multi-walled nanotubes; SW - Single-walled nanotubes

In summary, BNNTs and CNTs have many similar properties such as outstanding mechanical strength, high thermal conductivity etc. Nevertheless, BNNTs are white insulating nanomaterials with high thermal stability, thus they can be explored to be used in some particular fields, for instance, reinforcements for insulating composites.

1.4.2 Optical properties

Optical properties of BNNSs

As can be seen in Figure 1.12, the band gap of both CVD monolayer BNNSs [174] and CVD few-layered BNNSs [41] was studied by an optical absorption technique and estimated to be 6.07 eV and 5.92 eV, respectively.

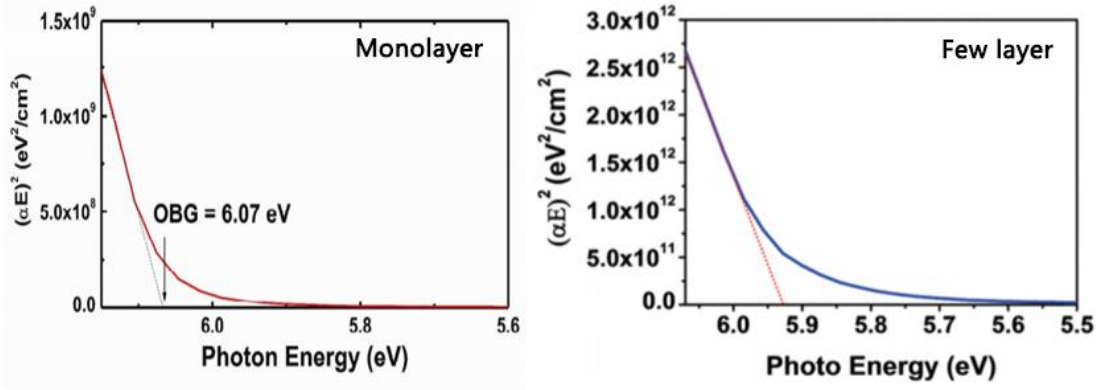

Figure 1.12 Optical band gap analysis of monolayer CVD BNNSs [174] and few-layered CVD BNNSs [41].

Bulk hBN single crystal exhibits a dominant peak at ~215 nm (in the deep UV region) with a series of s-like exciton absorption peaks [36]. Similar to bulk hBN, BNNSs also show a very strong absorption in this DUV region, which have both been verified by photoluminescence (PL) and cathodoluminescence (CL) characterizations (Figure 1.13 [175-176]). It should be noted that in the CL spectrum taken at low temperature (12 K) some new peaks appear (except for the main peak at 226.9 nm and shoulder peak at 233nm): the peaks at ~215 nm are from free excitons, the peaks at 220-240 nm can be assigned to impurities, defects [36] and a very broad small peak between 260-280 nm can probably be attributed to vacancies and residual stresses in the BNNSs [177].

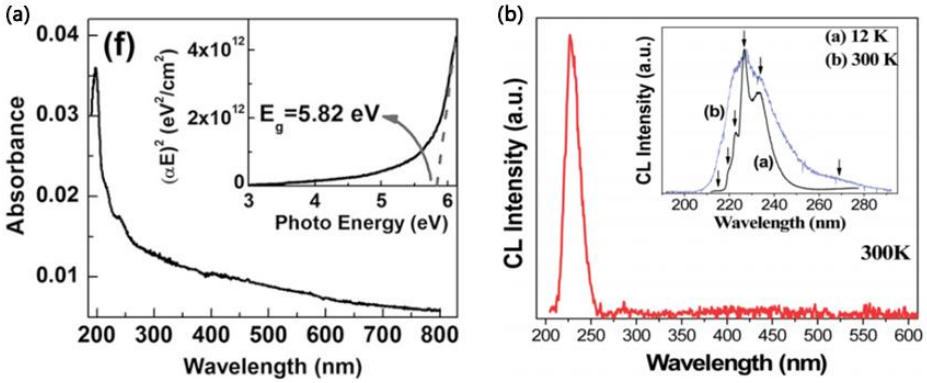

Figure 1.13 UV-vis spectrum [175] and CL spectrum [176] of BNNSs produced by vapor deposition.

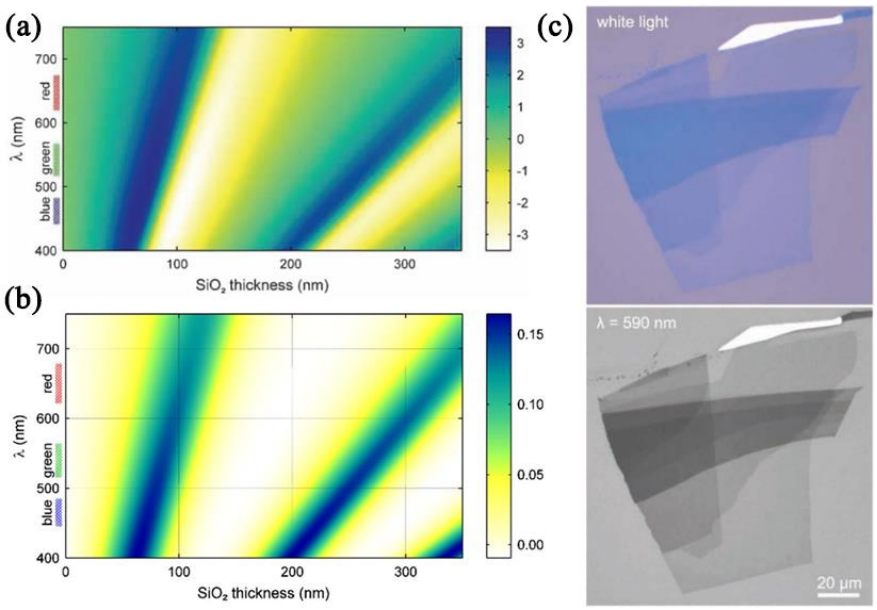

Figure 1.14 Color plot of the contrast as a function of wavelength and SiO_2 thickness (BNNSs (a) and graphene (b)) and hBN on top of a 90 nm SiO_2/Si wafer (the lower part is a monolayer) [42, 178].

Therefore, due to the high transparency (>99%) of BNNSs in the optical range of 250-900 nm, monolayer BNNSs cannot be detected by the human eye, even with classical interference enhancement using an oxidized silicon wafer with 300 nm SiO_2 coatings [42, 178]. At least 2.5% contrast difference for monolayer hBN is necessary for optical observation, and the optical contrast of BNNSs indeed increases monotonically with number of layers under a green light (516 nm) illumination [179]. To make monolayer BNNSs clearly visible under the optical microscope, an appropriate filtered optical wavelength and an optimum SiO_2 coating thickness on wafer are required, just like the case of graphene. Gorbachev et al. [42] revealed that thinner SiO_2 (80 ±10 nm) and narrow optical filters (green) are helpful to improve the contrast of few-layered BNNSs, and even monolayer. As shown in Figure 1.14, hBN and graphene show evident differences in optimal SiO_2 thickness and wavelength for good contrast (optical contrast value (0-0.15) on the graph for graphene is the real value, while 1 means 1% on the graph for BNNSs). A 90 nm SiO_2 coating is the best choice for achieving good contrast of BNNSs flake over a wide range of wavelength.

Gorbachev suggested that 3% optical contrast for BNNSs single layer can be achieved by using a Si wafer with 80±10 nm SiO_2 coating and green light filter. Although 3% contrast is much lower than 10% contrast of graphene, this value is enough for optical detection, which offers a hint for choosing an appropriate wavelength to make BNNS monolayers visible on PMMA beams, by spin coating 180 nm SU-8 on PMMA.

Optical properties of BNNTs

Due to their constant wide band gap, BNNTs possess a pure white appearance. Most of optical property studies about BNNTs focus on band structure calculations, band gap measurements and luminescence. Lauret et al. [170] studied the optical absorption of SW-BNNTs prepared by a laser ablation method, as illustrated in Figure 1.15. Bulk hBN shows an absorption peak at 6.15 eV, which is attributed to the saddle point transition in the band structure of bulk hBN [180]. A 5.6-5.8 eV band gap was estimated for bulk hBN in this work. After laser ablation, SW-BNNTs demonstrate two new absorption peaks at 4.45 eV, 5.5 eV. The peak at 6.15 eV originates from bulk hBN raw material. In the same year, Zhi et al. [181] estimated the band gap of MW-BNNTs using UV-vis absorption spectroscopy and CL spectroscopy. They reported an approximately 5.5 eV band gap for MW-BNNTs.

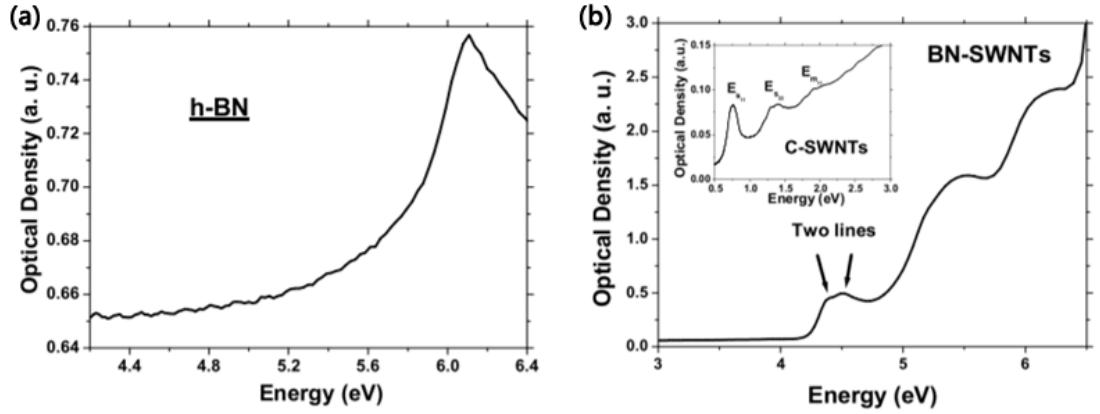

Figure 1.15 Optical absorption spectra of: (a) bulk hBN crystals for SW-BNNTs preparation. (b) SW-BNNTs (inset is the absorption of SW-CNTs as a contrast) [170].

PL and CL studies showed that BNNTs are effective violet and ultra-violet emission

materials [171, 182-183]. Four emission peaks were reported in relevant work: at ~230 nm which can be attributed to a near-band gap excitonic recombination [183], at ~279 nm and ~320 nm which have been attributed in different papers [184-186] to impurity and defects centers and band-gap transitions, and a special ~460 nm peak which was typically observed in oxygen-doped or surface-oxidized BNNTs (attributed to oxygen-centre emission) [182].

1.4.3 Mechanical properties

Mechanical properties of BNNSs

Before the systematic experimental measurements of the modulus of BNNSs, Qing et al. [188] simulated the deformation of a BNNS monolayer using Ab initio density functional theory. They predicted that the BNNS monolayer will undergo a non-linear elastic deformation up to an ultimate strength, which is then followed by a strain softening to the failure. They also predicted a 279.2 N/m in-plane Young's modulus of a BNNS monolayer. Another simulation study reported by Boldrin et al. [189] suggested that BNNSs show a similar tensile rigidity with bulk hBN. A 0.19 - 0.33 TPa·nm rigidity was calculated in this work. Experimental measurement for the bending modulus (defined as $12(1-\nu^2)D/t^3$ in this work, where ν, D, t are the Poisson's ratio, bending rigidity, thickness of 2D materials, respectively) of BNNSs was reported by Li et al. [187], BNNSs with <50 nm thickness were prepared using a tip-sonication method. The bending test was conducted on an AFM. BNNSs were fixed on a designed Si/SiO_2 substrate, a AFM probe tip was placed on the nanosheet and pushed the centre of the nanosheet down to the trench of the substrate and the linear-elastic force-displacement curves were recorded. The curves were then fitted and calculated using plate theory [190], 19 nanosheets with different thickness from 25 – 300nm with 1.2 – 3μm flake size were measured. It was found that the bending modulus of BNNSs increased with decreasing sheets thickness. The

thickness-dependent bending modulus was attributed to the layer distribution of stacking faults, therefore a higher width-to-thickness ratio will be helpful to reduce the stacking faults and achieve a higher modulus. This paper also mentioned that the BNNSs with ultrathin thickness should be prepared and a much higher bending modulus is expected to be achieved.

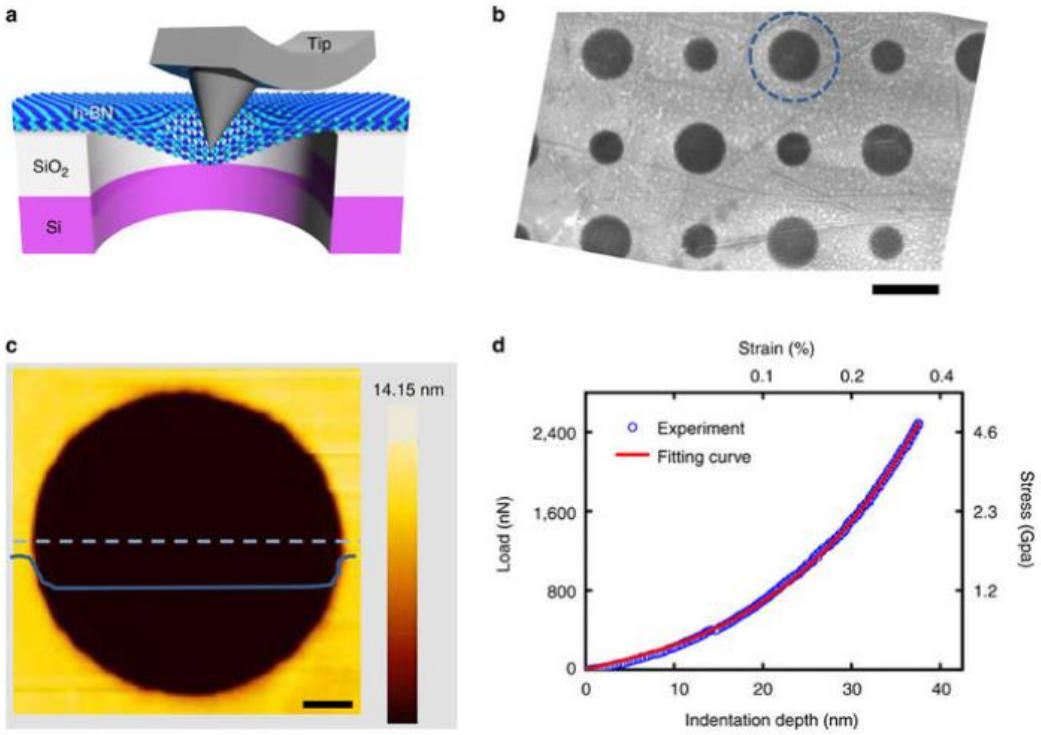

Figure 1.16 (a) Schematic diagram of the AFM nanoidentation method for Young's modulus measurement. (b) SEM image of a ~15nm CVD BNNSs on SiO_2/Si wafer with micro-wells of 1-1.5 nm diameters. (c) AFM image of suspended ~15nm BNNS film, solid line is the height profile. (d) Mechanical response of the BNNS film by nanoidentation [191].

Inspired by Hone's classical AFM nanoidentation method [140-141] for measuring the Young's modulus of graphene, similar work for CVD BNNSs was reported in 2010 [24] and 2015 [191]. First of all, Song et al. [24] reported the elastic modulus of a CVD bilayer BNNSs is $E^{2D}=112\pm8$ Nm^{-1} (that is, 0.334 ± 0.024 TPa), which is much lower than theoretical predictions (0.72-0.98 TPa if the thickness of a monolayer is

assumed to be 0.334nm). The degraded mechanical properties of bilayer BNNSs reported by Song were attributed to the presence of abundant defects and grain boundaries [192]. Kim et al. [191] later measured the Young's modulus of a ~15nm thick (~45 layer) CVD BNNS to be 1.16±0.1 TPa as illustrated in Figure 1.16. This is even higher than that of graphene monolayer.

More recently, a very important and systematic study on measuring the mechanical properties of BNNSs was reported by Falin et al. [84] They exfoliated high-purity hBN single crystals from Japan's NIMS and transferred BNNSs with different thickness onto a 90 nm SiO_2/Si wafer with micro-wells and directly measured relevant mechanical properties of BNNSs from monolayer to 9 layers, as shown in Figure 1.17. The AFM nanoidentation technique was employed for measurement and graphene with different thickness was also exfoliated and measured as a reference in this work.

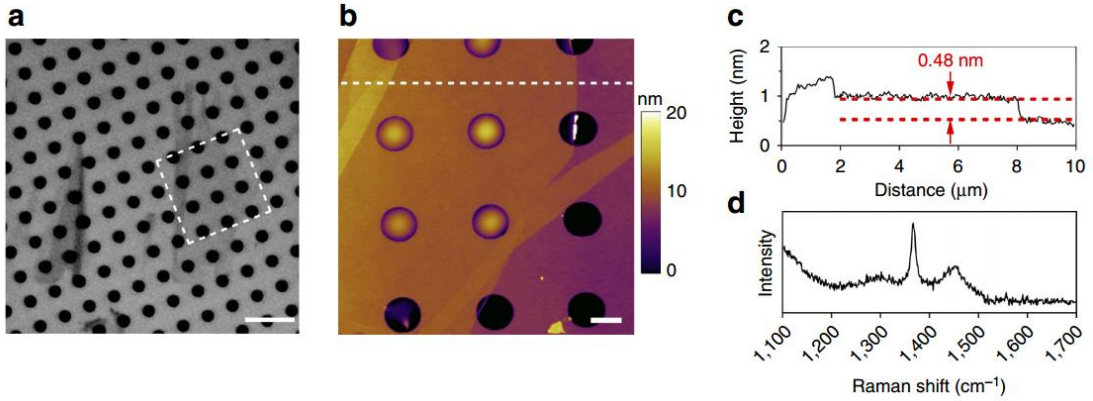

Figure 1.17 (a) Optical micrograph and (b) zoom-in AFM image of exfoliated monolayer on 90 nm SiO_2/Si wafer with micro-wells; (c) height profile along a dashed line in (b) which indicates monolayer BNNSs with ~6 μm lateral sizes. (d) Raman spectra of suspended monolayer BNNSs (the E_{2g} peak position is at 1366.5 cm^{-1}) [84].

The measured mechanical properties in this study are summarized in Table 1.5. In this work, the thickness of monolayer BNNS was assumed to be 0.334 nm and a Poisson ratio of 0.211 [188]; for graphene, 0.335 nm per layer and a 0.165 Poisson ratio were used.

Table 1.5 Mechanical properties of BNNSs and graphene with different number of layers measured in Ref 84.

	BNNSs				Graphene			
Properties	1 L	2 L	3 L	9 L	1 L	2 L	3 L	8 L
E^{2D}(Nm^{-1})	289±24	590±38	822±44	-	342±8	645±16	985±5	-
E (TPa)	0.86±0.07	-	-	0.86±0.00	1.03±0.02	-	-	0.94±0.00
Breaking strength (GPa)	70.5±5.5	68±6.8	76.9±2.3	-	125±0	107.7±4.3	105.6±6.0	85.3±5.4
Breaking strength (Nm^{-1})	23.6±1.8	45.4±4.5	77.0±2.3	-	41.9±0	72.1±2.9	106.2±6.0	228.6±14.5

L - Number of layers; E^{2D} - 2D effective Young's modulus; E - (Volumetric) Young's modulus

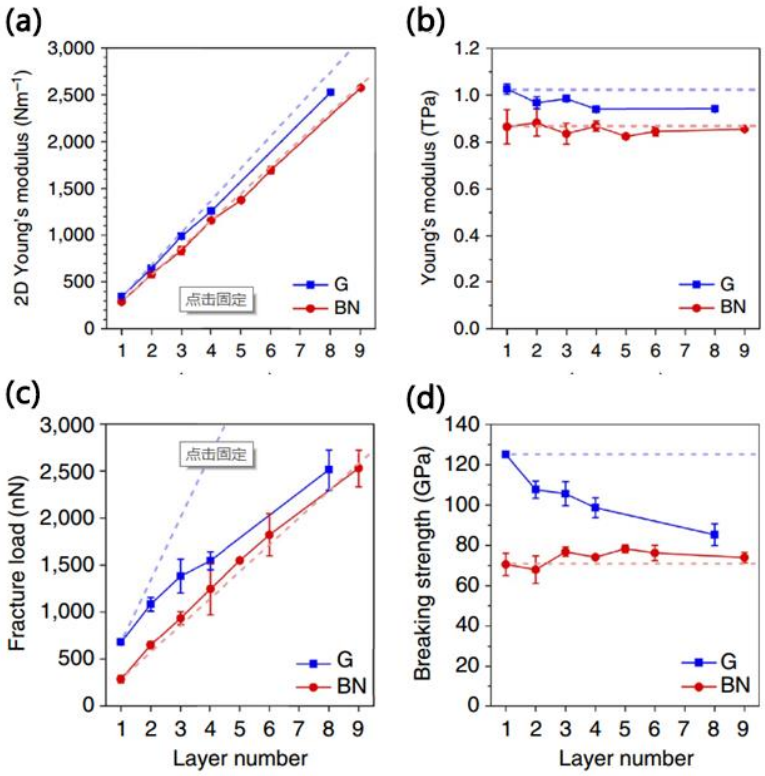

Figure 1.18 (a) 2D Young's modulus; (b) volumetric Young's modulus; (c) fracture load;

(d) breaking strength of graphene and BNNSs of different thickness [84].

As shown in Table 1.5, The Young's modulus of monolayer BNNSs is 0.86±0.07 TPa, which is close to but smaller than that of monolayer graphene (~1 TPa). The breaking strength of monolayer hBN is 70.5±5.5 GPa, smaller than the value of monolayer graphene. The relevant experimental results are consistent with theoretical predictions. In particular, it is found that graphene's breaking strength decrease by more than 30%, the Young's modulus declines from 1.03 TPa to 0.94 TPa when number of layers increases from 1 to 8, while the strength and Young's modulus of BNNSs is not sensitive to increasing thickness, as shown in Figure 1.18 (b-d) [84]. Specific DFT calculations were performed in this work and it is indicated that strong interlayer bonding force between adjacent BN layers (AA' stacking and partially ionic bonding) will bond the whole BNNS layer-by-layer structure, especially the area under the AFM tip, as sketched in the middle of Figure 1.19.

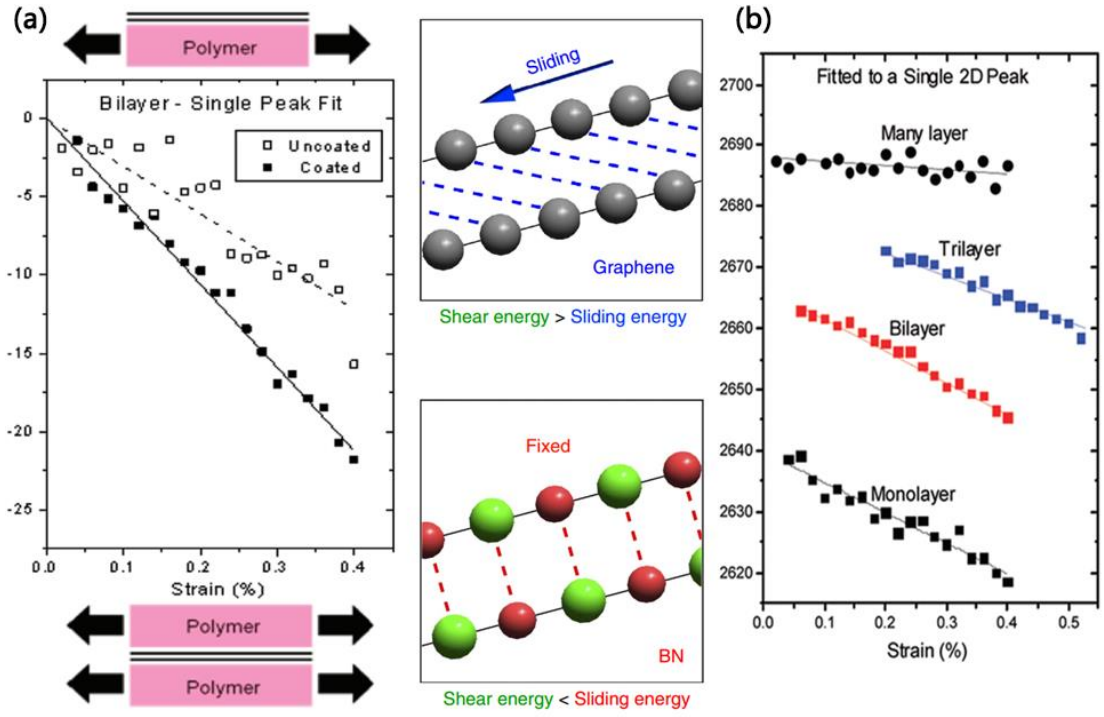

Figure 1.19 Raman 2D band shifts (fitted as one peak) of (a) Bilayer graphene coated and uncoated with a thin layer of polymer, indicating poor interlayer binding force; (b) mono-, bi-. tri-, many-layered graphene deformed on a polymer beam [193].

Previous work on a graphene model composite [193] in Manchester has reported that Raman 2D band shift rate tends to decrease with increasing number of layers, indicating a poor stress transfer between inner layers as reinforcement. It would be interesting to know what relevant data for BNNSs with same number of layers would look like. This will be a very important and meaningful future work, although effort will have to be made to overcome the opacity and weak Raman signal of mono-, bi-, tri-layer BNNSs.

Mechanical properties of BNNTs

Before the experimental measurements of modulus, theoretical studies already indicated a very high mechanical strength for BNNTs, but with a value slightly smaller than that of CNTs [158-159, 194-195]. In theoretical simulations, BNNTs are predicted to possess a Young's modulus ranging from 0.71-0.91 TPa, which is slightly smaller than the theoretical value (~1.22-1.25 TPa) of CNTs. Relevant studies also suggest that the yield strength of BNNTs was also slightly smaller than the value of CNTs. In addition, Dumitrica et al. [196] showed that the formation of defects in BNNTs required a higher formation but lower activation energy relative to CNTs. In other words, BNNTs should be stronger and more thermo-mechanically stable than CNTs at high temperatures (or after extremely long deformation times) but CNTs will be stronger than BNNTs at moderate temperatures [196].

The Young's modulus of a single MW-BNNTs (prepared by arc-discharge) was evaluated by Chopra et al [159]. By observing the amplitude of thermal vibration of a cantilevered BNNT in TEM, they elucidated a 1.22 ± 0.24 TPa axial Young's modulus for MW-BNNTs. This value is even higher than theoretical results [111]. In another study [194], a well-established electric-field-induced resonance method was used and an average 0.72 TPa effective elastic modulus was obtained. In 2007, Golberg et al. [66] measured the Young's modulus of BOCVD MW-BNNTs using their

well-established AFM-TEM technique. They obtained a Young's modulus of 0.5-0.6 TPa using this special technique. In 2010 [162], they used the same technique and evaluate a ~33 GPa breaking strength for MW-BNNTs.

Very recently, Zhou et al. [197] reported the precise AFM-TEM measurement of intrinsic elastic modulus of MW-BNNTs, and obtained a 906.2 GPa average modulus, with a 9.3% standard deviation (Figure 1.20). They also studied the effect of long–term electron irradiation on the mechanical properties of BNNTs. It is found that the radiation will induce the formation of the decrease of tube diameter and an outer tube shell with enough defects. The modulus of BNNTs gradually decreases to ~663 GPa with electron radiation, which is still 3x that of steel.

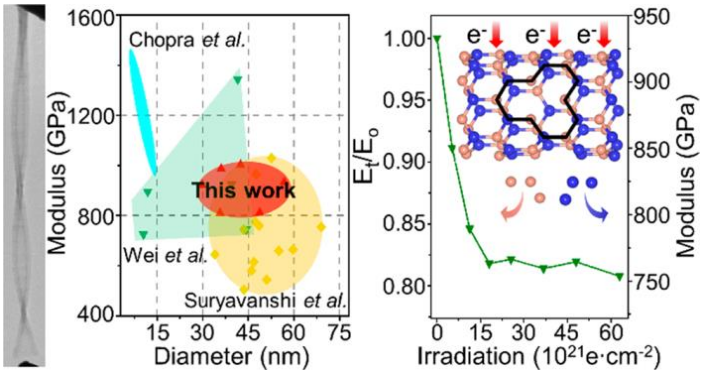

Figure 1.20 Elastic modulus of MW-BNNTs measured usinga high-order resonance technique in a HRTEM, and nanotube modulus reduction with electron radiation time [207].

BNNTs also exhibit interesting flexibility and perfect elasticity under loading. The nanotubes completely recover to their original tubular shape after a loading-unloading process, as shown in Figure 1.21 [198]. Garel et al. [199] also reported that BNNTs are 1 order of magnitude torsionally stronger than CNTs due to stronger inner layer-layer bonding.

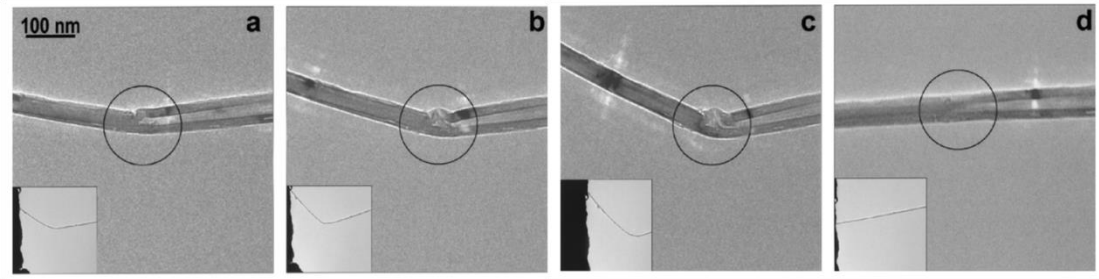

Figure 1.21 Consecutive HR-TEM images of a single BNNT during deformation process: as shown in (a-c), when a force was loaded, severe distortion can be observed on hBN tubular layers, while the original shape is fully restored after unloading (d) [198].

In addition to the measured mechanical properties of BNNTs, Nigues et al. [200] stretched the outer shell of MW-BNNTs and CNTs in a SEM and found that the interlayer friction within BNNTs is much stronger than that in CNTs, as illustrated in Figure 1.22.

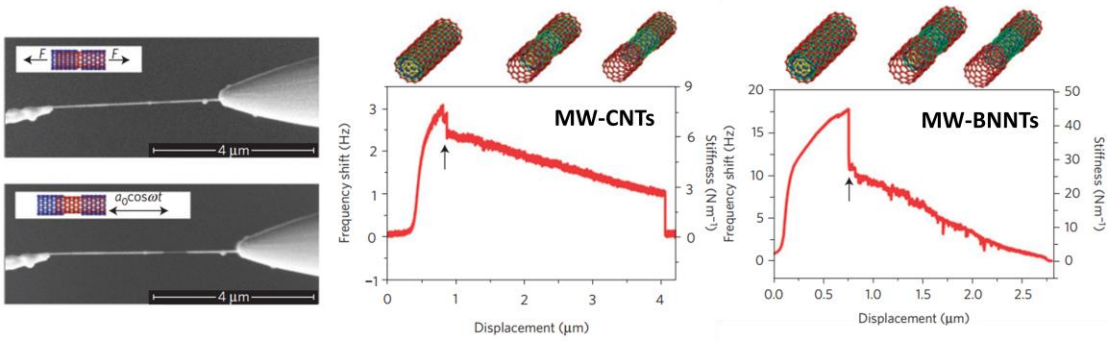

Figure 1.22 Schematic of tensile test for MW-CNTs and MW-BNNTs in a SEM and measured frequency shift change during the test [200].

BNNTs are also a very promising reinforcement due to their wide band gap, in particular, unique broad wide gap leads to potential applications as insulating ultra-strong fibrous filler for nanocomposites.

1.5 Conclusions

This chapter has reviewed the structure, preparation and properties of BNNSs & BNNTs. BNNSs & BNNTs have been found to owe comparable mechanical stiffness with graphene & CNTs, which makes them some of the strongest insulators. However, different from their carbon analogue, BNNSs & BNNTs exhibit much stronger inner layer-layer bonding and better thermal stability at high temperature. Considering their exceptional properties and low density, both BNNSs and BNNTs show great potential to be used as ideal reinforcements for composites requiring excellent mechanical strength, thermal conductivity and electrical insulation.

References

1. Iijima, S., Helical microtubules of graphitic carbon. *Nature* **1991,** *354* (6348), 56.
2. Novoselov, K. S.; Geim, A. K.; Morozov, S. V.; Jiang, D.; Zhang, Y.; Dubonos, S. V.; Grigorieva, I. V.; Firsov, A. A., Electric field effect in atomically thin carbon films. *Science* **2004,** *306* (5696), 666-669.
3. Chopra, N. G.; Luyken, R.; Cherrey, K.; Crespi, V. H.; Cohen, M. L.; Louie, S. G.; Zettl, A., Boron nitride nanotubes. *Science* **1995,** *269* (5226), 966-967.
4. Novoselov, K.; Jiang, D.; Schedin, F.; Booth, T.; Khotkevich, V.; Morozov, S.; Geim, A., Two-dimensional atomic crystals. *Proc. Natl. Acad. Sci. U. S. A.* **2005,** *102* (30), 10451-10453.
5. Pakdel, A.; Bando, Y.; Golberg, D., Nano boron nitride flatland. *Chem. Soc. Rev.* **2014,** *43* (3), 934-959.
6. Weng, Q.; Wang, X.; Wang, X.; Bando, Y.; Golberg, D., Functionalized hexagonal boron nitride nanomaterials: emerging properties and applications. *Chem. Soc. Rev.* **2016,** *45* (14), 3989-4012.
7. Golberg, D.; Bando, Y.; Huang, Y.; Terao, T.; Mitome, M.; Tang, C.; Zhi, C., Boron nitride nanotubes and nanosheets. *ACS Nano* **2010,** *4* (6), 2979-2993.
8. Lin, Y.; Connell, J. W., Advances in 2D boron nitride nanostructures: nanosheets, nanoribbons, nanomeshes, and hybrids with graphene. *Nanoscale* **2012,** *4* (22), 6908-6939.
9. Hod, O., Graphite and hexagonal boron-nitride have the same interlayer distance. Why? *Journal of Chemical Theory and Computation* **2012,** *8* (4), 1360-1369.
10. Li, L. H.; Chen, Y.; Behan, G.; Zhang, H.; Petravic, M.; Glushenkov, A. M., Large-scale mechanical peeling of boron nitride nanosheets by low-energy ball milling. *J. Mater. Chem.* **2011,** *21* (32), 11862-11866.
11. Li, L. H.; Chen, Y., Atomically Thin Boron Nitride: Unique Properties and Applications. *Adv. Funct. Mater.* **2016,** *26* (16), 2594-2608.
12. Pease, R., Crystal structure of boron nitride. *Nature* **1950,** *165* (4201), 722.
13. Kern, G.; Kresse, G.; Hafner, J., Ab initio calculation of the lattice dynamics and phase diagram of boron nitride. *Physical Review B* **1999,** *59* (13), 8551.
14. Yu, W.; Lau, W.; Chan, S.; Liu, Z.; Zheng, Q., Ab initio study of phase transformations in boron nitride. *Physical Review B* **2003,** *67* (1), 014108.
15. Zhi, C.; Bando, Y.; Tang, C.; Kuwahara, H.; Golberg, D., Large-Scale Fabrication of Boron Nitride Nanosheets and Their Utilization in Polymeric Composites with Improved Thermal and Mechanical Properties. *Adv. Mater.* **2009,** *21* (28), 2889-2893.
16. Golberg, D.; Bando, Y.; Tang, C. C.; Zhi, C. Y., Boron Nitride Nanotubes. *Adv. Mater.* **2007,** *19* (18), 2413-2432.
17. Wang, J.; Lee, C. H.; Yap, Y. K., Recent advancements in boron nitride nanotubes. *Nanoscale* **2010,** *2* (10), 2028-2034.
18. Rao, C.; Govindaraj, A., Synthesis of inorganic nanotubes. *Adv. Mater.* **2009,** *21*

(42), 4208-4233.

19. Ooi, N.; Rairkar, A.; Lindsley, L.; Adams, J., Electronic structure and bonding in hexagonal boron nitride. *J. Phys.: Condens. Matter* **2005,** *18* (1), 97.
20. Topsakal, M.; Aktürk, E.; Ciraci, S., First-principles study of two-and one-dimensional honeycomb structures of boron nitride. *Physical Review B* **2009,** *79* (11), 115442.
21. Qi, Y.; Hector Jr, L. G., Planar stacking effect on elastic stability of hexagonal boron nitride. *Appl. Phys. Lett.* **2007,** *90* (8), 081922.
22. Jiang, X.-F.; Weng, Q.; Wang, X.-B.; Li, X.; Zhang, J.; Golberg, D.; Bando, Y., Recent progress on fabrications and applications of boron nitride nanomaterials: a review. *Journal of Materials Science & Technology* **2015,** *31* (6), 589-598.
23. Zeng, H.; Zhi, C.; Zhang, Z.; Wei, X.; Wang, X.; Guo, W.; Bando, Y.; Golberg, D., "White graphenes": boron nitride nanoribbons via boron nitride nanotube unwrapping. *Nano Lett.* **2010,** *10* (12), 5049-5055.
24. Song, L.; Ci, L.; Lu, H.; Sorokin, P. B.; Jin, C.; Ni, J.; Kvashnin, A. G.; Kvashnin, D. G.; Lou, J.; Yakobson, B. I.; Ajayan, P. M., Large scale growth and characterization of atomic hexagonal boron nitride layers. *Nano Lett.* **2010,** *10* (8), 3209-15.
25. Alem, N.; Erni, R.; Kisielowski, C.; Rossell, M. D.; Gannett, W.; Zettl, A., Atomically thin hexagonal boron nitride probed by ultrahigh-resolution transmission electron microscopy. *Physical Review B* **2009,** *80* (15), 155425.
26. Blase, X.; De Vita, A.; Charlier, J.-C.; Car, R., Frustration effects and microscopic growth mechanisms for BN nanotubes. *Phys. Rev. Lett.* **1998,** *80* (8), 1666.
27. Golberg, D.; Bando, Y., Unique morphologies of boron nitride nanotubes. *Appl. Phys. Lett.* **2001,** *79* (3), 415-417.
28. Nardelli, M. B.; Brabec, C.; Maiti, A.; Roland, C.; Bernholc, J., Lip-lip interactions and the growth of multiwalled carbon nanotubes. *Phys. Rev. Lett.* **1998,** *80* (2), 313.
29. Marom, N.; Bernstein, J.; Garel, J.; Tkatchenko, A.; Joselevich, E.; Kronik, L.; Hod, O., Stacking and registry effects in layered materials: the case of hexagonal boron nitride. *Phys. Rev. Lett.* **2010,** *105* (4), 046801.
30. Warner, J. H.; Rummeli, M. H.; Bachmatiuk, A.; Büchner, B., Atomic resolution imaging and topography of boron nitride sheets produced by chemical exfoliation. *ACS Nano* **2010,** *4* (3), 1299-1304.
31. Alem, N.; Ramasse, Q. M.; Seabourne, C. R.; Yazyev, O. V.; Erickson, K.; Sarahan, M. C.; Kisielowski, C.; Scott, A. J.; Louie, S. G.; Zettl, A., Subangstrom edge relaxations probed by electron microscopy in hexagonal boron nitride. *Phys. Rev. Lett.* **2012,** *109* (20), 205502.
32. Meyer, J. C.; Chuvilin, A.; Algara-Siller, G.; Biskupek, J.; Kaiser, U., Selective sputtering and atomic resolution imaging of atomically thin boron nitride membranes. *Nano Lett.* **2009,** *9* (7), 2683-2689.

33. Han, W.-Q.; Wu, L.; Zhu, Y.; Watanabe, K.; Taniguchi, T., Structure of chemically derived mono-and few-atomic-layer boron nitride sheets. *Appl. Phys. Lett.* **2008,** *93* (22), 223103.
34. Lee, C.; Li, Q.; Kalb, W.; Liu, X.-Z.; Berger, H.; Carpick, R. W.; Hone, J., Frictional characteristics of atomically thin sheets. *Science* **2010,** *328* (5974), 76-80.
35. Dean, C. R.; Young, A. F.; Meric, I.; Lee, C.; Wang, L.; Sorgenfrei, S.; Watanabe, K.; Taniguchi, T.; Kim, P.; Shepard, K. L., Boron nitride substrates for high-quality graphene electronics. *Nature Nanotechnology* **2010,** *5* (10), 722.
36. Watanabe, K.; Taniguchi, T.; Kanda, H., Direct-bandgap properties and evidence for ultraviolet lasing of hexagonal boron nitride single crystal. *Nature Materials* **2004,** *3* (6), 404.
37. Kubota, Y.; Watanabe, K.; Tsuda, O.; Taniguchi, T., Deep ultraviolet light-emitting hexagonal boron nitride synthesized at atmospheric pressure. *Science* **2007,** *317* (5840), 932-934.
38. Taniguchi, T.; Watanabe, K., Synthesis of high-purity boron nitride single crystals under high pressure by using Ba–BN solvent. *J. Cryst. Growth* **2007,** *303* (2), 525-529.
39. Pacile, D.; Meyer, J.; Girit, Ç.; Zettl, A., The two-dimensional phase of boron nitride: Few-atomic-layer sheets and suspended membranes. *Appl. Phys. Lett.* **2008,** *92* (13), 133107.
40. Lin, Y.; Williams, T. V.; Connell, J. W., Soluble, exfoliated hexagonal boron nitride nanosheets. *The Journal of Physical Chemistry Letters* **2009,** *1* (1), 277-283.
41. Shi, Y.; Hamsen, C.; Jia, X.; Kim, K. K.; Reina, A.; Hofmann, M.; Hsu, A. L.; Zhang, K.; Li, H.; Juang, Z.-Y., Synthesis of few-layer hexagonal boron nitride thin film by chemical vapor deposition. *Nano Lett.* **2010,** *10* (10), 4134-4139.
42. Gorbachev, R. V.; Riaz, I.; Nair, R. R.; Jalil, R.; Britnell, L.; Belle, B. D.; Hill, E. W.; Novoselov, K. S.; Watanabe, K.; Taniguchi, T.; Geim, A. K.; Blake, P., Hunting for monolayer boron nitride: optical and Raman signatures. *Small* **2011,** *7* (4), 465-8.
43. Li, L. H.; Cervenka, J.; Watanabe, K.; Taniguchi, T.; Chen, Y., Strong oxidation resistance of atomically thin boron nitride nanosheets. *ACS Nano* **2014,** *8* (2), 1457-62.
44. Kim, K. K.; Hsu, A.; Jia, X.; Kim, S. M.; Shi, Y.; Hofmann, M.; Nezich, D.; Rodriguez-Nieva, J. F.; Dresselhaus, M.; Palacios, T.; Kong, J., Synthesis of monolayer hexagonal boron nitride on Cu foil using chemical vapor deposition. *Nano Lett.* **2012,** *12* (1), 161-6.
45. Lin, Y.; Williams, T. V.; Xu, T.-B.; Cao, W.; Elsayed-Ali, H. E.; Connell, J. W., Aqueous dispersions of few-layered and monolayered hexagonal boron nitride nanosheets from sonication-assisted hydrolysis: critical role of water. *The Journal of Physical Chemistry C* **2011,** *115* (6), 2679-2685.

46. Seifert, G.; Fowler, P.; Mitchell, D.; Porezag, D.; Frauenheim, T., Boron-nitrogen analogues of the fullerenes: electronic and structural properties. *Chem. Phys. Lett.* **1997,** *268* (5-6), 352-358.
47. Pokropivny, V. V.; Skorokhod, V. V.; Oleinik, G. S.; Kurdyumov, A. V.; Bartnitskaya, T. S.; Pokropivny, A. V.; Sisonyuk, A. G.; Sheichenko, D. M., Boron nitride analogs of fullerenes (the fulborenes), nanotubes, and fullerites (the fulborenites). *J. Solid State Chem.* **2000,** *154* (1), 214-222.
48. Banhart, F.; Kotakoski, J.; Krasheninnikov, A. V., Structural defects in graphene. *ACS Nano* **2010,** *5* (1), 26-41.
49. Ma, J.; Alfè, D.; Michaelides, A.; Wang, E., Stone-Wales defects in graphene and other planar s p 2-bonded materials. *Physical Review B* **2009,** *80* (3), 033407.
50. Jin, C.; Lin, F.; Suenaga, K.; Iijima, S., Fabrication of a freestanding boron nitride single layer and its defect assignments. *Phys. Rev. Lett.* **2009,** *102* (19), 195505.
51. Liu, Y.; Zou, X.; Yakobson, B. I., Dislocations and grain boundaries in two-dimensional boron nitride. *ACS Nano* **2012,** *6* (8), 7053-7058.
52. Gibb, A. L.; Alem, N.; Chen, J.-H.; Erickson, K. J.; Ciston, J.; Gautam, A.; Linck, M.; Zettl, A., Atomic resolution imaging of grain boundary defects in monolayer chemical vapor deposition-grown hexagonal boron nitride. *J. Am. Chem. Soc.* **2013,** *135* (18), 6758-6761.
53. Zobelli, A.; Gloter, A.; Ewels, C.; Seifert, G.; Colliex, C., Electron knock-on cross section of carbon and boron nitride nanotubes. *Physical Review B* **2007,** *75* (24), 245402.
54. Zhang, A.; Teoh, H. F.; Dai, Z.; Feng, Y. P.; Zhang, C., Band gap engineering in graphene and hexagonal BN antidot lattices: A first principles study. *Appl. Phys. Lett.* **2011,** *98* (2), 023105.
55. Chen, W.; Li, Y.; Yu, G.; Zhou, Z.; Chen, Z., Electronic structure and reactivity of boron nitride nanoribbons with stone-wales defects. *Journal of Chemical Theory and Computation* **2009,** *5* (11), 3088-3095.
56. Anota, E. C.; Gutiérrez, R. E. R.; Morales, A. E.; Cocoletzi, G. H., Influence of point defects on the electronic properties of boron nitride nanosheets. *J. Mol. Model.* **2012,** *18* (5), 2175-2184.
57. Yang, K.; Chen, Y.; Xie, Y.; Wei, X.; Ouyang, T.; Zhong, J., Effect of triangle vacancy on thermal transport in boron nitride nanoribbons. *Solid State Commun.* **2011,** *151* (6), 460-464.
58. Lin, Y.; Williams, T. V.; Cao, W.; Elsayed-Ali, H. E.; Connell, J. W., Defect functionalization of hexagonal boron nitride nanosheets. *The Journal of Physical Chemistry C* **2010,** *114* (41), 17434-17439.
59. Du, M.; Li, X.; Wang, A.; Wu, Y.; Hao, X.; Zhao, M., One-step exfoliation and fluorination of boron nitride nanosheets and a study of their magnetic properties. *Angew. Chem. Int. Ed. Engl.* **2014,** *53* (14), 3645-9.
60. Loiseau, A.; Willaime, F.; Demoncy, N.; Hug, G.; Pascard, H., Boron nitride nanotubes with reduced numbers of layers synthesized by arc discharge. *Phys.*

Rev. Lett. **1996,** *76* (25), 4737.

61. Arenal, R.; Stephan, O.; Cochon, J.-L.; Loiseau, A., Root-growth mechanism for single-walled boron nitride nanotubes in laser vaporization technique. *J. Am. Chem. Soc.* **2007,** *129* (51), 16183-16189.
62. Arenal, R.; Ferrari, A. C.; Reich, S.; Wirtz, L.; Mevellec, J. Y.; Lefrant, S.; Rubio, A.; Loiseau, A., Raman spectroscopy of single-wall boron nitride nanotubes. *Nano Lett.* **2006,** *6* (8), 1812-6.
63. Chen, Y. I., *Nanotubes and nanosheets: functionalization and applications of boron nitride and other nanomaterials*. CRC Press: Boca Raton, **2015**.
64. Panchal, M. B.; Upadhyay, S., Doubly-Clamped Single Walled Boron Nitride Nanotube Based Nanomechanical Resonators: A Computational Investigation of Their Behavior. *J. Nanotechnol. Eng. Med.* **2012,** *3* (4), 044501.
65. Arenal, R.; Blase, X.; Loiseau, A., Boron-nitride and boron-carbonitride nanotubes: synthesis, characterization and theory. *Advances in Physics* **2010,** *59* (2), 101-179.
66. Golberg, D.; Costa, P. M. F. J.; Lourie, O.; Mitome, M.; Bai, X. D.; Kurashima, K.; Zhi, C. Y.; Tang, C. C.; Bando, Y., Direct force measurements and kinking under elastic deformation of individual multiwalled boron nitride nanotubes. *Nano Lett.* **2007,** *7* (7), 2146-2151.
67. Balmain, W., Bemerkungen über die Bildung von Verbindungen des Bors und Siliciums mit Stickstoff und gewissen Metallen. *Adv. Synth. Catal.* **1842,** *27* (1), 422-430.
68. Haubner, R.; Wilhelm, M.; Weissenbacher, R.; Lux, B., Boron nitrides—properties, synthesis and applications. In *High Performance Non-Oxide Ceramics II*, Springer: Berlin Heidelberg, **2002**, pp 1-45.
69. Paine, R. T.; Narula, C. K., Synthetic routes to boron nitride. *Chem. Rev.* **1990,** *90* (1), 73-91.
70. Takahashi, T.; Itoh, H.; Takeuchi, A., Chemical vapor deposition of hexagonal boron nitride thick film on iron. *J. Cryst. Growth* **1979,** *47* (2), 245-250.
71. Motojima, S.; Tamura, Y.; Sugiyama, K., Low temperature deposition of hexagonal BN films by chemical vapour deposition. *Thin Solid Films* **1982,** *88* (3), 269-274.
72. Laubengayer, A.; Moews Jr, P.; Porter, R. F., The Condensation of Borazine to Polycyclic Boron-Nitrogen Frameworks by Pyrolytic Dehydrogenation1. *J. Am. Chem. Soc.* **1961,** *83* (6), 1337-1342.
73. Shore, S. G.; Parry, R. W., The crystalline compound ammonia-borane, 1 H3NBH3. *J. Am. Chem. Soc.* **1955,** *77* (22), 6084-6085.
74. Rudolph, S., BORON NITRIDE(BN). *Am. Ceram. Soc. Bull.* **2000,** *79* (6), 50.
75. Lipp, A.; Schwetz, K. A.; Hunold, K., Hexagonal boron nitride: fabrication, properties and applications. *J. Eur. Ceram. Soc.* **1989,** *5* (1), 3-9.
76. Rao, L.; Kaner, R. B., Rapid solid-state-precursor synthesis of crystalline boron nitride. *Inorg. Chem.* **1994,** *33* (15), 3210-3211.

77. Taniguchi, T.; Yamaoka, S., Spontaneous nucleation of cubic boron nitride single crystal by temperature gradient method under high pressure. *J. Cryst. Growth* **2001,** *222* (3), 549-557.
78. Kubota, Y.; Watanabe, K.; Tsuda, O.; Taniguchi, T., Hexagonal Boron Nitride Single Crystal Growth at Atmospheric Pressure Using Ni− Cr Solvent. *Chem. Mater.* **2008,** *20* (5), 1661-1663.
79. Zhigadlo, N. D., Crystal growth of hexagonal boron nitride (hBN) from Mg–B–N solvent system under high pressure. *J. Cryst. Growth* **2014,** *402*, 308-311.
80. Khan, M. H.; Liu, H. K.; Sun, X.; Yamauchi, Y.; Bando, Y.; Golberg, D.; Huang, Z., Few-atomic-layered hexagonal boron nitride: CVD growth, characterization, and applications. *Mater. Today* **2017,** 20 (10), 611-628.
81. Li, L. H.; Santos, E. J.; Xing, T.; Cappelluti, E.; Roldan, R.; Chen, Y.; Watanabe, K.; Taniguchi, T., Dielectric screening in atomically thin boron nitride nanosheets. *Nano Lett.* **2015,** *15* (1), 218-23.
82. Cai, Q.; Li, L. H.; Yu, Y.; Liu, Y.; Huang, S.; Chen, Y.; Watanabe, K.; Taniguchi, T., Boron nitride nanosheets as improved and reusable substrates for gold nanoparticles enabled surface enhanced Raman spectroscopy. *Phys. Chem. Chem. Phys.* **2015,** *17* (12), 7761-6.
83. Cai, Q.; Mateti, S.; Yang, W.; Jones, R.; Watanabe, K.; Taniguchi, T.; Huang, S.; Chen, Y.; Li, L. H., Boron Nitride Nanosheets Improve Sensitivity and Reusability of Surface-Enhanced Raman Spectroscopy. *Angew. Chem. Int. Ed. Engl.* **2016,** *55* (29), 8405-9.
84. Falin, A.; Cai, Q.; Santos, E. J. G.; Scullion, D.; Qian, D.; Zhang, R.; Yang, Z.; Huang, S.; Watanabe, K.; Taniguchi, T.; Barnett, M. R.; Chen, Y.; Ruoff, R. S.; Li, L. H., Mechanical properties of atomically thin boron nitride and the role of interlayer interactions. *Nat Commun* **2017,** *8*, 15815.
85. Stenger, I.; Schue, L.; Boukhicha, M.; Berini, B.; Placais, B.; Loiseau, A.; Barjon, J., Low frequency Raman spectroscopy of few-atomic-layer thick hBN crystals. *2D Materials* **2017,** *4* (3), 031003.
86. Schué, L.; Stenger, I.; Fossard, F.; Loiseau, A.; Barjon, J., Characterization methods dedicated to nanometer-thick hBN layers. *2D Materials* **2016,** *4* (1), 015028.
87. Schué, L.; Berini, B.; Betz, A. C.; Plaçais, B.; Ducastelle, F.; Barjon, J.; Loiseau, A., Dimensionality effects on the luminescence properties of hBN. *Nanoscale* **2016,** *8* (13), 6986-6993.
88. Lian, G.; Zhang, X.; Tan, M.; Zhang, S.; Cui, D.; Wang, Q., Facile synthesis of 3D boron nitride nanoflowers composed of vertically aligned nanoflakes and fabrication of graphene-like BN by exfoliation. *J. Mater. Chem.* **2011,** *21* (25), 9201-9207.
89. Coleman, J. N.; Lotya, M.; O'Neill, A.; Bergin, S. D.; King, P. J.; Khan, U.; Young, K.; Gaucher, A.; De, S.; Smith, R. J.; Shvets, I. V.; Arora, S. K.; Stanton, G.; Kim, H. Y.; Lee, K.; Kim, G. T.; Duesberg, G. S.; Hallam, T.; Boland, J. J.;

Wang, J. J.; Donegan, J. F.; Grunlan, J. C.; Moriarty, G.; Shmeliov, A.; Nicholls, R. J.; Perkins, J. M.; Grieveson, E. M.; Theuwissen, K.; McComb, D. W.; Nellist, P. D.; Nicolosi, V., Two-dimensional nanosheets produced by liquid exfoliation of layered materials. *Science* **2011,** *331* (6017), 568-71.

90. Bergin, S. D.; Nicolosi, V.; Streich, P. V.; Giordani, S.; Sun, Z.; Windle, A. H.; Ryan, P.; Niraj, N. P. P.; Wang, Z. T. T.; Carpenter, L., Towards Solutions of Single-Walled Carbon Nanotubes in Common Solvents. *Adv. Mater.* **2008,** *20* (10), 1876-1881.
91. Hernandez, Y.; Nicolosi, V.; Lotya, M.; Blighe, F. M.; Sun, Z.; De, S.; McGovern, I.; Holland, B.; Byrne, M.; Gun'Ko, Y. K., High-yield production of graphene by liquid-phase exfoliation of graphite. *Nature Nanotechnology* **2008,** *3* (9), 563.
92. Shen, J.; He, Y.; Wu, J.; Gao, C.; Keyshar, K.; Zhang, X.; Yang, Y.; Ye, M.; Vajtai, R.; Lou, J., Liquid phase exfoliation of two-dimensional materials by directly probing and matching surface tension components. *Nano Lett.* **2015,** *15* (8), 5449-5454.
93. Owens, D., Some thermodynamic aspects of polymer adhesion. *J. Appl. Polym. Sci.* **1970,** *14* (7), 1725-1730.
94. Zhou, K. G.; Mao, N. N.; Wang, H. X.; Peng, Y.; Zhang, H. L., A mixed-solvent strategy for efficient exfoliation of inorganic graphene analogues. *Angew. Chem. Int. Ed.* **2011,** *50* (46), 10839-10842.
95. Lei, W.; Mochalin, V. N.; Liu, D.; Qin, S.; Gogotsi, Y.; Chen, Y., Boron nitride colloidal solutions, ultralight aerogels and freestanding membranes through one-step exfoliation and functionalization. *Nature Communications* **2015,** *6*, 8849.
96. Sainsbury, T.; O'Neill, A.; Passarelli, M. K.; Seraffon, M.; Gohil, D.; Gnaniah, S.; Spencer, S. J.; Rae, A.; Coleman, J. N., Dibromocarbene functionalization of boron nitride nanosheets: Toward band gap manipulation and nanocomposite applications. *Chem. Mater.* **2014,** *26* (24), 7039-7050.
97. Chen, X.; Dobson, J. F.; Raston, C. L., Vortex fluidic exfoliation of graphite and boron nitride. *Chem. Commun.* **2012,** *48* (31), 3703-3705.
98. Jiao, L.; Zhang, L.; Wang, X.; Diankov, G.; Dai, H., Narrow graphene nanoribbons from carbon nanotubes. *Nature* **2009,** *458* (7240), 877.
99. Paffett, M.; Simonson, R.; Papin, P.; Paine, R., Borazine adsorption and decomposition at Pt (111) and Ru (001) surfaces. *Surf. Sci.* **1990,** *232* (3), 286-296.
100. Nagashima, A.; Tejima, N.; Gamou, Y.; Kawai, T.; Oshima, C., Electronic dispersion relations of monolayer hexagonal boron nitride formed on the Ni (111) surface. *Physical Review B* **1995,** *51* (7), 4606.
101. Preobrajenski, A.; Vinogradov, A.; Mårtensson, N., Monolayer of h-BN chemisorbed on Cu (1 1 1) and Ni (1 1 1): The role of the transition metal 3d states. *Surf. Sci.* **2005,** *582* (1-3), 21-30.
102. Preobrajenski, A.; Vinogradov, A.; Ng, M. L.; Ćavar, E.; Westerström, R.;

Mikkelsen, A.; Lundgren, E.; Mårtensson, N., Influence of chemical interaction at the lattice-mismatched h− B N⁄Rh (111) and h− B N⁄Pt (111) interfaces on the overlayer morphology. *Physical Review B* **2007,** *75* (24), 245412.

103. Lee, J. S.; Choi, S. H.; Yun, S. J.; Kim, Y. I.; Boandoh, S.; Park, J.-H.; Shin, B. G.; Ko, H.; Lee, S. H.; Kim, Y.-M., Wafer-scale single-crystal hexagonal boron nitride film via self-collimated grain formation. *Science* **2018,** *362* (6416), 817-821.
104. Zhang, K.; Feng, Y.; Wang, F.; Yang, Z.; Wang, J., Two dimensional hexagonal boron nitride (2D-hBN): synthesis, properties and applications. *Journal of Materials Chemistry C* **2017,** *5* (46), 11992-12022.
105. Han, W.-Q.; Yu, H.-G.; Liu, Z., Convert graphene sheets to boron nitride and boron nitride–carbon sheets via a carbon-substitution reaction. *Appl. Phys. Lett.* **2011,** *98* (20), 203112.
106. Gong, Y.; Shi, G.; Zhang, Z.; Zhou, W.; Jung, J.; Gao, W.; Ma, L.; Yang, Y.; Yang, S.; You, G., Direct chemical conversion of graphene to boron-and nitrogen-and carbon-containing atomic layers. *Nature Communications* **2014,** *5*, 3193.
107. Lin, T. W.; Su, C. Y.; Zhang, X. Q.; Zhang, W.; Lee, Y. H.; Chu, C. W.; Lin, H. Y.; Chang, M. T.; Chen, F. R.; Li, L. J., Converting graphene oxide monolayers into boron carbonitride nanosheets by substitutional doping. *Small* **2012,** *8* (9), 1384-1391.
108. Wang, X.; Pakdel, A.; Zhi, C.; Watanabe, K.; Sekiguchi, T.; Golberg, D.; Bando, Y., High-yield boron nitride nanosheets from 'chemical blowing': towards practical applications in polymer composites. *J. Phys.: Condens. Matter* **2012,** *24* (31), 314205.
109. Wu, P.; Zhu, W.; Chao, Y.; Zhang, J.; Zhang, P.; Zhu, H.; Li, C.; Chen, Z.; Li, H.; Dai, S., A template-free solvent-mediated synthesis of high surface area boron nitride nanosheets for aerobic oxidative desulfurization. *Chem. Commun.* **2016,** *52* (1), 144-147.
110. Xu, M.; Fujita, D.; Chen, H.; Hanagata, N., Formation of monolayer and few-layer hexagonal boron nitride nanosheets via surface segregation. *Nanoscale* **2011,** *3* (7), 2854-2858.
111. Zhi, C.; Bando, Y.; Tang, C.; Golberg, D., Boron nitride nanotubes. *Materials Science and Engineering: R: Reports* **2010,** *70* (3-6), 92-111.
112. Golberg, D.; Bando, Y.; Eremets, M.; Takemura, K.; Kurashima, K.; Yusa, H., Nanotubes in boron nitride laser heated at high pressure. *Appl. Phys. Lett.* **1996,** *69* (14), 2045-2047.
113. Golberg, D.; Rode, A.; Bando, Y.; Mitome, M.; Gamaly, E.; Luther-Davies, B., Boron nitride nanostructures formed by ultra-high-repetition rate laser ablation. *Diamond Relat. Mater.* **2003,** *12* (8), 1269-1274.
114. Zhou, G. W.; Zhang, Z.; Bai, Z. G., Catalyst effects on formation of boron nitride nano-tubules synthesized by laser ablation. *Solid State Commun.* **1999,** *109* (8), 555-559.

115. Zhi, C.; Bando, Y.; Tang, C.; Honda, S.; Sato, K.; Kuwahara, H.; Golberg, D., Purification of boron nitride nanotubes through polymer wrapping. *The Journal of Physical Chemistry B* **2006,** *110* (4), 1525-1528.
116. Han, W.; Bando, Y.; Kurashima, K.; Sato, T., Synthesis of boron nitride nanotubes from carbon nanotubes by a substitution reaction. *Appl. Phys. Lett.* **1998,** *73* (21), 3085-3087.
117. Shelimov, K. B.; Moskovits, M., Composite nanostructures based on template-grown boron nitride nanotubules. *Chem. Mater.* **2000,** *12* (1), 250-254.
118. Golberg, D.; Bando, Y.; Kurashima, K.; Sato, T., MoO3-promoted synthesis of multi-walled BN nanotubes from C nanotube templates. *Chem. Phys. Lett.* **2000,** *323* (1-2), 185-191.
119. Golberg, D.; Bando, Y.; Han, W.; Kurashima, K.; Sato, T., Single-walled B-doped carbon, B/N-doped carbon and BN nanotubes synthesized from single-walled carbon nanotubes through a substitution reaction. *Chem. Phys. Lett.* **1999,** *308* (3-4), 337-342.
120. Bechelany, M.; Bernard, S.; Brioude, A.; Cornu, D.; Stadelmann, P.; Charcosset, C.; Fiaty, K.; Miele, P., Synthesis of boron nitride nanotubes by a template-assisted polymer thermolysis process. *The Journal of Physical Chemistry C* **2007,** *111* (36), 13378-13384.
121. Dai, J.; Xu, L.; Fang, Z.; Sheng, D.; Guo, Q.; Ren, Z.; Wang, K.; Qian, Y., A convenient catalytic approach to synthesize straight boron nitride nanotubes using synergic nitrogen source. *Chem. Phys. Lett.* **2007,** *440* (4-6), 253-258.
122. Xu, L.; Peng, Y.; Meng, Z.; Yu, W.; Zhang, S.; Liu, X.; Qian, Y., A co-pyrolysis method to boron nitride nanotubes at relative low temperature. *Chem. Mater.* **2003,** *15* (13), 2675-2680.
123. Chen, Y.; Chadderton, L. T.; Gerald, J. F.; Williams, J. S., A solid-state process for formation of boron nitride nanotubes. *Appl. Phys. Lett.* **1999,** *74* (20), 2960-2962.
124. Chen, Y.; Conway, M.; Williams, J.; Zou, J., Large-quantity production of high-yield boron nitride nanotubes. *J. Mater. Res.* **2002,** *17* (8), 1896-1899.
125. Chen, Y.; Gerald, J. F.; Williams, J.; Bulcock, S., Synthesis of boron nitride nanotubes at low temperatures using reactive ball milling. *Chem. Phys. Lett.* **1999,** *299* (3-4), 260-264.
126. Yu, J.; Chen, Y.; Wuhrer, R.; Liu, Z.; Ringer, S. P., In situ formation of BN nanotubes during nitriding reactions. *Chem. Mater.* **2005,** *17* (20), 5172-5176.
127. Lourie, O. R.; Jones, C. R.; Bartlett, B. M.; Gibbons, P. C.; Ruoff, R. S.; Buhro, W. E., CVD growth of boron nitride nanotubes. *Chem. Mater.* **2000,** *12* (7), 1808-1810.
128. Wang, J.; Kayastha, V. K.; Yap, Y. K.; Fan, Z.; Lu, J. G.; Pan, Z.; Ivanov, I. N.; Puretzky, A. A.; Geohegan, D. B., Low temperature growth of boron nitride nanotubes on substrates. *Nano Lett.* **2005,** *5* (12), 2528-2532.
129. Ma, R.; Bando, Y.; Sato, T.; Kurashima, K., Growth, morphology, and structure of boron nitride nanotubes. *Chem. Mater.* **2001,** *13* (9), 2965-2971.

130. Kim, M. J.; Chatterjee, S.; Kim, S. M.; Stach, E. A.; Bradley, M. G.; Pender, M. J.; Sneddon, L. G.; Maruyama, B., Double-walled boron nitride nanotubes grown by floating catalyst chemical vapor deposition. *Nano Lett.* **2008,** *8* (10), 3298-3302.
131. Tang, C.; Bando, Y.; Sato, T.; Kurashima, K., A novel precursor for synthesis of pure boron nitride nanotubes. *Chem. Commun.* **2002,** (12), 1290-1291.
132. Zhi, C.; Bando, Y.; Tan, C.; Golberg, D., Effective precursor for high yield synthesis of pure BN nanotubes. *Solid State Commun.* **2005,** *135* (1-2), 67-70.
133. Smith, M. W.; Jordan, K. C.; Park, C.; Kim, J.-W.; Lillehei, P. T.; Crooks, R.; Harrison, J. S., Very long single-and few-walled boron nitride nanotubes via the pressurized vapor/condenser method. *Nanotechnology* **2009,** *20* (50), 505604.
134. Fathalizadeh, A.; Pham, T.; Mickelson, W.; Zettl, A., Scaled synthesis of boron nitride nanotubes, nanoribbons, and nanococoons using direct feedstock injection into an extended-pressure, inductively-coupled thermal plasma. *Nano Lett.* **2014,** *14* (8), 4881-4886.
135. Kim, K. S.; Kim, M. J.; Park, C.; Fay, C. C.; Chu, S.-H.; Kingston, C. T.; Simard, B., Scalable manufacturing of boron nitride nanotubes and their assemblies: a review. *Semicond. Sci. Technol.* **2016,** *32* (1), 013003.
136. Shimizu, Y.; Moriyoshi, Y.; Tanaka, H.; Komatsu, S., Boron nitride nanotubes, webs, and coexisting amorphous phase formed by the plasma jet method. *Appl. Phys. Lett.* **1999,** *75* (7), 929-931.
137. Lee, C. M.; Choi, S.; Choi, S.; Hong, S. H., Synthesis of boron nitride nanotubes by arc-jet plasma. *Current Applied Physics* **2006,** *6* (2), 166-170.
138. Kim, K. S.; Kingston, C. T.; Hrdina, A.; Jakubinek, M. B.; Guan, J. W.; Plunkett, M.; Simard, B., Hydrogen-Catalyzed, Pilot-Scale Production of Small-Diameter Boron Nitride Nanotubes and Their Macroscopic Assemblies. *ACS Nano* **2014,** *8* (6), 6211-6220.
139. Erickson, K. J.; Gibb, A. L.; Sinitskii, A.; Rousseas, M.; Alem, N.; Tour, J. M.; Zettl, A. K., Longitudinal splitting of boron nitride nanotubes for the facile synthesis of high quality boron nitride nanoribbons. *Nano Lett.* **2011,** *11* (8), 3221-3226.
140. Lee, C.; Wei, X.; Kysar, J. W.; Hone, J., Measurement of the elastic properties and intrinsic strength of monolayer graphene. *Science* **2008,** *321* (5887), 385-388.
141. Lee, C.; Wei, X.; Li, Q.; Carpick, R.; Kysar, J. W.; Hone, J., Elastic and frictional properties of graphene. *physica status solidi (b)* **2009,** *246* (11-12), 2562-2567.
142. Lindsay, L.; Broido, D., Enhanced thermal conductivity and isotope effect in single-layer hexagonal boron nitride. *Physical Review B* **2011,** *84* (15), 155421.
143. Balandin, A. A.; Ghosh, S.; Bao, W.; Calizo, I.; Teweldebrhan, D.; Miao, F.; Lau, C. N., Superior thermal conductivity of single-layer graphene. *Nano Lett.* **2008,** *8* (3), 902-907.
144. Lee, J.-U.; Yoon, D.; Kim, H.; Lee, S. W.; Cheong, H., Thermal conductivity of suspended pristine graphene measured by Raman spectroscopy. *Physical Review B* **2011,** *83* (8), 081419.

145. Liu, L.; Ryu, S.; Tomasik, M. R.; Stolyarova, E.; Jung, N.; Hybertsen, M. S.; Steigerwald, M. L.; Brus, L. E.; Flynn, G. W., Graphene oxidation: thickness-dependent etching and strong chemical doping. *Nano Lett.* **2008,** *8* (7), 1965-1970.
146. Zhu, Y.; Murali, S.; Cai, W.; Li, X.; Suk, J. W.; Potts, J. R.; Ruoff, R. S., Graphene and graphene oxide: synthesis, properties, and applications. *Adv. Mater.* **2010,** *22* (35), 3906-3924.
147. Hua Li, L.; Chen, Y.; Cheng, B.-M.; Lin, M.-Y.; Chou, S.-L.; Peng, Y.-C., Photoluminescence of boron nitride nanosheets exfoliated by ball milling. *Appl. Phys. Lett.* **2012,** *100* (26), 261108.
148. Jo, I.; Pettes, M. T.; Kim, J.; Watanabe, K.; Taniguchi, T.; Yao, Z.; Shi, L., Thermal conductivity and phonon transport in suspended few-layer hexagonal boron nitride. *Nano Lett.* **2013,** *13* (2), 550-554.
149. Zhou, H.; Zhu, J.; Liu, Z.; Yan, Z.; Fan, X.; Lin, J.; Wang, G.; Yan, Q.; Yu, T.; Ajayan, P. M., High thermal conductivity of suspended few-layer hexagonal boron nitride sheets. *Nano Research* **2014,** *7* (8), 1232-1240.
150. Cai, Q.; Scullion, D.; Gan, W.; Falin, A.; Zhang, S.; Watanabe, K.; Taniguchi, T.; Chen, Y.; Santos, E. J. G.; Li, L. H., High thermal conductivity of high-quality monolayer boron nitride and its thermal expansion. *Sci Adv* **2019,** *5* (6), eaav0129.
151. Ying, H.; Moore, A.; Cui, J.; Liu, Y.; Li, D.; Han, S.; Yao, Y.; Wang, Z.; Wang, L.; Chen, S., Tailoring the thermal transport properties of monolayer hexagonal boron nitride by grain size engineering. *2D Materials* **2019,** *7* (1), 015031.
152. Ghosh, S.; Bao, W.; Nika, D. L.; Subrina, S.; Pokatilov, E. P.; Lau, C. N.; Balandin, A. A., Dimensional crossover of thermal transport in few-layer graphene. *Nature Materials* **2010,** *9* (7), 555-558.
153. Akdim, B.; Pachter, R.; Duan, X.; Adams, W. W., Comparative theoretical study of single-wall carbon and boron-nitride nanotubes. *Physical Review B* **2003,** *67* (24), 245404.
154. Liu, Z.; Marder, T. B., B N versus C C: How Similar Are They? *Angew. Chem. Int. Ed.* **2008,** *47* (2), 242-244.
155. Wang, B.-C.; Tsai, M.-H.; Chou, Y.-M., Comparative theoretical study of carbon nanotubes and boron-nitride nanotubes. *Synth. Met.* **1997,** *86* (1-3), 2379-2380.
156. Blase, X.; Rubio, A.; Louie, S.; Cohen, M., Stability and band gap constancy of boron nitride nanotubes. *EPL (Europhysics Letters)* **1994,** *28* (5), 335.
157. Mintmire, J.; Dunlap, B.; White, C., Are fullerene tubules metallic? *Phys. Rev. Lett.* **1992,** *68* (5), 631.
158. Hernandez, E.; Goze, C.; Bernier, P.; Rubio, A., Elastic properties of C and B x C y N z composite nanotubes. *Phys. Rev. Lett.* **1998,** *80* (20), 4502.
159. Chopra, N. G.; Zettl, A., Measurement of the elastic modulus of a multi-wall boron nitride nanotube. *Solid State Commun.* **1998,** *105* (5), 297-300.
160. Coleman, J. N.; Khan, U.; Gun'ko, Y. K., Mechanical reinforcement of polymers

using carbon nanotubes. *Adv. Mater.* **2006,** *18* (6), 689-706.

161. Yu, M.-F.; Lourie, O.; Dyer, M. J.; Moloni, K.; Kelly, T. F.; Ruoff, R. S., Strength and breaking mechanism of multiwalled carbon nanotubes under tensile load. *Science* **2000,** *287* (5453), 637-640.
162. Wei, X.; Wang, M. S.; Bando, Y.; Golberg, D., Tensile tests on individual multi-walled boron nitride nanotubes. *Adv. Mater.* **2010,** *22* (43), 4895-4899.
163. Xiao, Y.; Yan, X.; Cao, J.; Ding, J.; Mao, Y.; Xiang, J., Specific heat and quantized thermal conductance of single-walled boron nitride nanotubes. *Physical Review B* **2004,** *69* (20), 205415.
164. Stewart, D. A.; Savic, I.; Mingo, N., First-principles calculation of the isotope effect on boron nitride nanotube thermal conductivity. *Nano Lett.* **2008,** *9* (1), 81-84.
165. Chang, C.; Fennimore, A.; Afanasiev, A.; Okawa, D.; Ikuno, T.; Garcia, H.; Li, D.; Majumdar, A.; Zettl, A., Isotope effect on the thermal conductivity of boron nitride nanotubes. *Phys. Rev. Lett.* **2006,** *97* (8), 085901.
166. Berber, S.; Kwon, Y.-K.; Tománek, D., Unusually high thermal conductivity of carbon nanotubes. *Phys. Rev. Lett.* **2000,** *84* (20), 4613.
167. Golberg, D.; Bando, Y.; Kurashima, K.; Sato, T., Synthesis and characterization of ropes made of BN multiwalled nanotubes. *Scripta Mater.* **2001,** *44* (8-9), 1561-1565.
168. Chen, Y.; Zou, J.; Campbell, S. J.; Le Caer, G., Boron nitride nanotubes: pronounced resistance to oxidation. *Appl. Phys. Lett.* **2004,** *84* (13), 2430-2432.
169. Yang, K.; Gu, M.; Han, H.; Mu, G., Influence of chemical processing on the morphology, crystalline content and thermal stability of multi-walled carbon nanotubes. *Mater. Chem. Phys.* **2008,** *112* (2), 387-392.
170. Lauret, J.; Arenal, R.; Ducastelle, F.; Loiseau, A.; Cau, M.; Attal-Tretout, B.; Rosencher, E.; Goux-Capes, L., Optical transitions in single-wall boron nitride nanotubes. *Phys. Rev. Lett.* **2005,** *94* (3), 037405.
171. Wu, J.; Han, W.-Q.; Walukiewicz, W.; Ager, J.; Shan, W.; Haller, E.; Zettl, A., Raman spectroscopy and time-resolved photoluminescence of BN and B x C y N z nanotubes. *Nano Lett.* **2004,** *4* (4), 647-650.
172. Harutyunyan, H.; Gokus, T.; Green, A. A.; Hersam, M. C.; Allegrini, M.; Hartschuh, A., Defect-induced photoluminescence from dark excitonic states in individual single-walled carbon nanotubes. *Nano Lett.* **2009,** *9* (5), 2010-2014.
173. Murakami, Y.; Lu, B.; Kazaoui, S.; Minami, N.; Okubo, T.; Maruyama, S., Photoluminescence sidebands of carbon nanotubes below the bright singlet excitonic levels. *Physical Review B* **2009,** *79* (19), 195407.
174. Kim, K. K.; Hsu, A.; Jia, X.; Kim, S. M.; Shi, Y.; Hofmann, M.; Nezich, D.; Rodriguez-Nieva, J. F.; Dresselhaus, M.; Palacios, T., Synthesis of monolayer hexagonal boron nitride on Cu foil using chemical vapor deposition. *Nano Lett.* **2011,** *12* (1), 161-166.
175. Wang, H.; Zhang, X.; Liu, H.; Yin, Z.; Meng, J.; Xia, J.; Meng, X. M.; Wu, J.; You,

J., Synthesis of Large-Sized Single-Crystal Hexagonal Boron Nitride Domains on Nickel Foils by Ion Beam Sputtering Deposition. *Adv. Mater.* **2015,** *27* (48), 8109-8115.

176. Sajjad, M.; Jadwisienczak, W. M.; Feng, P., Nanoscale structure study of boron nitride nanosheets and development of a deep-UV photo-detector. *Nanoscale* **2014,** *6* (9), 4577-4582.
177. Watanabe, K.; Taniguchi, T.; Niiyama, T.; Miya, K.; Taniguchi, M., Far-ultraviolet plane-emission handheld device based on hexagonal boron nitride. *Nature Photonics* **2009,** *3* (10), 591.
178. Blake, P.; Hill, E. W.; Castro Neto, A. H.; Novoselov, K. S.; Jiang, D.; Yang, R.; Booth, T. J.; Geim, A. K., Making graphene visible. *Appl. Phys. Lett.* **2007,** *91* (6), 063124.
179. Golla, D.; Chattrakun, K.; Watanabe, K.; Taniguchi, T.; LeRoy, B. J.; Sandhu, A., Optical thickness determination of hexagonal boron nitride flakes. *Appl. Phys. Lett.* **2013,** *102* (16), 161906.
180. Zunger, A.; Katzir, A.; Halperin, A., Optical properties of hexagonal boron nitride. *Physical Review B* **1976,** *13* (12), 5560.
181. Zhi, C.; Bando, Y.; Tang, C.; Xie, R.; Sekiguchi, T.; Golberg, D., Perfectly dissolved boron nitride nanotubes due to polymer wrapping. *J. Am. Chem. Soc.* **2005,** *127* (46), 15996-15997.
182. Tang, C.; Bando, Y.; Zhi, C.; Golberg, D., Boron–oxygen luminescence centres in boron–nitrogen systems. *Chem. Commun.* **2007,** (44), 4599-4601.
183. Jaffrennou, P.; Barjon, J.; Schmid, T.; Museur, L.; Kanaev, A.; Lauret, J.-S.; Zhi, C.; Tang, C.; Bando, Y.; Golberg, D., Near-band-edge recombinations in multiwalled boron nitride nanotubes: Cathodoluminescence and photoluminescence spectroscopy measurements. *Physical Review B* **2008,** *77* (23), 235422.
184. Oku, T.; Koi, N.; Suganuma, K., Electronic and optical properties of boron nitride nanotubes. *J. Phys. Chem. Solids* **2008,** *69* (5-6), 1228-1231.
185. Berzina, B.; Trinkler, L.; Krutohvostov, R.; Williams, R.; Carroll, D.; Czerw, R.; Shishonok, E., Photoluminescence excitation spectroscopy in boron nitride nanotubes compared to microcrystalline h-BN and c-BN. *Physica Status Solidi (c)* **2005,** *2* (1), 318-321.
186. Berzina, B.; Trinkler, L.; Korsak, V.; Krutohvostov, R.; Carroll, D.; Ucer, K.; Williams, R., Exciton luminescence of boron nitride nanotubes and nano-arches. *Physica Status Solidi (b)* **2006,** *243* (14), 3840-3845.
187. Peng, Q.; Ji, W.; De, S., Mechanical properties of the hexagonal boron nitride monolayer: Ab initio study. *Computational Materials Science* **2012,** *56*, 11-17.
188. Boldrin, L.; Scarpa, F.; Chowdhury, R.; Adhikari, S., Effective mechanical properties of hexagonal boron nitride nanosheets. *Nanotechnology* **2011,** *22* (50), 505702.
189. Li, C.; Bando, Y.; Zhi, C.; Huang, Y.; Golberg, D., Thickness-dependent bending

modulus of hexagonal boron nitride nanosheets. *Nanotechnology* **2009,** *20* (38), 385707.

190. Jing, G.; Ji, H.; Yang, W.; Xu, J.; Yu, D., Study of the bending modulus of individual silicon nitride nanobelts via atomic force microscopy. *Appl. Phys. A* **2006,** *82* (3), 475-478.
191. Kim, S. M.; Hsu, A.; Park, M. H.; Chae, S. H.; Yun, S. J.; Lee, J. S.; Cho, D. H.; Fang, W.; Lee, C.; Palacios, T.; Dresselhaus, M.; Kim, K. K.; Lee, Y. H.; Kong, J., Synthesis of large-area multilayer hexagonal boron nitride for high material performance. *Nat Commun* **2015,** *6*, 8662.
192. Ding, N.; Wu, C.-M. L.; Li, H., The effect of grain boundaries on the mechanical properties and failure behavior of hexagonal boron nitride sheets. *Phys. Chem. Chem. Phys.* **2014,** *16* (43), 23716-23722.
193. Gong, L.; Young, R. J.; Kinloch, I. A.; Riaz, I.; Jalil, R.; Novoselov, K. S., Optimizing the reinforcement of polymer-based nanocomposites by graphene. *ACS Nano* **2012,** *6* (3), 2086-2095.
194. Suryavanshi, A. P.; Yu, M.-F.; Wen, J.; Tang, C.; Bando, Y., Elastic modulus and resonance behavior of boron nitride nanotubes. *Appl. Phys. Lett.* **2004,** *84* (14), 2527-2529.
195. Verma, V.; Jindal, V.; Dharamvir, K., Elastic moduli of a boron nitride nanotube. *Nanotechnology* **2007,** *18* (43), 435711.
196. Dumitrică, T.; Yakobson, B. I., Rate theory of yield in boron nitride nanotubes. *Physical Review B* **2005,** *72* (3), 035418.
197. Zhou, X.; Tang, D. M.; Mitome, M.; Bando, Y.; Sasaki, T.; Golberg, D., Intrinsic and Defect-Related Elastic Moduli of Boron Nitride Nanotubes As Revealed by in Situ Transmission Electron Microscopy. *Nano Lett.* **2019,** *19* (8), 4974-4980.
198. Golberg, D.; Bai, X. D.; Mitome, M.; Tang, C. C.; Zhi, C. Y.; Bando, Y., Structural peculiarities of in situ deformation of a multi-walled BN nanotube inside a high-resolution analytical transmission electron microscope. *Acta Mater.* **2007,** *55* (4), 1293-1298.
199. Garel, J.; Leven, I.; Zhi, C.; Nagapriya, K. S.; Popovitz-Biro, R.; Golberg, D.; Bando, Y.; Hod, O.; Joselevich, E., Ultrahigh torsional stiffness and strength of boron nitride nanotubes. *Nano Lett.* **2012,** *12* (12), 6347-52.
200. Nigues, A.; Siria, A.; Vincent, P.; Poncharal, P.; Bocquet, L., Ultrahigh interlayer friction in multiwalled boron nitride nanotubes. *Nat Mater* **2014,** *13* (7), 688-93.

Chapter 2 BNNS and BNNT-based Nanocomposites

2.1 Introduction

Mechanisms of mechanical reinforcement by 1D materials and 2D materials are first of all summarized in this chapter, based on a recent review paper [1]. BNNSs and BNNTs-based polymer nanocomposites and their properties are reviewed. Enhanced mechanical properties are introduced in detail.

2.2 Composite reinforcement micromechanics

2.2.1 Rule of mixtures

The Young's modulus of a composite E_c can be estimated by simple "rule of mixture" as:

$$E_c = V_f E_f + (1-V_f)E_m \qquad (2.1)$$

where E_f, E_m are the Young's modulus of filler and matrix, respectively. V_f represents the volume fraction of filler in the composite. For precisely determining the E_c using this equation, it is assumed that [2]:

1. The size of the filler is infinite so the stress along the filler is uniform.
2. The orientation of the fillers is perfect and parallel to the uniaxial load.
3. The filler and matrix are well bonded without any interfacial failure.

However, above assumptions are difficult to be satisfied as the orientation, length (or aspect ratio), agglomeration etc. of fillers should been taken into account in the real case of composites. Therefore, a modified rule of mixtures has been proposed for the calculation of the modulus of a composite [1]:

$$E_c = \eta_o \eta_l V_f E_{eff} + (1-V_f)E_m \qquad (2.2)$$

where E_{eff} is the effective Young's modulus of the filler, η_o is the Krenchel orientation factor, which depends on the orientation of filler with respect to applied stress [3]. η_l is the length factor, which reflects the stress transfer efficiency from polymer matrix to filler. The length factor depends on the length of filler and interface between the filler and the matrix.

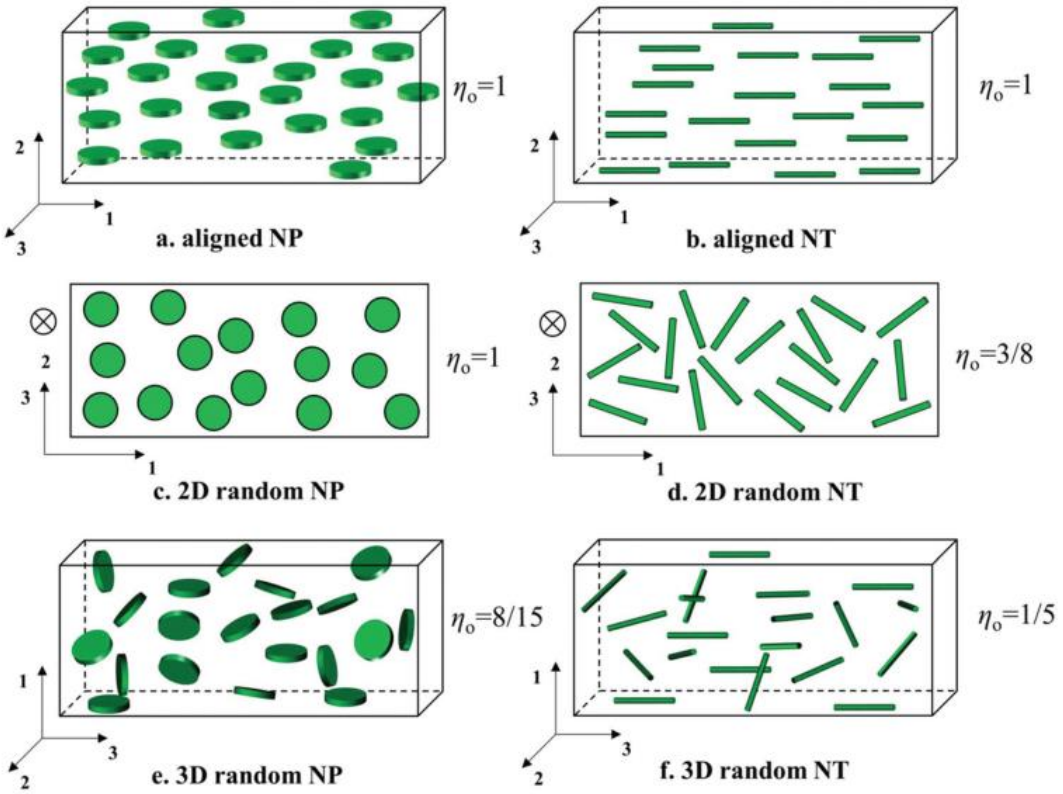

Figure 2.1 Schematic of 2D nanosheets (nanoplatelets) and 1D nanotubes nanocomposites with different nanofiller orientations [4].

The Krenchel orientation factor can be determined experimentally, by the use of different techniques, such as polarized Raman spectroscopy and X-ray diffraction, electron microscope etc., Liu et al. [4] summarized the Krenchel orientation factor of 1D nanotubes and 2D nanosheets (denoted as "nanoplatelets" in the paper) in polymers as shown Figure 2.1. In summary, the η_o for oriented nanosheets and nanotubes is 1, while for the case of 2D randomly distributed nanotubes and nanosheets η_o=3/8 and 1, respectively. For 3D randomly distributed nanotubes and nanosheets η_o=1/5 and 8/15, respectively. Since 1D and 2D nanofillers generally

show random distribution in polymer matrix, nanosheets exhibit higher reinforcing efficiency in the respect of orientation.

More recently, Li et al. [5] included an agglomeration factor: η_a in modified rule of mixtures: η_a equals to 1 if the dispersion of the filler is perfect and 0 for major agglomerations which reduce the effective stress transfer from the matrix to the filler. The modified rule of mixtures can be given as:

$$E_c = \eta_o \eta_l V_f \eta_a E_{eff} + (1 - V_f) E_m \qquad (2.3)$$

$V_f\eta_a$ can be considered as the effective volume fraction, which becomes the volume fraction if the dispersion of filler in the matrix is perfect.

2.2.2 Shear-lag model

The "rule of mixtures" was originally used for estimating the reinforcement of continuous fibres which were assumed to have infinite length. However, both nanotubes and nanosheets have very limited size, hence the stress transfer through interfacial adhesion is reduced if these nanofillers with finite length are used for reinforcement. Assuming the filler is aligned along the stress direction, the different intrinsic stiffness of filler and matrix leads to their different axial displacement (Figure 2.2).

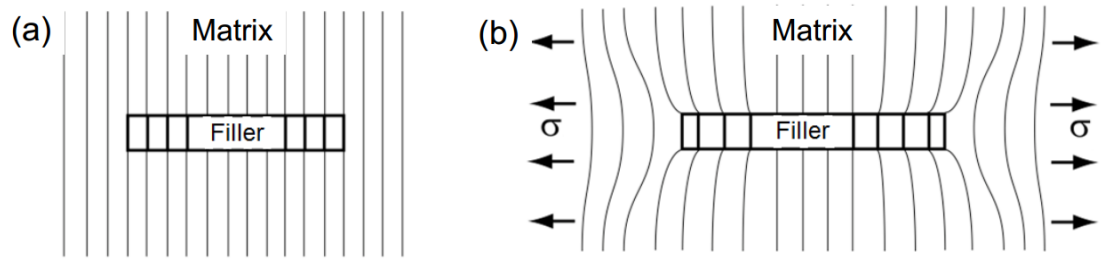

Figure 2.2 Schematic for the deformation of filler in composite [6].

As shown in Figure 2.2(b), it can be observed that the center of the filler deforms the

most under axial deformation, while the edges deform the least. Therefore, the interfacial shear stress at the edges of the filler is highest along the filler, due to large displacement between the matrix and the filler in these areas.

If the filler/matrix interface fails before or after the matrix yields depends on if the interface is stronger than matrix: stronger-matrix yields first; weaker-interfaces debond first. Therefore, it is important to evaluate the interfacial shear stress τ along the filler. Basically, the stress distribution along the filler can be fitted by two models: the Kelly-Tyson model [7] and the Cox model (*i.e.* shear-lag model) [8]. The filler is assumed to be linearly elastic in both models, while the matrix is assumed to be plastic in the Kelly-Tyson model, but linearly elastic in the Cox model, respectively.

In Kelly-Tyson model, τ is constant along the filler (Figure 2.3(b)), so there is a linear increase of the axial stress from edges to the center of the filler (Figure 2.3(c)).

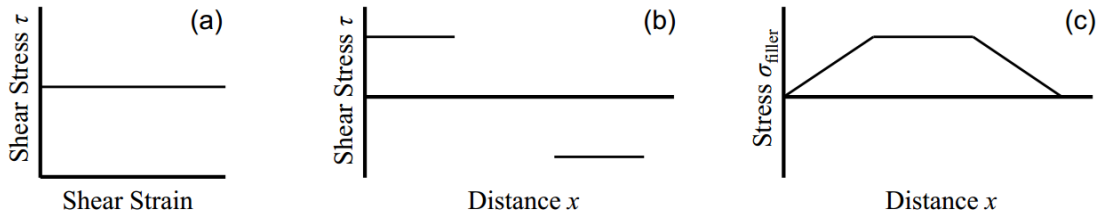

Figure 2.3 Kelly-Tyson model: (a) Stress-strain curve of the plastic matrix. (b) Shear stress and (c) Axial stress along the filler [6].

The shear-lag model estimates τ across the filler more accurately, in which the interfacial shear stress is not constant (Figure 2.4(b)).

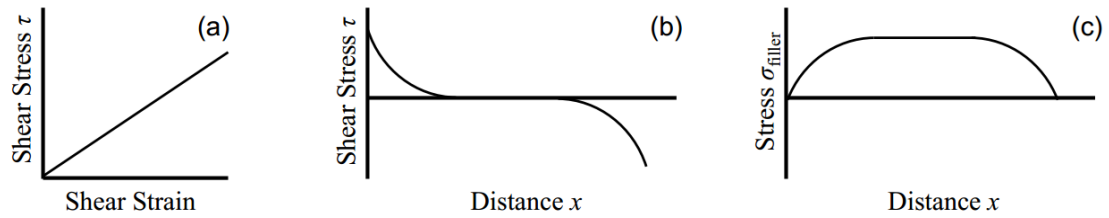

Figure 2.4 Shear-lag model: (a) Stress-strain curve of the elastic matrix. (b) Shear stress

and (c) Axial stress along the filler [6].

For 2D fillers such as graphene and BNNSs, the shear-lag model has been given as [9]:

$$\sigma_{\mathrm{f}} = E_{\mathrm{eff}}\varepsilon_{\mathrm{m}}\left[1-\frac{\cosh(nx/t)}{\cosh(nl/2t)}\right] = E_{\mathrm{eff}}\varepsilon_{\mathrm{m}}\left[1-\frac{\cosh(ns\frac{x}{l})}{\cosh(ns/2)}\right] \qquad (2.4)$$

where *s* is the aspect ratio of the 2D filler. *n*, has been widely accepted as a parameter for evaluating the interfacial stress transfer efficiency, which is defined as $n=\sqrt{\frac{2G_m}{E_{\mathrm{f}}}\left(\frac{t}{T}\right)}$ for the 2D filler. G_m is the shear modulus of the polymer matrix. E_{f} is the Young's modulus of the 2D filler. *t* is the thickness of the 2D filler and *T* is the thickness of polymer layers. If volume fraction of the filler can be considered as t/t+T, then t/T=V_{f}/(1-V_{f}). Therefore, τ (interfacial shear stress) of 2D filler is given by:

$$\tau_{2\mathrm{D}} = nE_{\mathrm{eff}}\varepsilon_{\mathrm{m}}\frac{\sinh(nx/t)}{\cosh(nl/2t)} = nE_{\mathrm{eff}}\varepsilon_{\mathrm{m}}\frac{\sinh(ns\frac{x}{l})}{\cosh(ns/2)} \qquad (2.5)$$

It can be seen in Equation 2.4 that the most efficient reinforcement is achieved when *ns* is high. In another words, 2D fillers with a high aspect ratio and strong interface with matrix are preferable for mechanical reinforcement. Length factor η_{l} for 2D filler can be given by using the Cox equation:

$$\eta_{\mathrm{l}} = 1 - \frac{\tanh(ns/2)}{ns/2} \qquad (2.6)$$

where *s* is the aspect ratio of the filler.

Similarly, for 1D fibres such as nanotubes, the stress on the filler σ_{f} can be modified as [1]:

$$\sigma_{\mathrm{f}} = E_{\mathrm{eff}}\varepsilon_{\mathrm{m}}\left[1-\frac{\cosh(nx/r)}{\cosh(nl/2r)}\right] \qquad (2.7)$$

where E_{eff} is the effective Young's modulus of the filler, ε_{m} is the strain applied on the

matrix, l is the length of the filler along the strain direction, x is the position in the filler. The length factor, η_l, for 1D filler can also be expressed as equation 2.6, where the parameter n is defined as:

$$n = \sqrt{\frac{2G_m}{E_{eff}} \frac{1}{\ln(R/r)}} \qquad (2.8)$$

where R and r represent the effective radius of the interface and the radius of the 1D filler, respectively. Based on equation 2.7, τ of 1D filler can be rewritten as:

$$\tau_{1D} = \frac{n}{2} E_{eff} \varepsilon_m \frac{\sinh(nx/r)}{\cosh(nl/2r)} \qquad (2.9)$$

In addition, both Kelly-Tyson model and shear-lag model describe the stress transfer from matrix to the filler where the strain in the filler builds up from the edges and reaches the applied strain on the matrix at a distance from the filler edge, and 90% of this distance is defined as the critical length (l_c) of the filler. It can be seen in Figure 2.5 that the region in the critical length exhibits very poor reinforcement while the center of the filler reinforces the composite sufficiently (if $l>l_c$). Our group's previous work suggested the l_c value of 1D fibres and 2D 1L graphene to be the order of several hundred microns [10] and ~3 μm [9] respectively. In order to achieve very sufficient reinforcement, it is usually suggested that the size of the filler needs to be 10 times of l_c. Fillers with size smaller than or this value can only provide limited reinforcement, especially when the filler size is of the order of l_c (Figure 2.5(b)) or the filler has fragmented into smaller shorter pieces at high strain (Figure 2.5(c)).

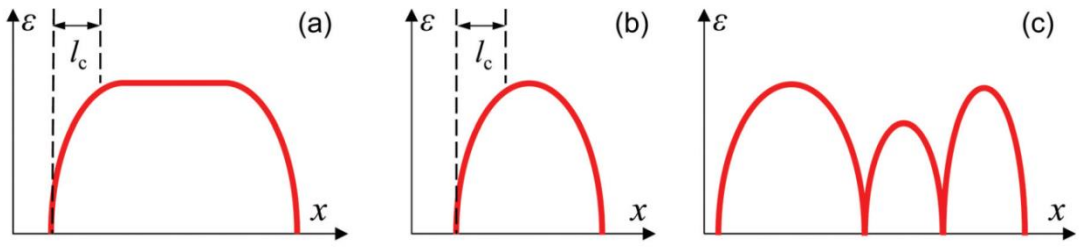

Figure 2.5 Strain distribution along the axial strain direction in a filler with (a) length much higher than l_c, (b) size comparable to l_c, (c) sufficient length but has fragmented into small pieces [1].

2.2.3 Other issues

In addition to rule of mixtures and shear-lag theory, Halpin-Tsai model [11] can also be used for predicting the Young's modulus of 1D & 2D materials-based composites. For the composite with uniaxially-aligned fillers, the Young's modulus $E_{\|}$ can be given by:

$$E_{\|} = E_{\mathrm{m}}\left[\frac{1+\eta_{\mathrm{L}} s V_{\mathrm{f}}}{1-\eta_{\mathrm{L}} V_{\mathrm{f}}}\right] \qquad (2.10)$$

where $\eta_{\mathrm{L}} = \dfrac{E_{\mathrm{f}}/E_{\mathrm{m}} - 1}{E_{\mathrm{f}}/E_{\mathrm{m}} + s}$, while for the composite with randomly-distributed fillers, the modulus E_{r} is modified as:

$$E_{\mathrm{r}} = E_{m}\left[\frac{3}{8}\frac{1+\eta_{\mathrm{L}} s V_{\mathrm{f}}}{1-\eta_{\mathrm{L}} V_{\mathrm{f}}} + \frac{5}{8}\frac{1+2\eta_{\mathrm{T}} s V_{\mathrm{f}}}{1-\eta_{\mathrm{T}} V_{\mathrm{f}}}\right] \qquad (2.11)$$

where $\eta_{\mathrm{T}} = \dfrac{E_{\mathrm{f}}/E_{\mathrm{m}} - 1}{E_{\mathrm{f}}/E_{\mathrm{m}} + 2}$. It should be noted that the definition of the parameter *s* varies in different studies [12-13]. It is generally dependent on both the boundary conditions and the geometry of the reinforcement [1].

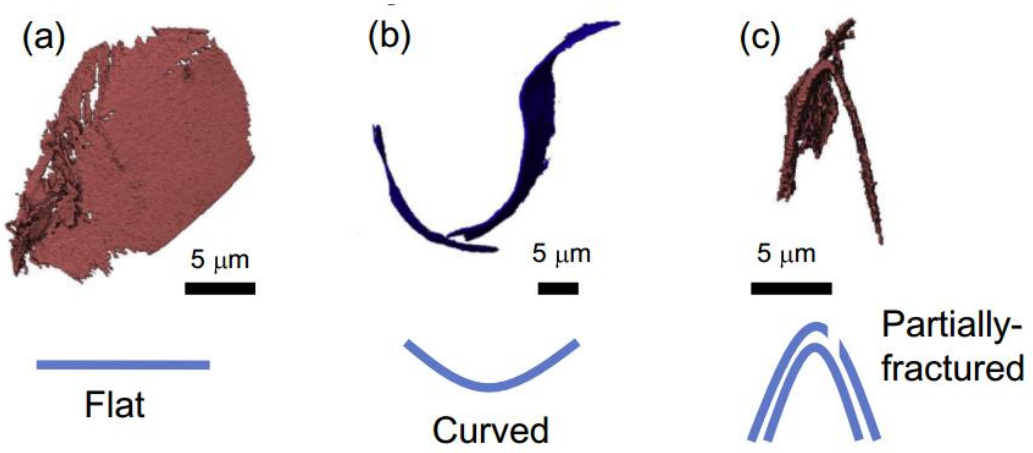

Figure 2.6 X-ray CT images showing the taxonomy of (a) a flat GNP flake, (b) two curved GNP flakes, (c) a curved GNP flake which fractured partially in the middle [14].

More recently, Li et al. [14] reported that the original lateral dimensions of 2D

materials are not always the same as their real effective length in composite, as the 2D materials tend to bend, fold, curve, break during the processing of composites (Figure 2.6), which will massively reduce their effective aspect ratio and reinforcement of the polymer matrix.

Interfacial adhesion between filler and matrix is another important factor on determining the efficiency of reinforcement. It is found that the interfacial shear stress between pristine graphene and a polymer is estimated to be order of 2 MPa [9], suggesting that the interface is dominated by van der Waals forces. Differently, the measured value of τ of pristine CNTs/polymer interface (around 50-90 MPa [15-16]) is much higher than that of graphene/polymer interface, which can be attributed to the nucleation effect of nanotubes which induces the polymer to form a crystalline coating on the shell of the nanotubes. Surface modification, by the means of both physical (such as interfacial roughing) and chemical (such as functionalization) way, is helpful on improving the adhesion between matrix and filler [17].

Apart from aspect ratio, flake size, interface and orientation, it is found that agglomerations and wrinkling of nanofillers also affect their reinforcing efficiency significantly, which has been systematically studied in relevant work on graphene and CNT-related nanocomposites. In brief, nanofillers with a very large surface area tend to agglomerated in nanocomposites, this is the key reason why the effective modulus of nanofillers massively drop at relatively high loading. For wrinkling on the surface of 2D materials, it can strengthen the interaction between 2D materials and matrix, thus providing better reinforcement [18]. On the other hand, the presence of wrinkles also reduces the aspect ratio of 2D materials.

2.3 BNNS & BNNT-based Nanocomposites

hBN-based nanostructures have many potential applications due to their special structures and excellent insulating, mechanical properties, thermal and chemical stabilities etc.. For instance, one of the most promising applications of BNNSs is as dielectric substrates in 2D materials-based electronic devices [19-21]. The applications of BNNSs and BNNTs were also extended to other fields such as composite nanofillers, thermally robust catalyst [22], field emitters [23], protective barriers for metals [24] etc.. Several papers have reviewed applications of hBN-based nanostructure and this review will focus on relevant work upon composites, particularly mechanical reinforcement of BNNSs and BNNTs upon polymer materials.

It should be noted that most of work upon BNNS/BNNT-based nanocomposites has focused more on the enhancement of the thermal conductivity of polymers. Taking a recent publication as an example, Chen et al. [25] reported the application of BNNSs/polymer nanocomposites in thermal management. They prepared oriented BNNSs-based composite films by folding and pressing electrospun composite nanofibres. As-prepared nanocomposites were found to be highly thermally conductive, and can be used as ideal thermal interface materials for heat-generating devices.

Apart from thermal conductivity, Wu et al. [26] reported that the addition of 10% BNNSs massively improves the fire resistance of polymers. Zhu et al. [27] reported that polymer-BNNSs-polymer sandwich-structure nanocomposite films could be used as high energy density dielectrics with merely 0.16 vol% BNNS concentration.

In contrast with graphene and CNTs, BNNSs and BNNTs have better thermal stability

and oxidation resistance, meanwhile have similar mechanical properties and thermal conductivity. Most importantly, hBN-based nanocomposites exhibit excellent electrical insulation, which is their key difference from graphene-based nanocomposites. Although more work has focused on the unique thermally conductive electrically insulating properties of hBN-based nanocomposites [28-32], the excellent mechanical properties of BNNSs and BNNTs make them suitable to be used as mechanical reinforcements for polymers [33]. Comparing with bulk hBN, BNNSs and BNNTs not only inherit its excellent thermal and insulating properties, but also exhibit more effective reinforcement for polymer matrix, due to their higher surface area and aspect ratio [34]. hBN-based materials do not absorb visible light due to their wide band gap, thus as-prepared composites have much higher light transparency than carbon-based composites, as illustrated in Figure 2.7 [28].

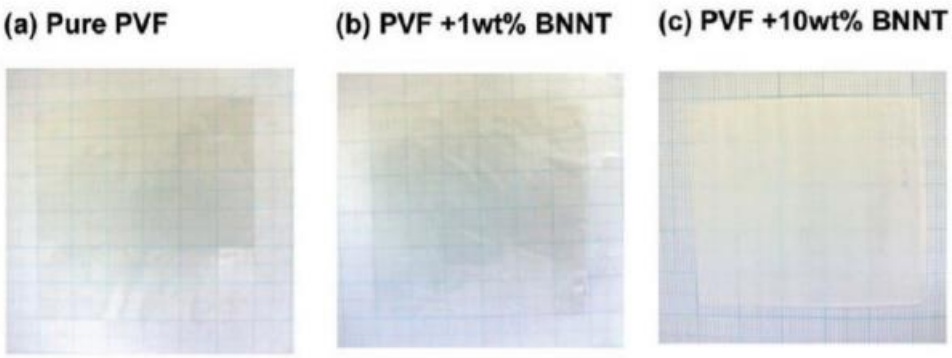

Figure 2.7 Optical photographs of (a) a pure poly(vinyl formal) (PVF) film; (b) a 1 wt% MW-BNNTs PVF nanocomposite film; (c) a 10 wt% MW-BNNTs PVF nanocomposite film. [28]

2.3.1 Mechanical properties of BNNS nanocomposites

In the case of BNNS-reinforced nanocomposites, initial work was reported by Zhi et al. [3]. They prepared liquid-exfoliated BNNSs using DMF as exfoliating reagent. As-prepared BNNSs were used for preparing BNNSs/PMMA nanocomposites with

high optical transparency. A 22% improvement in the elastic modulus and 11% improvement in the breaking strength of PMMA were obtained with only 0.3 wt% BNNSs loading. DSC results also showed a slight increase on the glass transition temperature (T_g) of PMMA from 69.7 ℃ to 72 ℃, as shown in Figure 2.8. A BNNS/PVA system was studied by Khan et al. [35], BNNSs with a high aspect ratio were exfoliated in solvent and then incorporated into PVA matrix. They achieved 40% enhancement on the modulus and strength of PVA matrix with the addition of only 0.12 vol% BNNSs [35].

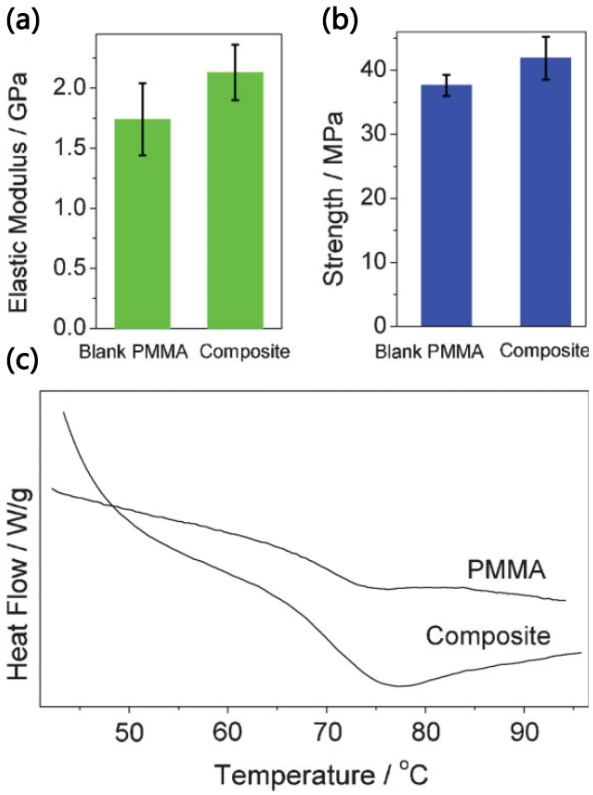

Figure 2.8 (a) Elastic modulus, (b) Breaking strength and (c) DSC curves of pure PMMA and 0.3 wt% BNNS/PMMA nanocomposites [3].

More recently, Jan et al. [36] reported the work on BNNS/poly(vinyl chloride) (PVC) nanocomposites. They prepared BNNSs with different flake sizes using liquid exfoliation and found a relatively low level of mechanical reinforcements in corresponding PVC nanocomposites due to the non-aligned nature of their BNNSs. However, after 300% uniaxial drawing was applied to the nanocomposite, both the

modulus and strength of nanocomposites increased massively, as shown in Figure 2.9(a). They attributed this further improvement not only to nanosheets alignment, but also the strain-induced exfoliation and deaggregation of the BNNSs in the nanocomposites. In addition, functionalized BNNSs were also prepared and found to achieve better mechanical reinforcements than pristine nanosheets [37]. For instance, Yu et al. [38] functionalized BNNSs with hyperbranched aromatic polyamide (HBP) and octadecylamine (ODA) molecules and used them as reinforcement for epoxy. BNNSs exhibit a higher level of reinforcement after the functionalization, as demonstrated from the storage modulus and glass transition temperature results shown in Figure 2.9(b, c).

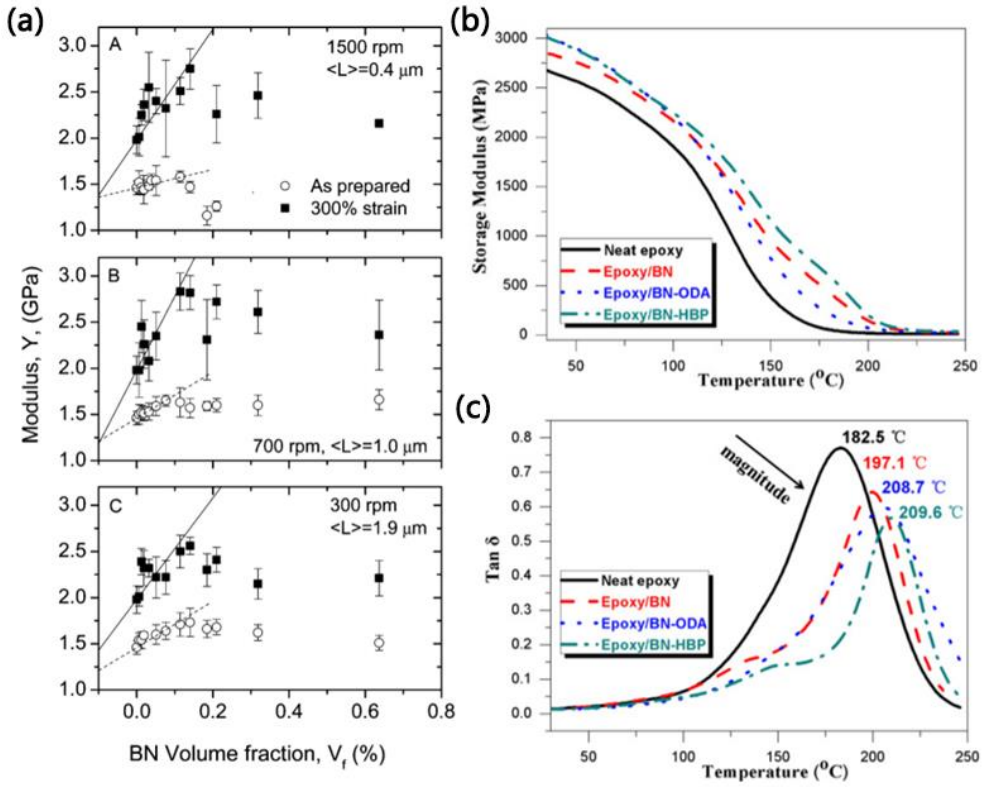

Figure 2.9 (a) Mechanical properties of PVC/BNNSs (with three different lateral sizes) nanocomposite films before and after 300% unaxial drawing [36]. (b, c) DMTA results of pure epoxy, BNNSs/epoxy, ODA-functionalized BNNSs/epoxy, HBP-functionalized BNNSs/epoxy nanocomposites [38].

Li et al. [39] reported a 6.2% enhancement on the tensile strength of polyamide (PA)

with the addition of 30 wt% BNNSs. Wang et al. [40] prepared BNNSs/polyimide (PI) nanocomposite aerogel with exceptional tensile strength and thermal conductivity. A very recent study from Zhu et al. [41] exhibited that the addition of 5 wt% BNNSs improved the tensile strength of thermoplastic polyurethane (TPU) film. Coleman et al. [42] reported a 53% improvement on the Young's modulus of a poly(ethylene terephthalate) (PET) film with 3 vol% addition of BNNSs. The authors also found that the addition of only 0.017 vol% already led a 27% modulus enhancement. Wu et al. [43] incorporated 10.5 vol% silane-functionalized BNNSs into styrene-butadiene rubber (SBR) and reported a dramatic improvement on both the tensile strength from 1.5 MPa to 18 MPa and the modulus from 0.9 MPa to 2.5 MPa of the neat SBR. In addition to the polymer-based nanocomposites, a BNNS/ceramic nanocomposite [44] was also studied and different levels of reinforcement upon mechanical performance were obtained.

2.3.2 Mechanical properties of BNNT nanocomposites

In 2006, Zhi et al. [45] first incorporated MW-BNNTs into polystyrene (PS) and measured the mechanical properties of nanocomposites. They mixed and sonicated BNNTs into two different solvents: chloroform and DMF for dispersion. In some experiments, a conjugated polymer poly(m-phenylenevinylene-co-2,5-dioctoxy-pphenylenevinylene) (PmPV) was mixed into the dispersion for functionalizing BNNTs and improve their solubility in solvents [46]. The PS matrix was then dissolved into a BNNT dispersion by magnetic stirring. The nanocomposites film was prepared by casting as-prepared BNNT/PS mixture onto glass slide, followed by solvent evaporation. Tensile test results suggested that a 1 wt% loading of pristine BNNTs improved the elastic modulus of PS up to 7% (DMF as solvent), which is not a high value, and the mechanical properties of PS became even worse when chloroform was used as solvent. This indicated a poor

dispersibility of pristine BNNTs into solvent, as well as the relatively-weak interfacial adhesion between the reinforcement and polymer matrix.

In contrast, PmPV-functionalized BNNTs exhibit a much higher enhancement, a highest 21% enhancement on elastic modulus was achieved with the addition of 1 wt% functionalized BNNTs. This initial work demonstrates that the addition of a small amount of BNNTs can significantly improve the mechanical properties of polymer matrix, in the case of relatively good dispersion in the nanocomposites and stronger interfacial interactions with polymer matrix. Therefore, a series of studies on the functionalization of BNNTs were performed, such as hydroxylation of BNNTs using H_2O_2 (Figure 2.10(a)) [47]. As shown in Figure 2.10(b), the dispersion of -OH functionalized BNNTs (BNNTs-OH) in water is much better than pristine BNNTs. Both BNNTs and BNNTs-OH were added into polycarbonate (PC) and a poly(vinyl butyral) (PVB) matrix for nanocomposites preparation. Tensile test results suggested BNNTs-OH to be a more effective enhancement for polymer matrix, as shown in Figure 2.10(c). A 1 wt% loading of pristine BNNTs improves the elastic modulus of PC by up to 20%. The addition of the same amount of BNNTs-OH further increases it by 31%. BNNTs-OH also shows a more effective reinforcement of the yield strength than Pristine BNNTs. Later, other work on different polymer matrix (such as poly(vinyl alcohol) (PVA)) [48], poly(vinylidene fluoride) (PVDF) [49]) all suggested that functionalization of BNNTs is necessary for optimizing their reinforcement of polymers. It is still possible to have a relatively good reinforcement using pristine BNNTs if their dispersion in the polymer is ideal. The elastic modulus of 1 wt% BNNTs/PMMA was improved up to 19% when nanotubes were well-dispersed in DMF solvent [50].

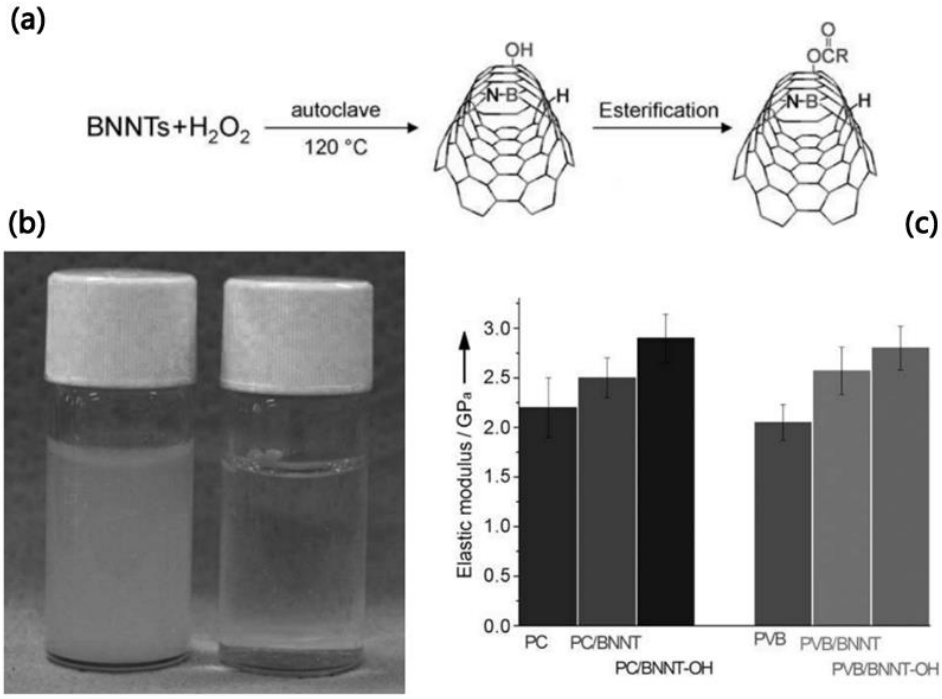

Figure 2.10 (a) Schematic diagram of the hydroxylation and esterification of BNNTs; (b) Optical photograph of aqueous dispersion of BNNTs-OH (left) and pristine BNNTs (right); (c) Elastic modulus of PC, 1 wt% BNNTs/PC, 1 wt% BNNTs-OH/PC and PVB, 1 wt% BNNTs/PVB, 1 wt% BNNTs-OH/PC [47].

2.4 Conclusions

This chapter has reviewed the micromechanics of nanocomposites reinforced by 2D and 1D nanomaterials. The properties, particularly mechanical properties of BNNSs and BNNTs-based nanocomposites have been covered in detail. Both BNNSs and BNNTs have been reported to be promising insulating reinforcements for polymers, but their poor interfacial adhesion with the matrix needs to be modified. More detailed work needs to be done to optimize the orientation, interfacial adhesion, agglomeration, aspect ratio, dimensions, inner layer-layer interaction of BNNSs & BNNTs in nanocomposites and their effect on mechanical reinforcement.

References

1. Papageorgiou, D. G.; Li, Z.; Liu, M.; Kinloch, I. A.; Young, R. J., Mechanisms of mechanical reinforcement by graphene and carbon nanotubes in polymer nanocomposites. *Nanoscale* **2020,** *12* (4), 2228-2267.
2. Padawer, G.; Beecher, N., On the strength and stiffness of planar reinforced plastic resins. *Polymer Engineering & Science* **1970,** *10* (3), 185-192.
3. Zhi, C.; Bando, Y.; Tang, C.; Kuwahara, H.; Golberg, D., Large-Scale Fabrication of Boron Nitride Nanosheets and Their Utilization in Polymeric Composites with Improved Thermal and Mechanical Properties. *Adv. Mater.* **2009,** *21* (28), 2889-2893.
4. Liu, H.; Brinson, L. C., Reinforcing efficiency of nanoparticles: A simple comparison for polymer nanocomposites. *Compos. Sci. Technol.* **2008,** *68* (6), 1502-1512.
5. Li, Z.; Chu, J.; Yang, C.; Hao, S.; Bissett, M. A.; Kinloch, I. A.; Young, R. J., Effect of functional groups on the agglomeration of graphene in nanocomposites. *Compos. Sci. Technol.* **2018,** *163*, 116-122.
6. Gibson, R. F., *Principles of composite material mechanics*. CRC press: **2016**.
7. Kelly, A.; Macmillan, N. H., Strong Solids. *Oxford University Press, Walton Street, Oxford OX 2 6 DP, UK, 1986.* **1986**.
8. Cox, H., The elasticity and strength of paper and other fibrous materials. *British Journal of Applied Physics* **1952,** *3* (3), 72.
9. Gong, L.; Kinloch, I. A.; Young, R. J.; Riaz, I.; Jalil, R.; Novoselov, K. S., Interfacial stress transfer in a graphene monolayer nanocomposite. *Adv. Mater.* **2010,** *22* (24), 2694-2697.
10. Andrews, M.; Young, R., Fragmentation of aramid fibres in single-fibre model composites. *Journal of Materials Science* **1995,** *30* (22), 5607-5616.
11. Affdl, J. H.; Kardos, J., The Halpin-Tsai equations: a review. *Polymer Engineering & Science* **1976,** *16* (5), 344-352.
12. Liang, J.; Huang, Y.; Zhang, L.; Wang, Y.; Ma, Y.; Guo, T.; Chen, Y., Molecular-level dispersion of graphene into poly (vinyl alcohol) and effective reinforcement of their nanocomposites. *Adv. Funct. Mater.* **2009,** *19* (14), 2297-2302.
13. Zhang, X.; Liu, T.; Sreekumar, T.; Kumar, S.; Moore, V. C.; Hauge, R. H.; Smalley, R. E., Poly (vinyl alcohol)/SWNT composite film. *Nano Lett.* **2003,** *3* (9), 1285-1288.
14. Li, Z.; Slater, T. J.; Ma, X.; Yu, Y.; Young, R. J.; Burnett, T. L., The taxonomy of graphite nanoplatelets and the influence of nanocomposite processing. *Carbon* **2019,** *142*, 99-106.
15. Barber, A. H.; Cohen, S. R.; Wagner, H. D., Measurement of carbon nanotube–polymer interfacial strength. *Appl. Phys. Lett.* **2003,** *82* (23), 4140-4142.

16. Coleman, J. N.; Cadek, M.; Blake, R.; Nicolosi, V.; Ryan, K. P.; Belton, C.; Fonseca, A.; Nagy, J. B.; Gun'ko, Y. K.; Blau, W. J., High performance nanotube-reinforced plastics: Understanding the mechanism of strength increase. *Adv. Funct. Mater.* **2004,** *14* (8), 791-798.
17. Terrones, M.; Martín, O.; González, M.; Pozuelo, J.; Serrano, B.; Cabanelas, J. C.; Vega-Díaz, S. M.; Baselga, J., Interphases in graphene polymer-based nanocomposites: achievements and challenges. *Adv. Mater.* **2011,** *23* (44), 5302-5310.
18. Ramanathan, T.; Abdala, A.; Stankovich, S.; Dikin, D.; Herrera-Alonso, M.; Piner, R.; Adamson, D.; Schniepp, H.; Chen, X.; Ruoff, R., Functionalized graphene sheets for polymer nanocomposites. *Nature Nanotechnology* **2008,** *3* (6), 327-331.
19. Dean, C. R.; Young, A. F.; Meric, I.; Lee, C.; Wang, L.; Sorgenfrei, S.; Watanabe, K.; Taniguchi, T.; Kim, P.; Shepard, K. L., Boron nitride substrates for high-quality graphene electronics. *Nature Nanotechnology* **2010,** *5* (10), 722.
20. Xue, J.; Sanchez-Yamagishi, J.; Bulmash, D.; Jacquod, P.; Deshpande, A.; Watanabe, K.; Taniguchi, T.; Jarillo-Herrero, P.; LeRoy, B. J., Scanning tunnelling microscopy and spectroscopy of ultra-flat graphene on hexagonal boron nitride. *Nature Materials* **2011,** *10* (4), 282.
21. Mayorov, A. S.; Gorbachev, R. V.; Morozov, S. V.; Britnell, L.; Jalil, R.; Ponomarenko, L. A.; Blake, P.; Novoselov, K. S.; Watanabe, K.; Taniguchi, T., Micrometer-scale ballistic transport in encapsulated graphene at room temperature. *Nano Lett.* **2011,** *11* (6), 2396-2399.
22. Wang, L.; Sun, C.; Xu, L.; Qian, Y., Convenient synthesis and applications of gram scale boron nitride nanosheets. *Catalysis Science & Technology* **2011,** *1* (7), 1119-1123.
23. Terrones, M.; Charlier, J.-C.; Gloter, A.; Cruz-Silva, E.; Terres, E.; Li, Y.; Vinu, A.; Zanolli, Z.; Dominguez, J.; Terrones, H., Experimental and theoretical studies suggesting the possibility of metallic boron nitride edges in porous nanourchins. *Nano Lett.* **2008,** *8* (4), 1026-1032.
24. Li, L. H.; Xing, T.; Chen, Y.; Jones, R., Boron nitride nanosheets for metal protection. *Advanced Materials Interfaces* **2014,** *1* (8).
25. Chen, J.; Huang, X.; Sun, B.; Jiang, P., Highly Thermally Conductive Yet Electrically Insulating Polymer/Boron Nitride Nanosheets Nanocomposite Films for Improved Thermal Management Capability. *ACS Nano* **2019,** *13* (1), 337-345.
26. Wu, Y.; Xue, Y.; Qin, S.; Liu, D.; Wang, X.; Hu, X.; Li, J.; Wang, X.; Bando, Y.; Golberg, D.; Chen, Y.; Gogotsi, Y.; Lei, W., BN Nanosheet/Polymer Films with Highly Anisotropic Thermal Conductivity for Thermal Management Applications. *ACS Appl Mater Interfaces* **2017,** *9* (49), 43163-43170.
27. Zhu, Y.; Zhu, Y.; Huang, X.; Chen, J.; Li, Q.; He, J.; Jiang, P., High Energy Density Polymer Dielectrics Interlayered by Assembled Boron Nitride Nanosheets. *Advanced Energy Materials* **2019,** *9* (36), 1901826.

28. Terao, T.; Bando, Y.; Mitome, M.; Zhi, C.; Tang, C.; Golberg, D., Thermal conductivity improvement of polymer films by catechin-modified boron nitride nanotubes. *The Journal of Physical Chemistry C* **2009,** *113* (31), 13605-13609.
29. Xu, Y.; Chung, D., Increasing the thermal conductivity of boron nitride and aluminum nitride particle epoxy-matrix composites by particle surface treatments. *Compos. Interfaces* **2000,** *7* (4), 243-256.
30. Wattanakul, K.; Manuspiya, H.; Yanumet, N., Effective surface treatments for enhancing the thermal conductivity of BN-filled epoxy composite. *J. Appl. Polym. Sci.* **2011,** *119* (6), 3234-3243.
31. Huang, X.; Zhi, C.; Jiang, P.; Golberg, D.; Bando, Y.; Tanaka, T., Polyhedral oligosilsesquioxane-modified boron nitride nanotube based epoxy nanocomposites: an ideal dielectric material with high thermal conductivity. *Adv. Funct. Mater.* **2013,** *23* (14), 1824-1831.
32. Cho, H.-B.; Tu, N. C.; Fujihara, T.; Endo, S.; Suzuki, T.; Tanaka, S.; Jiang, W.; Suematsu, H.; Niihara, K.; Nakayama, T., Epoxy resin-based nanocomposite films with highly oriented BN nanosheets prepared using a nanosecond-pulse electric field. *Mater. Lett.* **2011,** *65* (15-16), 2426-2428.
33. Meng, W.; Huang, Y.; Fu, Y.; Wang, Z.; Zhi, C., Polymer composites of boron nitride nanotubes and nanosheets. *J. Mater. Chem. C* **2014,** *2* (47), 10049-10061.
34. Wang, X.; Pakdel, A.; Zhang, J.; Weng, Q.; Zhai, T.; Zhi, C.; Golberg, D.; Bando, Y., Large-surface-area BN nanosheets and their utilization in polymeric composites with improved thermal and dielectric properties. *Nanoscale Research Letters* **2012,** *7* (1), 662.
35. Khan, U.; May, P.; O'Neill, A.; Bell, A. P.; Boussac, E.; Martin, A.; Semple, J.; Coleman, J. N., Polymer reinforcement using liquid-exfoliated boron nitride nanosheets. *Nanoscale* **2013,** *5* (2), 581-7.
36. Jan, R.; May, P.; Bell, A. P.; Habib, A.; Khan, U.; Coleman, J. N., Enhancing the mechanical properties of BN nanosheet–polymer composites by uniaxial drawing. *Nanoscale* **2014,** *6* (9), 4889-4895.
37. Kiran, M.; Raidongia, K.; Ramamurty, U.; Rao, C., Improved mechanical properties of polymer nanocomposites incorporating graphene-like BN: Dependence on the number of BN layers. *Scripta Mater.* **2011,** *64* (6), 592-595.
38. Yu, J.; Huang, X.; Wu, C.; Wu, X.; Wang, G.; Jiang, P., Interfacial modification of boron nitride nanoplatelets for epoxy composites with improved thermal properties. *Polymer* **2012,** *53* (2), 471-480.
39. Li, S.; Yang, T.; Zou, H.; Liang, M.; Chen, Y., Enhancement in thermal conductivity and mechanical properties via large-scale fabrication of boron nitride nanosheets. *High Perform. Polym.* **2017,** *29* (3), 315-327.
40. Wang, J.; Liu, D.; Li, Q.; Chen, C.; Chen, Z.; Song, P.; Hao, J.; Li, Y.; Fakhrhoseini, S.; Naebe, M.; Wang, X.; Lei, W., Lightweight, Superelastic Yet Thermoconductive Boron Nitride Nanocomposite Aerogel for Thermal Energy Regulation. *ACS Nano* **2019,** *13* (7), 7860-7870.

41. Zhu, Z.; Li, C.; Songfeng, E.; Xie, L.; Geng, R.; Lin, C.-T.; Li, L.; Yao, Y., Enhanced thermal conductivity of polyurethane composites via engineering small/large sizes interconnected boron nitride nanosheets. *Compos. Sci. Technol.* **2019,** *170*, 93-100.
42. Xie, S.; Istrate, O. M.; May, P.; Barwich, S.; Bell, A. P.; Khan, U.; Coleman, J. N., Boron nitride nanosheets as barrier enhancing fillers in melt processed composites. *Nanoscale* **2015,** *7* (10), 4443-4450.
43. Wu, X.; Liu, H.; Tang, Z.; Guo, B., Scalable fabrication of thermally conductive elastomer/boron nitride nanosheets composites by slurry compounding. *Compos. Sci. Technol.* **2016,** *123*, 179-186.
44. Yue, C.; Liu, W.; Zhang, L.; Zhang, T.; Chen, Y., Fracture toughness and toughening mechanisms in a (ZrB2–SiC) composite reinforced with boron nitride nanotubes and boron nitride nanoplatelets. *Scripta Mater.* **2013,** *68* (8), 579-582.
45. Zhi, C.; Bando, Y.; Tang, C.; Honda, S.; Kuwahara, H.; Golberg, D., Boron nitride nanotubes/polystyrene composites. *J. Mater. Res.* **2006,** *21* (11), 2794-2800.
46. Zhi, C.; Bando, Y.; Tang, C.; Xie, R.; Sekiguchi, T.; Golberg, D., Perfectly dissolved boron nitride nanotubes due to polymer wrapping. *J. Am. Chem. Soc.* **2005,** *127* (46), 15996-15997.
47. Zhi, C.; Bando, Y.; Terao, T.; Tang, C.; Kuwahara, H.; Golberg, D., Chemically activated boron nitride nanotubes. *Chemistry–An Asian Journal* **2009,** *4* (10), 1536-1540.
48. Zhou, S.-J.; Ma, C.-Y.; Meng, Y.-Y.; Su, H.-F.; Zhu, Z.; Deng, S.-L.; Xie, S.-Y., Activation of boron nitride nanotubes and their polymer composites for improving mechanical performance. *Nanotechnology* **2012,** *23* (5), 055708.
49. Thakur, V. K.; Yan, J.; Lin, M.-F.; Zhi, C.; Golberg, D.; Bando, Y.; Sim, R.; Lee, P. S., Novel polymer nanocomposites from bioinspired green aqueous functionalization of BNNTs. *Polymer Chemistry* **2012,** *3* (4), 962-969.
50. Zhi, C. Y.; Bando, Y.; Wang, W. L.; Tang, C. C.; Kuwahara, H.; Golberg, D., Mechanical and Thermal Properties of Polymethyl Methacrylate-BN Nanotube Composites. *Journal of Nanomaterials* **2008,** *2008*, 1-5.

Chapter 3 Raman Spectra of BNNSs and BNNTs

3.1 Introduction

Since Sir C. V. Raman discovered Raman scattering in 1928 [1], Raman spectroscopy has been widely used for detecting vibrations in molecules. Different from the Infrared absorption which results from a change of molecular "dipole moment", Raman scattering is due to the change of the polarizability [2].

In the early stage, Raman scattering was observed using sunlight and human eye as the light source and detector, respectively [3]. The signal of sunlight-activated Raman scattering is so weak that only approximately one in 10^6-10^8 photons [2] in the light can be scattered, which makes its detection very hard. The application of Raman spectroscopy was therefore limited until the 1960s, when high power laser sources and better detection system were introduced in the Raman systems [3].

Raman spectroscopy is now a very powerful technique to characterize the molecular vibrations, especially for non-polar C-C bond-constructed carbon-based materials, such as graphite [4], CNTs [5], graphene [6] etc.. Raman spectroscopy is non-destructive under low laser output power and spectra can be obtained from objects on the micron scale. Meanwhile it does not require complicated sample preparation.

Raman spectroscopy has been widely used for distinguishing the diameter, number of walls, bundling etc. of 1D CNTs [5, 7] and the number of layers, crystal structure, density of defects etc. of 2D graphene [8-9]. It has also been demonstrated that Raman is a powerful characterization for understanding the structure and properties of new types of 2D materials [10-11]. This chapter will give a review on the principles of

Raman spectroscopy, Raman spectra of BNNSs and BNNTs and the application of Raman spectroscopy in 1D & 2D material-based nanocomposites.

3.2 Principles of Raman scattering

3.2.1 Classical theory

Regarding an incident light as an oscillating electric field, the electric field strength E at a time t_0 can be given by:

$$E = E_0 \cos 2\pi \nu_0 t_0 \qquad (3.1)$$

where E_0 is the vibrational amplitude and ν_0 is the frequency of the light.

When a molecule intercalates into the oscillating electric field, the field interacts with this molecule and induces the distortion of its electron distribution [12]. It alternates the electric dipole moment, P and induces scattering:

$$P = \alpha E \qquad (3.2)$$

where α is the molecular polarizability, which is a measurement of the ability of a molecule to respond dynamically to the electric field. For a small amplitude vibration, α can be given as [13]:

$$\alpha = \alpha_0 + \left(\frac{\partial \alpha}{\partial q}\right)_0 q + ... \qquad (3.3)$$

where α_0 is the equilibrium molecular polarizability, q is the displacement of nucleus, thus $(\partial\alpha/\partial q)_0$ represents the change rate of polarizability against the nuclear displacement. q can be given as [3]:

$$q = q_0 \cos 2\pi \nu_q t_0 \qquad (3.4)$$

where q_0 and ν_q represent the amplitude of vibration and frequency of the nucleus, respectively. Substituting Equation 3.1, 3.3, 3.4 into Equation 3.2 gives:

$$P = \alpha_0 E_{_0} \cos 2\pi v_0 t_0 + \frac{1}{2} q_0 E_0 \left(\frac{\partial \alpha}{\partial q}\right)_0 \left[\cos\left[(v_0 + v_q)t_0\right] + \cos\left[(v_0 - v_q)t_0\right]\right] \quad (3.5)$$

It can be seen in Equation 3.5 that three components v_0, v_0-v_q, v_0+v_q give rise to the fluctuation of the electric dipole and consequent scattering. The first term corresponds to the "Rayleigh scattering", for which v_0 has the same frequency as the incident light. The second term represents the "Raman scattering", including the "Stokes mode" and "anti-Stokes mode" which correspond to the scattering occurring at a frequency of (v_0+v_q) and (v_0-v_q), respectively. According to the second term, the Raman scattering only occurs if $(\partial\alpha/\partial q)_0 \neq 0$, in other words, the change of polarizability against the nuclear displacement is necessary for a vibration to be Raman active [14].

3.2.2 Quantum theory

The Raman scattering can also be understood by Quantum theory, where the incident light can be regarded as a beam of photons [12]. The photon energy of the incident light E_i can be expressed as:

$$E_i = hv_0 \quad (3.6)$$

where h is the Planck's constant and v_0 is the vibrational frequency of incident photons.

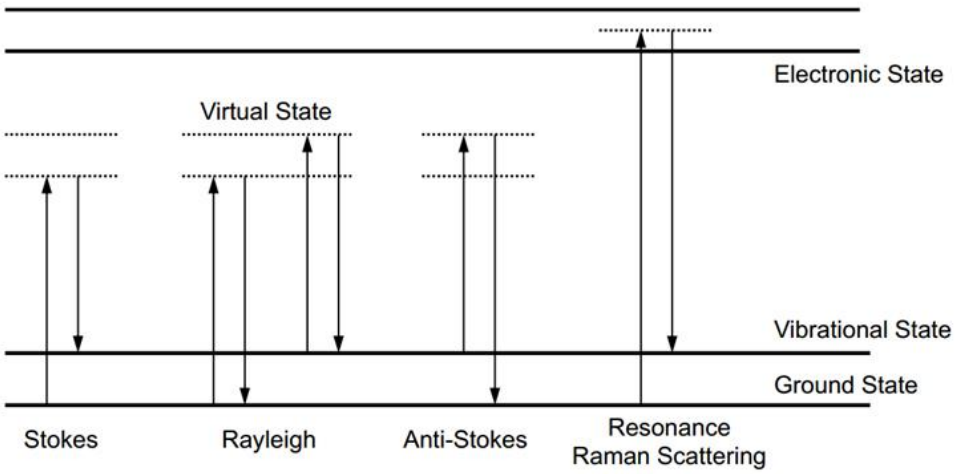

Figure 3.1 Schematic diagram of Rayleigh scattering and Raman scattering (Stokes

mode, anti-Stokes mode, resonance Raman scattering) [2, 15].

When the photons in the light interact with the electrons in the molecule, the cloud of electrons around the nuclei is distorted and the molecule is excited. If the photon energy matches the energy gap of between the excited and ground state, the molecule absorbs the photon energy and jumps to an "excited state" [2]. If not, the molecule can also be excited to a "virtual state", as shown in Figure 3.1 [2, 15].

The energy of scattered photons E_s can be expressed through the conservation of energy principle [12]:

$$E_i + E_1 = E_s + E_2 \qquad (3.7)$$

where E_1 and E_2 are the energy of molecule before and after scattering, respectively. The change of molecular energy E_2 - E_1 can be given by:

$$E_2 - E_1 = E_i - E_s = h(\nu_i - \nu_s) = h\Delta\nu_0 \qquad (3.8)$$

where $\Delta\nu_0$ is the frequency change after scattering. Therefore, the Raman shift (Raman wavenumber) ω can be given by [15]:

$$\omega = \frac{h\Delta\nu_0}{hc} = \frac{\Delta\nu_0}{c} \qquad (3.9)$$

The unit of ω is usually defined as cm^{-1}, c denotes the speed of light.

When ω=0, the molecule absorbs the energy of photon and excited to a virtual state, which is followed by an immediate re-radiation then back to original ground state. This elastic scattering process is defined as "Rayleigh scattering", where no energy transfers occurs between the photons and molecules.

When ω>0, the excited molecule in the virtual state goes back to a lower excite state rather than the original state, thus the molecule absorbs the energy from the photons. This inelastic process is the Raman "Stokes mode".

When ω<0, the molecule is originally in the excited state before interaction with the photons but drops to ground state after scattering, the energy of the molecule is transferred to photons. This inelastic process is the Raman "anti-Stokes mode".

Typically, the Stokes mode and anti-Stokes mode have the same values of ω, but the intensity of anti-Stokes mode is usually much weaker than that of Stokes mode. This can be explained by the Boltzmann distribution in that the electrons tend to be in a lower energy state [2], that is, there are fewer molecules in the excited state than in the ground state at room temperature.

As can be seen in Figure 3.1, the Raman scattering also occurs through a resonance process, where the molecule is excited to or very close to a real electronic state, rather than a virtual state. Resonance Raman scattering can massively enhance the intensity by a factor of 10^3 to 10^6, and this has been widely used in the study of nanocarbon-based composites [16].

3.3 Instrumentation

3.3.1 Raman spectrometer

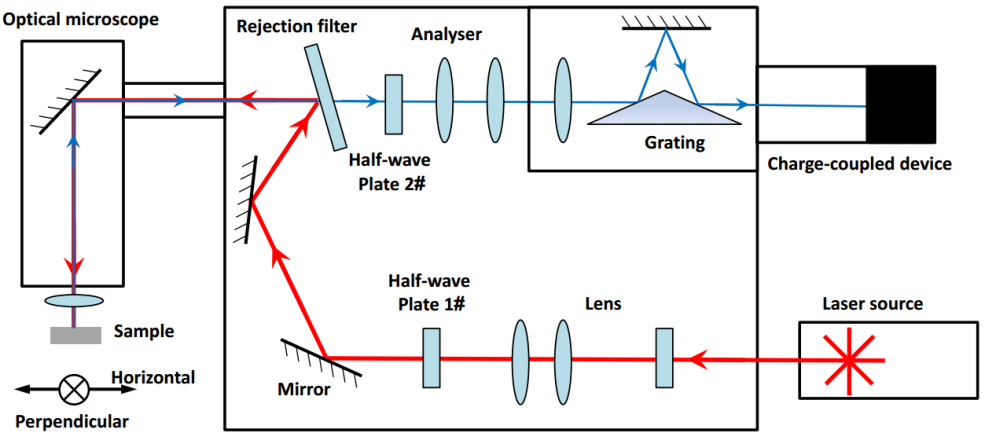

Figure 3.2 Schematic diagram of a Raman spectrometer. Red line: incident radiation;

Blue line: scattered radiation [12, 15].

A Horiba LABRAM HR Evolution Raman spectrometer equipped with a Kimmon Koha 325 nm He-Cd NUV laser, a Coherent 488 nm sapphire laser and a CVI Melles Griot 633 nm He-Ne laser was used for the Raman spectra collection in this work. As shown in Figure 3.2, an optical microscope was used to observe and find the sample for characterization. The laser was focused on the surface of the sample using an objective lens and Raman scattering was collected and analyzed by a charge-coupled device (CCD). In order to avoid local laser heating and damage on the sample, the laser power was minimized to 1-1.5 mW. Generally, the exposure time was 20-30s and the signal was accumulated 5 times for denoising.

3.3.2 Raman spectra fitting

A Lorentzian function is generally used for fitting the Raman spectra to determine the band intensity, width and position [15-16]:

$$I = \frac{I_{\mathrm{P}}(2\Gamma)^2}{(2\Gamma)^2 + (\omega - \omega_0)} \qquad (3.10)$$

where I is the intensity of Raman band at any given Raman frequency ω. I_{P} is the intensity of the Raman band at peak position ω_0. 2Γ is the full width at half maximum (FWHM) of the Raman band.

3.3.3 In-situ Raman deformation test

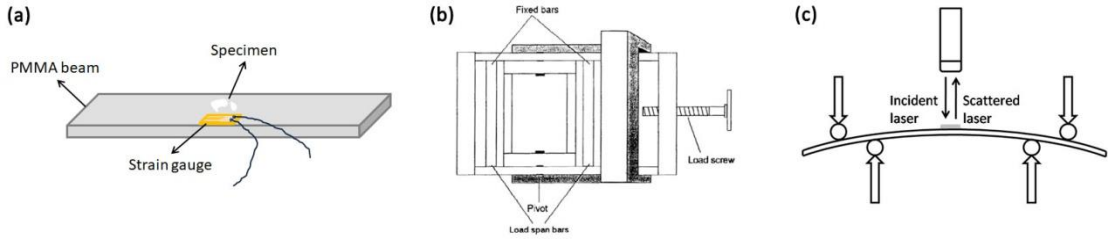

Figure 3.3 Schematic diagrams of (a) PMMA beam with a specimen and strain gauge on its top. (b) Four-point bending rig [14]. (c) In-situ Raman deformation test.

In-situ deformation of specimens was performed by transferring the specimens on the top of a 5 mm thick PMMA beam. A resistance strain gauge connected to a multimeter was fixed close to the specimens using super glue. The change of specimen surface strain can thus be monitored by reading the resistance of the gauge (Figure 3.3(a)). The beam was inserted into a four-point bending rig (Figure 3.3(b)), which was then placed on the stage of the optical microscope in the Raman spectrometer. The beam was stretched (or compressed) stepwise and the Raman spectra were collected in-situ from the centre of the specimen at each strain level [15], as shown in Figure 3.3(c).

3.4 Raman spectra of BNNSs

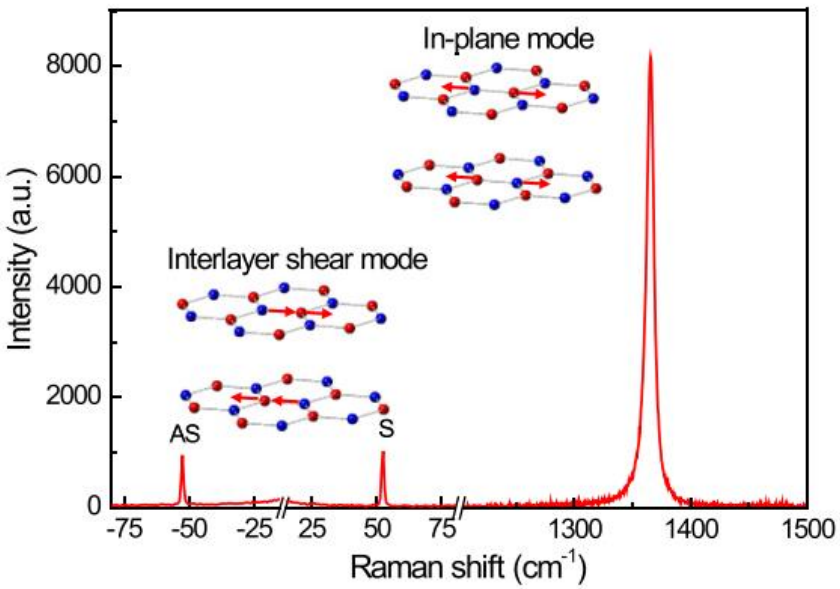

Figure 3.4 Raman spectrum of a NIMS bulk hBN single crystal [17].

Crystalline hBN has a D_{6h}^4 space group symmetry and the zone-center optical phonons can be given by equation [18]:

$$\Gamma = 2E_{2g} + 2B_{1g} + A_{2u} + E_{1u} \qquad (3.11)$$

where A_{2u} and E_{1u} phonon modes are IR active, B_{1g} phonon modes are optically inactive and the E_{2g} is the only Raman-sensitive mode, which is related to the G band of graphene [8]. Typically, the E_{2g} modes originate from in-plane atomic displacements: a high frequency mode due to B atoms and N atoms moving against each other within a plane. There is another low frequency mode due to interlayer shearing (ISM), which arises in the ultra low frequency region in the Raman spectra. Generally, the position of the high frequency intralayer E_{2g} mode of different hBN-based materials is reported in the range of 1363-1374 cm^{-1} [19-20], while the position of interlayer shear mode is in the range of 49-52.5 cm^{-1} (Stokes scattering) [19, 21]. The ISM peaks of bulk hBN located at 52.5 cm^{-1} (Stokes scattering) and -52.5 cm^{-1} (anti-Stokes scattering), and it is predicted that ISM peaks

will shift to lower frequency as the number of layers decreases [22]. Figure 3.4 [17] demonstrates the typical Raman spectrum of Japan's NIMS hBN single crystal. A strong peak at 1366 cm^{-1} (Stokes scattering, intralayer shear mode) and two weak interlayer shearing peaks are observed. However, it should be noted that the Raman signal in hBN is still quite weak in contrast to the cases of graphene, MoS_2 etc. This is due to the lack of resonance as a result of the wide band gap of hBN compared to accessible excitation energies in Raman spectroscopy (excessively-high energy will damage the lattice or induce sample heating and a consequent Raman band shift). The non-resonant character of Raman scattering in hBN increases the difficulty of Raman measurement for the material. Additionally, Raman spectra of hBN-based structures do not show a D band due to the lack of a Kohn anomaly [23]. This is the reason why majority of previous work about the Raman spectra of BNNSs focused much more on the relatively-strong in-plane shear mode, as shown in Figure 3.5 [23-24].

The Raman E_{2g} band position of BNNSs in different reports in the literature is different but all lie within a range between 1364-1372 cm^{-1} approximately. As summarized below the in-plane Raman E_{2g} peak of bulk hBN is at ~1366-1366.8 cm^{-1} in relevant papers in Table 3.1:

Table 3.1 In-plane Raman E_{2g} shear mode band positions of BNNSs in different work.

Reference	hBN source	Preparation Method	Intralayer Raman E_{2g} shear mode band position (cm^{-1})			
			1L	2L	3L	4L
[24]	NIMS	Scotch tape	1368.3-1370	1363.2-1366.9	1365.5	1365±0.5
[23]	NIMS	Scotch tape	1370.5±0.8	1370.0±0.6	1367.8±0.4	1367.2±0.4
[25]	NIMS	Scotch tape	1369.4	1368.5	-	-
[26]	NIMS	Scotch tape	1370.5	1370.0	1368.1	-
[27]	NIMS	Scotch tape	1369.6±0.6	1369.0±0.5	1367.5±0.2	-
[27]	NIMS	Scotch tape	1367.3±0.3*	1367.0±0.1*	1367±0.2*	-

[28]	NIMS	Scotch tape	1366.5*	-	-	-
[29]	#	Scotch tape	1364.7	1364.8	1364.8	1365
[29]	#	Scotch tape	1363.7*	1363.9*	1364.5*	1364.7*
[30]	#	Scotch tape	1366.5	1366.2	~1366.4	1366.9
[31]	-	CVD	~1373	-	-	-
[32]	-	CVD	~1370	-	-	-
[33]	-	CVD	~1371	1370	-	-
[34]	-	CVD	~1373	-	-	-
[35]	-	CVD	~1370			
[36]	-	CVD	-	-	~1373	-

L - Number of layers; * - the value of suspended BNNSs on wafer with micro-wells.

- Manchester Nanomaterials

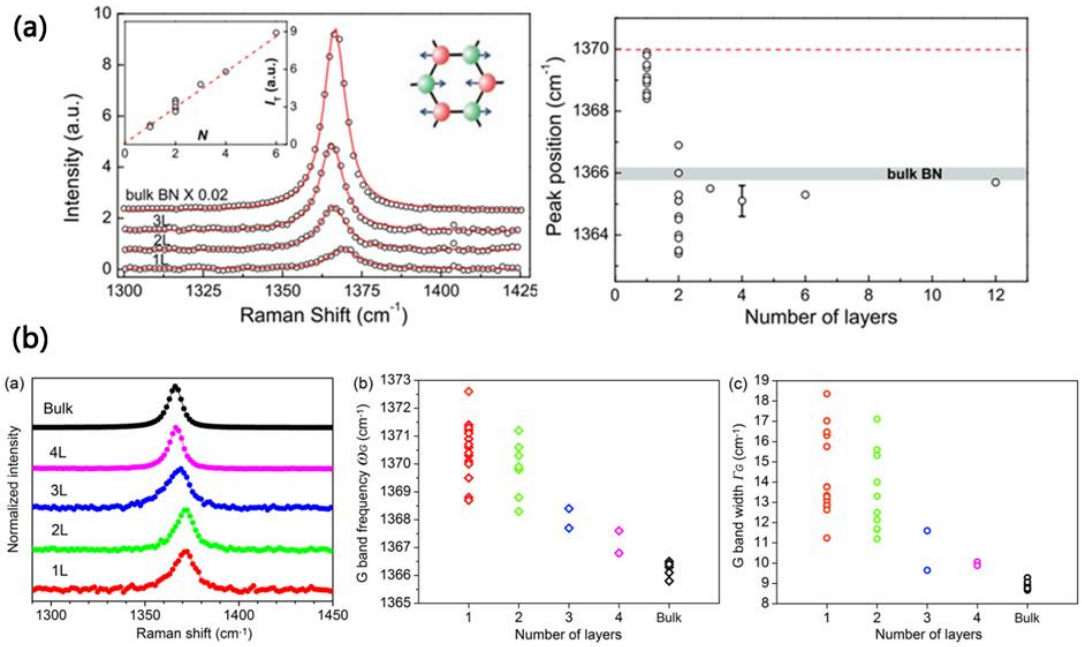

Figure 3.5 Raman spectra of 1-4L BNNSs in different studies [23-24].

Initially, Gorbachev et al. [24] systematically studied the Raman band position of mono-, bi-, trilayer BNNSs, as shown in Figure 3.5(a). It can be observed that the peak intensity of E_{2g} mode increases significantly with an incremental number of

layers, but it should be noted that the intensity of monolayer hBN is actually 50 times smaller than that of 1L graphene's G peak under the same measurement conditions. In addition, monolayer BNNSs show a relatively-large blue shift (2-4 cm^{-1}) with respect to the original position of bulk hBN at 1366 cm^{-1}, while the Raman band of bilayer BNNSs (~1365 cm^{-1}) shifts slightly downwards. When the crystal is thicker than 5 layers, no strong peak position variation was observed in this work.

Chen et al. [23, 25] exfoliated BNNSs with different thickness and studied their Raman spectra, and did not find the characteristic red band shift of bilayer hBN in their Raman results. A uniform and stepwise blue shift from bulk hBN to monolayer hBN was usually observed in their work (Figure 3.5(b)). Although different band shifts of bilayer hBN were reported, both Gorbachev and Chen [23-25] confirmed that the intensity for the BNNSs Raman E_{2g} band is proportional to the number of layers for the first several layers and band width gradually decreases with increasing number of layers. It can be confirmed that the Raman band of 1L BNNSs is rather weak but broad. In addition, some recent work [27-28] upon suspended BNNSs on Si wafers with micro-wells has revealed the effect of a strain-induced substrate upon the Raman band position of BNNSs, as shown in Figure 3.6. It was therefore proposed that the blue shift might be attributed to different flexibility and levels of strain caused by the substrate [27]. In addition, some other important factors should be considered when collecting Raman spectra and confirming the band position, such as: calibration, local temperature increase caused by the laser (which will induce a red shift) [17, 20, 37], interlayer interactions between adjacent layers which will slightly elongate B-N bonds and induce a phonon softening process - red shift.

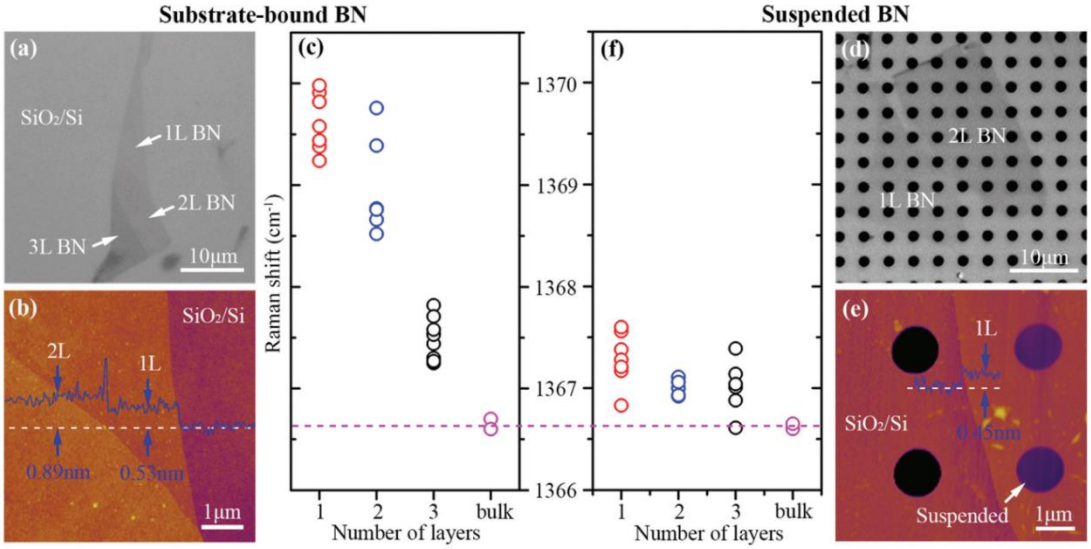

Figure 3.6 (a-b) Optical and (d-e) AFM images of supported and suspended mono-, bi-, tri- and many-layered BNNSs on 90 nm SiO_2/Si wafers. (c, f) Raman band positions of supported and suspended BNNSs [27].

More recently, inspired by work on using ultra low frequency (ULF) Raman spectroscopy to quantify the number of layers of graphene and other 2D materials [10, 38], Stenger et al. [17, 37] reported that interlayer shear mode (weaker peak in ULF region) can also be used to identify the number of layers (except for monolayer which does not have adjacent layers) for BNNSs. A red shift of Stokes scattering peak and blue shift of anti-Stokes scattering peak were simultaneously observed when the number of layers decreased, as shown in Figure 3.7 [17]. However, relevant publications mentioned that a complicated air removal process using argon gas is needed before the test, and the sample temperature should be well-controlled below 50 K to prevent a self-heating induced Raman band red shift.

More recently, Ling et al. [39] found that stimulated Raman scattering (SRS) can massively enhance the sensitivity of Raman spectra of BNNSs, which allows the high resolution imaging of the BNNSs to be obtained with an exposure time 4 orders of magnitude shorter than conventional Raman spectra. The authors also reported that

the hBN E_{2g} mode is insensitive to the stacking order and polarization of BNNSs, meanwhile the intensity of this mode is almost linearly related to the thickness of BNNSs up to ~70 nm. This modified Raman technique has great potential to be used for rapidly identifying the thickness of BNNSs.

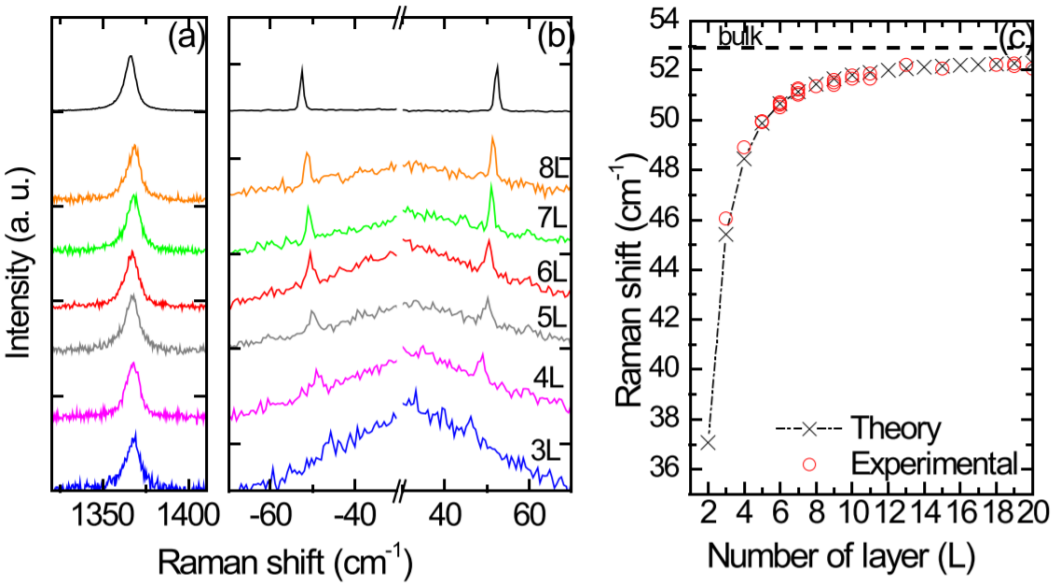

Figure 3.7 Raman spectra of mechanically-exfoliated BNNSs with different number of layers in (a) high frequency and (b) ULF regions [17]. (c) Position of interlayer shear mode at ULF regions as a function of the BNNSs number of layers.

3.5 Raman spectra of BNNTs

Density functional theory (DFT) studies [40] and Raman intensity calculations [41-42] upon SW-BNNTs predicted that the most intense peak in the spectra should be the transverse optical A_1 mode, as illustrated in Figure 3.8(a) [40]. A_1 mode can be constructed by folding the Raman active optical E_{2g} mode (1365 cm^{-1}) of bulk hBN [20, 43]. Theoretically [44], the radial breathing mode (RBM) of BNNTs is between 100-200 cm^{-1} (Figure 3.8(b) [42]), but this mode is usually hard to detect due to its low frequency. RBM modes are unique and reliable features of SW-BNNTs [20]. Calculations of Popov indicated that the Raman band frequency of the RBM mode depends highly on the radius of BNNTs, as shown in Figure 3.8(c) [41]; Relevant

calculation also predicted that the Raman spectra of BNNTs depend strongly on their chiralities (helicities). As shown in Figure 3.8(d) [41], (17, 0) Zigzag, (15, 4) chiral and (10, 10) armchair BNNTs exhibit different calculated phonon modes and Raman spectra.

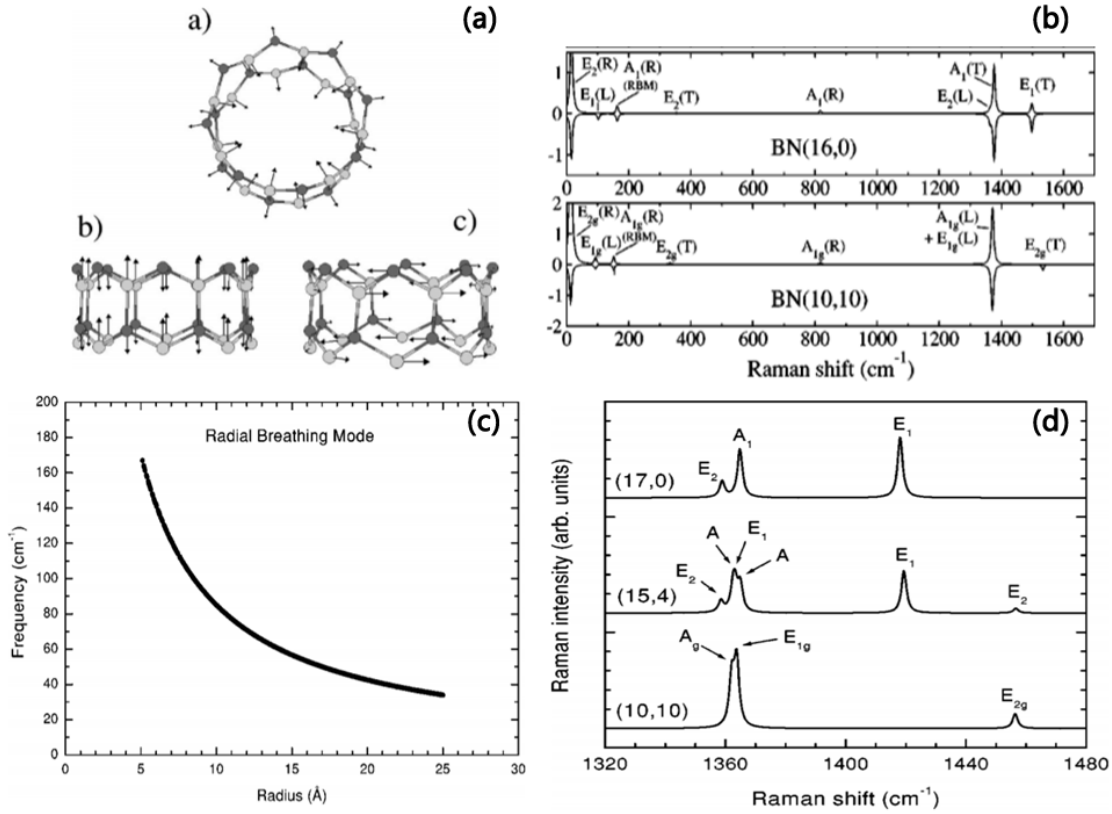

Figure 3.8 Theoretical calculation of the Raman spectra of BNNTs. (a) Sketch of A modes in a zigzag BN nanotube; (b) *ab* initio and model Raman spectra of a (16, 0) zigzag BN tube and a (10, 10) armchair tube; (c) Calculated radius dependence of the frequency of RBM for tubes with radius between 0.5-0.25 nm; (d) Calculated Raman spectra of (17, 0) Zigzag, (15, 4) chiral and (10, 10) armchair BNNTs [40-42].

Experimental measurements for the Raman spectra of BNNTs were also reported, but only a very few papers have investigated BNNTs due to difficulties in their synthesis [20, 45-46]. Zhi et al. [45] reported that the typical Raman spectrum of MW-BNNTs is similar to that of bulk hBN (at 1366 cm^{-1}), which exhibits a strong peak at 1363.6 cm^{-1} (denoted as the G band in other literature). They attributed the ~4

cm^{-1} red shift to lower frequency to curvature-induced phonon softening [40] and perfect crystallinity, they also suggested that the FWHM of the BNNT E_{2g} mode is always wider than that of bulk hBN, due to a smaller "crystal size". Arenal et al. [20] studied the UV laser-excited Raman spectra of synthesized SW-BNNTs and found a different blue shift phenomenon of G band to 1370 cm^{-1}. They attributed this shift to the absence of interaction of the neighbouring sheets. The band position is highly consistent with that of the 1L BNNSs E_{2g} mode. The paper also provided another explanation for Ref 45, as they thought there should not be a distinct E_{2g} band shift due to the interaction of neighboring sheets in multi-walled BNNTs. They attributed the distinct red shift to anharmonic effects (e.g. local temperature increased by the laser). They also attributed the 880 cm^{-1} peak of the MW-BNNTs in Ref 46 to residual boric acid. In this work, experimental studies on armchair SW-BNNTs considered the Raman G mode as a composite signal of A_g mode and E_{2g} mode (A_1 and E_g modes in the case of chiral and zigzag type). Figure 3.9 shows the typical Raman spectra (curve (a) in left graph, the peak at 1597 cm^{-1} is due to the holey carbon membrane of the TEM grid) and calculated frequencies of optical A mode and E mode with increasing tube diameter [20].

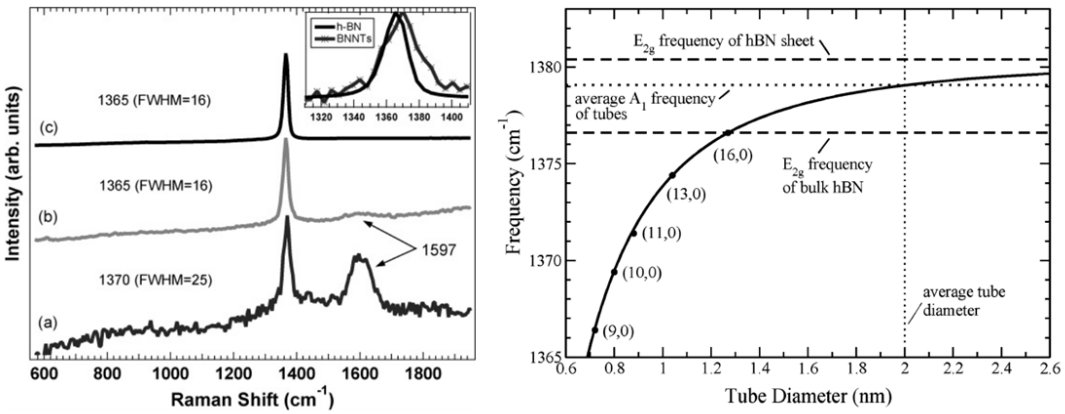

Figure 3.9 Left: Raman spectra of (a) SW-BNNTs; (b) hBN particles generated during the preparation of SW-BNNTs and (c) highly-crystalline hBN powder. Right: Calculated frequencies of optical Raman A mode and E modes of SW-BNNTs as a function of tube diameter [20].

3.6 Strain-induced Raman band shifts in BNNSs and BNNTs

3.6.1 Pressure-induced Raman band shifts

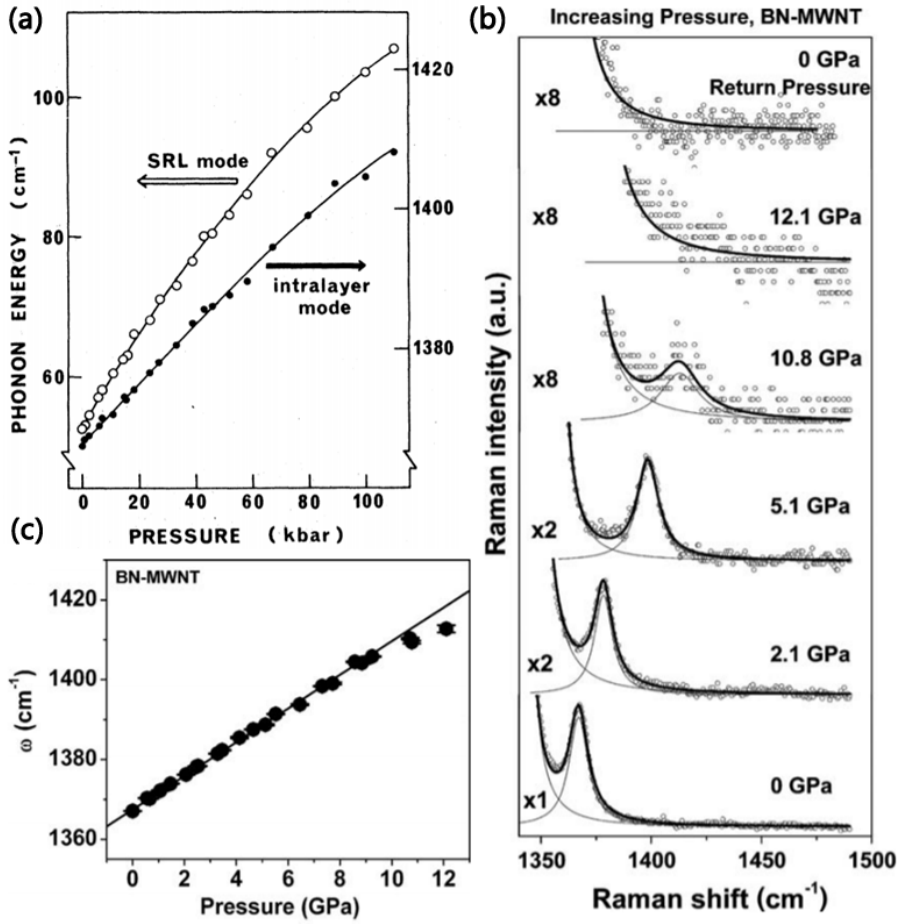

Figure 3.10 (a) Pressure-Raman frequency shifts of the interlayer shear mode (so-called SRL mode in the graph) and the in-plane (intralayer) shear mode in bulk hBN [47]. (b-c) Pressure-Raman frequency shift of the MW-BNNT G band [48].

It is well-known that Raman bands are strain sensitive and tensile strain upon 2D materials causes an increase in the Dirac cone separation leading to phonon softening (red shift of Raman peak), while compressive strain leads to phonon hardening (blue shift). Our group's previous work on carbon fibres [49], CNTs [50], graphene [51], MoS_2 [52] and WS_2 [53] has further confirmed this conclusion. Sato et al. [47] first reported the Raman band shift of bulk hBN under high pressure, where they

pressurized hBN powder in a diamond-avil cell. A 4:1 mixture of methanol/ethanol was used as a pressure medium in the cell. The pressure was raised from 1 bar to 110 kbar and Raman spectra were recorded using a 488 nm laser. Figure 3.10(a) exhibits the pressure-Raman frequency plot of the interlayer shear mode and the in-plane mode of bulk hBN. The modes both shifted to higher frequencies when pressure was increased, and the pressure dependence of the shifts of two modes is nearly linear, although a relatively large quadratic effect was observed for the interlayer shear mode. The mean shifts of interlayer and in-plane shear mode were estimated to be 0.5 cm^{-1}/kbar (5 cm^{-1}/GPa) and 0.4 cm^{-1}/kbar (4 $cm^{-1/}$GPa), respectively. This work confirms that the Raman modes of hBN are sensitive to pressure-induced strain.

In 2006, Saha et al. [48] reported the pressure-induced Raman band shift of MW-BNNTs. They also used diamond anvil cell technique for the measurements. From Figure 3.10(b), an obvious G band blue shift of MW-BNNTs was observed when a pressure was applied. A well-fitted linear relationship between applied pressure and G band frequency shift can be seen in Figure 3.10(c) and band shift rate was calculated to be 4.2 cm^{-1}/GPa, a value close to that of bulk hBN. Additionally, it can be deduced from Figure 3.10(b) that a phase transfer from MW-BNNTs to amorphous BN occurred after an applied pressure of >12 GPa, as the Raman mode totally disappeared even after the pressure was reduced from 12.1 GPa to ambient. The increasing band width with incremental pressure further verified the phase change during the process. In addition, this work also reported a phase change from bulk hBN to wurtzite BN when a high pressure was applied.

3.6.2 Thermally-induced Raman band shifts

Thermally-induced Raman band shifts of BNNSs have also been reported by a series of studies. Li et al. [54] reported -18 cm^{-1} and -12 cm^{-1} red shifts for the Raman

in-plane E_{2g} mode of ~16.2 nm and ~36.2 nm thick BNNSs, after their temperature was increased from -194 ℃ to 200 ℃, respectively. Cai et al. [55] reported the first measurement of the thermal conductivity of 1L-3L BNNSs, using an optothermal Raman technique. In this work, 1L-3L BNNSs were exfoliated and transferred on Si wafer with special microwells and trenches (Figure 3.11(a-b)), thus some regions of the BNNSs were suspended. A heating stage was used for controlling the temperature of BNNSs and Raman spectra was recorded at each temperature level. It can be seen in Figure 3.11(c-d) that both suspended and supported 1L BNNSs exhibit different degree of red shift with increasing temperature. As summarized in Figure 3.11(e), the band shift rates for 1-3L suspended BNNSs were -0.022±0.001, -0.021±0.001 and -0.022±0.001 cm^{-1}/K, respectively, close to that of bulk hBN (-0.019±0.001 cm^{-1}/K). They attributed the shift to the (1) thermal expansion of hBN lattice; (2) anharmonic phonon-phonon effects. Seremetis et al. [56] reported the temperature-induced Raman band shift of thicker BNNSs (Figure 3.11(f)): -0.032 (3.9 nm), -0.022 (41.9 nm), -0.017 (137.9 nm,), -0.015 (466.5 nm) cm^{-1}/K, respectively when temperature < 305 K. It is therefore found the band shift rate of BNNSs decreases with number of layers. Very recently, Cai et al. [57] replaced natural boron (^{Natrual}B: 80.1 ^{11}B and 19.9% ^{10}B) in hBN with pure ^{10}B and ^{11}B and successfully exfoliated 1L ^{10}BN and ^{11}BN nanosheets. The thermal-induced Raman band shifts rates of 1L ^{10}BN and ^{11}BN nanosheets were -0.022±0.002 and -0.022±0.002, respectively, very close to that of 1L ^{Natural}BN measured by an identical method.

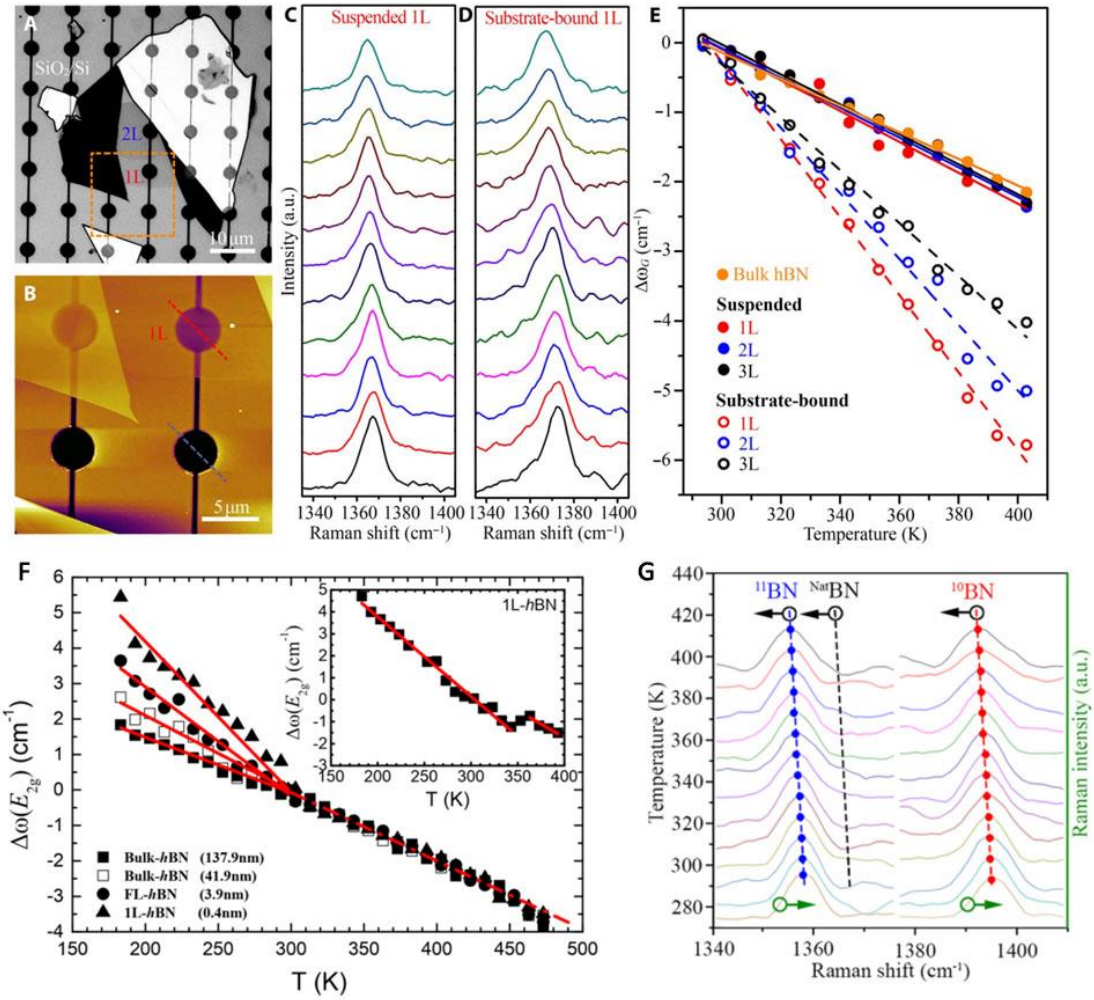

Figure 3.11 (a-b) Optical and AFM images of mechanically-exfoliated 1L and 2L BNNSs and (c-e) Raman E_{2g} band position of suspended and supported 1L-3L BNNSs as a function of temperature [55]. (f) Raman E_{2g} band position of 1L BNNSs, few-layer BNNSs with different thickness and bulk hBN as a function of temperature [56]. (g) Raman E_{2g} band position of suspended 1L ^{10}BNNSs, ^{Natural}BNNSs, ^{11}BNNSs as a function of temperature [57].

In 1991, Exarhos et al. [58] heated a polycrystalline boron nitride coatings from room temperature to 2340 K in a tube furnace and simultaneously recorded the in-plane Raman E_{2g} band. They found a prominent red shift (< -60 cm^{-1}) at high temperature, as shown in Figure 3.12(a). Stenger et al. [17] reported a -0.023 cm^{-1}/K and -0.06 cm^{-1}/K temperature coefficients for in-plane and interlayer shear mode frequency

shifts in bulk hBN single crystals, respectively (Figure 3.12(c)). Later, Arutyunyan et al. [59] first reported the thermally-induced Raman band shift of SW-BNNTs. They heated a SW-BNNTs contained boron nitride soot from 77-600 K in a oven and estimated a -0.014 cm^{-1}/℃ and -0.027 cm^{-1}/℃ thermal coefficient for the G mode of BNNTs and in-plane E_{2g} mode of bulk hBN, respectively (Figure 3.12(b)). Lu et al. [60] studied the Raman band shift of MW-BNNTs with a bamboo-like structure and reported a -0.01 cm^{-1}/K temperature coefficient of the G mode in MW-BNNTs.

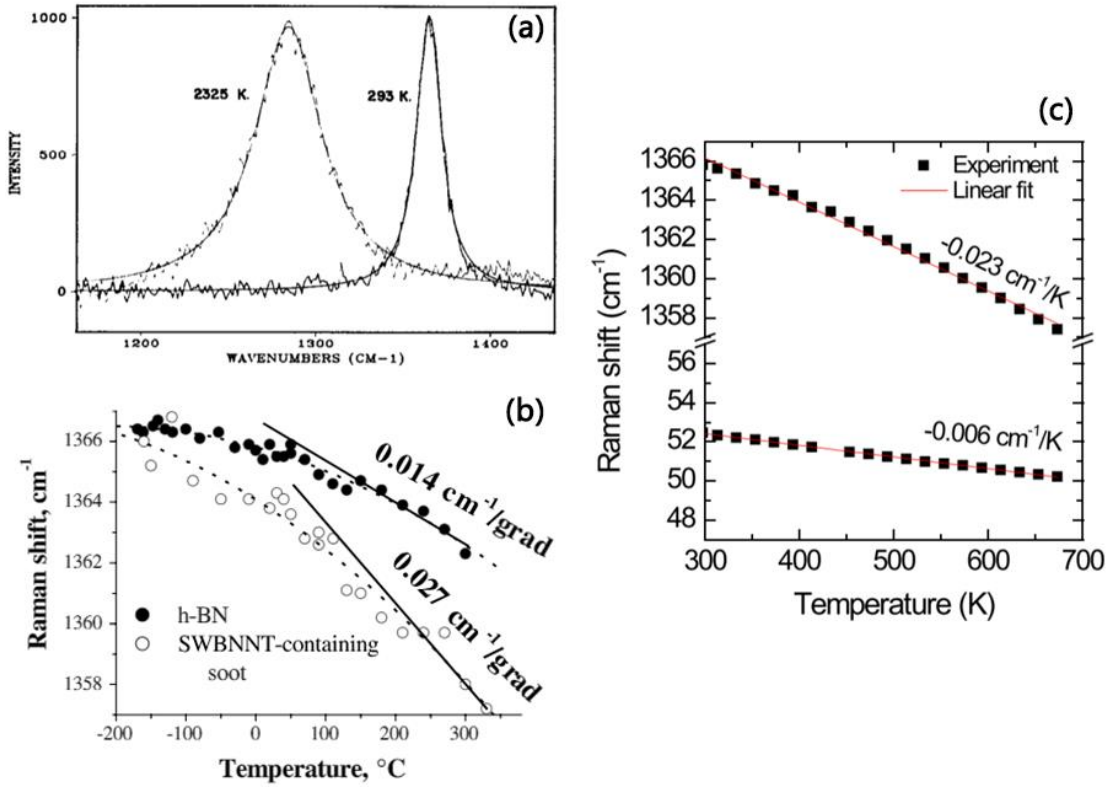

Figure 3.12 (a) Raman spectra of bulk hBN film at 293 K and 2325 K [58]. (b) Dependence of Raman G band position in hBN and SW-BNNTs on the temperature [59]. (c) Temperature-Raman frequency shift graph of interlayer shear mode and in-plane (intralayer) shear mode in bulk hBN single crystals [17].

3.6.3 Mechanical deformation-induced Raman band shifts

To our knowledge, tensile and compressed strain-induced Raman band shifts of BNNSs has only been reported in very limited recent work, while no band shift of BNNTs were reported before. Cai et al. [27] exfoliated and transferred BNNSs on SiO_2/Si wafer, then heated the BNNSs/wafer up to 400 ℃ under argon atmosphere for 1 h. It should be noted particularly that the Raman measurement was preformed after the heated sample was cooled down to room temperature. The thermal expansion coefficient of SiO_2 coating ($0.75 \times 10^{-6}\,K^{-1}$) is much higher than that of hBN ($1.91 \times 10^{-9}T - 2.96 \times 10^{-6}$) $℃^{-1}$ [61] and an interfacial compressive strain (the BNNSs expanded but the SiO_2 coating shrank) will be generated during the heating-cooling process. This deduction was verified by the blue shift in Raman spectra before and after thermal treatment, as shown in Figure 3.13. The Raman E_{2g} band blue shift rates for the 1L, 2L, 3L BNNSs were 3.0 ± 0.7 cm^{-1}, 2.7 ± 0.8 cm^{-1}, 2.2 ± 0.6 cm^{-1}, respectively and no band shift was observed for bulk hBN. They also performed a first-order calculation and deduced the Grüneisen parameter of 1L BNNSs to be 0.64, which is smaller than that of 1L graphene (1.2) [62] but much higher than that of bulk hBN (0.1) [63].

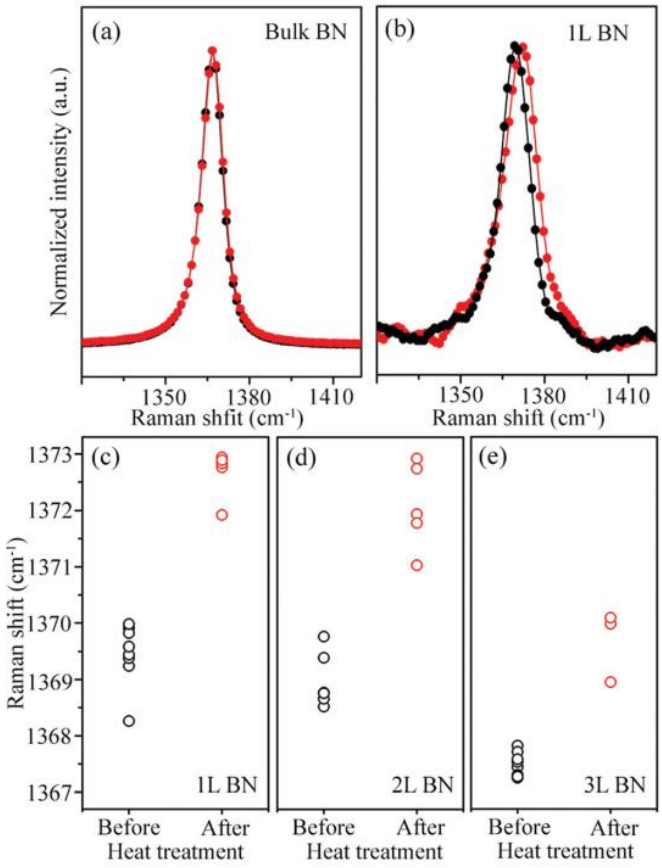

Figure 3.13 Raman spectra of (a) bulk and (b) 1L BNNSs on SiO_2/Si wafer; (c-e) Raman in-plane E_{2g} band blue shift of 1L, 2L, 3L BNNSs before and after 400 ℃ thermal treatment-cooling down process [27].

More recently, Bera et al. [64] reported the blue shifts of Raman E_{2g} mode of wrinkled BNNSs with different number of layers (Figure 3.14(a)). It was reported that the Raman band position of free-standing BNNSs is independent of number of layers [17], thus the blue shift was attributed to the residual strain in the wrinkled BNNSs. The residual strain in the BNNSs was found to increase with an increasing number of layers as more strain was relaxed by wrinkling in thinner BNNSs. Androulidakis et al. [30] first studied the uniaxial strain-induced Raman band shift of 2L-4L BNNSs. They exfoliated and transferred 2L-4L BNNSs on a SU-8/PMMA substrate, the polymer substrate was then stretched uniaxially to different strain levels. Although the Raman signal of BNNSs on polymer substrate is very weak due to the wide band gap

of hBN, both obvious band splitting and a shift to lower frequency with increasing tensile strain was observed on the E_{2g} band of 2L-4L BNNSs at ~1368 cm^{-1} (Figure 3.14(b)). It was found that the shift of E_{2g} band frequency showed a linear relationship with applied strain at the beginning but soon become irregular when the strain was higher than ~0.2-0.3% (Figure 3.14(c-d)), suggesting a relatively poor interfacial interaction between the BNNSs and polymer substrate. In addition, the E_{2g} band shift rates were almost constant when number of layers increased from 2-4, demonstrating strong layer-layer bonding inside BNNSs. On the other hand, it must be noted that the curve fitting is quite difficult and a relatively large error may exist in this work.

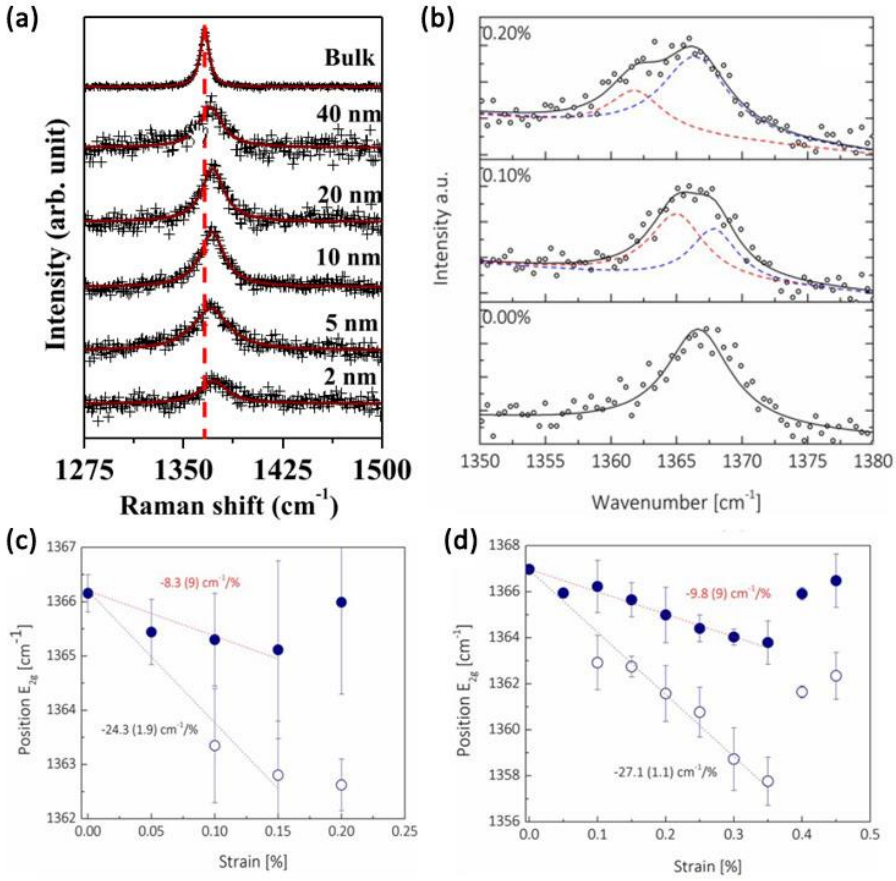

Figure 3.14 (a) Raman spectra of wrinkled CVD-grown BNNSs films with different thickness on sapphire substrate [64]. (b) Uniaxial-strain induced Raman E_{2g} band shift of 2L BNNSs. The position of Raman E_{2g} band of (c) 2L and (d) 4L BNNSs as a function of the tensile strain [30].

3.7 Raman spectra of 1D materials, 2D materials/polymer nanocomposites

Previous work on CNTs, graphene/polymer composites in Manchester has demonstrated that Raman spectroscopy is a powerful non-destructive technique for investigating the reinforcement of 1D and 2D materials on polymer matrix [65-66]. Here a brief introduction of the relevant Raman techniques will be given.

3.7.1 Raman spectra of 2D graphene/polymer nanocomposites

Interface/critical length In 2010, Gong et al. [51] reported the uniaxial tensile strain-induced Raman band shift of a 1L graphene sandwiched by two thin layers of polymers (i.e. 1L graphene model composite). The linear Raman 2D band shift rate of the center of the 1L graphene flake was found to be around -60 cm^{-1}/% strain, while this linear shift became irregular after 0.4% strain (Figure 3.15(a)), suggesting graphene/polymer interfacial failure at low strain. The authors then monitored the Raman 2D band shifts along the tensile axis across the 1L graphene flake and estimated the strain distribution from the edges to the center. It was found that the strain builds up from the edges and kept constant across the middle of the flake. The strain distribution at 0.4% matrix strain (Figure 3.15(c)) could be fitted well by shear-lag theory with *ns*~20, indicating good interfacial bonding between graphene and polymer matrix. In this case, the interfacial shear stress was estimated to be ~2.3 MPa, which is a relatively low value for polymer composites. In addition, the interfacial shear stress further decreases to only around ~0.3 MPa after matrix strain increases to 0.6% and interfacial failed (Figure 3.15(d)). The above results demonstrate that the interfacial adhesion between polymer matrix and pristine graphene is weak as stress can only be transferred through van der Waals bonding from the matrix to the graphene. Furthermore, it can be seen in Figure 3.15(c) that 1.5

μm is needed for the strain to rise from zero at the edges to around 90% of the middle plateau value, making the critical length (l_c) of the graphene reinforcement of ~3 μm. Therefore, it is suggested that 1L graphene flakes of ~30 μm (~10l_c) are needed for sufficient reinforcement on polymers.

Later, Li et al. [67] studied the deformation of wrinkled 1L graphene and found that the downshift rate of its 2D band (-12.5 cm^{-1}/% strain) decreases to less than 25% of that of mechanically exfoliated 1L graphene (Figure 3.15(b)). It was deduced that the delaminated wrinkles separate the flat flake into many ~1 μm (<l_c of 1L graphene) long isolated islands that slow down the shift rate.

To prove the enhanced interface of functionalized graphene/polymer, Zhang et al. [68] oxidized 1L graphene and studied its adhesion with polymer substrate using in-situ Raman deformation test. As shown in Figure 3.15(e), interfacial sliding happened at the edges of pristine 1L graphene at relatively high matrix strain and strain in the flake could no longer be well fitted by shear-lag theory. In contrast, interfacial stress transfer at high matrix strain is more effective in the case of oxidized monolayer and the interfacial shear stress after interfacial sliding was calculated to be ~1.7 MPa, four times higher than that of pristine 1L graphene.

In summary in-situ Raman deformation tests can be used for investigating the interfacial adhesion between 2D reinforcement and polymer matrix. Moreover, strain mapping can estimate the l_c of 2D materials and detect the deformation-induced fragmentation inside the nanocomposites [69].

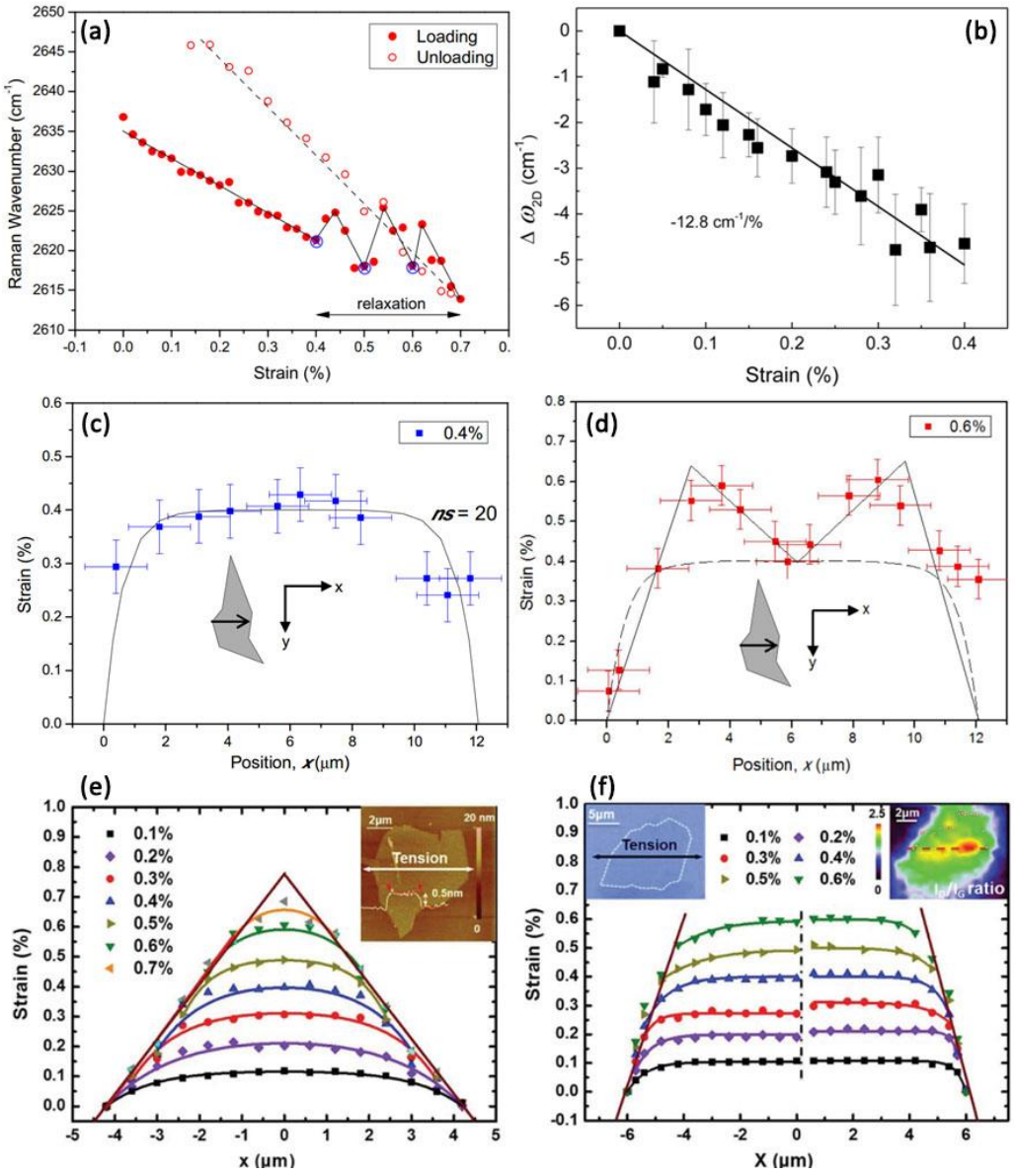

Figure 3.15 Uniaxial-strain induced Raman 2D band position of (a) mechanically exfoliated 1L graphene sandwiched by two thin layers of polymers [51] and (b) wrinkled 1L graphene as a function of tensile strain [67]. Distribution of strain in the 1L graphene in the direction of the tensile axis at (c) 0.4% and (d) 0.6% strain [51]. Distribution of strain in the (e) pristine 1L graphene and (f) oxidized 1L graphene in the direction of the tensile axis at different strain levels [68].

Layer-layer stress transfer efficiency Gong et al. [70] further studied the effect of number of layers on the effective Young's modulus of graphene in the model nanocomposites, by comparing the 2D band shift rate of 1L-3L graphene with and

without polymer top coating. It was found that the band shift rate of 1L graphene is independent of the existence of top coating, while that of 2L graphene obviously decreases if stress can only be transferred from bottom polymer substrate. This suggests the relatively poor stress transfer between the graphene layers, as the shift rate of uncoated 3L and few-layer graphene further decreases (see Figure 1.21(b)). The authors came up with a layer-layer stress transfer efficiency of ~0.6 for coated graphene, i.e. the effective Young's modulus of 3L graphene drops to 85% of that of 1L graphene, while the reinforcing efficiency of >7L graphene further drops to lower than half.

Bulk nanocomposites Raman spectroscopy can also be used for evaluating the morphology and reinforcement of graphene-based materials nondestructively in a polymer matrix. First of all, the dispersion of the graphene-based 2D materials can be estimated by mapping the intensity ratio of the graphene band relative to that of the band of matrix. Figure 3.16(a) [71] depicts the dispersion of graphite nanoplatelets (GNPs) in epoxy evaluated by mapping the intensity ratio of graphene 2D band and an epoxy band. The red coloured areas in the mapping graph represent the agglomeration of GNPs. It can be seen that the density of red areas increases with the GNPs concentration, suggesting that 2D materials tend to agglomerate in the composites at high loading.

Secondly, the orientation of graphene-based 2D materials in the polymer matrix can be characterized by polarized Raman spectroscopy. Figure 3.16(b) [72] demonstrates the polarized Raman study (VV polarization) of a graphene oxide (GO)/polymer nanocomposites film where GO flakes are randomly oriented in-plane in the matrix. The incident laser is parallel to the *z* axis (perpendicular to the GO flakes) in the schematic diagram and the Raman D band intensity of GO (I_D) keeps almost constant as the film is rotated (Figure 3.16(b)-2). In contrast, when the incident is parallel to

the *x* axis, the intensity of D band maximizes when the laser is parallel to the specimen edge plane but minimizes when it is perpendicular to the edge (Figure 3.16(b)-3). It is found that Figure 3.16(b)-3 can be fitted well by the equation: $I_D = 0.56\cos^4\theta_x + 0.44$ (where θ_x is the rotate angle of the film relative to *y* axis in the schematic), indicating that VV polarized Raman spectroscopy can precisely reflect the orientation of 2D materials in the composites.

Finally, the effective Young's modulus of graphene-based 2D materials can be evaluated from the slope of the plot of 2D or D band position against applied uniaxial strain [65]. For example, Li et al. [72] reported the uniaxial tensile strain-induced linear Raman D band downshifts of graphene oxide in GO/epoxy nanocomposites with different GO loadings (Figure 3.16(c)-1, 2). The authors found the D band shift rate decreases with GO loading, which is highly consistent with the change of effective modulus of GO calculated from modified rule of mixtures as illustrated in Figure 3.16(c)-3. For graphene based 2D materials, the effective Young's modulus E_{eff} can be estimated by

$$E_{\text{eff}} = \frac{\partial \omega_{\text{D}}}{\partial \varepsilon}\frac{1050}{30} = \frac{\partial \omega_{\text{2D}}}{\partial \varepsilon}\frac{1050}{60}\,(\text{GPa}) \qquad (3.12)$$

where $\partial\omega_D/\partial\varepsilon$ and $\partial\omega_{2D}/\partial\varepsilon$ are the band shift rate of D band and 2D band, respectively. 1050 (GPa), 30, 60 are the intrinsic Young's modulus, D band shift per unit strain [73], 2D band shift per unit strain of 1L graphene, respectively.

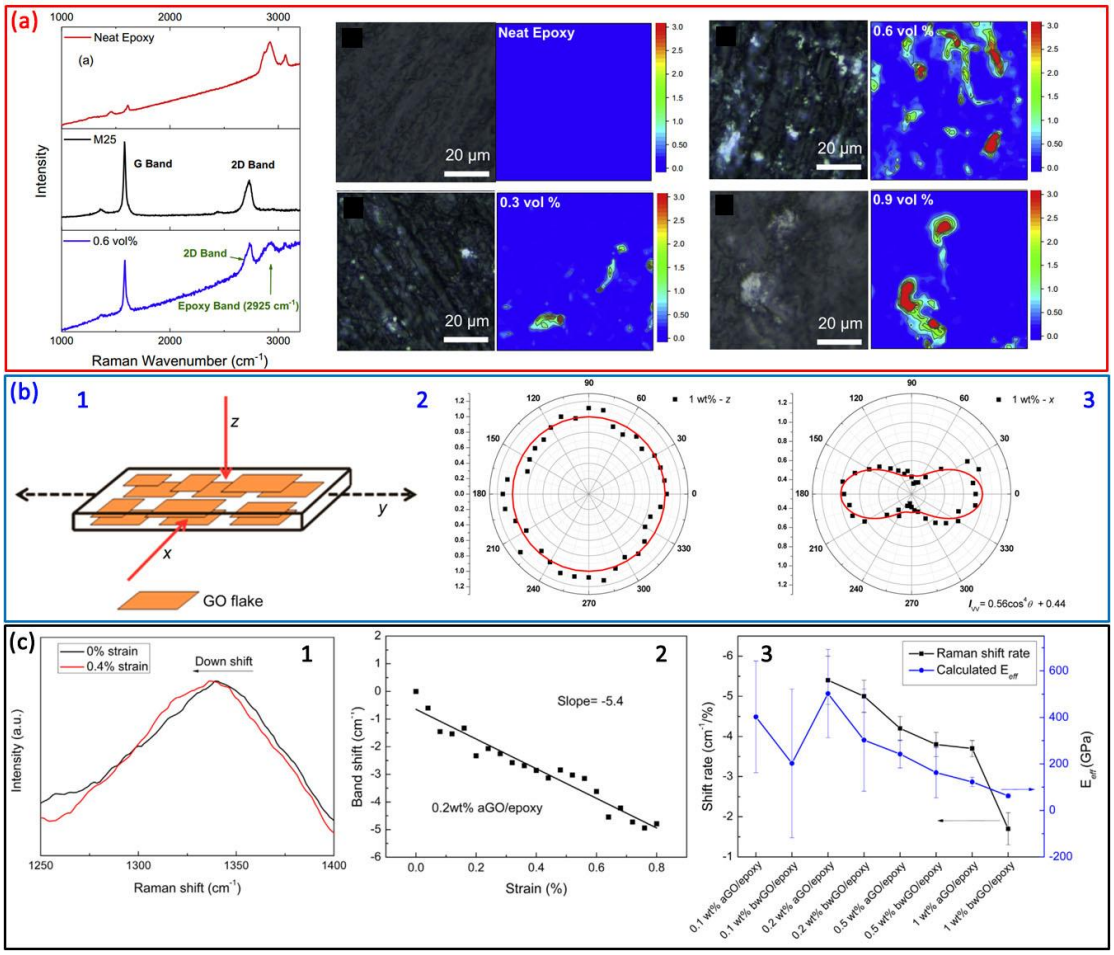

Figure 3.16 (a) Raman mappings of the intensity ratio of the graphene 2D band and an epoxy band at 2925 cm^{-1} for the GNPs/epoxy nanocomposites at different GNPs loadings [71]. (b) Polar plots of the normalized intensity of the graphene oxide D band using a VV polarization: (2) parallel to z axis, (3) parallel to the *x* axis in the schematic [72]. (c) Uniaxial tensile strain-induced Raman D band downshift of graphene oxide (denoted as aGO in this work) in a 0.2 wt% aGO/epoxy nanocomposite and (3) D band shift rates and calculated effective modulus of aGO in nanocomposites with different aGO loadings [74].

3.7.2 Raman spectra of 1D nanotube/polymer nanocomposites

Identifying individual SWCNTs in nanofibers It is well known that the band gap of SWCNTs depends on their chirality [75] and in any batch of SWCNTs prepared by classical methods (such as HiPco) there are both metallic and semiconducting

SWCNTs with totally different chiral vectors and band gaps. Hence, when the SWCNTs are excited by a laser with particular energy, only very limited number of nanotubes whose band gaps are close to the laser energy undergo resonance Raman scattering (Figure 3.17(a)) in which there is a 10^3-10^6 enhancement on their Raman band intensities. Additionally, the radial breathing mode (RBM, illustrated in Figure 3.17(b)) frequency (ω_{RBM}) of SWCNTs is independent of the chirality but sensitive to the nanotube diameter d [76], which can be expressed as

$$\omega_{\mathrm{RBM}} = \frac{A}{d} + B \qquad (3.13)$$

where A and B are constants affected by the nanotubes preparation method and surrounding environment. Therefore, when one has some SWCNTs that are resonant with the exciting frequency of the laser then one obtains a series of RBMs in the range of 180-320 cm^{-1} [77-78]. When one has only one isolated nanotube in resonance with the laser then one obtains an individual RBM. Therefore, resonant Raman spectroscopy can be used to detect individual SWCNTs in the nanocomposites. Figure 3.17(c-e) exhibits the Raman RBMs of individual electrospun 0.04% SWCNTs/PVA nanofibres excited by 1.49 eV, 1.59 eV, 1.96 eV lasers and some single RBMs can be seen in the three graphs, indicating the existence of isolated SWCNTs in the nanofibres.

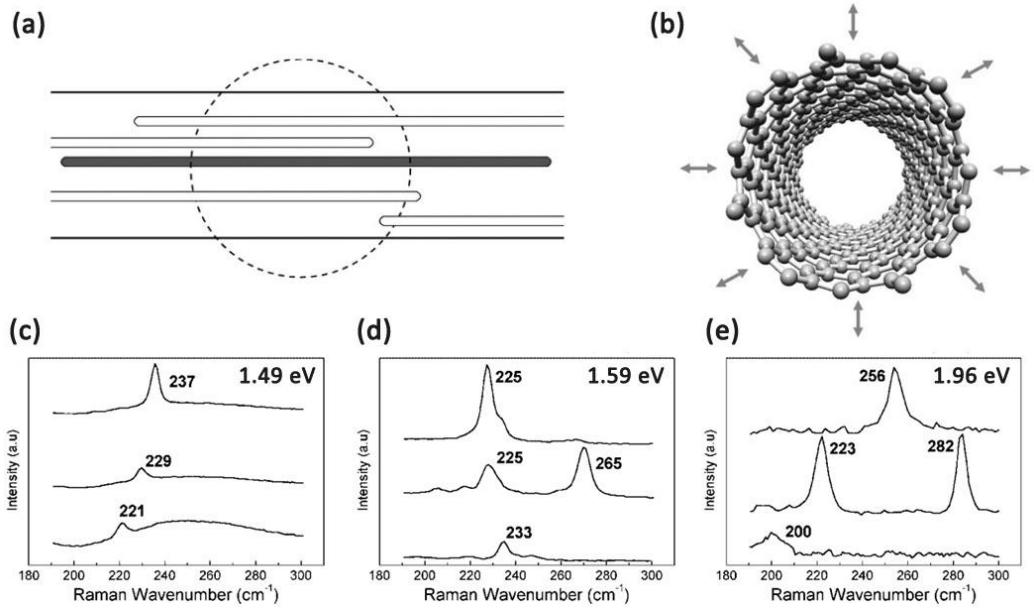

Figure 3.17 (a) Schematic diagram of the microstructure of a single SWCNTs/polymer

nanofibre, in which the shaded nanotube is the only one in resonance with the laser spot (dashed line) [77]. (b) Schematic diagram of the RBM of SWCNTs. RBMs of individual electrospun 0.04% SWCNTs/PVA nanofibres excited by (c) 1.49 eV, (d) 1.59 eV, (e) 1.96 eV lasers [78].

Stress transfer between adjacent layers within double-walled (DW) and MWCNTs

Similar to the case of graphene, the layer-layer bonding within DWCNTs and MWCNTs can be evaluated by understanding their Raman bands shift rate. Cui et al. [79] characterized the Raman 2D (denoted as G' in Ref 79) band shifts of both DWCNTs and SWCNTs in CNTs/epoxy nanocomposite. Different from the 2D band of SWCNTs (Figure 3.18(b)) which is a typical single band, the Raman 2D band of DWCNTs (Figure 3.18(a)) can be fitted as two sub-bands $2D_1$ and $2D_2$ corresponding to the spectra of inner walls and outer walls of the DWCNTs. It is found that the band shifts of $2D_1$ band (-1.1 cm^{-1}/% strain, Figure 3.18(c)) is much lower than that of $2D_2$ band (-9.2 cm^{-1}/% strain, Figure 3.18(d)), indicating a very poor stress transfer from outer shell to inner shell.

Deng et al. [80] found that the 2D band shift rate of MWCNTs (-3.4 cm^{-1}/% strain) in 0.1 wt% CNTs/epoxy nanocomposite is over four times lower than that of SWCNTs (-14.1 cm^{-1}/% strain) (Figure 3.18(e)). On the other hand, CNTs/epoxy interfacial slippage occurred for the SWCNTs at 0.5% strain while the inner-wall slippage delayed the outer shell/epoxy interfacial failure in the case of DWCNTs (i.e. better interfacial stress transfer). The authors modelled the deformation of MWCNTs and reported a ~0.7 interlayer stress transfer efficiency for the MWCNTs/epoxy nanocomposites (Figure 3.18(f)). This work also suggested that the outer shell of the MWCNTs takes the majority of the load in the nanocomposites and increasing number of inner layers decreases both the layer-layer stress transfer efficiency and the reinforcement efficiency of the nanotubes.

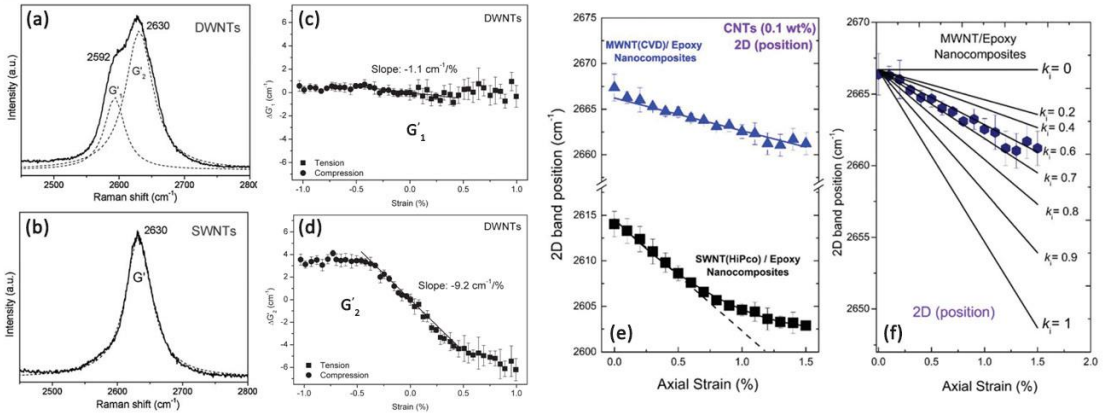

Figure 3.18 Raman 2D bands of (a) DWCNTs and (b) SWCNTs in CNTs/epoxy nanocomposites. Uniaxial tensile strain-induced Raman shift of (c) $2D_1$ band for the inner walls and (d) $2D_2$ band for the outer walls of the DWCNTs [79]. (e) Raman 2D band position of SWCNTs and MWCNTs in 0.1 wt% CNTs/epoxy nanocomposites as a function of strain. (f) Measured Raman 2D band position of MWCNTs and theoretical simulation of layer-layer stress transfer efficiency parameters (straight lines) as a function of strain [80].

Orientation and reinforcement of CNTs in nanocomposites CNTs demonstrate highly anisotropic mechanical properties, their longitudinal modulus (~1000 GPa) is almost 70 times the transverse modulus (~15 GPa) [81-82], the mechanical properties of corresponding nanocomposites are thus highly determined by the orientation of 1D nanotubes. Polarized Raman spectroscopy is a powerful technique in evaluating the orientation of CNTs (particularly individual SWCNTs) in the nanocomposites. This is based on the antenna effect where the Raman band intensity of 1D nanotubes is a maximum when the nanotube axis is parallel to the incident and scattered laser and a minimum when the nanotube axis is perpendicular to the laser polarization [16], as illustrated in Figure 3.19(a) [83]. Generally, a VV configuration, where both the incident and scattered laser are parallel to the axis of the spectrometer, and a VH configuration, where incident light is parallel and the scattered laser is perpendicular to the axis, are used for polarized Raman characterization. For the VV configuration, the Raman band intensity I_{VV} for perfectly-aligned CNTs is proportional to $\cos^4\alpha$,

where α is the angle between the nanotube axis and laser polarization [83].

Very recently, Chang et al. [84] reported the polarized Raman study of the orientation of BNNTs in nanocomposites fibres, Figure 3.19(b) and Figure 3.19(c) demonstrate the intensity change of BNNTs Raman G band (~1370 cm^{-1}) with fibre axis/laser angle under a VV configuration in a BNNTs/polyacrylonitrile (PAN) fibre without and with an extra 12× hot drawing step, respectively. It is very clear that the BNNTs in drawn fibres have higher orientation, which is reflected by more obvious change on the intensity of the Raman band with polarization angle in Figure 3.19(c).

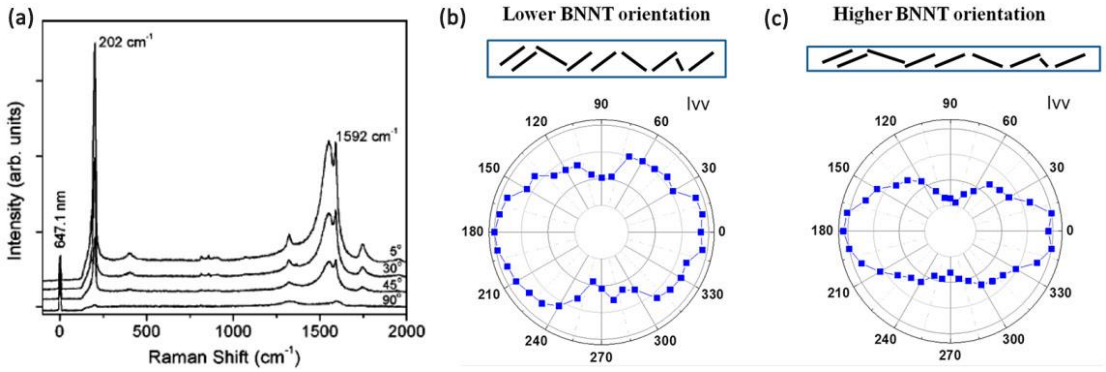

Figure 3.19 (a) VV polarized Raman spectra of a SWCNT/PMMA fibre at different angles relative to the axis of laser polarization [83]. (b) Polar plots of the BNNT Raman G band (~1370 cm^{-1}) intensity as a function of rotation angle under a VV configuration in the BNNTs/PAN fiber without and with an extra 12× hot drawing [84].

Based on the polarized Raman study and in-situ deformation of oriented SWCNTs/PVA electrospun nanofibre and randomly distributed composite film, Deng et al. [85] suggested that the effective Young's modulus of SWCNTs (E_{eff}) in the nanocomposites can be given by

$$E_{\text{eff}} = -\frac{S_0}{0.05} \qquad (3.14)$$

where S_0 is the Raman 2D band shift rate, -0.05 represents the -5 cm^{-1}/% universal calibration 2D band shift rate for 1D carbon fibres [14]. For perfectly-aligned SWCNTs in the nanocomposites, $S_0=S_{\text{aligned}}(0)$, while for randomly-oriented system,

$S_0=1.3S_{VV}(0)=3.3S_{VH}(0)$.

3.8 Aims of this project

Chapter 1, 2 have suggested that both BNNSs and BNNTs are very promising reinforcements for polymer materials, but their morphology and structure in the nanocomposites have not been studied systematically unlike graphene and CNTs. Chapter 3 has shown that (1) Raman spectra of BNNSs and BNNTs are strain sensitive and (2) Raman spectroscopy has been widely used on investigating the deformation of carbon-based 1D and 2D materials and their reinforcement on polymer matrix. However, different from the much stronger resonant Raman scattering of graphene and CNTs, the activation of resonant Raman scattering in BNNSs and BNNTs is far more difficult due to their wide band gap. This is the reason why BNNSs and BNNTs in nanocomposites have been only rarely studied using Raman spectroscopy. Nonetheless, it is still possible to excite the electrons of BNNSs and BNNTs to a virtual state and obtain non-resonant Raman scattering, although this signal is significantly weaker than would be achieved with resonance Raman scattering.

This project will look at the application of non-resonance Raman spectroscopy for the study of BNNSs & BNNTs-reinforced nanocomposites in the following areas:

For 2D BNNSs:

1. To study the critical length of few-layer BNNSs by linear Raman mapping across single BNNS flake.
2. To estimate the layer-layer stress transfer efficiency in BNNSs by comparing the Raman band shift of BNNSs with different thickness.
3. To investigate the effect of dispersion, thickness, aspect ratio, interface of BNNSs

on their reinforcement on PVA matrix nanocomposites, by the use of Raman spectroscopy and mechanical testing.

For 1D BNNTs:

1. To study the dispersion, bundling, orientation, interface, effective modulus of BNNTs in nanocomposites using non-resonance Raman spectroscopy.
2. To investigate the effect of functionalization of BNNTs with –OH groups, upon both their dispersion and stress transfer in the nanocomposites.
3. To prepare electrospun BNNTs/PVA nanofibres and study the orientation of BNNTs using polarized Raman spectroscopy.

References

1. Raman, C. V., A change of wave-length in light scattering. *Nature* **1928,** *121* (3051), 619-619.
2. Smith, E.; Dent, G., *Modern Raman Spectroscopy: a practical approach.* John Wiley & Sons, Ltd: Hoboken, **2005**.
3. Ferraro, J. R., *Introductory Raman Spectroscopy*. Academic, Press, Inc.: San Diego: **2003**.
4. Tuinstra, F.; Koenig, J. L., Raman spectrum of graphite. *The Journal of Chemical Physics* **1970,** *53* (3), 1126-1130.
5. Dresselhaus, M. S.; Dresselhaus, G.; Saito, R.; Jorio, A., Raman spectroscopy of carbon nanotubes. *Phys. Rep.* **2005,** *409* (2), 47-99.
6. Malard, L.; Pimenta, M. A.; Dresselhaus, G.; Dresselhaus, M., Raman spectroscopy in graphene. *Phys. Rep.* **2009,** *473* (5-6), 51-87.
7. Dresselhaus, M.; Dresselhaus, G.; Jorio, A.; Souza Filho, A.; Saito, R., Raman spectroscopy on isolated single wall carbon nanotubes. *Carbon* **2002,** *40* (12), 2043-2061.
8. Ferrari, A. C.; Meyer, J.; Scardaci, V.; Casiraghi, C.; Lazzeri, M.; Mauri, F.; Piscanec, S.; Jiang, D.; Novoselov, K.; Roth, S., Raman spectrum of graphene and graphene layers. *Phys. Rev. Lett.* **2006,** *97* (18), 187401.
9. Can çado, L. G.; Jorio, A.; Ferreira, E. H. M.; Stavale, F.; Achete, C. A.; Capaz, R. B.; Moutinho, M. V. O.; Lombardo, A.; Kulmala, T. S.; Ferrari, A. C., Quantifying Defects in Graphene via Raman Spectroscopy at Different Excitation Energies. *Nano Lett.* **2011,** *11* (8), 3190-3196.
10. Liang, L.; Zhang, J.; Sumpter, B. G.; Tan, Q.-H.; Tan, P.-H.; Meunier, V., Low-frequency shear and layer-breathing modes in Raman scattering of two-dimensional materials. *ACS Nano* **2017,** *11* (12), 11777-11802.
11. Zhang, S.; Zhang, N.; Zhao, Y.; Cheng, T.; Li, X.; Feng, R.; Xu, H.; Liu, Z.; Zhang, J.; Tong, L., Spotting the differences in two-dimensional materials - the Raman scattering perspective. *Chem. Soc. Rev.* **2018,** *47* (9), 3217-3240.
12. Gong, L. Deformation Micromechanics of Graphene Nanocomposites. PhD Thesis, The University of Manchester, **2013**.
13. Grasselli, J. G.; Bulkin, B. J., *Analytical Raman Spectroscopy*. Wiley: New York, **1991**.
14. Cooper, A. I. Structure/Property Relationships in Particulate Composites. PhD Thesis, The University of Manchester, **2000**.
15. Li, Z. Raman Spectroscopic Studies of the Mechanics of Graphene-based Nanocomposites. PhD Thesis, The University of Manchester, **2015**.
16. Deng, L. Raman Spectroscopic Studies of Carbon Nanotube Composite Fibres. PhD Thesis, The University of Manchester, **2010**.
17. Stenger, I.; Schue, L.; Boukhicha, M.; Berini, B.; Placais, B.; Loiseau, A.; Barjon, J., Low frequency Raman spectroscopy of few-atomic-layer thick hBN crystals.

2D Materials **2017,** *4* (3), 031003.

18. Pakdel, A.; Bando, Y.; Golberg, D., Nano boron nitride flatland. *Chem. Soc. Rev.* **2014,** *43* (3), 934-959.
19. Pakdel, A.; Zhi, C.; Bando, Y.; Nakayama, T.; Golberg, D., Boron nitride nanosheet coatings with controllable water repellency. *ACS Nano* **2011,** *5* (8), 6507-6515.
20. Arenal, R.; Ferrari, A. C.; Reich, S.; Wirtz, L.; Mevellec, J. Y.; Lefrant, S.; Rubio, A.; Loiseau, A., Raman spectroscopy of single-wall boron nitride nanotubes. *Nano Lett.* **2006,** *6* (8), 1812-6.
21. Kuzuba, T.; Era, K.; Ishii, T.; Sato, T., A low frequency Raman-active vibration of hexagonal boron nitride. *Solid State Commun.* **1978,** *25* (11), 863-865.
22. Zhang, X.; Han, W.; Wu, J.; Milana, S.; Lu, Y.; Li, Q.; Ferrari, A.; Tan, P., Raman spectroscopy of shear and layer breathing modes in multilayer MoS 2. *Physical Review B* **2013,** *87* (11), 115413.
23. Li, L. H.; Cervenka, J.; Watanabe, K.; Taniguchi, T.; Chen, Y., Strong oxidation resistance of atomically thin boron nitride nanosheets. *ACS Nano* **2014,** *8* (2), 1457-62.
24. Gorbachev, R. V.; Riaz, I.; Nair, R. R.; Jalil, R.; Britnell, L.; Belle, B. D.; Hill, E. W.; Novoselov, K. S.; Watanabe, K.; Taniguchi, T.; Geim, A. K.; Blake, P., Hunting for monolayer boron nitride: optical and Raman signatures. *Small* **2011,** *7* (4), 465-8.
25. Li, L. H.; Santos, E. J.; Xing, T.; Cappelluti, E.; Roldan, R.; Chen, Y.; Watanabe, K.; Taniguchi, T., Dielectric screening in atomically thin boron nitride nanosheets. *Nano Lett.* **2015,** *15* (1), 218-23.
26. Cai, Q.; Li, L. H.; Yu, Y.; Liu, Y.; Huang, S.; Chen, Y.; Watanabe, K.; Taniguchi, T., Boron nitride nanosheets as improved and reusable substrates for gold nanoparticles enabled surface enhanced Raman spectroscopy. *Phys. Chem. Chem. Phys.* **2015,** *17* (12), 7761-6.
27. Cai, Q.; Scullion, D.; Falin, A.; Watanabe, K.; Taniguchi, T.; Chen, Y.; Santos, E. J.; Li, L. H., Raman signature and phonon dispersion of atomically thin boron nitride. *Nanoscale* **2017,** *9* (9), 3059-3067.
28. Falin, A.; Cai, Q.; Santos, E. J. G.; Scullion, D.; Qian, D.; Zhang, R.; Yang, Z.; Huang, S.; Watanabe, K.; Taniguchi, T.; Barnett, M. R.; Chen, Y.; Ruoff, R. S.; Li, L. H., Mechanical properties of atomically thin boron nitride and the role of interlayer interactions. *Nat Commun* **2017,** *8*, 15815.
29. Androulidakis, C.; Galiotis, C., Thermomechanical behaviour of hexagonal boron nitride at elevated temperatures. *2D Materials* **2020,** *7* (4), 045011.
30. Androulidakis, C.; Koukaras, E. N.; Poss, M.; Papagelis, K.; Galiotis, C.; Tawfick, S., Strained hexagonal boron nitride: Phonon shift and Grüneisen parameter. *Physical Review B* **2018,** *97* (24).
31. Kim, G.; Jang, A.-R.; Jeong, H. Y.; Lee, Z.; Kang, D. J.; Shin, H. S., Growth of high-crystalline, single-layer hexagonal boron nitride on recyclable platinum foil.

Nano Lett. **2013,** *13* (4), 1834-1839.

32. Lu, G.; Wu, T.; Yuan, Q.; Wang, H.; Wang, H.; Ding, F.; Xie, X.; Jiang, M., Synthesis of large single-crystal hexagonal boron nitride grains on Cu–Ni alloy. *Nat Commun* **2015,** *6*, 6160.
33. Gao, Y.; Ren, W.; Ma, T.; Liu, Z.; Zhang, Y.; Liu, W.-B.; Ma, L.-P.; Ma, X.; Cheng, H.-M., Repeated and controlled growth of monolayer, bilayer and few-layer hexagonal boron nitride on Pt foils. *ACS Nano* **2013,** *7* (6), 5199-5206.
34. Tay, R. Y.; Park, H. J.; Ryu, G. H.; Tan, D.; Tsang, S. H.; Li, H.; Liu, W.; Teo, E. H. T.; Lee, Z.; Lifshitz, Y., Synthesis of aligned symmetrical multifaceted monolayer hexagonal boron nitride single crystals on resolidified copper. *Nanoscale* **2016,** *8* (4), 2434-2444.
35. Lee, J. S.; Choi, S. H.; Yun, S. J.; Kim, Y. I.; Boandoh, S.; Park, J.-H.; Shin, B. G.; Ko, H.; Lee, S. H.; Kim, Y.-M., Wafer-scale single-crystal hexagonal boron nitride film via self-collimated grain formation. *Science* **2018,** *362* (6416), 817-821.
36. Hong, S.; Lee, C.-S.; Lee, M.-H.; Lee, Y.; Ma, K. Y.; Kim, G.; Yoon, S. I.; Ihm, K.; Kim, K.-J.; Shin, T. J.; Kim, S. W.; Jeon, E.-c.; Jeon, H.; Kim, J.-Y.; Lee, H.-I.; Lee, Z.; Antidormi, A.; Roche, S.; Chhowalla, M.; Shin, H.-J.; Shin, H. S., Ultralow-dielectric-constant amorphous boron nitride. *Nature* **2020,** *582* (7813), 511-514.
37. Schué, L.; Stenger, I.; Fossard, F.; Loiseau, A.; Barjon, J., Characterization methods dedicated to nanometer-thick hBN layers. *2D Materials* **2016,** *4* (1), 015028.
38. Tan, P.; Han, W.; Zhao, W.; Wu, Z.; Chang, K.; Wang, H.; Wang, Y.; Bonini, N.; Marzari, N.; Pugno, N., The shear mode of multilayer graphene. *Nature Materials* **2012,** *11* (4), 294.
39. Ling, J.; Miao, X.; Sun, Y.; Feng, Y.; Zhang, L.; Sun, Z.; Ji, M., Vibrational Imaging and Quantification of Two-Dimensional Hexagonal Boron Nitride with Stimulated Raman Scattering. *ACS Nano* **2019,** *13* (12), 14033-14040.
40. Wirtz, L.; Rubio, A.; de La Concha, R. A.; Loiseau, A., Ab initio calculations of the lattice dynamics of boron nitride nanotubes. *Physical Review B* **2003,** *68* (4), 045425.
41. Popov, V. N., Lattice dynamics of single-walled boron nitride nanotubes. *Physical Review B* **2003,** *67* (8), 085408.
42. Wirtz, L.; Lazzeri, M.; Mauri, F.; Rubio, A., Raman spectra of BN nanotubes: Ab initio and bond-polarizability model calculations. *Physical Review B* **2005,** *71* (24), 241402.
43. Reich, S.; Ferrari, A.; Arenal, R.; Loiseau, A.; Bello, I.; Robertson, J., Resonant Raman scattering in cubic and hexagonal boron nitride. *Physical Review B* **2005,** *71* (20), 205201.
44. Sánchez-Portal, D.; Hernandez, E., Vibrational properties of single-wall nanotubes and monolayers of hexagonal BN. *Physical Review B* **2002,** *66* (23),

235415.

45. Zhi, C.; Bando, Y.; Tang, C.; Golberg, D.; Xie, R.; Sekigushi, T., Phonon characteristics and cathodolumininescence of boron nitride nanotubes. *Appl. Phys. Lett.* **2005,** *86* (21), 213110.
46. Wu, J.; Han, W.-Q.; Walukiewicz, W.; Ager, J.; Shan, W.; Haller, E.; Zettl, A., Raman spectroscopy and time-resolved photoluminescence of BN and B x C y N z nanotubes. *Nano Lett.* **2004,** *4* (4), 647-650.
47. Kuzuba, T.; Sato, Y.; Yamaoka, S.; Era, K., Raman-scattering study of high-pressure effects on the anisotropy of force constants of hexagonal boron nitride. *Physical Review B* **1978,** *18* (8), 4440.
48. Saha, S.; Muthu, D.; Golberg, D.; Tang, C.; Zhi, C.; Bando, Y.; Sood, A., Comparative high pressure Raman study of boron nitride nanotubes and hexagonal boron nitride. *Chem. Phys. Lett.* **2006,** *421* (1-3), 86-90.
49. Robinson, I.; Zakikhani, M.; Day, R.; Young, R.; Galiotis, C., Strain dependence of the Raman frequencies for different types of carbon fibres. *J. Mater. Sci. Lett.* **1987,** *6* (10), 1212-1214.
50. Cooper, C.; Young, R.; Halsall, M., Investigation into the deformation of carbon nanotubes and their composites through the use of Raman spectroscopy. *Composites Part A: Applied Science and Manufacturing* **2001,** *32* (3-4), 401-411.
51. Gong, L.; Kinloch, I. A.; Young, R. J.; Riaz, I.; Jalil, R.; Novoselov, K. S., Interfacial stress transfer in a graphene monolayer nanocomposite. *Adv. Mater.* **2010,** *22* (24), 2694-2697.
52. Rice, C.; Young, R.; Zan, R.; Bangert, U.; Wolverson, D.; Georgiou, T.; Jalil, R.; Novoselov, K., Raman-scattering measurements and first-principles calculations of strain-induced phonon shifts in monolayer MoS 2. *Physical Review B* **2013,** *87* (8), 081307.
53. Wang, F.; Kinloch, I. A.; Wolverson, D.; Tenne, R.; Zak, A.; O'Connell, E.; Bangert, U.; Young, R. J., Strain-induced phonon shifts in tungsten disulfide nanoplatelets and nanotubes. *2D Materials* **2016,** *4* (1), 015007.
54. Li, X.; Liu, J.; Ding, K.; Zhao, X.; Li, S.; Zhou, W.; Liang, B., Temperature Dependence of Raman-Active In-Plane E 2g Phonons in Layered Graphene and h-BN Flakes. *Nanoscale Research Letters* **2018,** *13* (1), 25.
55. Cai, Q.; Scullion, D.; Gan, W.; Falin, A.; Zhang, S.; Watanabe, K.; Taniguchi, T.; Chen, Y.; Santos, E. J. G.; Li, L. H., High thermal conductivity of high-quality monolayer boron nitride and its thermal expansion. *Sci Adv* **2019,** *5* (6), eaav0129.
56. Seremetis, L.; Koukaras, E. N.; Alexandri, S.; Michail, A.; Kalosakas, G.; Parthenios, J.; Galiotis, C.; Tsirkas, S.; Grammatikopoulos, S.; Papagelis, K., Thermomechanical Response of Supported Hexagonal Boron Nitride Sheets of Various Thicknesses. *The Journal of Physical Chemistry C* **2020,** *124* (22), 12134-12143.
57. Cai, Q.; Scullion, D.; Gan, W.; Falin, A.; Cizek, P.; Liu, S.; Edgar, J. H.; Liu, R.;

Cowie, B. C. C.; Santos, E. J. G.; Li, L. H., Outstanding Thermal Conductivity of Single Atomic Layer Isotope-Modified Boron Nitride. *Phys. Rev. Lett.* **2020,** *125* (8), 085902.

58. Exarhos, G. J.; Schaaf, J. W., Raman scattering from boron nitride coatings at high temperatures. *J. Appl. Phys.* **1991,** *69* (4), 2543-2548.
59. Arutyunyan, N.; Obraztsova, E.; Silly, M.; Jaffrennou, P.; Attal-Tretout, B.; Loiseau, A.; Chuvilin, A., Thermal effects in Raman spectra of hexagonal boron nitride and nanotube-containing boron nitride soot. *Physica Status Solidi (b)* **2006,** *243* (13), 3316-3319.
60. Lu, J.; Ren, Q.; Sun, L.; Yu, J.; Chen, Y.; Shen, X.; Chen, Z., Temperature-dependent Raman spectra of bamboo-like boron nitride nanotubes. *Applied Physics Express* **2014,** *7* (2), 022401.
61. Pease, R. S., An X-ray study of boron nitride. *Acta Crystallogr.* **1952,** *5* (3), 356-361.
62. Mohiuddin, T.; Lombardo, A.; Nair, R.; Bonetti, A.; Savini, G.; Jalil, R.; Bonini, N.; Basko, D.; Galiotis, C.; Marzari, N., Uniaxial strain in graphene by Raman spectroscopy: G peak splitting, Grüneisen parameters, and sample orientation. *Physical Review B* **2009,** *79* (20), 205433.
63. Kern, G.; Kresse, G.; Hafner, J., Ab initio calculation of the lattice dynamics and phase diagram of boron nitride. *Physical Review B* **1999,** *59* (13), 8551.
64. Bera, K.; Chugh, D.; Patra, A.; Tan, H. H.; Jagadish, C.; Roy, A., Strain distribution in wrinkled hBN films. *Solid State Commun.* **2020,** *310*, 113847.
65. Papageorgiou, D. G.; Li, Z.; Liu, M.; Kinloch, I. A.; Young, R. J., Mechanisms of mechanical reinforcement by graphene and carbon nanotubes in polymer nanocomposites. *Nanoscale* **2020,** *12* (4), 2228-2267.
66. Kinloch, I. A.; Suhr, J.; Lou, J.; Young, R. J.; Ajayan, P. M., Composites with carbon nanotubes and graphene: An outlook. *Science* **2018,** *362* (6414), 547-553.
67. Li, Z.; Kinloch, I. A.; Young, R. J.; Novoselov, K. S.; Anagnostopoulos, G.; Parthenios, J.; Galiotis, C.; Papagelis, K.; Lu, C.-Y.; Britnell, L., Deformation of wrinkled graphene. *ACS Nano* **2015,** *9* (4), 3917-3925.
68. Wang, G.; Dai, Z.; Liu, L.; Hu, H.; Dai, Q.; Zhang, Z., Tuning the interfacial mechanical behaviors of monolayer graphene/PMMA nanocomposites. *ACS Appl Mater Interfaces* **2016,** *8* (34), 22554-22562.
69. Young, R. J.; Gong, L.; Kinloch, I. A.; Riaz, I.; Jalil, R.; Novoselov, K. S., Strain mapping in a graphene monolayer nanocomposite. *Acs Nano* **2011,** *5* (4), 3079-3084.
70. Gong, L.; Young, R. J.; Kinloch, I. A.; Riaz, I.; Jalil, R.; Novoselov, K. S., Optimizing the reinforcement of polymer-based nanocomposites by graphene. *ACS Nano* **2012,** *6* (3), 2086-2095.
71. Li, Z.; Slater, T. J.; Ma, X.; Yu, Y.; Young, R. J.; Burnett, T. L., The taxonomy of graphite nanoplatelets and the influence of nanocomposite processing. *Carbon* **2019,** *142*, 99-106.

72. Li, Z.; Young, R. J.; Kinloch, I. A., Interfacial stress transfer in graphene oxide nanocomposites. *ACS Appl Mater Interfaces* **2013,** *5* (2), 456-63.
73. Ferralis, N., Probing mechanical properties of graphene with Raman spectroscopy. *Journal of Materials Science* **2010,** *45* (19), 5135-5149.
74. Li, Z.; Young, R. J.; Wang, R.; Yang, F.; Hao, L.; Jiao, W.; Liu, W., The role of functional groups on graphene oxide in epoxy nanocomposites. *Polymer* **2013,** *54* (21), 5821-5829.
75. Cadek, M.; Coleman, J.; Ryan, K.; Nicolosi, V.; Bister, G.; Fonseca, A.; Nagy, J.; Szostak, K.; Beguin, F.; Blau, W., Reinforcement of polymers with carbon nanotubes: the role of nanotube surface area. *Nano Lett.* **2004,** *4* (2), 353-356.
76. Saito, R.; Takeya, T.; Kimura, T.; Dresselhaus, G.; Dresselhaus, M., Raman intensity of single-wall carbon nanotubes. *Physical Review B* **1998,** *57* (7), 4145.
77. Kannan, P.; Eichhorn, S. J.; Young, R. J., Deformation of isolated single-wall carbon nanotubes in electrospun polymer nanofibres. *Nanotechnology* **2007,** *18* (23), 235707.
78. Kannan, P.; Young, R. J.; Eichhorn, S. J., Debundling, isolation, and identification of carbon nanotubes in electrospun nanofibers. *Small* **2008,** *4* (7), 930-3.
79. Cui, S.; Kinloch, I. A.; Young, R. J.; No é, L.; Monthioux, M., The Effect of Stress Transfer Within Double-Walled Carbon Nanotubes Upon Their Ability to Reinforce Composites. *Adv. Mater.* **2009,** *21* (35), 3591-3595.
80. Young, R. J.; Deng, L.; Wafy, T. Z.; Kinloch, I. A., Interfacial and internal stress transfer in carbon nanotube based nanocomposites. *Journal of Materials Science* **2015,** *51* (1), 344-352.
81. Liu, T.; Kumar, S., Effect of orientation on the modulus of SWNT films and fibers. *Nano Lett.* **2003,** *3* (5), 647-650.
82. Popov, V.; Van Doren, V.; Balkanski, M., Elastic properties of crystals of single-walled carbon nanotubes. *Solid State Commun.* **2000,** *114* (7), 395-399.
83. Hwang, J.; Gommans, H.; Ugawa, A.; Tashiro, H.; Haggenmueller, R.; Winey, K. I.; Fischer, J. E.; Tanner, D.; Rinzler, A., Polarized spectroscopy of aligned single-wall carbon nanotubes. *Physical Review B* **2000,** *62* (20), R13310.
84. Chang, H.; Lu, M.; Arias-Monje, P. J.; Luo, J.; Park, C.; Kumar, S., Determining the Orientation and Interfacial Stress Transfer of Boron Nitride Nanotube Composite Fibers for Reinforced Polymeric Materials. *ACS Applied Nano Materials* **2019,** *2* (10), 6670-6676.
85. Deng, L.; Eichhorn, S. J.; Kao, C. C.; Young, R. J., The effective Young's modulus of carbon nanotubes in composites. *ACS Appl Mater Interfaces* **2011,** *3* (2), 433-40.

Chapter 4 Stress Transfer in hBN Nanosheets*

4.1 Introduction

As reviewed in Chapter 1, two-dimensional (2D) hexagonal boron nitride (hBN) nanosheets (BNNSs) exhibit extraordinary oxidation resistance [1] and chemical and thermal stability [2-3]. In addition, the reduced electron-delocalization in the B-N π bonds leads to a large ~6 eV indirect band gap [4], making BNNSs both electrically insulating and optically transparent [5]. The exceptional thermal and electrical properties of BNNSs suggest that they have potential to be used as nanofillers for polymer nanocomposites [6-7] and researchers on BNNS/polymer composites have concentrated principally upon the modification of the thermal conductivity and insulating properties by the addition of BNNSs [8-12]. Mechanical reinforcement has, in contrast, been less well studied (see Chapter 2).

Although BNNSs have been investigated for mechanical reinforcement for a number of years, it is only recently that their fundamental mechanical properties have been studied systematically [13]. By using AFM nanoindentation [14], the Young's modulus of exfoliated single-crystalline monolayer (1L) BNNSs was measured to be 0.87 ± 0.07 TPa with a breaking strengths of 70.5±5.5 GPa. Such impressive mechanical properties make BNNSs amongst the strongest insulators. More importantly, this work also revealed that interlayer bonding within BNNSs appears to be much stronger than in the case of multi-layer graphene. The Young's modulus and strength of graphene decrease rapidly with increasing thickness. Both properties remain almost constant for BNNSs when the number of layers increases from 1 to 9. This conclusion was further confirmed by the Raman spectroscopy study from

*This chapter is based on a paper, "Interlayer and Interfacial Stress Transfer in hBN Nanosheets", 2D Materials, 2021.

Androulidakis et al. [15], where the uniaxial strain-induced in-plane E_{2g} Raman mode (normally denoted as the "G band") shift rates of BNNSs was almost constant when the number of layers increased from two to four. However, the level of layer-layer stress transfer efficiency of BNNSs during deformation is, to our knowledge, yet to be quantified.

In the present chapter, Raman spectroscopy is used to study the effect of both the BNNS thickness and lateral dimensions upon stress transfer from a polymer substrate. The uniaxial strain-induced G band shift rates of BNNSs with different thickness from 6.5 nm to ~100 nm are measured and the layer-layer stress transfer efficiency of BNNSs is determined. Both the BNNS/polymer interfacial adhesion and the BNNSs lateral length for realizing efficient interfacial stress transfer are evaluated by mapping the strain along a hBN nanosheet of 11 μm length and 17 nm in thickness at incremental substrate strain. This work will provide guidance on optimizing the reinforcement of polymer-based nanocomposites by few-layer BNNSs.

4.2 Experimental

4.2.1 Materials

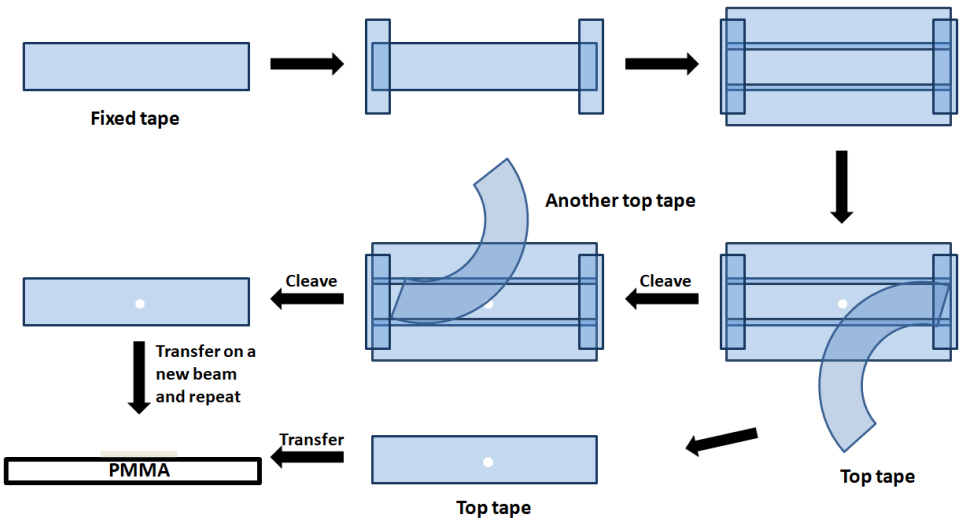

Figure 4.1 Schematic of tape exfoliation of BNNSs.

For mechanical exfoliation, large commercial hexagonal boron nitride (hBN) single crystals were purchased from HQ Graphene and used as received. The single crystals were exfoliated mechanically and the flakes transferred using the standard tape cleavage technique [16]. The BNNSs were exfoliated using blue adhesive tape (Nitto Denko Corporation) and deposited directly on the centre of a rectangular PMMA beam with no top coat applied, as illustrated in Figure 4.1.

4.2.2 Characterization

The BNNSs on the PMMA beams were identified and characterised using the Zeiss optical microscope on a Horiba LabRAM Evolution HR spectrometer with a 50× lens. The thickness of the BNNSs on the beams was measured using a Nanowizard atomic force microscope (AFM) (JPK Instruments) operated in the QI mode.

4.2.3 In situ Raman Deformation Studies

The Horiba LabRAM Evolution HR spectrometer equipped with a 488 nm sapphire laser was used for the analysis of the mechanically-exfoliated BNNSs. The in-situ Raman deformation analysis was conducted by inserting the BNNS-loaded PMMA beams into a four-point-bending rig fixed on the Raman microscope stage. A resistance strain gauge was used on the PMMA beam surface to monitor the strain applied on the PMMA substrate. The beams were deformed up to 0.4% strain in ~0.04% intervals and Raman spectra were collected and peak fitted at each strain level. The exposure time for each Raman scan was 20 s with a power output ~1.3 mW and a laser spot size of ~2 μm using a 50× objective lens. The most prominent Raman band of hBN is the E_{2g} mode which originates from in-plane atomic displacement and is

equivalent to the G band of graphene [17]. Raman line mapping was undertaken using a 100× objective lens.

4.3 Results and Discussion

4.3.1 Strain-induced Raman band shifts

Figure 4.2 gives the result of in-situ Raman deformation studies of two BNNSs transferred onto a PMMA beam. An incremental strain up to 0.4% was applied parallel to the long axis of the BNNSs as shown in Figure 4.2(a). The Raman spectra obtained at three different spots (marked and denoted as spots 1 (red), 2 (black), 3 (Green) in Figure 4.2(b&c)) were recorded simultaneously at each strain level. As shown in Figure 4.2(e-g), the measured thickness of the BNNSs at each spot 1-3 is 10.0 nm, 8.8 nm and 20.0 nm, respectively. The corresponding spectra obtained under similar conditions at each spot are shown in Figure 4.2(d) and it can be seen that spot 3, from the thickest BNNS, exhibits the strongest hBN G band (the very intense peak at ~1450 cm^{-1} is C-H band of PMMA).

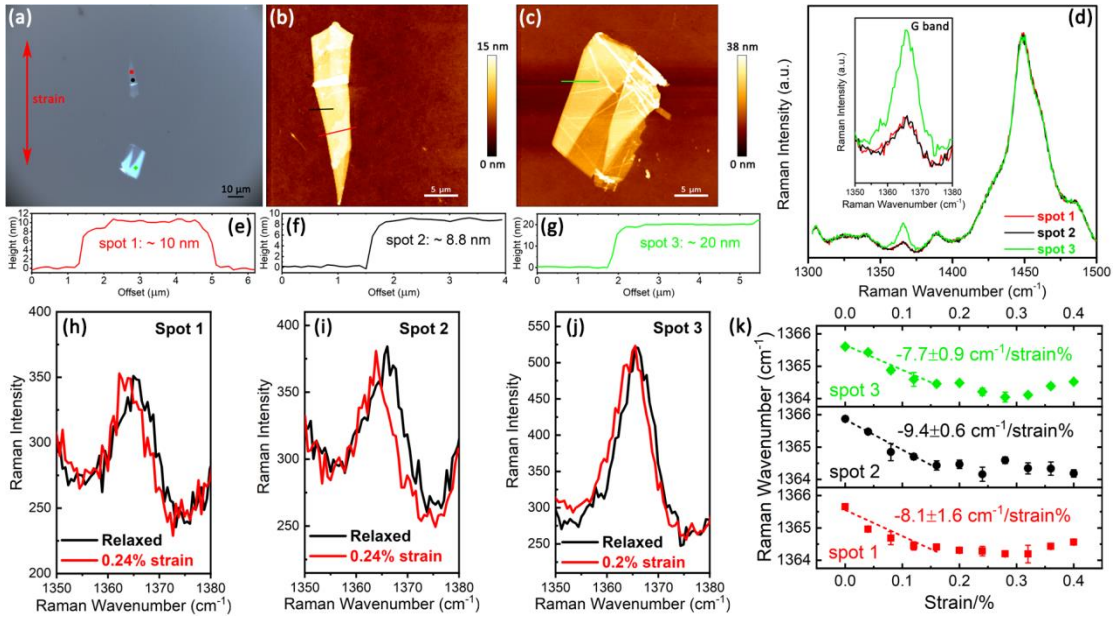

Figure 4.2 (a) Optical micrograph and (b&c) AFM images of 3 marked spots on the two

BNNS flakes. (d) Raman spectra of the 3 marked spots on the BNNSs. (e-g) The height profiles correspond to the three solid lines in (b&c). (h-j) Raman spectra of the 3 marked spots on the BNNSs before and after up to 0.24% tensile strain was applied. (k) The position of Raman G band as a function of tensile strain for the 3 marked spots on the BNNSs.

It can be seen in Figures 4.2(h-j) that the G bands of the Raman spectra collected at the three spots all shifted to lower wavenumber under the application of tensile strain. Figure 4.2(k) shows that there was a linear downshift to lower frequency up to ~0.2% strain and the derived shift rates in the low strain region for spots 1-3 are -8.1 ±1.6 cm^{-1}/%, -9.4 ± 0.6 cm^{-1}/%, -7.7 ± 0.9 cm^{-1}/%, respectively. These measurements show that the shift rate drops slightly as the thickness of the BNNSs increases from 8.8 nm to 20 nm. This suggests that, unlike few-layer graphene, where there is a significant decrease in shift rate (per % stain) with increasing flake thickness due to easy inter-layer sliding [18], the layer-layer interaction inside the BNNSs is relatively strong [13, 15]. These rates of G-band shift are similar to those reported in an earlier study upon the deformation of exfoliated BNNSs on a PMMA substrate [15]. Some broadening G-band was sometimes observed as shown in Figure 4.3 but we did not, however, see any band splitting, possibly as the result of the low levels of applied strain used in our study.

It can also be observed in Figure 4.2(k) that the downshift of the three spots reduces when the strain exceeds ~0.2%, indicating possible BNNS slippage on the substrate at a relatively low strain. This implies that surface modification of pristine BNNSs may be necessary ensure their interfacial adhesion with a polymer matrix in order to realize good reinforcement, as we have reported in a study upon hBN nanotubes in nanocomposites [19], and will be demonstrated in Chapter 6.

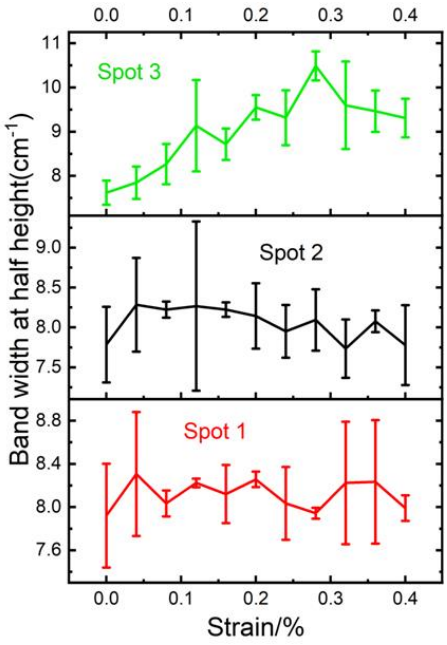

Figure 4.3 Width of the G band as a function of strain during deformation for the band shifts shown for spots 1-3 in Figure 4.2.

4.3.2 Interlayer stress transfer

To investigate further the effect of the number of layers, we exfoliated more BNNSs and studied their Raman G band shift rates as a function of thickness (see Table 4.1). The highest downshift rate (-11.9 cm^{-1}/%) was found for a hBN nanosheet of 9.4 nm thickness (28 layers, assuming an individual layer thickness of 0.333 nm [20]), and the shift rate was found to gradually decrease with an increasing number of layers eventually dropping to ~ -2cm^{-1}/% when the thickness increased to ~100 nm (300 layers). The data in Table 4.1 are plotted in Figure 4.4. They are fitted to the equation for the effect of the number of layers upon the Raman band shift rate ($d\omega/d\varepsilon$) derived in a previous study upon few-layer graphene [18]

$$(d\omega_G / d\varepsilon) = \frac{(d\omega_G / d\varepsilon)_{reference}}{\left[N - k(N-1)\right]} \qquad (4.1)$$

where N is the number of layers and k is the interlayer transfer efficiency. The parameter $(d\omega_G/d\varepsilon)_{reference}$ is the reference G band shift rate and taking this to be

-11cm^{-1}/%, gives interlayer transfer efficiency *k* of ~0.99 (i.e. 99% efficient). This is much higher than the stress transfer efficiency determined for few-layer graphene (0.6 – 0.8) [18]. Most of the measurements in Figure 4.4 were taken during deformation from a region approximately the middle of the BNNS. It will be shown below that the strain will vary with position on the flake which might account for some of the scatter of the data in Figure 4.4.

The Grüneisen parameter can be determined using the relationship

$$\gamma_G = \frac{\Delta\omega_G}{\omega_G^0(1-\nu)\varepsilon} \qquad (4.2)$$

where the Raman frequency of the G band (ω_G^0) can be fixed at 1366 cm^{-1} and the Poissons ratio of the PMMA matrix ν=0.35 [15, 21]. Setting $\Delta\omega_G/\varepsilon = (d\omega_G/d\varepsilon)_{reference}$, the γ_G of the BNNS is calculated to be 1.23, a value close to the measured γ_G for BNNS with a >10 number of layers (1.04) reported by Androulidakis *et al*. [15].

Table 4.1 Raman G band shift rate of exfoliated BNNSs with lengths > 10 μm and different thickness

Thickness (nm)	Distance to edge (μm)	Raman shift rate (cm^{-1}/%)	Flake length (μm)
6.5	5.9	-6.6±0.1	19.3
8.8	12.7	-9.4±0.6	27.3
9.4	13.7	-11.9±0.9	29.3
10	11.2	-8.1±1.6	27.3
17	6.5	-5.4±0.6	11.1
20	7.4	-7.7±0.9	23.5
25	9	-6.2±0.4	45.5
43	26.6	-4.0±0.4	59
54	7	-4.6±0.6	19.2

68	9.6	-2.8±0.1	25
94	6.1	-2.9±0.2	> 100

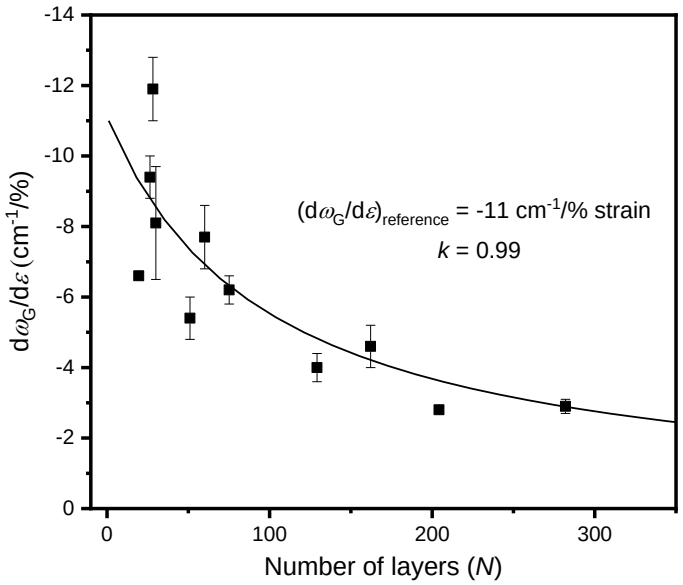

Figure 4.4 Raman G band shift rate of BNNSs as a function of number of layers. The curve is Equation (4.1) plotted using a value of $(d\omega_G/d\varepsilon)_{reference}$ of -11 cm^{-1}/% strain.

The evaluation of the parameter *k* can also be used to predict the dependence of the Young's modulus of a 2D material in a nanocomposite upon the number of layers, *N*. In the case of 2D materials laid on the surface of the polymer beam without any top coating, such as in this present study, the effective modulus E_{eff} is given by [18]

$$E_{eff} = \frac{E_{2D\ material}}{\left[N - k(N-1)\right]} \qquad (4.3)$$

where $E_{2D\ material}$ is the Young's modulus of the 2D material monolayer. A value of k = 0.99 means that E_{eff} will only fall to half of the monolayer value for 100-layer BNNS (N = 100). This can be contrasted with the behaviour of multilayer graphene for which k is in the range of 0.6-0.8. The modulus falls rapidly to half the monolayer value for N = 5 when k~0.7. Hence it appears that it is less important to achieve a high degree of exfoliation to very thin nanosheets, when using hBN in nanocomposites, than in the case of graphite and graphene.

4.3.3 Strain mapping

Previous work on 1L graphene [22] has demonstrated that it is possible to monitor stress transfer from a substrate to the flake of a 2D material by mapping the strain along the flake.

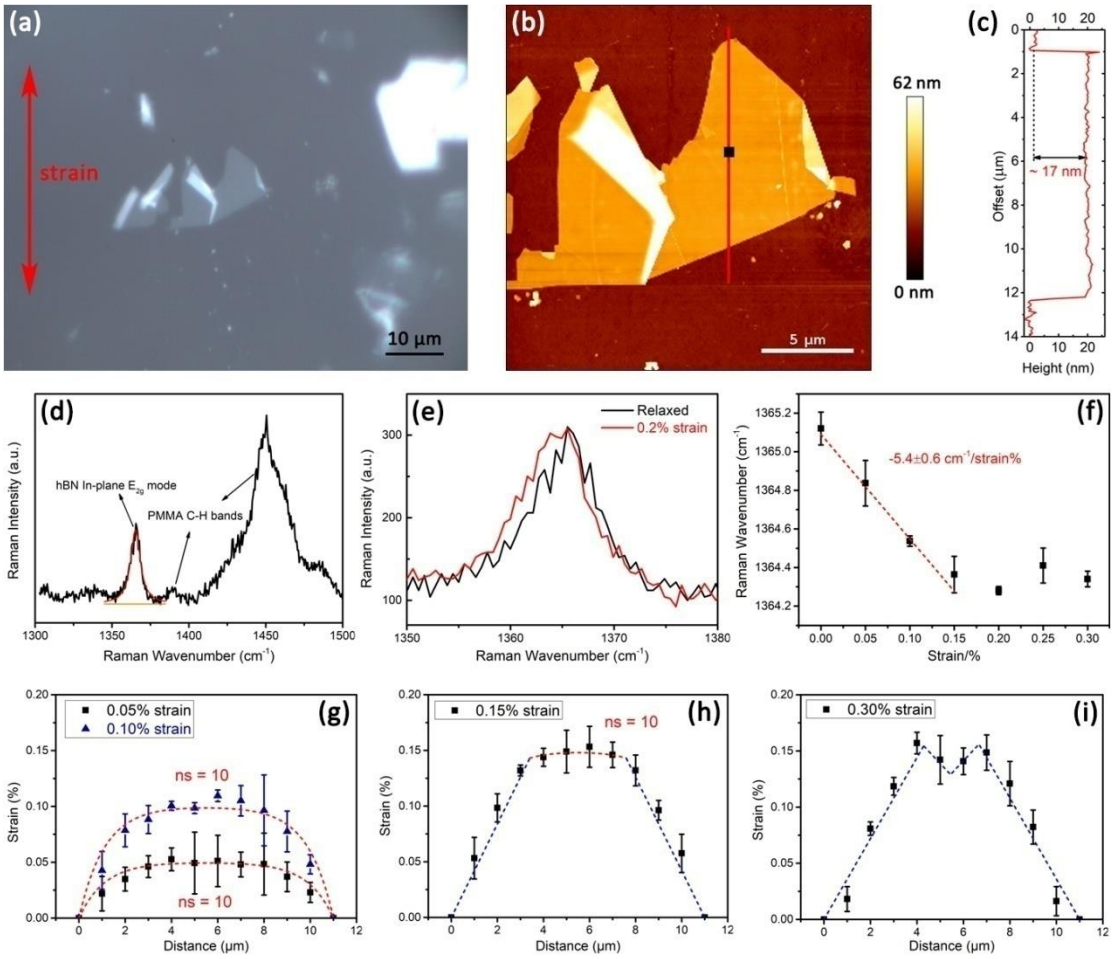

Figure 4.5 (a) Optical micrograph and (b) AFM image of the hBN nanosheet used for linear Raman strain mapping (the black square in (b) marks the spectra collection position for (d-f)). (c) The AFM height profile corresponding to the solid red line in (b). (d) Raman spectrum of the hBN nanosheet. (e) Raman spectra of the BNNS obtained before and after a 0.2% tensile strain was applied. (f) The position of G band position as a function of tensile strain. Distribution of strain in the hBN nanosheet in the direction of the tensile axis along the solid line in (b) at: (g) 0.05%, 0.1% strain, (h) 0.15% strain and (i) 0.30% strain.

Figure 4.5(a&b) shows a hBN nanosheet of 11 μm length and 17 nm (Figure 4.2(c)) in thickness deformed in tension parallel to its axis. To improve the spatial resolution of the linear strain mapping, an objective lens with the highest resolution (×100) was used to minimize the laser spot size to ~1.5 μm. Thus an intense G band for the BN nanosheet can be seen in Figure 4.5(d). Figure 4.5(e) shows the Raman spectra obtained from the middle of the nanosheet (marked by a black square in Figure 4.5(b)) before and after 0.2% strain was applied. It can be seen that the G band clearly shifts to lower frequency and broadens after deformation. The broadening is a result of band splitting [15] but the band has for simplicity been fitted to a single peak in this present study. As shown in Figure 4.5(f), there is a linear red shift of the G band with stepwise straining up to 0.15%. The shift stops at 0.2% strain and eventually became irregular when a higher tensile strain was applied.

The Raman G band position was monitored along the solid line in Figure 4.5(b) in 1 μm steps. Figure 4.5(g) shows the variation of axial strain across the BNNSs flake when a low strain (≤0.1%) was applied to PMMA substrate. It can be seen that the strain builds up from the two edges and becomes constant along the middle of the nanosheet where the strain in the flake equals to the applied matrix strain. This is exactly analogous to what was observed for the strain distribution of a polymer-sandwiched graphene monolayer under relatively low strain (<0.4%) [22] for which there was good bonding between 2D material and polymer matrix. This behaviour can be analyzed by the well-established shear-lag theory [23-24] where it is assumed that the elastic stress is transferred from the matrix to the reinforcement through a shear stress at 2D material/polymer interface. The variation of strain in the BNNS, ε_{BNNS}, is given as [25]

$$\varepsilon_{BNNS} = \varepsilon_m \left[1 - \frac{\cosh\left(ns \frac{x}{l} \right)}{\cosh(ns/2)} \right] \qquad (4.4)$$

where

$$n = \sqrt{\frac{2G_m}{E_{\text{BNNS}}}\left(\frac{t}{T}\right)} \qquad (4.5)$$

and ε_m is the applied matrix strain, s is the aspect ratio of the BNNS, x represents the position in the flake, l is the length of the flake, G_m is the matrix shear modulus, E_{BNNS} is the Young's modulus of the BNNS, t is the thickness of the BNNS and T is the total thickness of polymer matrix. The parameter n has been widely accepted as a parameter for evaluating the interfacial stress transfer efficiency. The dashed line in Figure 4.5(g) is a reasonable fit of Equation (4.4) to the Raman mapping results using $ns \approx 10$. The aspect ratio for the hBN nanosheet in Figure 4.5 is s = 10 μm/17 nm ≈ 590. Since for this BNNS, ns = 10 and so n = 0.017. This value of n is some 30× larger that the value of $n = 6\times10^{-4}$ determined for a sandwiched graphene monolayer on a polymer substrate [22]. The higher value of n implies that better stress transfer can be expected between BNNSs and a polymer matrix than for graphene, presumably a result of the more polar nature of the bonding in hBN.

It can be seen in Figure 4.5(g) that the strain rises to about 90% of the plateau value over about 3 μm from the edge, suggesting the critical length l_c of the few-layer BNNS reinforcement of the order of 6 μm. The value of critical length determined for monolayer graphene using a similar approach is ~3 μm [22], but it should be noted that the BNNS flake in Figure 4.5 is 17 nm thick. Hence the critical aspect ratio, s_c, for this 50-layer BNNS is ~350 compared with a value of around 10^4 (≈3 μm/0.35 nm) for monolayer graphene. This is further indication that BNNSs should give good reinforcement in nanocomposites at lower levels of exfoliation than for graphene. The importance of the aspect ratio upon stress transfer is highlighted in Figure 4.6. This shows that a 4 μm wide and 20 nm thick (aspect ratio, s~200) BNNS has a lower Raman band shift rate than a thicker (54 nm) BNNS for which s> 350.

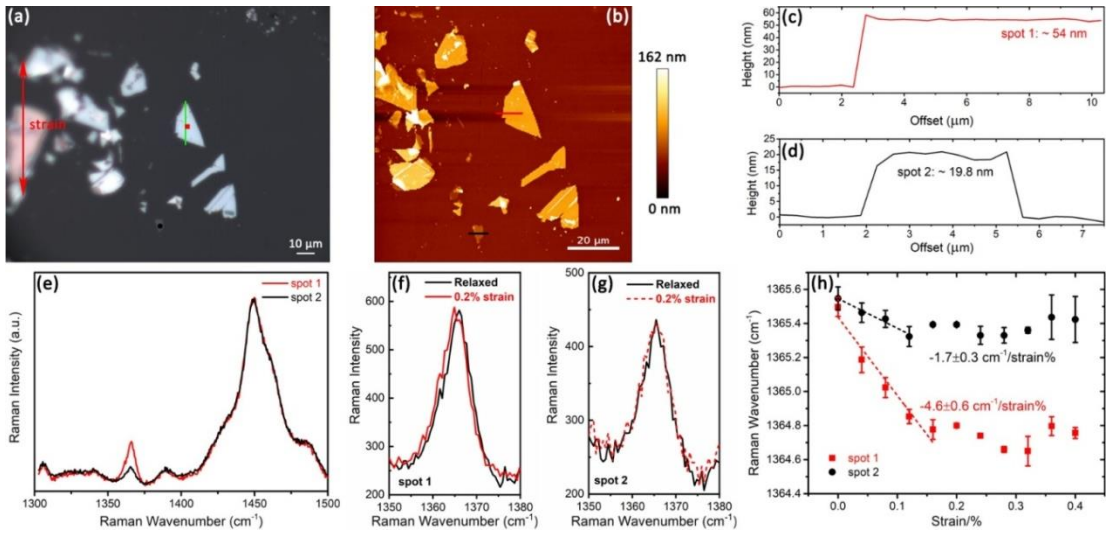

Figure 4.6 (a) Optical micrograph and (b) AFM image of the marked spots on two BNNS flakes. (c&d) The height profiles corresponding to the two solid lines in (b). (e) Raman spectra of 2 marked spots on the BNNSs. (f&g) Raman spectra of the 2 marked spots on the BNNSs before and after 0.2% tensile strain was applied. (h) The positions of the Raman G band as a function of tensile strain for the 2 marked spots on the BNNSs showing a large shift rate for spot 1 from a thicker BNNS with larger lateral dimensions than the thinner BNNS in spot 2, only 4 μm wide.

For a well-bonded 2D BNNS/polymer interface, the interfacial shear stress τ_i can be given by [22]

$$\tau_i = nE_{BNNS}\varepsilon_m \frac{\sinh(ns\frac{x}{l})}{\cosh(ns/2)} \qquad (4.6)$$

The Young's modulus of a 17 nm thick hBN nanosheet without a top coating can be calculated using Equation (4.3). It is found that the effective modulus of BNNSs drops from 0.87 TPa (modulus of 1L BNNS [13]) to ~0.60 TPa when the thickness increases to 17 nm (~50 layers). Hence the maximum value of τ_i at the edges of the 11 μm long hBN nanosheet for ns = 10 is calculated to be 4.7 MPa increasing to 9.4 MPa when ε_m is 0.05% and 0.1%, respectively. In the case of a graphene monolayer a maximum value of τ_i at 0.4% applied strain was found to be only ~2.3 MPa [22],

confirming the better stress transfer for the hBN nanosheet on the polymer substrate.

When ε_m is increased up to 0.15% (Figure 4.5(h)), an approximate linear strain variation develops from the edges to the centre of the flake, up to ~3.5 μm from the edges. It is found that shear-lag theory can no longer be used to fit the strain variation at both edges of the flake, but it still can be fitted in the centre of the flake (red dashed line), where the strain in the flake keeps almost constant at around 0.15%. This situation is analogous to the partially-debonded situation in the single fibre pull-out test [26], where interfacial failure starts at the edges of the reinforcement and propagates gradually to the center of the fibre. In our case, it appears that the BNNS/polymer interface has started to fail at the edges of the nanosheet but continuous interfacial debonding has not reached the centre of the flake at this stage. Stress is transferred by interfacial friction (i.e. friction between the mismatched BNNS and the polymer, which will usually result in residual stress) [27] along the failed interface and the value of τ_i in this region can be determined from the slope of the linear fit (blue dashed line) in Figure 4.5(h) using the force balance equation [22]

$$\frac{\mathrm{d}\varepsilon_{\mathrm{BNNS}}}{\mathrm{d}x} = -\frac{\tau_i}{E_{\mathrm{BNNS}}t} \qquad (4.7)$$

which gives a value of 4.3 MPa of τ_i at edges of the flake.

When the strain is increased further to 0.3%, it is found that the BNNS/polymer interface has completely failed as shown in Figure 4.5(i). In this case the strain linearly increases from the edges to the center of the flake up to only ~0.15% strain (much smaller than ε_m) and dips in the middle of the flake. This suggests that the interfacial debonding has reached the centre of the flake and stress transfer throughout the nanosheet is taking place through interfacial friction. In this case, the value of τ_i for the failed interface is estimated to be 3.8 MPa. This can again be contrasted with the behavour of a graphene monolayer [22] where a value of τ_i of only 0.3-0.8 MPa

was determined for a failed interface at 0.6% applied strain confirming the better stress transfer for the BNNSs.

4.4 Conclusions

Stress transfer both between the individual layers within exfoliated hBN nanosheets and between an hBN nanosheet and a polymer substrate has been followed through the use of Raman spectroscopy. Overall it has been demonstrated that the efficiency of stress transfer both between the individual hBN layers in the nanosheets and between the nanosheets and the substrate is better for BNNSs than for mono- or multi-layer graphene. The implication of this study is that BNNSs should give rise to better reinforcement in nanocomposites than exfoliated graphene nanosheets as long as the BNNS/polymer interface remains intact.

References

1. Li, L. H.; Cervenka, J.; Watanabe, K.; Taniguchi, T.; Chen, Y., Strong oxidation resistance of atomically thin boron nitride nanosheets. *ACS Nano* **2014,** *8* (2), 1457-62.
2. Paine, R. T.; Narula, C. K., Synthetic routes to boron nitride. *Chem. Rev.* **1990,** *90* (1), 73-91.
3. Weng, Q.; Wang, X.; Wang, X.; Bando, Y.; Golberg, D., Functionalized hexagonal boron nitride nanomaterials: emerging properties and applications. *Chem. Soc. Rev.* **2016,** *45* (14), 3989-4012.
4. Cassabois, G.; Valvin, P.; Gil, B., Hexagonal boron nitride is an indirect bandgap semiconductor. *Nature Photonics* **2016,** *10* (4), 262.
5. Jiang, X.-F.; Weng, Q.; Wang, X.-B.; Li, X.; Zhang, J.; Golberg, D.; Bando, Y., Recent Progress on Fabrications and Applications of Boron Nitride Nanomaterials: A Review. *Journal of Materials Science & Technology* **2015,** *31* (6), 589-598.
6. Meng, W.; Huang, Y.; Fu, Y.; Wang, Z.; Zhi, C., Polymer composites of boron nitride nanotubes and nanosheets. *J. Mater. Chem. C* **2014,** *2* (47), 10049-10061.
7. Yin, J.; Li, J.; Hang, Y.; Yu, J.; Tai, G.; Li, X.; Zhang, Z.; Guo, W., Boron Nitride Nanostructures: Fabrication, Functionalization and Applications. *Small* **2016,** *12* (22), 2942-68.
8. Xie, B.-H.; Huang, X.; Zhang, G.-J., High thermal conductive polyvinyl alcohol composites with hexagonal boron nitride microplatelets as fillers. *Compos. Sci. Technol.* **2013,** *85*, 98-103.
9. Wu, Y.; Xue, Y.; Qin, S.; Liu, D.; Wang, X.; Hu, X.; Li, J.; Wang, X.; Bando, Y.; Golberg, D.; Chen, Y.; Gogotsi, Y.; Lei, W., BN Nanosheet/Polymer Films with Highly Anisotropic Thermal Conductivity for Thermal Management Applications. *ACS Appl Mater Interfaces* **2017,** *9* (49), 43163-43170.
10. Kuang, Z.; Chen, Y.; Lu, Y.; Liu, L.; Hu, S.; Wen, S.; Mao, Y.; Zhang, L., Fabrication of highly oriented hexagonal boron nitride nanosheet/elastomer nanocomposites with high thermal conductivity. *Small* **2015,** *11* (14), 1655-9.
11. Chen, J.; Huang, X.; Sun, B.; Jiang, P., Highly Thermally Conductive Yet Electrically Insulating Polymer/Boron Nitride Nanosheets Nanocomposite Films for Improved Thermal Management Capability. *ACS Nano* **2019,** *13* (1), 337-345.
12. Wu, K.; Wang, J.; Liu, D.; Lei, C.; Liu, D.; Lei, W.; Fu, Q., Highly Thermoconductive, Thermostable, and Super-Flexible Film by Engineering 1D Rigid Rod-Like Aramid Nanofiber/2D Boron Nitride Nanosheets. *Adv. Mater.* **2020**, 1906939.
13. Falin, A.; Cai, Q.; Santos, E. J. G.; Scullion, D.; Qian, D.; Zhang, R.; Yang, Z.; Huang, S.; Watanabe, K.; Taniguchi, T.; Barnett, M. R.; Chen, Y.; Ruoff, R. S.; Li, L. H., Mechanical properties of atomically thin boron nitride and the role of interlayer interactions. *Nat Commun* **2017,** *8*, 15815.

14. Lee, C.; Wei, X.; Kysar, J. W.; Hone, J., Measurement of the elastic properties and intrinsic strength of monolayer graphene. *Science* **2008,** *321* (5887), 385-388.
15. Androulidakis, C.; Koukaras, E. N.; Poss, M.; Papagelis, K.; Galiotis, C.; Tawfick, S., Strained hexagonal boron nitride: Phonon shift and Grüneisen parameter. *Physical Review B* **2018,** *97* (24).
16. Novoselov, K. S.; Jiang, D.; Schedin, F.; Booth, T. J.; Khotkevich, V. V.; Morozov, S. V.; Geim, A. K., Two-dimensional atomic crystals. *Proc. Natl. Acad. Sci. U. S. A.* **2005,** *102* (30), 10451-3.
17. Ferrari, A. C.; Meyer, J.; Scardaci, V.; Casiraghi, C.; Lazzeri, M.; Mauri, F.; Piscanec, S.; Jiang, D.; Novoselov, K.; Roth, S., Raman spectrum of graphene and graphene layers. *Phys. Rev. Lett.* **2006,** *97* (18), 187401.
18. Gong, L.; Young, R. J.; Kinloch, I. A.; Riaz, I.; Jalil, R.; Novoselov, K. S., Optimizing the reinforcement of polymer-based nanocomposites by graphene. *ACS Nano* **2012,** *6* (3), 2086-2095.
19. Wang, W.; Li, Z.; Prestat, E.; Hashimoto, T.; Guan, J.; Kim, K. S.; Kingston, C. T.; Simard, B.; Young, R. J., Reinforcement of Polymer-Based Nanocomposites by Thermally Conductive and Electrically Insulating Boron Nitride Nanotubes. *ACS Applied Nano Materials* **2019,** *3* (1), 364-374.
20. Golla, D.; Chattrakun, K.; Watanabe, K.; Taniguchi, T.; LeRoy, B. J.; Sandhu, A., Optical thickness determination of hexagonal boron nitride flakes. *Applied Physics Letters* **2013,** *102* (16).
21. Peng, X.; Wei, Q.; Copple, A., Strain-engineered direct-indirect band gap transition and its mechanism in two-dimensional phosphorene. *Physical Review B* **2014,** *90* (8), 085402.
22. Gong, L.; Kinloch, I. A.; Young, R. J.; Riaz, I.; Jalil, R.; Novoselov, K. S., Interfacial stress transfer in a graphene monolayer nanocomposite. *Adv. Mater.* **2010,** *22* (24), 2694-2697.
23. Cox, H., The elasticity and strength of paper and other fibrous materials. *British Journal of Applied Physics* **1952,** *3* (3), 72.
24. Nairn, J. A., A variational mechanics analysis of the stresses around breaks in embedded fibers. *Mech. Mater.* **1992,** *13* (2), 131-154.
25. Papageorgiou, D. G.; Li, Z.; Liu, M.; Kinloch, I. A.; Young, R. J., Mechanisms of mechanical reinforcement by graphene and carbon nanotubes in polymer nanocomposites. *Nanoscale* **2020,** *12* (4), 2228-2267.
26. Bannister, D.; Andrews, M.; Cervenka, A.; Young, R., Analysis of the single-fibre pull-out test by means of Raman spectroscopy: Part II. Micromechanics of deformation for an aramid/epoxy system. *Compos. Sci. Technol.* **1995,** *53* (4), 411-421.
27. Kelly, A.; Macmillan, N., Strong Solids, Clarendon. Oxford New York: **1986**.

Chapter 5 Mechanisms of Reinforcement of Polymer-Based Nanocomposites by hBN Nanosheets†

5.1 Introduction

Opto-thermal Raman measurement [1] and AFM nanoindentation [2] have confirmed the hBN nanosheets (BNNSs) to be one of the thermally-conductive and strongest insulators (Chapter 1). The BNNSs are thus anticipated to be promising multi-functional nanofillers for polymer nanocomposites [3-4] (see Chapter 2). Although impressive reinforcements on different polymer matrices with the addition of low content of BNNSs were reported [5-9], research upon mechanical properties of BNNSs/polymer nanocomposites has still not been studied systematically.

Chapter 4 demonstrated the Raman spectroscopic study to investigate the mechanisms of stress transfer in individual BNNSs and it was found that the efficiency of stress transfer both between the individual hBN layers in the nanosheets and between the nanosheets and the substrate is better for BNNSs than for mono- or multi-layer graphene. In addition, it was shown that shear-lag theory, that is widely used to analyse conventional fibre-reinforced composites [10], could be used at the nano-level for the BNNSs.

It is well established that the reinforcement of polymers by carbon-based nanofillers is controlled by stress transfer from the matrix to the reinforcement [11] and this can be followed using Raman spectroscopy and following stress-induced band shifts [12]. In this chapter, Raman spectroscopy has been used to characterize the dispersion of the BNNSs in the PVA and the level of stress transfer from the PVA to the BNNSs. To

†This chapter is based on a paper, "Mechanisms of Reinforcement of Polymer-Based Nanocomposites by hBN Nanosheets", submitted.

study the effect of the geometry of the BNNSs upon the level of reinforcement in polymer-based nanocomposites [13], three types of BNNSs with different geometries have been prepared, two of which have similar lateral dimensions and two that have a similar aspect ratio (length/thickness). PVA nanocomposites with different loadings of the three types of BNNSs have been prepared and this enables the effect of BNNS volume fraction and geometry upon the mechanical properties such as Young's modulus, yield stress and breaking strength, to be determined. The reinforcement of the polymer has been modelled using a combination of the rule of mixtures and modified shear lag theory. It has also been suggested that the BNNSs with the larger aspect ratio demonstrate a superior level of reinforcement.

5.2 Experimental

5.2.1 Materials

For liquid-phase exfoliation (LE), two different sources of bulk boron nitride crystals were employed: 1. Sigma hBN crystals (Sigma Aldrich) with ~1 μm average flake size (Figure 5.1(a)); 2. Momentive hBN crystals (Momentive Performance Materials) with ~40μm average flake size (Figure 5.1(b)). Isopropanol (IPA, > 99.5%) was purchased from Fisher Scientific and used as received. The PVA powder (MW ~89000-98000, 99+% hydrolyzed) was purchased from Sigma Aldrich and used as received.

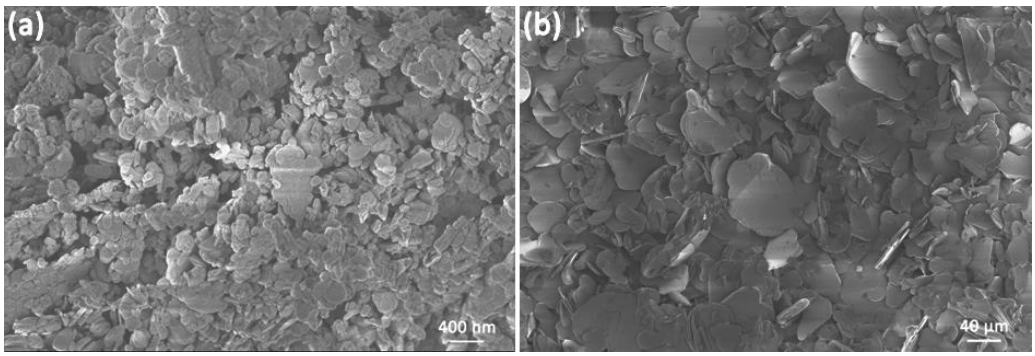

Figure 5.1 SEM images of Sigma (a) and Momentive (b) boron nitride crystals used for

liquid-phase exfoliation.

5.2.2 Liquid-Phase Exfoliation

Liquid-phase exfoliation [14] was conducted with reference to previous work [15-16]. Around 4 g boron nitride crystals were added to a 400 mL mixture of isopropanol/deionized water (DW) (1:1). The solutions were then sonicated in an Elmasonic P70H sonication bath (220 W effective power output, Elma Schmidbauer GmbH). The sonication frequency was fixed at 37 kHz. The sonication power and time were 40% of maximum power and 12 h for the Sigma crystals, and 60% and 18 h for the Momentive crystals, respectively. The as-prepared dispersions were then centrifuged with different rotation speeds, using a benchtop centrifuge (Thermo Fisher Scientific).

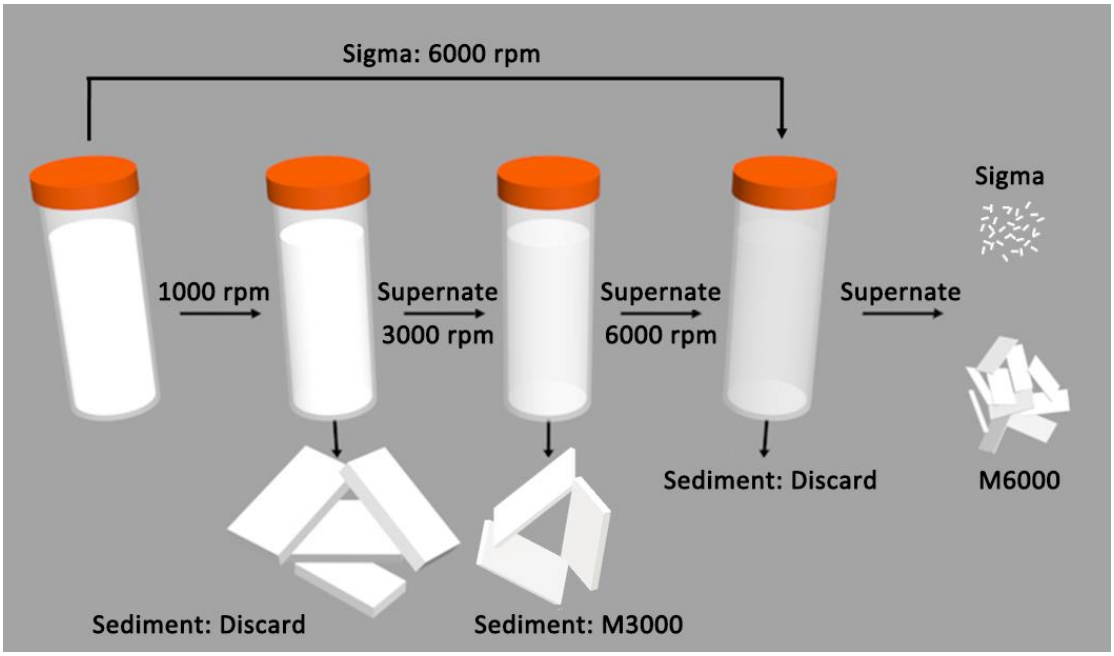

Figure 5.2 Schematic of liquid-phase preparation of Sigma, M3000, M6000 BNNSs.

As shown in Figure 5.2, the supernatant liquid from the Sigma BNNSs was collected directly after a 30 min centrifugation at 6000 rpm. Then the nanosheets (denoted as Sigma) were obtained following filtration and overnight vacuum drying at 80 ℃. The

dispersion of the Momentive BNNSs was first centrifuged at 1000 rpm for 30 min. The sediment was isolated and discarded, so that large and thick BNNSs that had not been sufficiently exfoliated were thus removed. The supernatant liquid after the first isolation was then centrifuged at 3000 rpm for another 30 min. The sediments were collected and denoted as M3000 nanosheets. The supernatant liquid after the second isolation was finally centrifuged at 6000 rpm for 30 min. The as-obtained diluted supernatant was isolated from the sediments (that were discarded) and filtered, dried and denoted as M6000 nanosheets. In summary, 3 types of exfoliated BNNSs with different aspect ratios, lateral size and thickness (Sigma, M3000 and M6000) were thus prepared for the nanocomposite fabrication.

5.2.3 Preparation of the BNNS/PVA Nanocomposite Films

To prepare the BNNS/PVA nanocomposites, a measured amount of the exfoliated BNNSs was added to DW and the mixture was then sonicated in an ultrasonic bath at 60% power for 1 hour to obtain a homogeneous dispersion. A measured amount of PVA powder was added into BNNS/DW dispersion to give a mass ratio of the PVA to DW of 10 wt% and a loading of 0.1-1 wt% nanosheets relative to the PVA. The BNNS/PVA/DW solution was then mixed using magnetic stirring, heated to 90 ℃ in a water bath and held for 3 hours. This was followed by natural cooling and an extra 2 hour moderate bath sonication using 40 wt% power, to achieve good mixing.

The as-prepared BNNS/PVA aqueous solutions were cast onto different substrates. For mechanical testing, the solutions were cast onto glass petri dishes. For the Raman deformation testing, the solutions were cast onto PMMA beams. All of the nanocomposite films were left in an oven for 2 days and dried at 60 ℃, followed by overnight vacuum treatment to remove any residual moisture.

5.2.4 Characterization of the Liquid-phase Exfoliated BNNSs and BNNS/PVA Nanocomposite Films

The sizes of the 3 types of exfoliated BNNSs were estimated using a Zeiss Ultra 55 scanning electron microscopy (SEM) operated at ~2 kV (in-lens mode) and a Nanowizard atomic force microscope (AFM) (JPK Instruments) in the QI mode. The thickness of the BNNSs was measured using the same AFM. In addition, a PANalytical X'Pert Pro X-ray (0.154 nm wavelength) diffractometer (XRD) was used to investigate the quality of the BNNSs prepared. The Horiba LabRAM Evolution HR Raman spectrometer equipped with a Coherent 488 nm sapphire laser was employed to evaluate the dispersion of the BNNSs in the PVA nanocomposites. Raman mapping was undertaken on two 100 × 100 μm^2 areas of the 1 wt% BNNS/PVA films mapped in 2μm steps.

A Q100 differential scanning calorimeter (DSC) (TA Instruments) was used to study the effect of the addition of the BNNSs upon the crystallization of the PVA matrix. A heat-cool-heat procedure from 10 ℃ to 250 ℃ was set up, with a 10 ℃/min ramp rate. In addition, XRD patterns of the nanocomposite films were obtained using the above-mentioned diffractometer.

5.2.5 Mechanical Testing

An Instron-3344 universal testing machine with a 100 N load cell was used for the evaluating the mechanical properties of the neat PVA and BNNS/PVA nanocomposite films. The BNNS/PVA nanocomposite samples with different loadings were cut into standard dumbbell-shaped specimens with a 15 mm gauge length and 4 mm width. The thickness of each specimen (generally between 0.2-0.3 mm) was measured individually using a micrometer. The samples were then conditioned in a mechanical

testing laboratory for 1 day, in which the temperature and humidity were controlled at 23.0 ± 0.1 ℃ and 50 ± 5%, respectively. In total 4 specimens for each kind (3 types of BNNSs with different loadings and neat PVA) of sample were tested for averaging the data. The strain was determined from the cross-head displacement and the crosshead speed was set at 2 mm/min.

5.2.6 In situ Raman Deformation Studies

A Horiba LabRAM Evolution HR spectrometer equipped with 488 nm sapphire laser was used for the analysis of the BNNS/PVA nanocomposites. The in-situ Raman deformation analysis was conducted by inserting the BNNS-loaded PMMA beams into a four-point-bending rig fixed on the Raman microscope stage. A resistance strain gauge was used on the PMMA beam surface to monitor the strain applied on the PMMA substrate. The beams were deformed up to 0.4% strain in ~0.04% intervals and Raman spectra were collected and fitted at each strain level. The exposure time for each Raman scan was 20 s with a power output ~1.3 mW and a laser spot size of ~2 μm. The most prominent Raman band of hBN is the E_{2g} mode (denoted as the G band) which originates from in-plane atomic displacement and is equivalent to the G band of graphene [17].

5.3 Results and Discussion

5.3.1 Characterization of the individual BNNSs

Figure 5.3 shows the measured dimensions of three types of the LE-BNNSs in terms of the average length (*L*), thickness (*t*). As shown in Figure 5.3(a), the AFM scan of LE Sigma suggests it has a small average lateral sheet length, with a maximum BNNS length of ~500 nm. This is the result of the ~1 μm size of original Sigma crystals. The

height profile along the line scan in Figure 5.3(a) shows that the LE Sigma BNNSs have a range of thickness that is generally lower than 10 nm. In addition some ultrathin mono- and bilayer BNNSs even can be obtained. The sheet length and thickness data of Sigma BNNSs are summarized as histograms in Figure 5.3(d&g). The measured length of Sigma ranges between ~50 nm and ~500 nm with a mean value of around 200 nm. The thickness varies between 0-20 nm, with the majority ranging from ~1 nm to ~10 nm. The mean thickness of the Sigma BNNSs was found to be 5.4 nm (i.e. ~15 layers).

Significantly larger BNNSs can be seen in the AFM image of M3000 shown in Figure 5.3(b). The histogram in Figure 5.3(e) suggests that the length of M3000 BNNSs is in the range 2 μm to 5 μm and with a mean value of ~3.6 μm. The height profile of the line scan in Figure 5.3(b) and histogram in Figure 5.3(h) suggest that M3000 is much thicker than the Sigma BNNSs, and the thickness of some nanosheets reaches several hundred microns. The mean sheet thickness of M3000 was ~110 nm. In contrast for the sediment separated from dispersion after relatively low speed centrifugation, the AFM images and corresponding height profile in Figure 5.3(c) and Figure 5.4(a) demonstrate that the M6000 BNNSs are much thinner with smaller lateral dimensions than the M3000 BNNSs. Histograms in Figure 5.3(f&i) demonstrate that the length of the M6000 BNNSs is in the range 0.3-2 μm with a thickness between 1 nm and 6 nm. The mean length and thickness of M6000 were ~1.1 μm and ~5 nm, respectively. The accuracy of AFM results was further verified by SEM observation of the BNNSs. SEM images of the three types of BNNSs in Figures 5.4(b-e) show good consistency with the AFM observations in Figure 5.3.

The aspect ratio ($s = L/t$) of 2D materials is a key parameter for evaluating their reinforcement on nanocomposites [11]. A histogram showing the measured distribution of L/t for the Sigma BNNSs is shown in Figure 5.3(j) and the mean aspect

ratio of Sigma BNNSs was found to be ~63. Figure 5.3(k) shows the measured distribution of *L*/*t* for M3000 and the mean aspect ratio is ~55. A histogram of the distribution of *L*/*t* for the M6000 BNNSs is shown in Figure 5.3(l) and the mean aspect ratio of M6000 BNNSs was found to be ~350. Properties of three types of LE-BNNSs were summarized in Table 5.1.

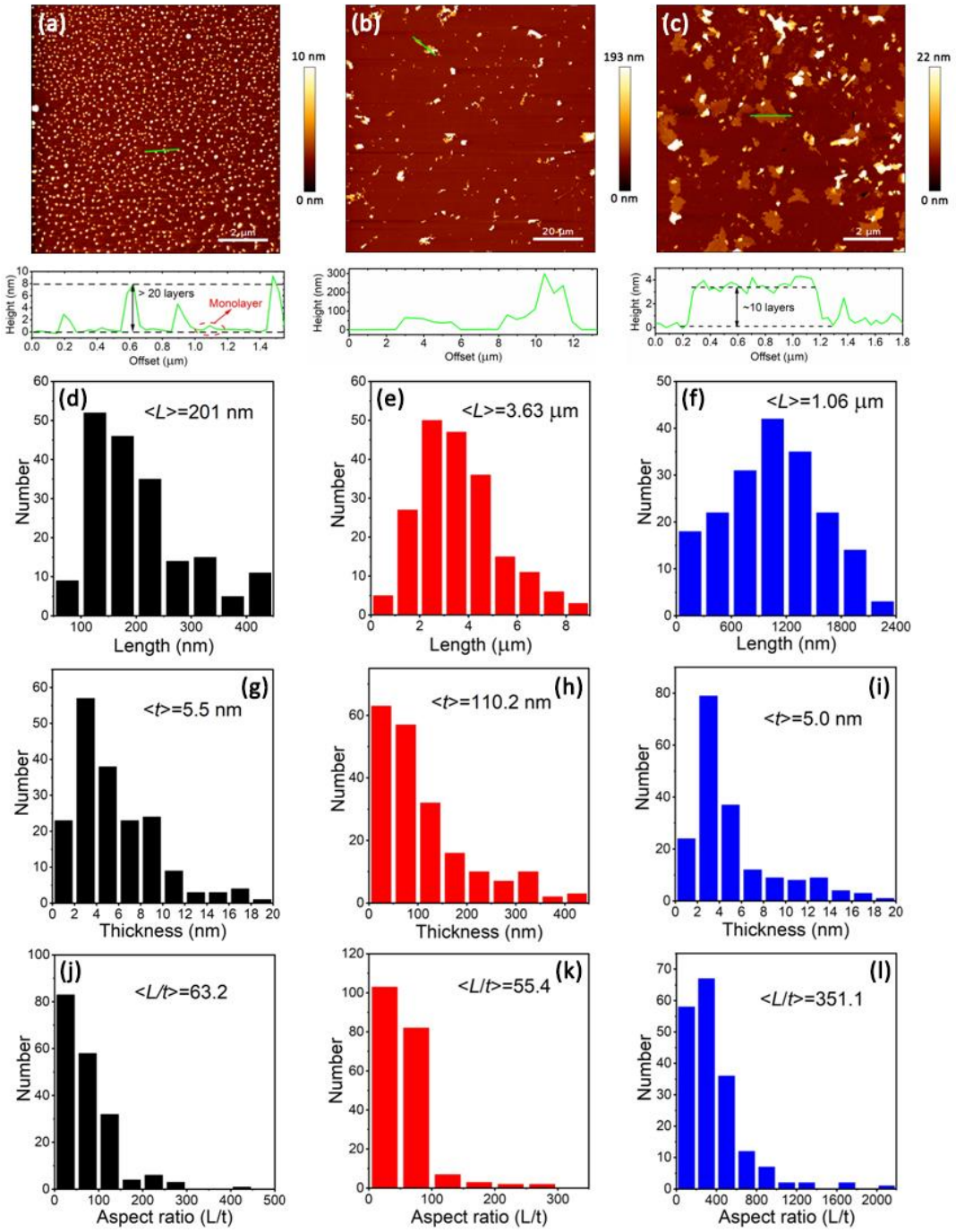

Figure 5.3 AFM images and height profiles of the line scans in the corresponding images (a-c), histograms of length (d-f), thickness (g-i), aspect ratio (j-l) of Sigma (left),

M3000 (middle) and M6000 (right) BNNSs. Some 200 examples of each type of BNNS were measured to generate the histograms.

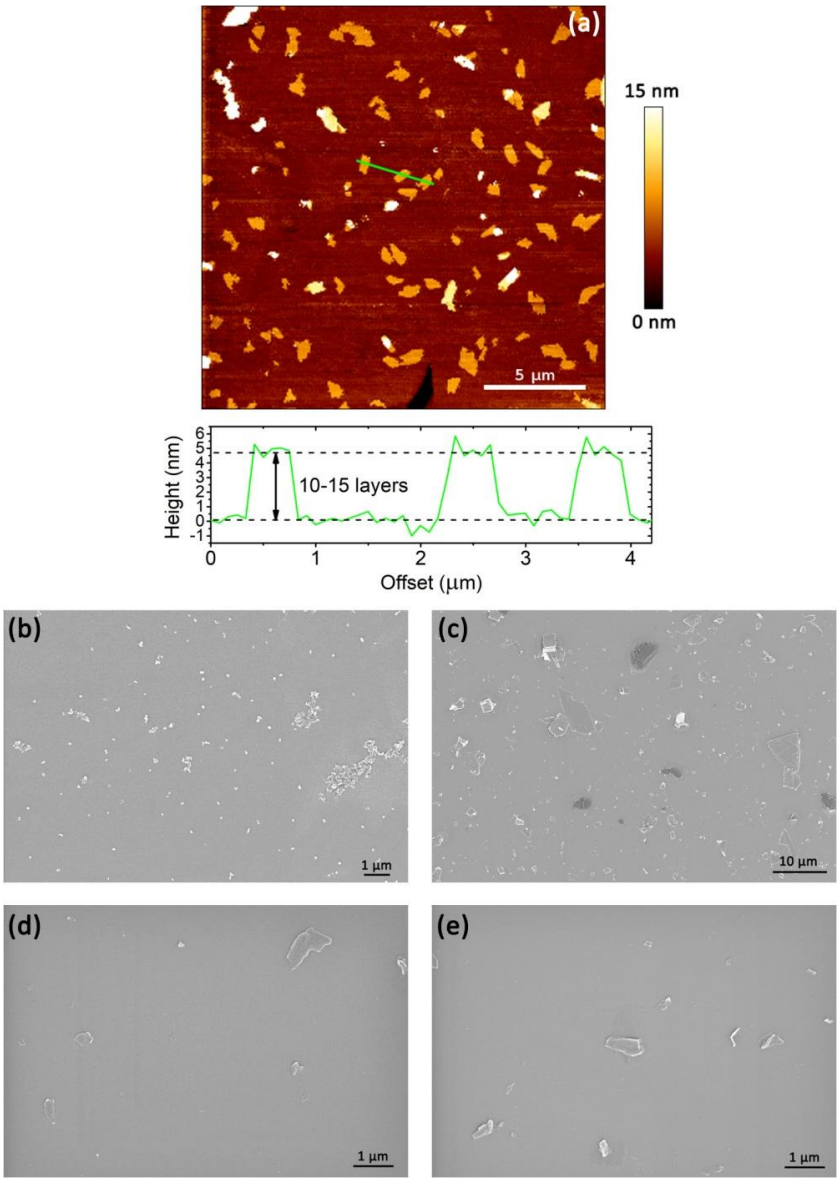

Figure 5.4 (a) AFM image of M6000 BNNSs and corresponding height profile of solid line; SEM images of Sigma (b), M3000 (c), M6000 (d, e).

Table 5.1 Properties of three types of LE-BNNSs

BNNSs	Sigma	M3000	M6000
<*L*> (μm)	0.20	3.63	1.06
<*t*> (nm)	5.5	110.2	5.0
<*L*/*t*>	63.2	55.4	351.1

XRD patterns of Sigma and M6000 are shown in Figure 5.5, compared to the XRD pattern of the original crystals. No obvious changes on diffraction peaks shape and position of both nanosheets were observed, indicating the preservation of the hBN 2D crystal structure after the liquid-phase exfoliation. The Raman spectra of Sigma and M6000 BNNSs are presented in Figure 5.5(c) and 5.5(d), respectively. It can be observed that both of the nanosheets show a simple spectrum with a well-defined G band at ~1366 cm^{-1}, characteristic of the intralayer hBN E_{2g} mode. No obvious shift of the G band position was observed following the liquid-phase exfoliation but the band intensity of both types of BNNS decreases, suggesting a smaller average thickness of the LE-BNNSs compared with that of the original crystals.

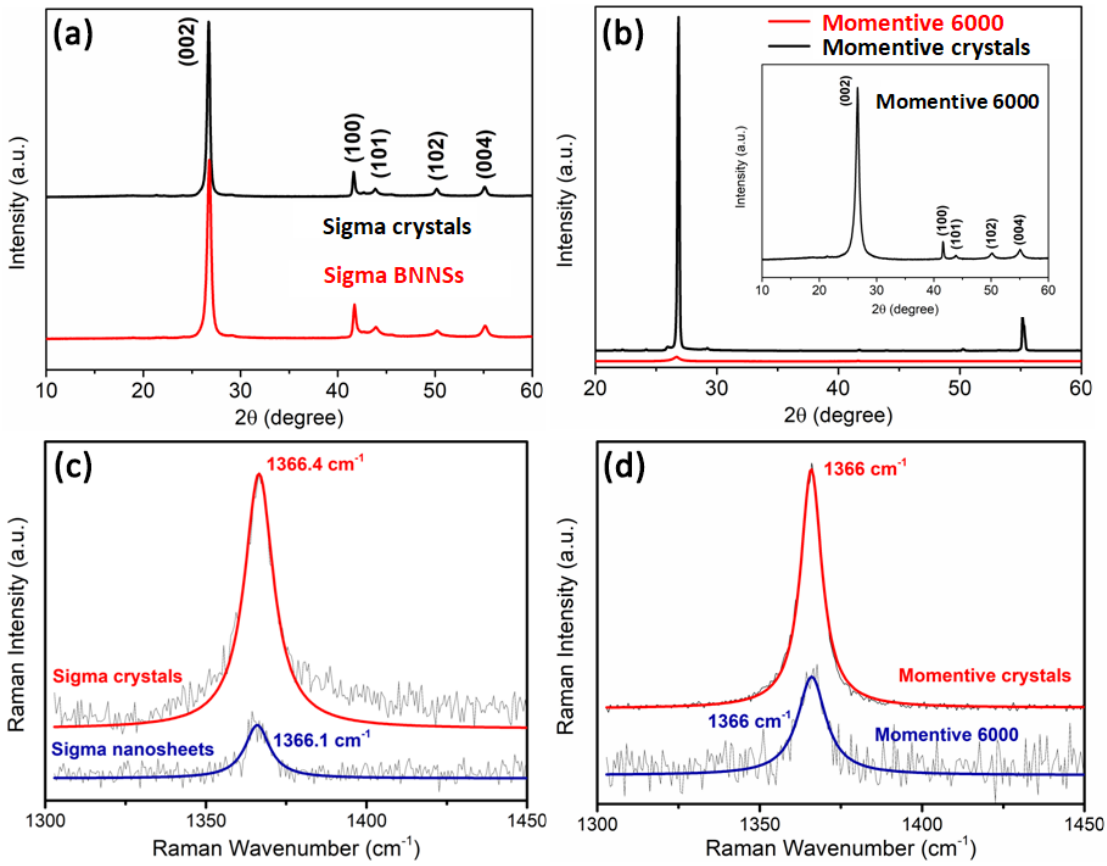

Figure 5.5 XRD patterns of (a) Sigma hBN crystals and BNNSs and (b) Momentive crystals and M6000 BNNSs. Raman spectra of (c) Sigma BN crystals and BNNSs and (d) Momentive crystals and M6000 BNNSs.

It is interesting to point out that, despite their differences in lateral dimensions and

thicknesses, the mean aspect ratios of Sigma and M3000 are similar. On the other hand, M6000 has a similar average thickness to the Sigma BNNSs, but 5 times the average length, and therefore aspect ratio, than Sigma. We have therefore produced a set of exfoliated BNNSs that will enable the effects of BNNS length, thickness and aspect ratio upon the reinforcement of a polymer matrix to be evaluated separately by comparing the mechanical properties of nanocomposites reinforced by similar loadings of the three different types of LE BNNSs.

5.3.2 Dispersion of the BNNTs in the Nanocomposites- Raman mapping

The dispersion of BNNSs in the PVA matrix was evaluated by mapping the intensity ratio of the BNNS Raman G band at ~1366 cm^{-1} relative to that of the PVA band at ~1447 cm^{-1} as shown in Figure 5.6. Compared with the Raman bands of the PVA matrix, the Raman spectra of 1 wt% BNNSs (M6000)/PVA spectra shown in Figure 5.6(a) showed a relatively-weak signal of BNNSs, which may be explained by the non-resonance Raman scattering of BNNSs due to their wide band gap [18]. Figure 5.6(b) shows the BNNS G band at 1366 cm^{-1} more clearly. It is surrounded by the Raman bands of the polymer matrix band that can be deconvoluted from the C-H & O-H bending modes of PVA. It is reported that the intensity of the G band of BNNSs increases with the number of layers [19], thus the much thicker M3000 BNNSs exhibit a stronger G band than M6000 and Sigma BNNSs, as shown in Figure 5.6(c).

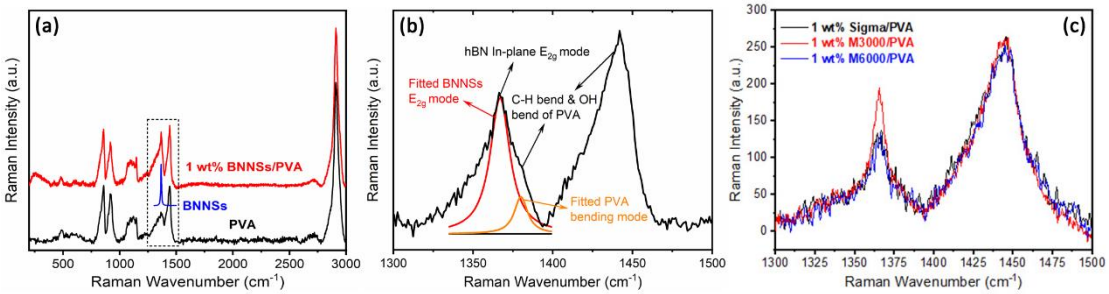

Figure 5.6 (a) Raman spectra of PVA and 1 wt% BNNSs (M6000)/PVA

nanocomposites. (b) Raman spectra of 1 wt% BNNSs/PVA nanocomposites in the range 1300 – 1500 cm^{-1}. (c) Raman spectra of 3 types of BNNSs/PVA at 1 wt% loading.

Optical micrographs of nanocomposites with 1wt% loadings of the three different types of BNNSs are shown in Figure 5.7 along with 100 × 100 μm^2 Raman maps of the 3 types of 1 wt% BNNS/PVA nanocomposite films. As can be seen in Figure 5.7(d), the Raman map of the 1 wt% Sigma/PVA is filled by homogeneous light blue areas, implying a relatively uniform dispersion of the Sigma BNNSs in the PVA matrix, although since the average sheet size for Sigma (200 nm) is smaller than the Raman laser spot size (~2 μm), only the overall level of dispersion can be evaluated. In contrast, intensity distribution in the Raman map of the 1 wt% M3000/PVA is not so homogeneous. The colour range in Figure 5.7(e) suggests that I_{1366}/I_{1447} varies between 0.4 and 1.2 and high intensity ratio red areas were observed throughout the map, showing the existence of thick BNNSs or agglomerates in the nanocomposites. The Raman map of M6000 in Figure 5.7(f) shows a relatively-homogeneous intensity distribution, suggesting it has a better dispersion than M3000 in the PVA. Nevertheless, a few red areas can still be seen in Figure 5.7(f), suggesting that some of the M6000 BNNSs also agglomerated at this relatively high loading.

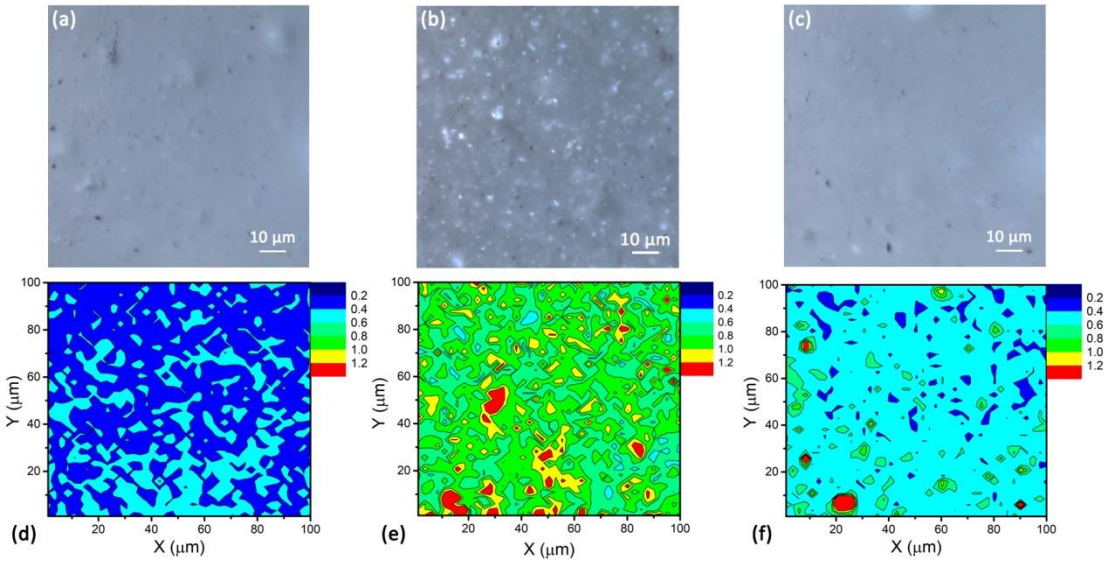

Figure 5.7 Optical micrograph and 100 μm×100 μm Raman mapping (I_{1366}/I_{1447}) intensity ratio of a 1 wt% (a&d) Sigma/PVA, (b&e) M3000/PVA, (c&f) M6000/PVA

nanocomposites film.

5.3.3 Mechanical Properties of the Nanocomposites

The stress-strain curve for the PVA and three types of BNNSs/PVA nanocomposite with 0.1 wt% loadings of the BNNSs are shown in Figure 5.8(a&b). It is clear to see that just 0.1 wt% addition of M6000 increases Young's modulus, yield and breaking strength of PVA matrix significantly. In contrast, the addition of the same loading of Sigma BNNSs produces very limited reinforcement (modulus increase) of the polymer. A decline of both the yield stress and breaking strength was also observed. The addition of 0.1 wt% of M3000 leads to a noticeable increase in the Young's modulus, but only limited enhancement of the yield stress and breaking strength of the PVA.

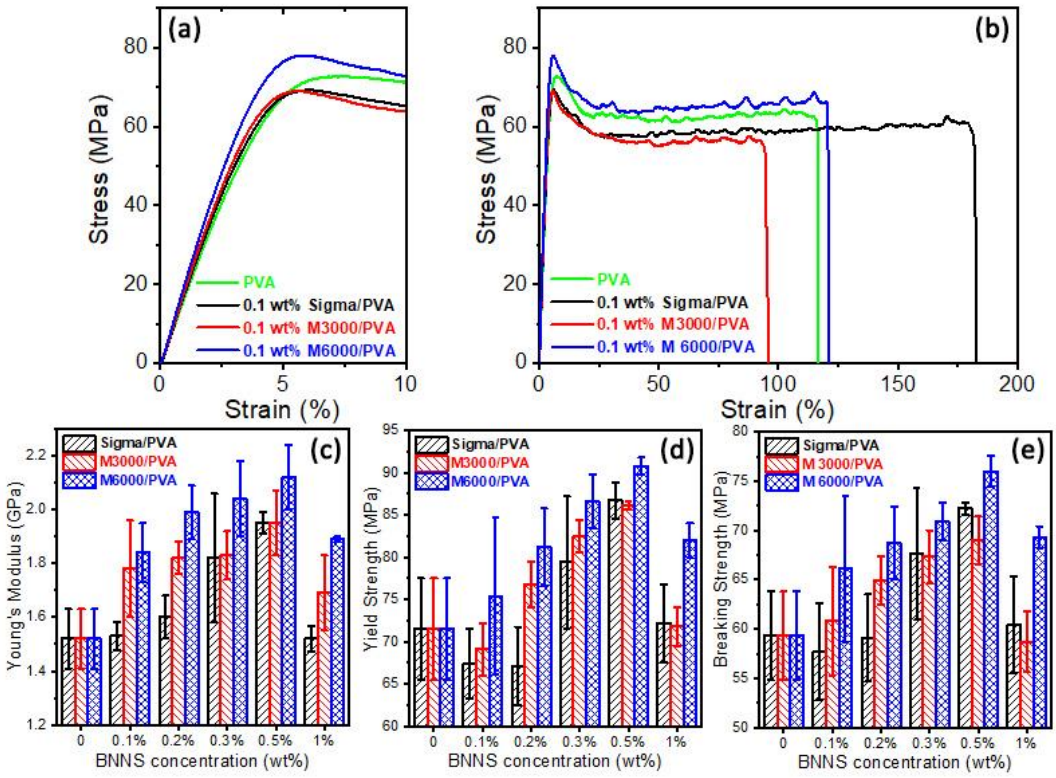

Figure 5.8 (a) Elastic region and (b) full range stress-strain curves for three types of BNNSs/PVA nanocomposites and PVA films at 0.1 wt% loading. (c) Young's modulus, (d) Yield stress and (e) Breaking strength of the three types of nanocomposite films for

different BNNS loadings.

DSC results in Table 5.2 have shown that the addition of 1 wt% of all three types of BNNSs does not change the melting temperature of crystals, T_m, or the crystallinity of the PVA and nanocomposites films significantly.

Table 5.2 DSC results of neat PVA and 3 kinds of 1 wt% BNNSs/PVA films.

Materials	T_m (℃)	$\triangle H_m$ (J/g)	f_c
Neat PVA -1	229.8±1.4	59.8±4.3	37.1%
1 wt/% Sigma/PVA	230.5±0.9	60.9±4.4	37.8%
1 wt/% M3000/PVA	231.0±1.2	56.8±5.2	35.2%
1 wt/% M6000/PVA	228.3±1.8	55.1±4.6	34.1%

The degree of crystallinity (f_c) was determined as the ratio between the heat of fusion (ΔH_m) of the film and the thermodynamic enthalpy of melting of a 100% crystalline PVA [20-21] (ΔH^0_m, the standard value of 162 J/g was used in this work [22]). It can be seen in Table 5.2 that the presence of all three kinds of BNNSs in PVA matrix did not induce obvious change on T_m and f_c, so it is unlikely that any of the variation in the mechanical properties of the nanocomposites are the result of changes in the PVA matrix.

5.3.4 Stress-induced Raman band shifts for 1 wt% BNNSs/PVA nanocomposites

The position of the BNNS G band has been shown to be strain sensitive [23]. It is therefore possible to use the well-established in-situ Raman deformation test to evaluate stress transfer to the BNNSs in the nanocomposites (see Chapter 3&4). Shifts

of the Raman G band in three kinds of 1 wt% BNNS/PVA nanocomposites were found during the deformation, as illustrated in Figure 5.9.

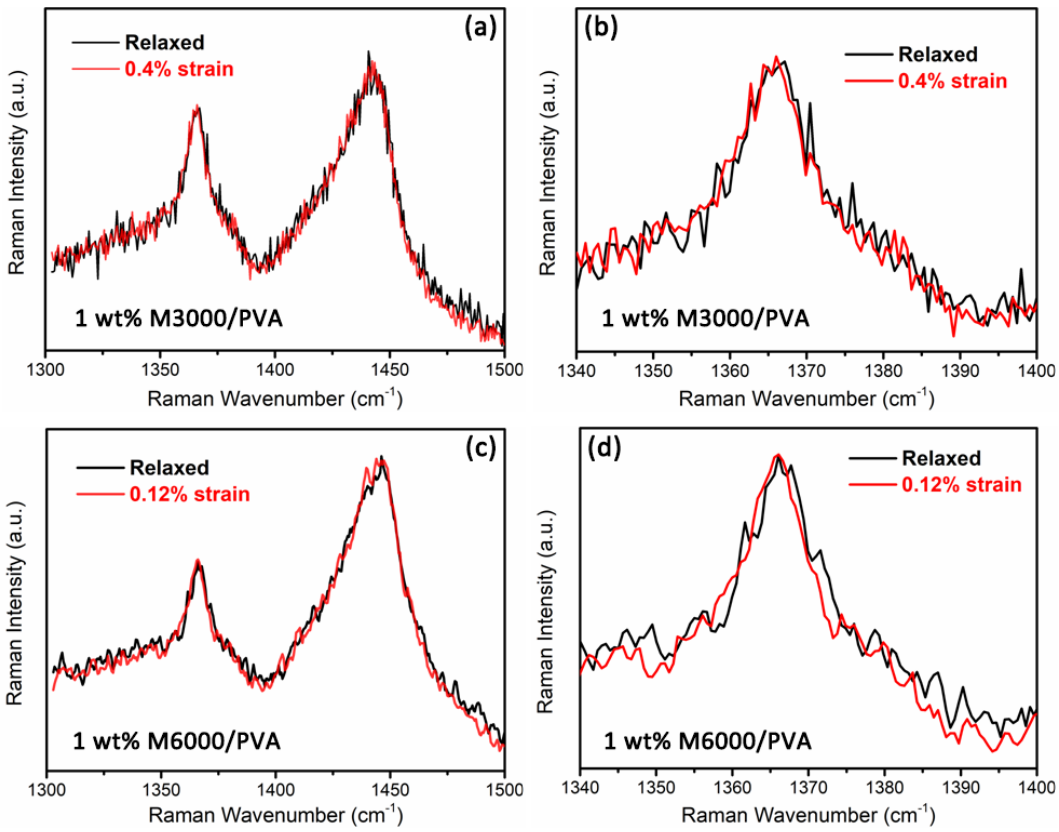

Figure 5.9 (a&b) Raman G band shift of BNNSs in 1 wt% Momentive 3000/PVA film at 0.4% strain. (c&d) Raman G band shift of BNNSs in 1 wt% Momentive 6000/PVA film at 0.12% strain.

Figure 5.10 presents the dependence of the peak position upon strain and it is seen that the smallest rate of band shift was detected for the 1 wt% Sigma/PVA nanocomposite sample, indicating poor stress transfer from polymer matrix to the BNNSs. This is consistent with tensile test result that Sigma shows very little reinforcement of the PVA at 1 wt% loading. Higher levels of the BNNS G band were found for the 1 wt% M3000/PVA (Figure 5.10(b)) and 1 wt% M6000/PVA (Figure 5.10(c)) samples which also show better reinforcement in the mechanical testing data (Figure 5.8). The band shift data in Figure 5.10 were fitted to straight lines for data points up to 0.3% strain. At higher strains it was found that no further band shift occurred which can be attributed to interfacial slippage between BNNSs and PVA at

low strain, indicating a limited level of adhesion between the BNNSs and PVA matrix, as had been reported in Chapter 4.

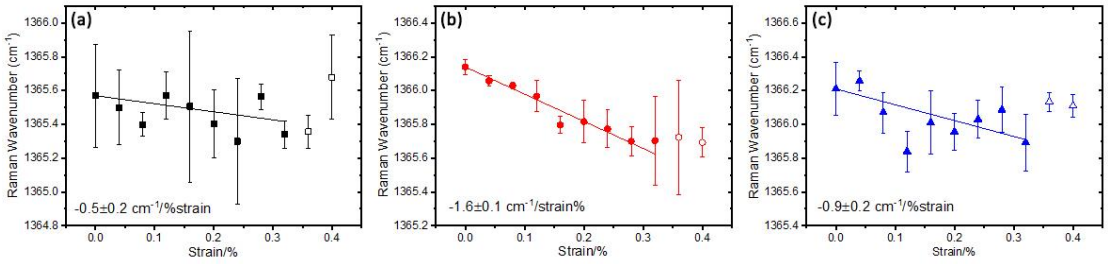

Figure 5.10 Raman G band shift of the BNNSs in (a) 1 wt% Sigma/PVA, (b) M3000 and (c) M6000/PVA nanocomposite films as a function of strain.

It should also be pointed out that well-defined Raman band shift were not found for all specimens and some examples of scattered band shift data for the three BNNSs are show in Figure 5.11. This scatter is probably because the Raman laser spot size of ~2 μm is of similar dimensions to the size of the BNNSs in the M3000 and M6000 nanocomposites which means that band shifts are essentially sometimes being measured on the edges of the BNNSs.

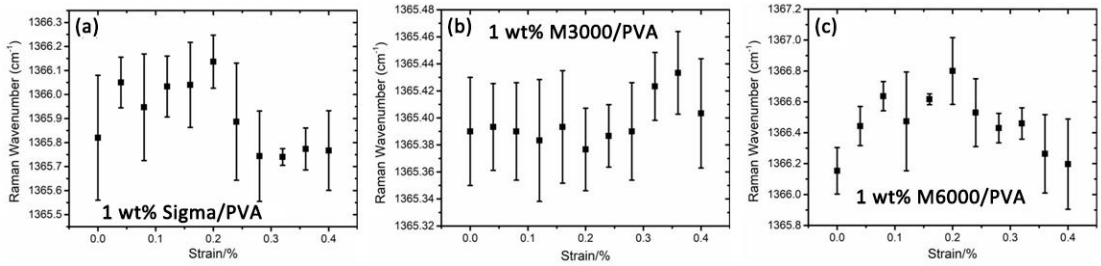

Figure 5.11 Raman G band shift of the BNNSs in (a) 1 wt% Sigma/PVA, (b) M3000 and (c) M6000/PVA nanocomposite films as a function of strain.

5.3.5 Modelling of the Mechanical Properties of the Nanocomposites

It has been demonstrated previously that the Young's modulus of a nanocomposite, E_c,

can be analysed using the modified rule of mixtures [11, 24] (see Chapter 2):

$$E_c = E_{eff} V_{BNNSs} + E_m(1 - V_{BNNSs}) \qquad (5.1)$$

where E_{eff} and E_m are the effective Young's moduli of the BNNSs and the Young's modulus of PVA, respectively. V_{BNNSs} is the volume fraction of BNNSs in the nanocomposites.

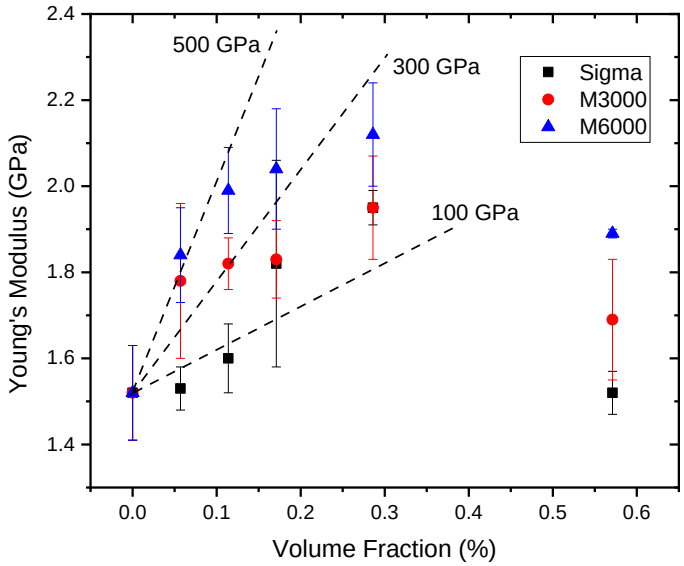

Figure 5.12 Dependence of the Young's modulus of the BNNS/PVA nanocomposites, E_c, upon the volume fraction of the BNNSs, V_{BNNSs}. The dashed lines correspond to the different stated values of E_{eff} in Equation (5.1).

The original formulations of the nanocomposites were prepared in terms of the weight fraction of BNNSs and it is possible to do the conversion to V_f using a density of hBN of 2.27 g/cm^3 [25] and 1.3 g/cm^3 for PVA [26]. The BNNS loading may be converted from mass fraction W_{BNNSs} (wt%) to volume fraction V_{BNNSs} (vol%) using:

$$V_{BNNSs} = \frac{W_{BNNSs}\rho_{PVA}}{W_{BNNSs}\rho_{PVA} + (1 - W_{BNNSs})\rho_{BNNSs}} \qquad (5.2)$$

where ρ_{BNNS} and ρ_{PVA} represent the densities of BNNTs and PVA.

Figure 5.12 shows the dependence of the Young's modulus of the nanocomposites upon volume fraction of the three different types of BNNSs using the data from

Figure 5.8(c) and listed in Table 5.3. The dashed lines are fits to Equation (5.1) for different values of the effective Young's modulus, E_{eff} (It should be noted that these lines are just general fits for the Young's modulus at low BNNSs concentrations (0 vol%-0.115 vol%), more accurate fits could be achieved by supplementing more concentration gradients at low BNNSs volume fraction, such as 0.01 vol%, 0.02 vol% etc.). It can be seen that the values of E_c initially increase with increasing volume fraction but then fall away above a volume fraction of 0.4%, due probably to agglomeration occurring at higher loadings (Figure 5.7). Overall it can be seen that the highest level of reinforcement is found for the M6000 BNNSs and the lowest level was for the Sigma BNNSs. At low volume fractions the data for the Sigma BNNSs fall close to the line for E_{eff} = 100 GPa whereas the data points for the M6000 BNNSs are close to the line for E_{eff} = 500 GPa. The Sigma and M6000 BNNSs are of similar thickness (~5 nm) but the M6000 BNNSs have larger lateral dimensions and a higher aspect ratio, $s = L/t$ (Figure 5.3).

Table 5.3 Mechanical properties of three types of nanocomposite films.

Materials	Young's modulus (GPa)	Yield stress (MPa)	Breaking strength (MPa)	Volume Fraction (%)
Neat PVA	1.52 ±0.11	71.5 ±6.0	59.3 ±4.5	0
0.1 wt% Sigma/PVA	1.53 ±0.05	67.4 ±4.1	57.7 ±4.9	0.057
0.1 wt% M3000/PVA	1.78 ±0.18	69.1 ±3.1	60.8 ±5.5	0.057
0.1 wt% M6000/PVA	1.84 ±0.11	75.4 ±9.3	66.1 ±7.4	0.057
0.2 wt% Sigma/PVA	1.60 ±0.08	67.1 ±4.6	59.1 ±4.4	0.115
0.2 wt% M3000/PVA	1.82 ±0.06	76.8 ±2.7	64.9 ±2.4	0.115
0.2 wt% M6000/PVA	1.99 ±0.10	81.2 ±4.6	68.7 ±3.7	0.115
0.3 wt% Sigma/PVA	1.82 ±0.24	79.4 ±7.8	67.6 ±6.7	0.173
0.3 wt% M3000/PVA	1.83 ±0.09	82.5 ±1.9	67.3 ±2.7	0.173
0.3 wt% M6000/PVA	2.04 ±0.14	86.6 ±3.2	70.9 ±1.9	0.173

0.5 wt% Sigma/PVA	1.95 ±0.04	86.7 ±2.2	72.2 ±0.6	0.286
0.5 wt% M3000/PVA	1.95 ±0.12	86.1 ±0.5	69.0 ±2.4	0.286
0.5 wt% M6000/PVA	2.12 ±0.12	90.8 ±1.0	76.0 ±1.6	0.286
1 wt% Sigma/PVA	1.52 ±0.05	72.2 ±4.6	60.4 ±4.9	0.575
1 wt% M3000/PVA	1.69 ±0.14	71.8 ±2.3	58.7 ±3.1	0.575
1 wt% M6000/PVA	1.89 ±0.01	82.0 ±2.0	69.3 ±1.1	0.575

The effective modulus of the BNNSs in the nanocomposites is given by [11]

$$E_{\text{eff}}=\eta_{\text{l}}\eta_{\text{o}}E_{\text{BNNSs}} \qquad (5.3)$$

where E_{BNNSs} is the Young's modulus of hBN nanosheets. The Krenchel orientation factor η_{o} enables the effect of filler orientation upon the reinforcement efficiency to be determined and it ranges from 8/15 for randomly oriented to 1 for well-aligned flakes [27-28]. Since the specimens for the mechanical property measurements were prepared by casting a thin film, it is likely that the BNNSs are mainly aligned in-plane and so η_{o} can be taken as being close to unity. The length factor, η_{l}, which has a value of between 0 and 1, reflects the dependence of reinforcement on flake length and increases with the flake aspect ratio *s* [29]. The length factor η_{l} is given by [13]

$$\eta_{\text{l}} = 1 - \frac{\tanh(ns/2)}{ns/2} \qquad (5.4)$$

where *s* is the aspect ratio and *n* is given as (see Chapter 2)

$$n=\sqrt{\frac{2G_{\text{m}}}{E_{\text{f}}}\left(\frac{t}{T}\right)} \qquad (5.5)$$

G_{m} is the shear modulus of the polymer, *l* is the length of BNNS along with strain direction, and *t* and *T* are the thickness of the BNNS and the representative volume. In practice *n* can be considered to be a fitting parameter and was shown in Chapter 4 to be of the order of 0.017 for the deformation of a single hBN sheet on a polymer substrate. Another issue to consider is that the Young's modulus of the BNNSs may depend upon their thickness (i.e. number of layers) due to easy shear between the

individual layers. Chapter 4 has demonstrated that, unlike multi-layer graphene, there is relatively good interlayer stress transfer within BNNSs, so this effect can be neglected in the present study.

Any differences in the value of E_{eff} for the three different BNNSs will therefore be controlled principally by the value of η_l through Equation (5.4). The Sigma material has an average aspect ratio of s = 63 (Figure 5.3(j)) so using a value of n = 0.017, a value of η_l~0.1 is obtained from Equation (5.4) for this material. In contrast the M6000 material has an average aspect ratio of s = 351 (Figure 5.3(i)) which leads to a value of η_l~0.65. Using a value of E_{BNNSs} of 800 GPa (0.8 TPa) for hBN [30], then Equation (5.3) predicts value of E_{eff} ~80 GPa for the Sigma BNNSs and one of ~520 GPa for the M6000 BNNSs. These value of E_{eff} are very similar to those used to fit the data for the nanocomposites at low volume fractions in Figure 5.12. Hence it implies that the values of the effective Young's modulus of the BNNSs in the nanocomposites are controlled by their aspect ratios, with M6000 being the best material having the highest aspect ratio. Sheets of M3000 have larger lateral dimensions than M6000 (Figure 5.3) but are thicker and have an inferior aspect ratio and so do not give such good reinforcement (Figure 5.12). Sheets of the Sigma material have similar thickness to those of M6000 but smaller lateral dimensions which again leads to a lower aspect ratio and inferior reinforcement (Figure 5.12). It should also be pointed out that Figure 5.12 also shows that the level of reinforcement decreases with increasing volume fraction showing that the BNNSs are prone to agglomeration leading to a poorer dispersion. Hence future studies will be needed to develop techniques to improve the distribution of the BNNSs in the nanocomposites if better levels of reinforcement are needed.

It is possible to also estimate the effective Young's modulus of the BNNSs independently from the stress-induced Raman band shifts shown in Figure 5.10.

Unfortunately this could only be done as a result of the relatively weak Raman scattering from hBN for the highest 1 wt% loading of BNNSs (V_f~0.6%), for which there is agglomeration of the BNNSs. The effective modulus of the reinforcement is given by [31]

$$E_{\text{eff}} = \frac{\mathrm{d}\omega(E_{2g})}{\mathrm{d}\varepsilon} \cdot \frac{E_{\text{BNNSs}}}{\mathrm{d}\omega\left(E_{2g}\right)/\mathrm{d}\varepsilon(\text{ref})} \qquad (5.6)$$

where $\mathrm{d}\omega(E_{2g})/\mathrm{d}\varepsilon$ is the shift rate of the hBN Raman E_{2g} band as the function of strain. The reference band shift rate value, $\mathrm{d}\omega(E_{2g})/\mathrm{d}\varepsilon(\text{ref})$ found in Chapter 4 for the deformation of isolated monolayer sheets can be taken as -11 cm^{-1}/% although there is a small decrease as the sheet thickness increases. If the Young's modulus of a monolayer hBN sheet, E_{BNNSs} is taken as 800 GPa then the value of $\mathrm{d}\omega(E_{2g})/\mathrm{d}\varepsilon$ of -0.9 $\pm$ 0.2 cm^{-1}/% strain measured for M6000 in Figure 5 leads to an effective modulus of E_{eff} of ~100 GPa. This is consistent with the value expected for the agglomerated BNNSs in Figure 5.12 at 0.6% volume fraction.

5.4 Conclusions

It has been found that the addition of hBN nanosheets (BNNSs) to poly(vinyl alcohol) can lead to an increase in the Young's modulus, yield strength and breaking strength of the polymer. The level of reinforcement is found to increase with an increasing loading of the BNNSs but the performance decrease above about 0.5 wt% of the filler as the result of agglomeration effects. The use of BNNSs with different geometries has demonstrated that the best levels of reinforcement are found with the BNNSs with the highest aspect ratio which are shown to have an effective Young's modulus in the nanocomposites in excess of 500 GPa at low loadings. It is suggested that future studies should concentrate upon chemical functionalization of the BNNSs to strengthen the interface between the filler and polymer matrix and methods to improve the dispersion of the BNNSs in the polymer matrix.

References

1. Cai, Q.; Scullion, D.; Gan, W.; Falin, A.; Zhang, S.; Watanabe, K.; Taniguchi, T.; Chen, Y.; Santos, E. J. G.; Li, L. H., High thermal conductivity of high-quality monolayer boron nitride and its thermal expansion. *Sci Adv* **2019,** *5* (6), eaav0129.
2. Lee, C.; Wei, X.; Kysar, J. W.; Hone, J., Measurement of the elastic properties and intrinsic strength of monolayer graphene. *Science* **2008,** *321* (5887), 385-388.
3. Meng, W.; Huang, Y.; Fu, Y.; Wang, Z.; Zhi, C., Polymer composites of boron nitride nanotubes and nanosheets. *J. Mater. Chem. C* **2014,** *2* (47), 10049-10061.
4. Yin, J.; Li, J.; Hang, Y.; Yu, J.; Tai, G.; Li, X.; Zhang, Z.; Guo, W., Boron Nitride Nanostructures: Fabrication, Functionalization and Applications. *Small* **2016,** *12* (22), 2942-68.
5. Zhi, C.; Bando, Y.; Tang, C.; Kuwahara, H.; Golberg, D., Large-Scale Fabrication of Boron Nitride Nanosheets and Their Utilization in Polymeric Composites with Improved Thermal and Mechanical Properties. *Adv. Mater.* **2009,** *21* (28), 2889-2893.
6. Khan, U.; May, P.; O'Neill, A.; Bell, A. P.; Boussac, E.; Martin, A.; Semple, J.; Coleman, J. N., Polymer reinforcement using liquid-exfoliated boron nitride nanosheets. *Nanoscale* **2013,** *5* (2), 581-7.
7. Wang, X.; Zhi, C.; Li, L.; Zeng, H.; Li, C.; Mitome, M.; Golberg, D.; Bando, Y., "Chemical Blowing" of Thin-Walled Bubbles: High-Throughput Fabrication of Large-Area, Few-Layered BN and Cx-BN Nanosheets. *Adv. Mater.* **2011,** *23* (35), 4072-4076.
8. Lee, D.; Lee, B.; Park, K. H.; Ryu, H. J.; Jeon, S.; Hong, S. H., Scalable exfoliation process for highly soluble boron nitride nanoplatelets by hydroxide-assisted ball milling. *Nano Lett.* **2015,** *15* (2), 1238-1244.
9. Jan, R.; May, P.; Bell, A. P.; Habib, A.; Khan, U.; Coleman, J. N., Enhancing the mechanical properties of BN nanosheet-polymer composites by uniaxial drawing. *Nanoscale* **2014,** *6* (9), 4889-95.
10. Kelly, A.; Macmillan, N., Strong Solids, Clarendon. Oxford New York: **1986**.
11. Papageorgiou, D. G.; Li, Z.; Liu, M.; Kinloch, I. A.; Young, R. J., Mechanisms of mechanical reinforcement by graphene and carbon nanotubes in polymer nanocomposites. *Nanoscale* **2020,** *12* (4), 2228-2267.
12. Gong, L.; Kinloch, I. A.; Young, R. J.; Riaz, I.; Jalil, R.; Novoselov, K. S., Interfacial stress transfer in a graphene monolayer nanocomposite. *Adv. Mater.* **2010,** *22* (24), 2694-2697.
13. Young, R. J.; Liu, M.; Kinloch, I. A.; Li, S.; Zhao, X.; Vallés, C.; Papageorgiou, D. G., The mechanics of reinforcement of polymers by graphene nanoplatelets. *Composites Science and Technology* **2018,** *154*, 110-116.
14. Li, Z.; Young, R. J.; Backes, C.; Zhao, W.; Zhang, X.; Zhukov, A. A.; Tillotson, E.; Conlan, A. P.; Ding, F.; Haigh, S. J.; Novoselov, K. S.; Coleman, J. N.,

Mechanisms of Liquid-Phase Exfoliation for the Production of Graphene. *ACS Nano* **2020,** *14* (9), 10976-10985.

15. Zhou, K. G.; Mao, N. N.; Wang, H. X.; Peng, Y.; Zhang, H. L., A mixed-solvent strategy for efficient exfoliation of inorganic graphene analogues. *Angewandte Chemie International Edition* **2011,** *50* (46), 10839-10842.
16. Chen, J.; Huang, X.; Zhu, Y.; Jiang, P., Cellulose Nanofiber Supported 3D Interconnected BN Nanosheets for Epoxy Nanocomposites with Ultrahigh Thermal Management Capability. *Adv. Funct. Mater.* **2017,** *27* (5), 1604754.
17. Ferrari, A. C.; Meyer, J.; Scardaci, V.; Casiraghi, C.; Lazzeri, M.; Mauri, F.; Piscanec, S.; Jiang, D.; Novoselov, K.; Roth, S., Raman spectrum of graphene and graphene layers. *Physical Review Letters* **2006,** *97* (18), 187401.
18. Wang, W.; Li, Z.; Prestat, E.; Hashimoto, T.; Guan, J.; Kim, K. S.; Kingston, C. T.; Simard, B.; Young, R. J., Reinforcement of Polymer-Based Nanocomposites by Thermally Conductive and Electrically Insulating Boron Nitride Nanotubes. *ACS Applied Nano Materials* **2019,** *3* (1), 364-374.
19. Gorbachev, R. V.; Riaz, I.; Nair, R. R.; Jalil, R.; Britnell, L.; Belle, B. D.; Hill, E. W.; Novoselov, K. S.; Watanabe, K.; Taniguchi, T.; Geim, A. K.; Blake, P., Hunting for monolayer boron nitride: optical and Raman signatures. *Small* **2011,** *7* (4), 465-8.
20. Willcox, P. J.; Howie Jr, D. W.; Schmidt-Rohr, K.; Hoagland, D. A.; Gido, S. P.; Pudjijanto, S.; Kleiner, L. W.; Venkatraman, S., Microstructure of poly (vinyl alcohol) hydrogels produced by freeze/thaw cycling. *J. Polym. Sci., Part B: Polym. Phys.* **1999,** *37* (24), 3438-3454.
21. Ricciardi, R.; Auriemma, F.; Gaillet, C.; De Rosa, C.; Laupr être, F., Investigation of the crystallinity of freeze/thaw poly (vinyl alcohol) hydrogels by different techniques. *Macromolecules* **2004,** *37* (25), 9510-9516.
22. Blaine, R. L., Thermal applications note.
23. Androulidakis, C.; Koukaras, E. N.; Poss, M.; Papagelis, K.; Galiotis, C.; Tawfick, S., Strained hexagonal boron nitride: Phonon shift and Gr üneisen parameter. *Physical Review B* **2018,** *97* (24).
24. Young, R. J.; Lovell, P. A., *Introduction to polymers*. CRC Press: Boca Baton, **2011**.
25. Lipp, A.; Schwetz, K. A.; Hunold, K., Hexagonal Boron Nitride: Fabrication, Properties and Applications. *Journal of the European Ceramic Society* **1989,** *5*, 3-9.
26. Liang, J.; Huang, Y.; Zhang, L.; Wang, Y.; Ma, Y.; Guo, T.; Chen, Y., Molecular-level dispersion of graphene into poly (vinyl alcohol) and effective reinforcement of their nanocomposites. *Adv. Funct. Mater.* **2009,** *19* (14), 2297-2302.
27. Krenchel, H., *Fibre Reinforcement*. Akademisk Forlag: Copenhagen, **1964**.
28. Li, Z.; Young, R. J.; Wilson, N. R.; Kinloch, I. A.; Vall és, C.; Li, Z., Effect of the orientation of graphene-based nanoplatelets upon the Young's modulus of

nanocomposites. *Composites Science and Technology* **2016,** *123,* 125-133.

29. Chou, T.-W., *Microstructural Design of Fiber Composites*. Cambridge University Press: Cambridge, **1992**.
30. Falin, A.; Cai, Q.; Santos, E. J. G.; Scullion, D.; Qian, D.; Zhang, R.; Yang, Z.; Huang, S.; Watanabe, K.; Taniguchi, T.; Barnett, M. R.; Chen, Y.; Ruoff, R. S.; Li, L. H., Mechanical properties of atomically thin boron nitride and the role of interlayer interactions. *Nat Commun* **2017,** *8,* 15815.
31. Wang, F.; Li, S.; Bissett, M. A.; Kinloch, I. A.; Li, Z.; Young, R. J., Strain engineering in monolayer WS_2 and WS_2 nanocomposites. *2D Materials* **2020,** *7* (4), 045022.

Chapter 6 Reinforcement of Polymer-based Nanocomposites by Boron Nitride Nanotubes‡

6.1 Introduction

Benefitting from a similar crystal structure with their graphitic analogue, as outlined in Chapter 1, one-dimensional (1D) boron nitride nanotubes (BNNTs) inherit the extraordinary mechanical properties and thermal conductivities of carbon nanotubes (CNTs) [1]. A recent experimental evaluation from Zhou *et al*. [2] reported an elastic modulus of over 900 GPa for MW-BNNTs that decreased gradually to a plateau of~660 GPa (over three times that of steel) on irradiation due to the formation of equilibrium defective surface cavities. This endows thermally conductive and electrically insulating BNNTs with great potential to be used as specialty reinforcements for nanocomposites that require both electrical insulation and good thermal stability. However, it is still necessary to find a more effective and feasible method to provide evaluation of the microstructure of BNNTs inside nanocomposites, that is both instructive and beneficial for optimizing mechanical and thermal enhancement.

In this present chapter, a straightforward and non-destructive method for appraising the dispersion and interfacial stress transfer of BNNTs in polymer nanocomposites using non-resonance Raman spectroscopy is employed in a similar way to how it was used in Chapters 4&5. Various loadings of multi-walled BNNTs are incorporated into poly(vinyl alcohol) (PVA) and prepare nanocomposites films. Although the activation of resonant Raman scattering (significant signal enhancement [3]) in BNNTs is

‡This chapter is based on a paper, “Reinforcement of Polymer-Based Nanocomposites by Thermally Conductive and Electrically Insulating Boron Nitride Nanotubes”, ACS Applied Nano Materials, 2019, 3(1): 364-374.

difficult due to its wide and chirality-independent band gap (Figure 6.1), it is still possible to excite the electrons of BNNTs to a virtual state and obtain non-resonant Raman scattering of BNNTs in the polymer matrix. The nanotube dispersion in the nanocomposites is studied by Raman mapping tests. Interfacial stress transfer from the PVA matrix to the BNNTs is investigated from the stress-induced Raman band shifts of the BNNTs in the matrix and this behaviour is correlated with the mechanical properties of the nanocomposites. The effect of surface functionalization of BNNTs [4-8] upon both their dispersion and stress transfer in the nanocomposites is also discussed.

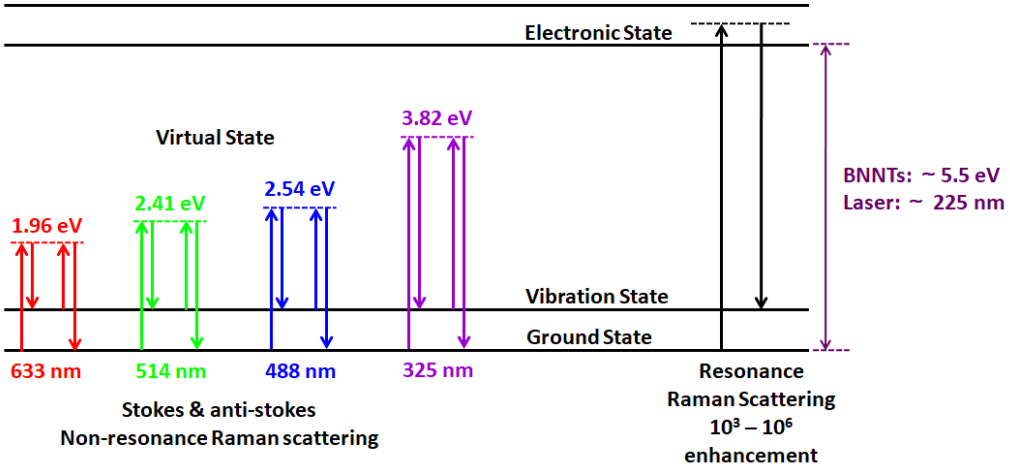

Figure 6.1 Schematic of resonance Raman scattering and non-resonance Raman scattering of boron nitride nanotubes.

6.2 Experimental

6.2.1 Materials

The multi-walled(MW) boron nitride nanotubes (BNNTs) were synthesized using a hydrogen-catalyzed induction plasma processing method [9] and purified before use [10] (see Chapter 1). These purified BNNTs have relatively small diameters and a variable number of walls. The PVA (MW ~89000-98000, 99+% hydrolyzed) was purchased from Sigma Aldrich and used as received. The hydrogen peroxide (H_2O_2,

30 wt% solution in water) was used as received for the BNNTs functionalization.

6.2.2 Functionalization of the BNNTs

The hydroxyl functionalization of the BNNTs was carried out following the previous report by Zhi *et al.* [5]. Around 20 mg of BNNTs was dispersed into 20 ml H_2O_2 (30 wt% aqueous solution) by magnetic stirring for 12 h and low-power bath sonication for 4h. The dispersion was then transferred into a 100 ml autoclave within a Teflon liner. After being sealed, the autoclave was put into a temperature-controlled oven and kept at 120 ℃ for 24 h. After natural cooling, the BNNTs were filtrated and washed several times with distilled water, followed by drying overnight in a vacuum oven at 40 ℃. The OH-BNNTs were then used to prepare nanocomposites.

6.2.3 Preparation of BNNTs/PVA Nanocomposites

To prepare the BNNTs/PVA nanocomposites, PVA powder was added into distilled water at room temperature (RT) and the mass ratio of PVA to DW was 14 wt%. The appropriate amount of BNNTs was added to PVA/DW solution to give 0.1 to ~ 1 wt% nanotubes loadings relative to the PVA amount. The solution was mixed using magnetic stirring, heated to 90 ℃ in a water bath and held for 3 hours. This was followed by extra overnight stirring at RT to achieve sufficient mixing. The as-prepared BNNTs/PVA suspension was ultrasonicated using a sonication probe (Q700 sonicator, QSonica) with maximum power output of 700 W. The probe was used for 2 min and left to rest for 2 min before the power was applied again. The total power time was 1 h. The amplitude used was 50%, which is a relatively low value to avoid damage to both the BNNTs and PVA polymer chains. This resulting nanocomposite aqueous solution was then used to manufacture the nanocomposite

specimens.

The BNNTs/PVA nanocomposite films were prepared by casting the nanocomposite aqueous solution on different substrates. For mechanical testing, the solution was casted onto glass petri dishes. For the Raman deformation testing, the solution was casted onto PMMA beams. In both cases, the nanocomposites films were allowed to dry for at least 72 hours, to ensure residual moisture had evaporated fully. The thin films for TEM characterization were prepared by direct spin casting the nanocomposite aqueous solution onto copper TEM grids.

6.2.4 Characterization of the BNNTs and OH-BNNTs

The purity of the BNNTs was investigated using: a TGA/DSC 1 system (Mettler-Toledo), samples were heated from room temperature to 800 °C in both nitrogen and air atmosphere; a Horiba LabRAM Evolution HR Raman spectrometer with a Coherent 488 nm sapphire laser and a PANalytical X'Pert Pro X-ray diffractometer (1.54A wavelength). The morphology and structure of BNNTs were observed using an EVO 50 SEM (Zeiss) and a Talos F200X high resolution TEM system (FEI). The functionalization of BNNTs was studied by X-ray photoelectron spectroscopy (XPS) using a Kratos Axis Ultra X-ray photoelectron spectrometer; Fourier transform infrared spectra (FTIR) using a Nicolet 5700 spectrometer (Thermo Fisher Scientific), in the transmission mode (3 scans for each run). Scanning transmission electron microscopy annular dark field (STEM-ADF) and energy loss spectroscopy (EELS) mapping were performed using an aberration corrected Titan G2 80-200 kV S/TEM system (FEI). The convergence and EELS collection angle were 21 and 48 mrad, respectively. TEMs were operating at an acceleration voltage of 200 kV. Contact angle measurements were undertaken using a Krüss Drop shape Analyzer DSA100.

6.2.5 Mechanical Testing

The tensile properties of the neat PVA and BNNT/PVA nanocomposites were evaluated using an Instron-1122 universal testing machine with a 100 N load cell. All the film samples were cut into dumbbell-shaped specimens with a 15 mm gauge length, 4 mm width and a thickness of around 0.1 mm measured using a micrometer. The samples were allowed to condition in an environmentally-controlled mechanical testing laboratory for 24 h, in which the temperature is kept at 23.0 ± 0.1 ℃ and humidity controlled at 50 ± 5%. The crosshead speed was set at 2 mm/min and 4 specimens of the nanocomposites for each level of BNNTs loading were tested. The specimen strain was determined from the cross-head displacement.

6.2.6 Raman Spectroscopy

All of the Raman measurements were conducted using a Horiba LabRAM Evolution HR Raman spectrometer equipped with a Kimmon Koha 325 nm He-Cd NUV laser, a Coherent 488 nm sapphire laser and a CVI Melles Griot 633 nm He-Ne laser. The 488 nm sapphire laser, with ~1.4 mW output power and 30 s exposure time, was found to be the most suitable for the Raman characterization studies.

For the Raman mapping, several 100 μm × 100 μm areas of different film samples were mapped in 2 μm step intervals.

For in-situ Raman deformation analysis of the nanocomposite films, the PMMA beams covered with BNNTs/PVA nanocomposite films were inserted into a four-point-bending rig located on the Raman microscope stage. A resistance strain gauge was attached to the PMMA specimen surface using cyanoacrylate adhesive to monitor the strain applied to the beam. The beams were deformed up to 0.4 % strain

in ~0.04% intervals and the Raman spectra were collected at each strain level. The laser spot size used was ~2 μm.

6.3 Results and Discussion

6.3.1 As-Purified BNNTs

Figure 6.2 shows high-resolution TEM images of the as-purified BNNTs. It can be seen that there is a mixture of BNNTs with different numbers of walls, the majority of which have 2-5 walls (5-10 nm in diameter) with some having >10 walls (>20 nm in diameter). The distribution of wall numbers is shown in Figure 6.2(f) and significantly, no single-walled BNNTs were found. This is consistent with the TEM observation from the original report [9]. Other TEM observations (Figure 6.3(b)) showed that bundled structures were still maintained even after a long time bath sonication in isopropanol (IPA) [11], suggesting that debundling of the BNNTs may not be easy.

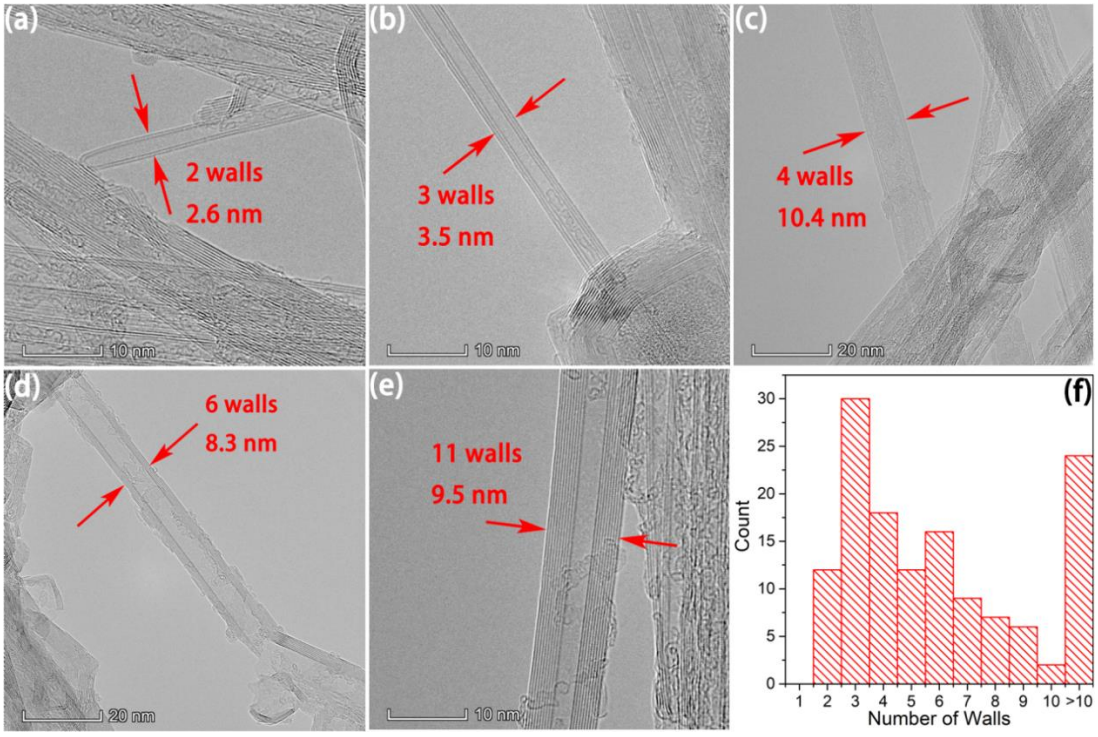

Figure 6.2 High-resolution TEM images of a BNNTs bundle containing DW-BNNTs (a), a three-walled BNNT (b), a four-walled BNNT (c), a six-walled BNNT (d) and an

11-walled BNNT (e). (f) Distribution of wall number of the MWBNNTs used in this work.

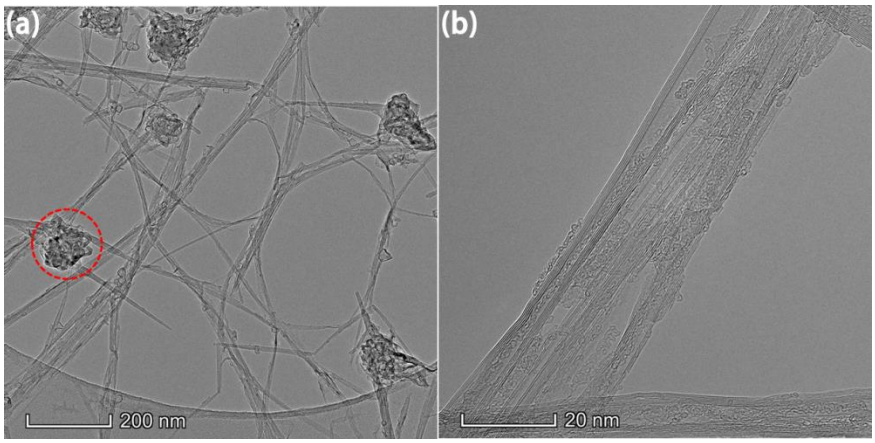

Figure 6.3 (a-b) TEM images of BNNTs bundling and some hBN shells.

The purity of BNNTs was also studied by a number of other techniques. TGA was undertaken both under nitrogen and air atmospheres. From Figure 6.4(a, b), although the mass of BNNTs decreases slowly when they are heated from RT to 800 ℃ in nitrogen and air atmosphere, the mass loss is only around 3.5 wt% in both cases indicating the high purity of the BN-based nanostructures in the sample. The EELS spectrum of the BNNTs is shown in Figure 6.4(c), in which a clear boron K-edge at 189 eV and nitrogen K-edge at 401 eV can be identified. The B/N ratio of the spectrum is estimated to be ~1, suggesting mainly B-N chemical bonding in the tube walls. XRD pattern of BNNTs (Figure 6.4(d)) exhibits a weak peak at $2\theta = 21.5°$ and a shoulder peak at $2\theta = 25.9°$, corresponding to the pattern of the boron hydride structure [12]. Hence, these two peaks are attributed to amorphous $B_xN_yH_z$ intermediates. The strong peak at $2\theta = 26.8°$, weak peaks at $2\theta = 41.8°$ and $55.2°$ correspond to the (002), (100), (004) reflections of hBN [13].

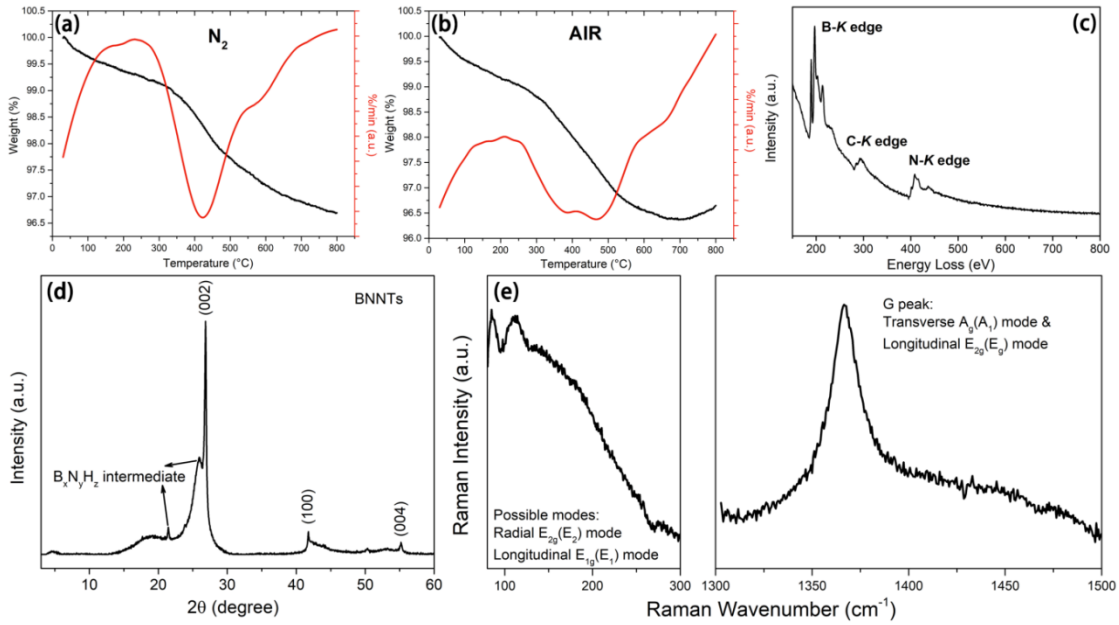

Figure 6.4 TGA and DTG plot of BNNTs in a nitrogen atmosphere (a) and an air atmosphere (b). (c) EELS spectra of BNNTs. (d) XRD pattern of BNNTs. (e) Raman spectra of BNNTs in the low frequency range and high frequency range respectively.

6.3.2 Functionalized BNNTs

The functionalization of the BNNTs is illustrated schematically in Figure 6.5(a). The elemental composition of BNNTs before and after hydroxylation was studied by XPS as shown in Figure 6.5(b-f). From full-range XPS spectra of the BNNTs, it is interesting that two distinct binding energy peaks at ~284.5 eV and ~532.5 eV were observed, indicating the existence of carbon and oxygen on the surface of the nanotubes. As the BNNTs samples were prepared using a carbon-free method [9-10] and no organic solvent was used during the preparation of XPS specimens, surface carbon and oxygen on the BNNTs must come from unavoidable contaminations from air, such as adherent CO_2 on the outer shell of nanotubes. A much weaker C 1s peak was observed in the full spectra of OH-BNNTs, indicating that some C, O-containing impurities or attachments were removed after functionalization. Although carbon contaminations are removed, the O 1s peak remains stable since the elemental

composition of oxygen decreases only slightly from 4.14 at% to 3.77 at% after hydroxylation (Table 6.1). Since the majority of surface contaminations were removed, it thus confirms that the oxygen content of the OH-BNNTs derives principally from the OH functional groups on the wall surfaces of the BNNTs.

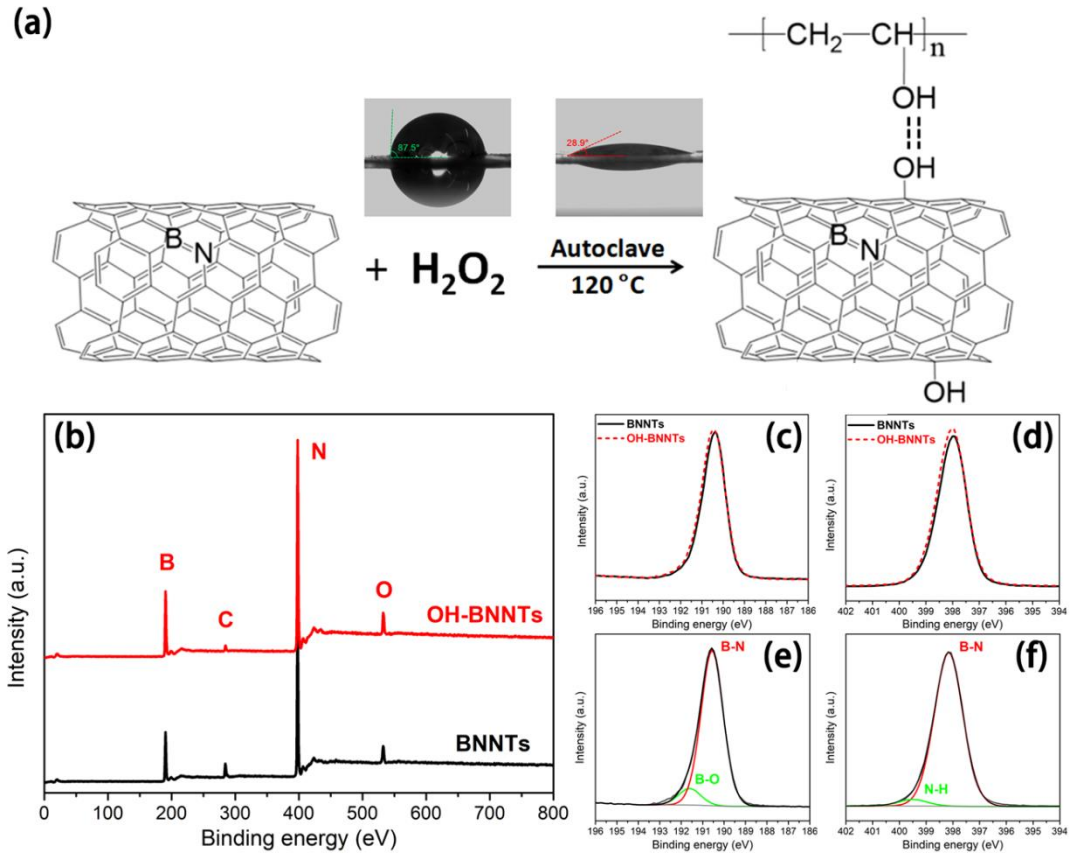

Figure 6.5 (a) Schematic of hydroxylation of BNNTs also showing the resultant change in water contact angle. (b) XPS survey spectra of as-purified BNNTs and OH-BNNTs. (c, e) XPS B 1s spectra of BNNTs and OH-BNNTs. (d, f) XPS N 1s spectra of BNNTs and OH-BNNTs.

Table 6.1 Elemental composition of BNNTs and OH-BNNTs measured by XPS

	B	N	C	O
BNNTs	43.64 at%	43.73 at%	8.49 at%	4.14 at%
OH-BNNTs	47.70 at%	46.00 at%	2.53 at%	3.77 at%

The accuracy of the XPS analysis was verified further from FTIR spectra, as shown in

Figure 6.6(a). The FTIR spectrum of pristine BNNTs is highly consistent with that of hBN crystals, in which the in-plane B-N stretching mode at ~1400 cm^{-1} and out-of-plane B-N-B stretching mode at ~800 cm^{-1} are clearly observed, indicating the hexagonal B_3N_3 ring structure of BNNTs [14-15]. Additionally, the weak peak at ~3150 cm^{-1} in the FTIR spectrum of BNNTs can be assigned to be the stretching mode of N-H bonding, proving the presence of $B_xN_yH_z$ intermediates in the BNNTs. In contrast to BNNTs, the FTIR spectrum of OH-BNNTs exhibits a wide and intense absorption peak at 3400-3500 cm^{-1} which corresponds to O-H bonding, demonstrating the successful hydroxylation of BNNTs. Meanwhile, the weak peak at ~3150 cm^{-1} from $B_xN_yH_z$ intermediates was not observed, indicating that it might be digested during the reaction.

The contact angle of water on BNNTs film decreases remarkably from 87.5 ° (Figure 6.6(b)) to 28.9 ° (Figure 6.6(c)) after the modification with H_2O_2.

The EELS spectrum (Figure 6.6(d)) of OH-BNNTs exhibits an individual wide energy loss peak at 535 - 540 eV, corresponding to 1sσ* transition of oxygen K-edge, therefore the bonding type of oxygen is likely to be sp3, rather than sp2. The XRD pattern (Figure 6.6(e)) of BNNTs does not show any difference after –OH functionalization, indicating an intact crystal structure after reaction with H_2O_2. TEM EELS mappings of OH-BNNTs imply the attachment of abundant oxygen on the nanotube walls after functionalization (note that some oxygen might come from unavoidable SiO_2 contamination during TEM sample preparation, but almost no Si was detected in both outer walls of BNNTs bundles). The success of –OH functionalization of the BNNTs is therefore confirmed.

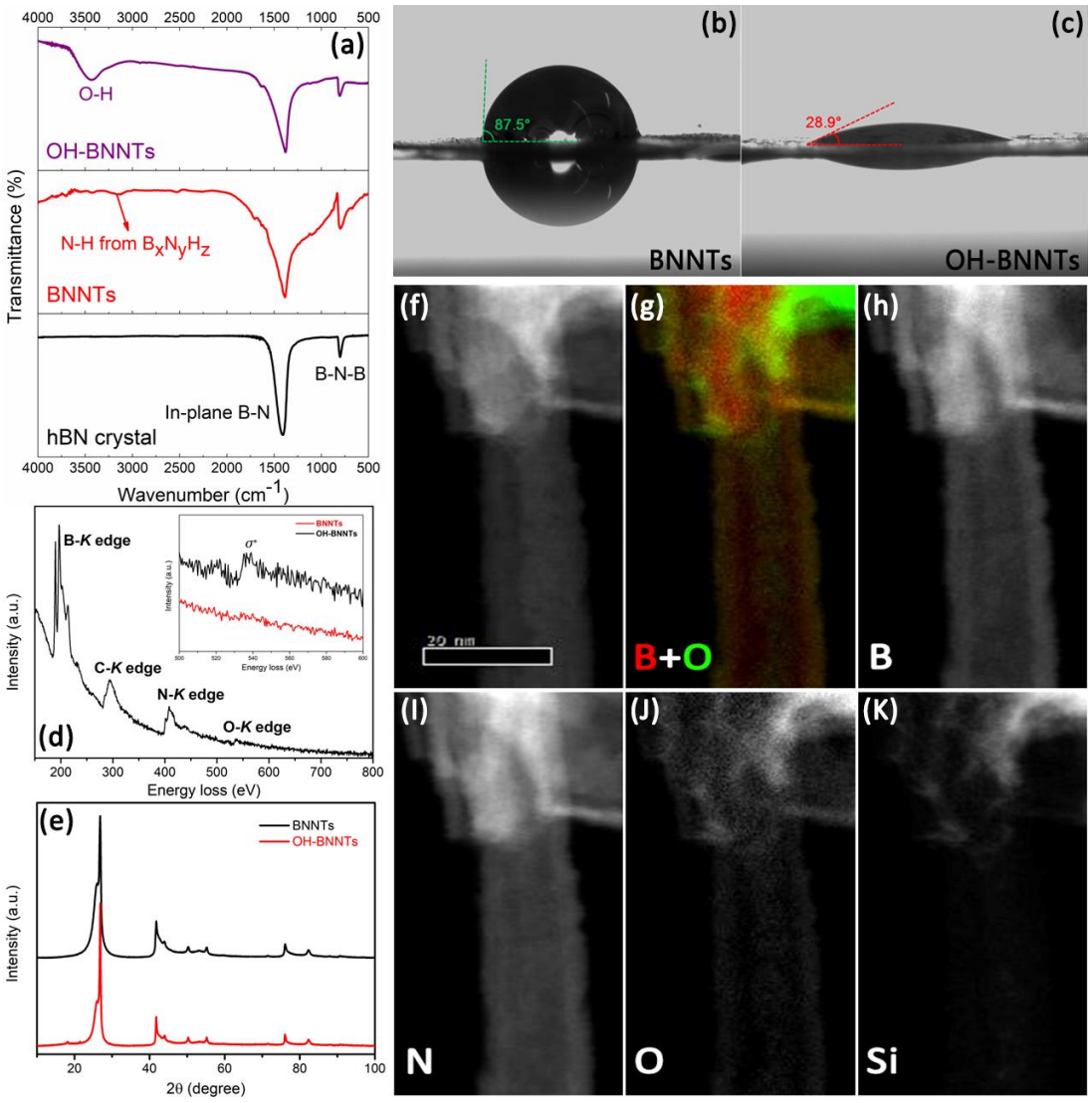

Figure 6.6 (a) FTIR spectra of hBN crystal, BNNTs and OH-BNNTs. Water contact angle of a film of BNNTs (b) and OH-BNNTs (c). (d) EELS spectra of BNNTs and OH-BNNTs. (e) XRD pattern of BNNTs and OH-BNNTs. (f-k) TEM EELS mapping of Boron, Nitrogen, Oxygen elements and few Si contaminations on OH-BNNTs.

6.3.3 Raman Spectroscopy

The Raman spectra of the as-purified and functionalized BNNTs are shown in Figure 6.7(a) and (b) respectively. It can be seen that both materials show a simple spectrum with a well-defined G band at 1368 cm^{-1}, characteristic of hBN [16]. Raman spectroscopy was also employed to characterise the PVA/BNNTs nanocomposites.

Previous studies [17-21] have shown that well-defined Raman spectra can be obtained from CNTs even very low loadings CNTs (<0.05 wt%) in polymer-based nanocomposites. This is because the CNTs undergo resonance Raman scattering so that the strength of the Raman signal is very much higher than that of the polymer matrix. In contrast, it is only possible to detect the G band of the BNNTs in the PVA composites at loadings in excess of around 1% as can be seen in Figure 6.7(c) where an extra peak is present in the PVA nanocomposite at around 1370 cm^{-1} among the Raman bands for the PVA matrix. This is shown more clearly in Figure 6.7(d) where the BNNT G band at 1368 cm^{-1} is deconvoluted from the surrounding Raman bands of the PVA. (See the similar analysis in Chapter 5)

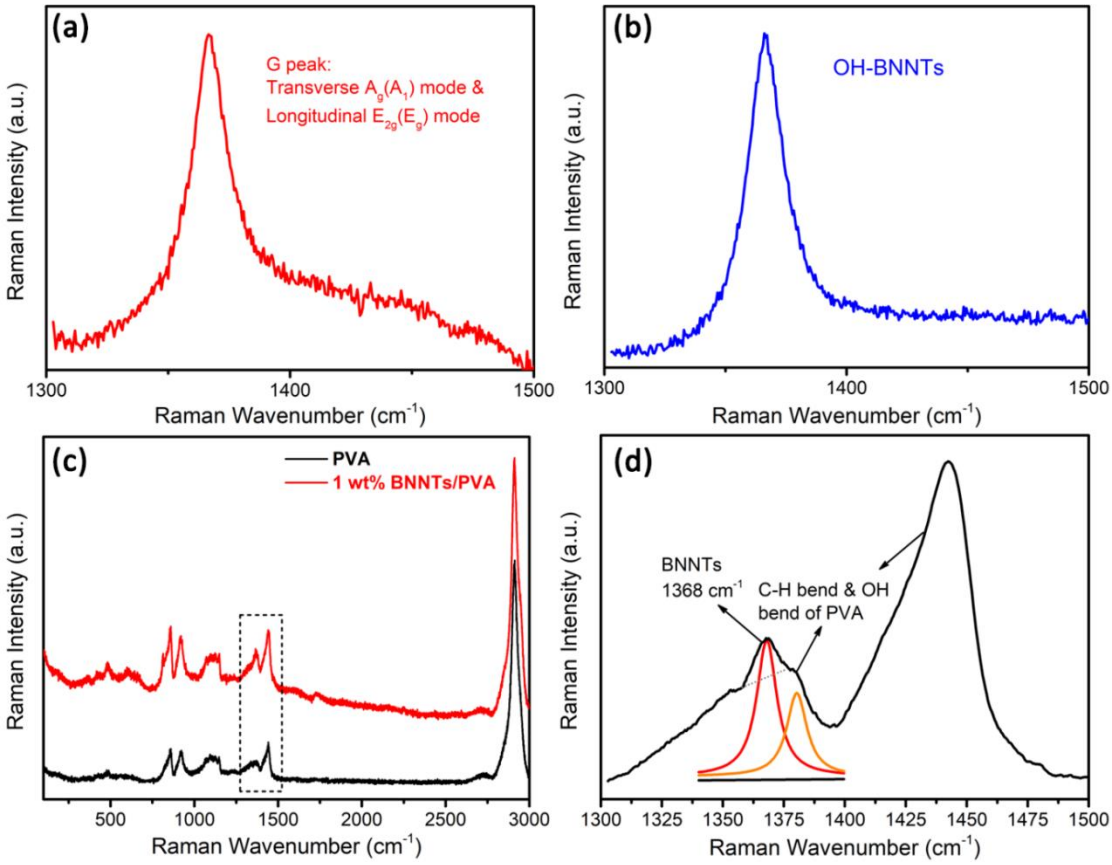

Figure 6.7 (a) Raman spectra of BNNTs (b) Raman spectrum of functionalized BNNTs (c) Full-range Raman spectra of 1 wt% BNNTs/PVA nanocomposites. (d) Zoom-in Raman spectra of 1 wt% BNNTs/PVA nanocomposites.

The spectra in Figure 6.7 were obtained using a 488 nm sapphire laser but a

systematic study was also undertaken to see if it was possible to employ lasers of different wavelength to optimise the analysis of the PVA/BNNTs composites, as shown in Figure 6.8. In principle, a laser with shorter wavelength and higher energy should be favourable, but potential damage to the polymer matrix needs also to be considered. In situ Raman characterization of 1 wt% BNNTs/PVA nanocomposites was performed using a 488 nm laser and a 633 nm laser with similar output power (achieved by adjusting the power of the 488 nm sapphire laser), as shown in Figure 6.8(a, b). Figure 6.8(c) gives the corresponding Raman spectra for Figure 6.8(a, b). It can be seen that the 488 nm laser gives rise to much more intense Raman bands for both the BNNTs (~1368 cm^{-1}) and PVA matrix (~1447 cm^{-1}) than the 633 nm laser. Ideally, UV lasers are expected to give stronger Raman bands of BNNTs, but the high energy of a 325 nm NUV laser causes damage to the polymer matrix, even with a low output power, as illustrated in Figure 6.8(d, e). Hence, UV lasers are not appropriate for the investigation of BNNT/polymer composites systems due to their unavoidable damage to the matrix, although they have been used widely to study the Raman spectra of BNNTs [22] and BN [23]. Hence, it was decided that the 488 nm laser would be the optimum one to be used.

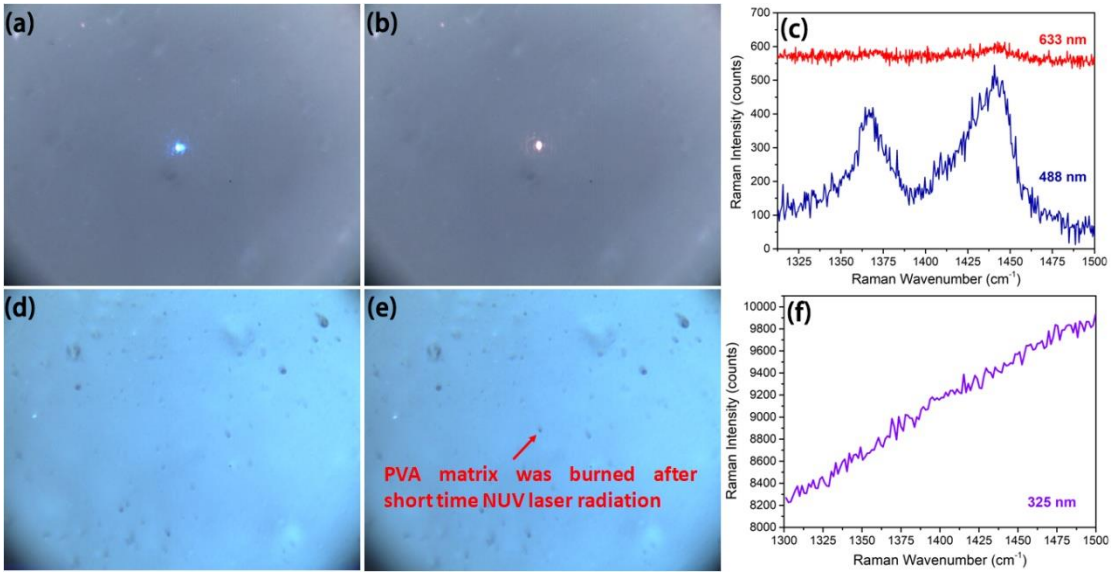

Figure 6.8 Optical graph of 1 wt% BNNTs/PVA nanocomposites in-situ radiated by a 488 nm blue laser (a) and a 633 red laser (b) with same power. (c) Raman spectra of 1

wt% BNNTs/PVA nanocomposites recorded using a 488 nm and a 633 nm laser with the same power. (d, e) Optical graph of 1 wt% BNNTs/PVA nanocomposites before and after radiated by a 325 nm NUV laser. (f) Raman spectra of 1 wt% BNNTs/PVA nanocomposites recorded after short time NUV radiation.

The dispersion of BNNTs in polymer matrix was assessed by mapping the intensity ratio of the BNNT G band at ~1368 cm^{-1} relative to that of the PVA band at ~1447 cm^{-1}. Figure 6.9(a) demonstrates the 100 μm × 100 μm Raman map of a 1 wt% BNNTs/PVA nanocomposites film with a relatively poor dispersion of nanotubes, in which the BNNTs were distributed into PVA matrix by a 4 hour bath sonication. Several >10 μm-scale white particles can be observed in the optical micrograph of the nanocomposite film that appear to be agglomerations of the BNNTs. These particles are imaged as brightly-coloured areas in the Raman map, implying that the ratio I_{1386}/I_{1447} can be used to map the distribution of the BNNTs in the nanocomposites. A finer dispersion of BNNTs in PVA matrix was realized by 1 hour probe sonication and fewer agglomerations can be observed by the optical micrograph shown in Figure 6.9(b) and confirmed in the Raman map. The dispersion of the OH-BNNTs in the nanocomposites was also evaluated as shown in Figure 6.9(c) where it can be seen that the functionalization improves the dispersion further.

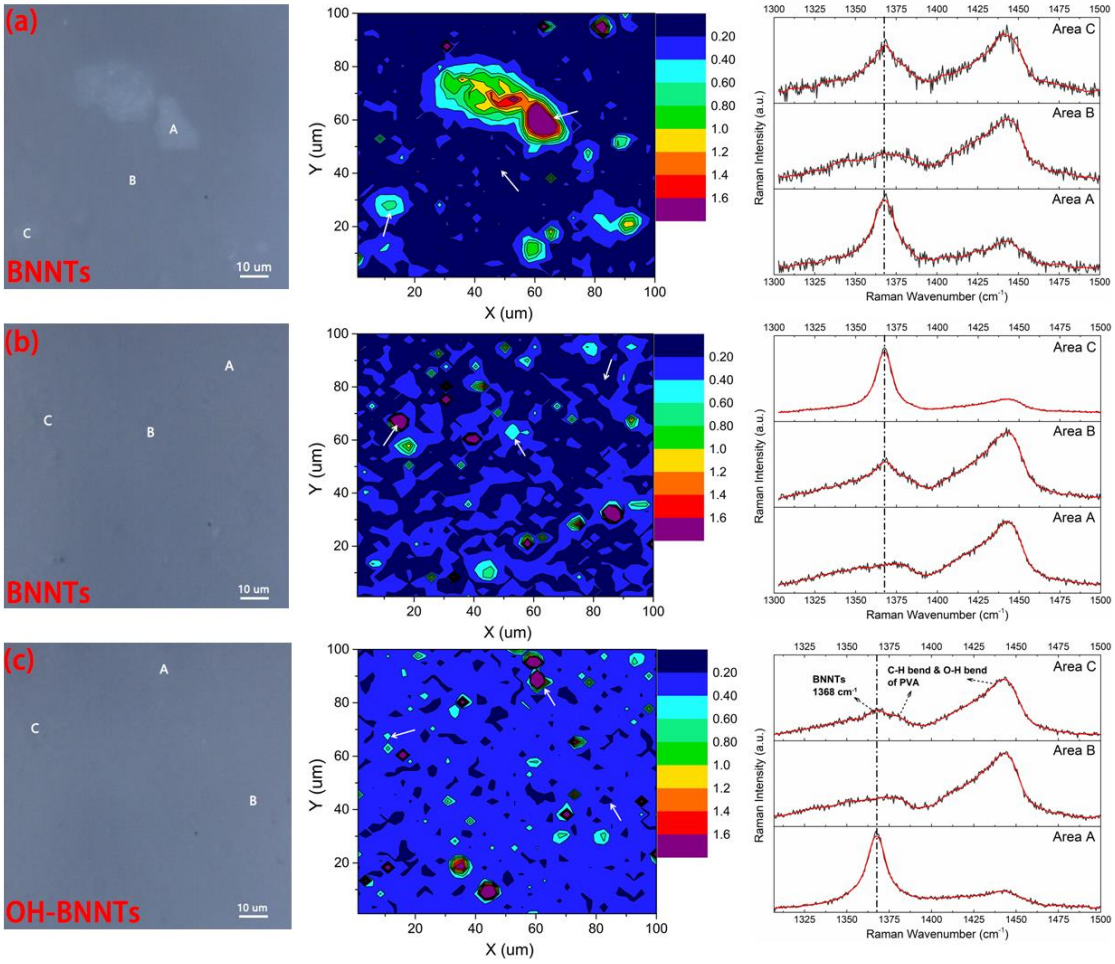

Figure 6.9 Optical micrographs, 100 μm × 100 μm Raman mapping (I_{1386}/I_{1447} intensity ratio), Raman spectra of area A, B, C in corresponding optical micrographs of (a) A 1 wt% BNNTs/PVA nanocomposites film prepared by mixing BNNTs using a 4 h sonication bath. (b) A 1 wt% BNNTs/PVA nanocomposites film prepared by mixing BNNTs using a 1h probe sonication. (c) A 1 wt% OH-BNNTs/PVA nanocomposites film prepared by mixing BNNTs using a 1h probe sonication.

The dispersion of the BNNTs in the PVA was also studied using transmission electron microscopy (TEM) as shown in Figure 6.10. It is found that many BNNTs are still in the form of bundles as verified by TEM (Figure 6.10(b)) and HRTEM (Figure 6.10(c, d)), although some individual MW-BNNTs can also be detected (Figure 6.10(e)).

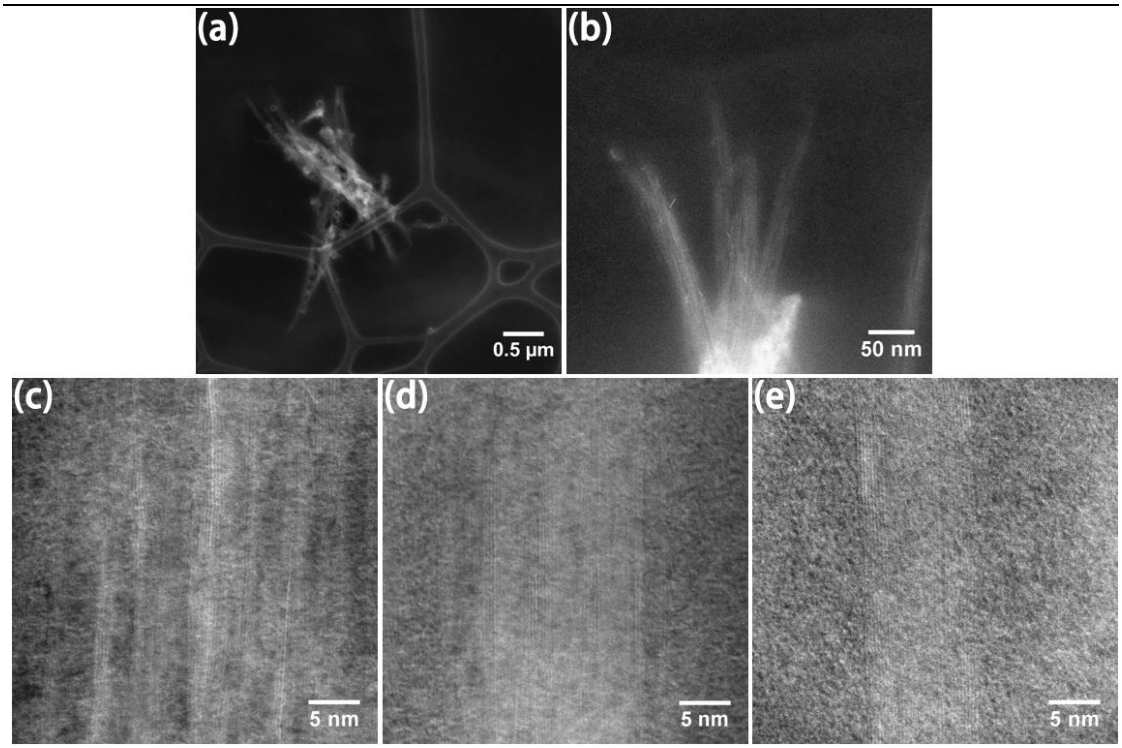

Figure 6.10 (a) STEM-ADF image of a BNNTs agglomeration. (b) STEM-ADF image of several separated BNNTs bundles. (c, d) HR STEM-ADF images of independent BNNTs bundles in BNNTs/PVA nanocomposites. (e) HR STEM-ADF image of an individual MW-BNNT in a 1 wt% BNNTs/PVA composites film dispersed using probe sonication.

6.3.4 Mechanical Properties

Stress-Strain Behaviour The stress-strain curves for the PVA matrix and BNNTs/PVA nanocomposite with 1wt% loading of the as-purified BNNTs are shown in Figure 6.11. It is clear that the addition of the BNNTs increases both the yield stress and fracture stress of the polymer. The stress/strain curve for the OH-BNNTs/PVA nanocomposite with a 1 wt% loading is also shown in Figure 6.11. It can be seen that the nanocomposite with the OH-BNNTs has a higher Young's modulus, yield strength and breaking strength than the nanocomposite film with the unfunctionalized BNNTs at the same loading. The mechanical properties determined from the stress-strain curves for all the nanocomposite films studies are summarized in Figure 6.11(c) & Table 6.2.

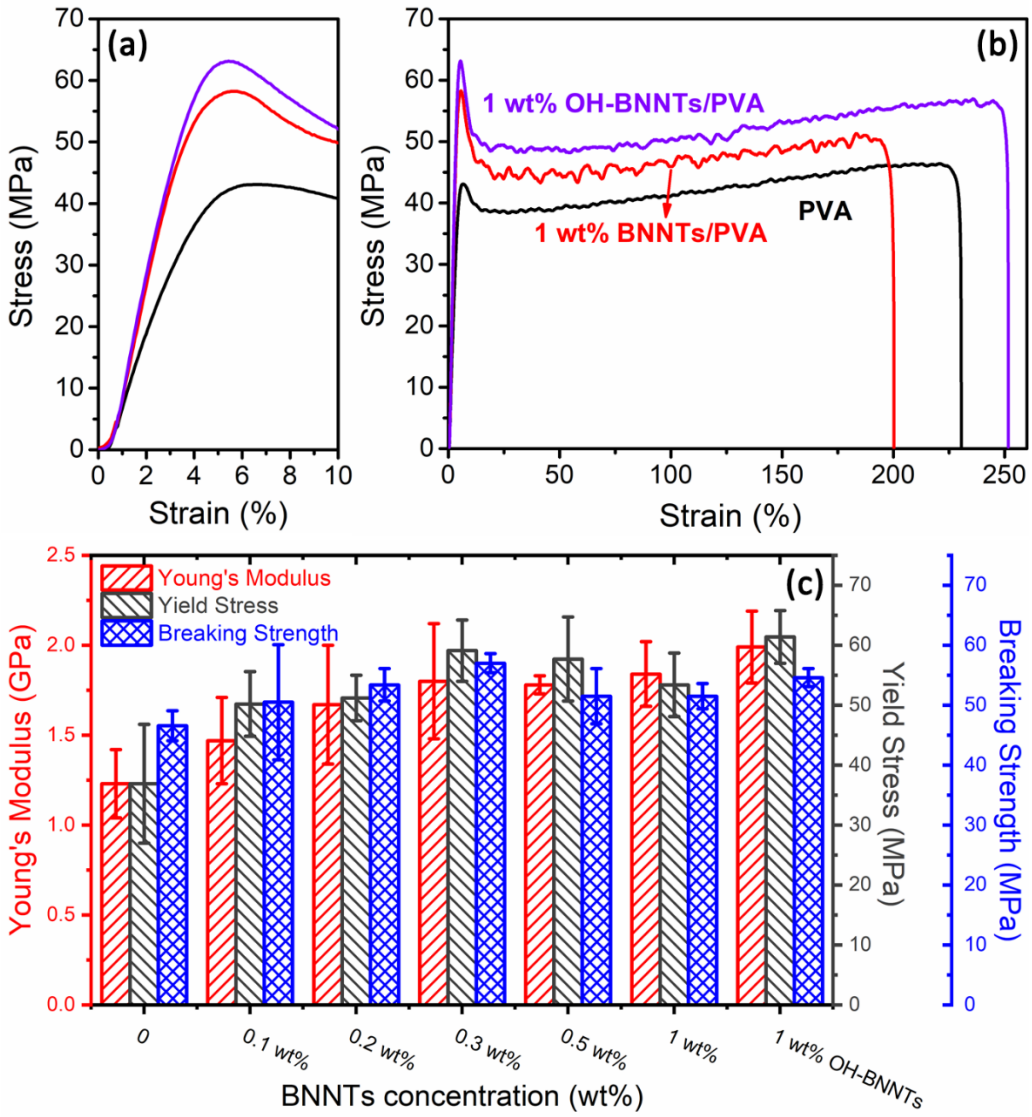

Figure 6.11 (a) Elastic region and (b) full range stress/strain curves for the as-purified and functionalised BNNTs/PVA nanocomposite and PVA films at 1 wt% loading. (c) Mechanical properties of neat PVA and BNNTs/PVA films.

Table 6.2 Tensile test results of neat PVA and BNNTs/PVA films.

Materials	Young's modulus (GPa)	Yield stress (MPa)	Breaking strength (MPa)	E_{eff} (GPa)
Neat PVA	1.23 ± 0.19	36.9 ± 9.9	46.6 ± 2.5	-
0.1 wt% BNNTs/PVA	1.47 ± 0.24	50.2 ± 5.4	50.5 ± 9.6	680
0.2 wt% BNNTs/PVA	1.67 ± 0.33	51.2 ± 3.8	53.4 ± 2.7	630
0.3 wt% BNNTs/PVA	1.80 ± 0.32	59.1 ± 5.1	57.0 ± 1.6	540

0.5 wt% BNNTs/PVA	1.78 ±0.05	57.7±7.0	51.5±4.6	310
1 wt% BNNTs/PVA	1.84 ±0.18	53.4±5.3	51.5±2.1	180
1 wt% OH-BNNTs/PVA	1.99 ±0.20	61.4±4.4	54.6±1.5	220

Stress-Induced Raman Band Shifts Shifts of the BNNT Raman G band in the BNNTs/PVA nanocomposites with a 1 wt% loading were monitored during deformation as shown in Figure 6.12. The spectra were obtained from areas of the nanocomposites showing relative a uniform distribution of the BNNTs (Figure 6.12). Three different areas were chosen at random and it can be seen that there is some variation in the rate of downshift of the G band with a maximum value of -4.2 ±1.7 cm^{-1}/% being obtained in one area. This variability is probably the result of different levels of dispersion and different populations of BNNTs within the 2 μm laser spot. Nevertheless, it is found that the downshift of the G band stops at ~0.2% strain, above which it remains constant or actually shifts back, most likely the result of breakdown of the BNNT/PVA interface.

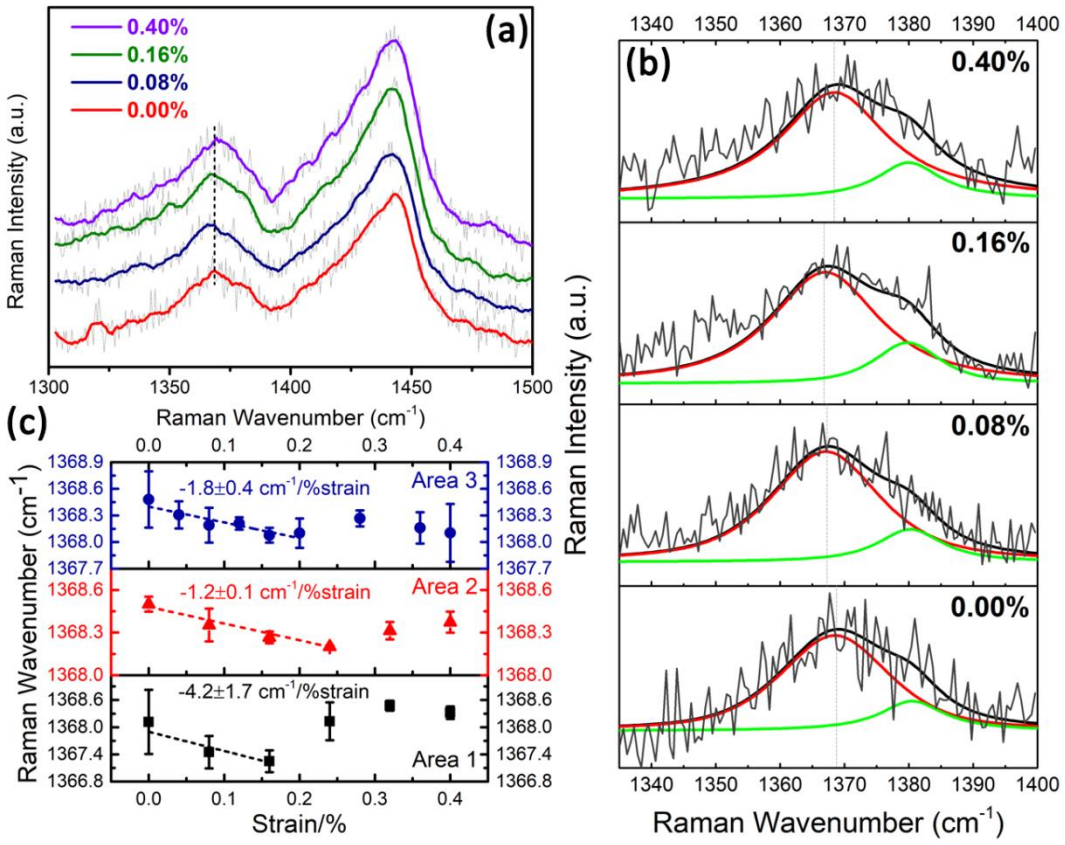

Figure 6.12 (a) Raman spectra of a region (area A in Figure 6.9(b)) with relatively homogeneous BNNTs dispersion in 1 wt% BNNTs/PVA film before and during tensile deformation and (b) Fitted zoom-in Raman G band shift of area A at different incremental strains. (c) G band shifts of three relatively homogeneous areas in 1 wt% BNNTs/PVA film as a function of strain.

Stress-induced shifts of the G band were also monitored for the OH-BNNTs/PVA nanocomposite with a 1 wt% loading of functionalized nanotubes as shown in Figure 6.13. In this case, a higher band-shift rate of -6.4 ±1.3 cm^{-1}/% is obtained with a linear shift up to a strain of ~0.4%. The higher shift rate and greater linear region are an indication of the better dispersion and stronger interface for the OH-BNNTs in the PVA than for the unfunctionalized nanotubes (Figure 6.12).

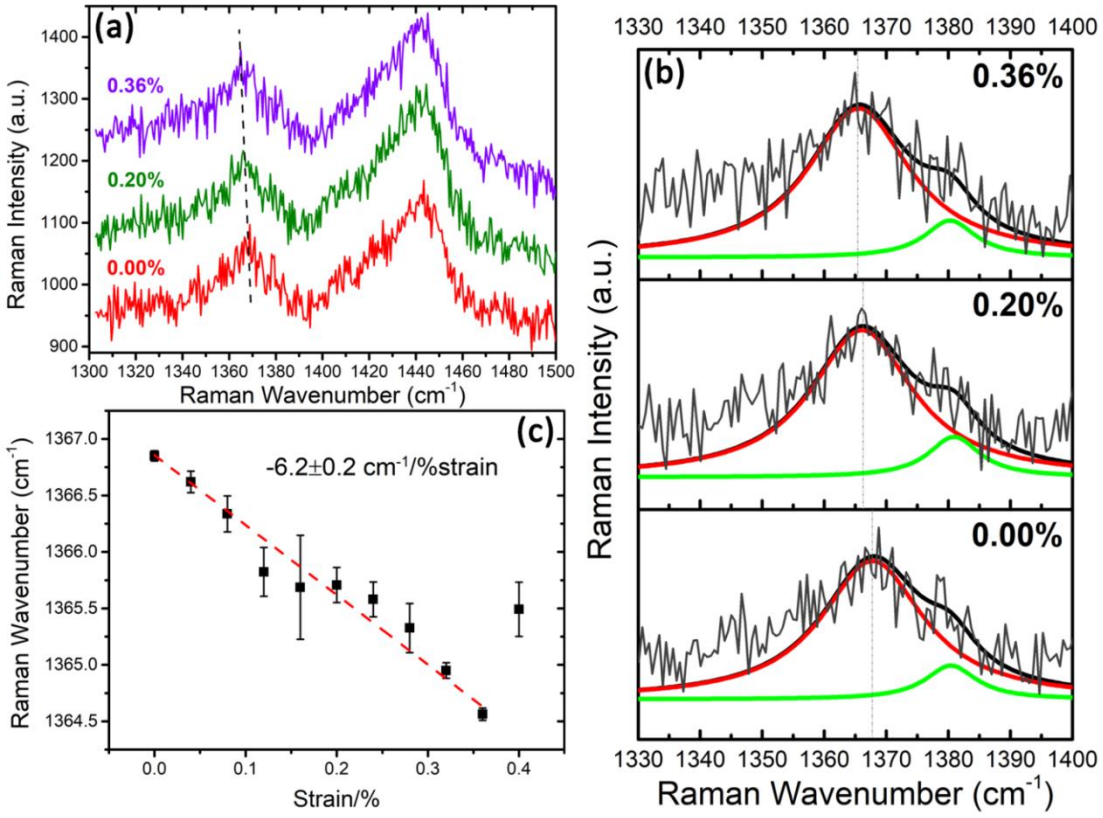

Figure 6.13 (a) Raman G band of OH-BNNTs at incremental strains. (b) Fitted zoom-in Raman G band shift of OH-BNNTs at incremental strains. (c) Shift of the G band position for OH-BNNTs in 1 wt% OH-BNNTs/PVA film as a function of strain.

6.3.5 Micromechanics of Deformation

It is well established that for both carbon nanotubes and graphene, the modified rule of mixtures can be used to account for the dependence of the Young's modulus of the nanocomposite, E_c, upon the volume fraction of the nanofiller (see Chapter 3). In the case of BNNTs, E_c will have a relationship of the form [18]

$$E_c = \eta_o \eta_l V_{BNNTs} E_{BNNTs} + (1 - V_{BNNTs}) E_m \qquad (6.1)$$

where V_{BNNTs} is the volume fraction of the BNNTs, E_{BNNTs} is the Young's modulus of the BNNTs and E_m is the Young's modulus of the matrix. Additionally, η_o is the orientation parameter and η_l the length parameter of the BNNTs filler.

The BNNTs loading may be converted from mass fraction W_{BNNTs} (wt%) to volume fraction V_{BNNTs} (vol%) using:

$$V_{BNNTs} = \frac{W_{BNNTs}\rho_{PVA}}{W_{BNNTs}\rho_{PVA} + (1 - W_{BNNTs})\rho_{BNNTs}} \qquad (6.2)$$

where ρ_{BNNTs} and ρ_{PVA} represent the densities of BNNTs and PVA, which are 1.38 g/cm^3 (the value for MW-BNNTs determined by Zhi et al. [24], but found to be highly dependent on the preparation method) and 1.3 g/cm^3 [25], respectively. As a result, a mass fraction of 1 wt% BNNTs/PVA corresponds to a volume fraction of around 0.94 vol%.

Polarized Raman spectroscopy shows that the orientation of BNNTs in nanocomposites film is random (see chapter 7). Thus we can take the value of η_o to be 3/8, the value of a random in-plane distribution of fibers [18]. This means that the effective Young's modulus of the BNNTs in the nanocomposites is given by $\eta_l E_{BNNTs}$ (=E_{eff}). The values of E_{eff} determined from the Young's modulus data are listed in Table 6.2. The dependence of E_{eff} upon V_{BNNTs} using the data from Table 6.2 is shown in Figure 6.14. It can be seen that the effective Young's modulus of the BNNTs decreases with increasing volume fraction. This implies that there is good distribution

of BNNTs at low volume fraction but that it becomes worse as the volume fraction increases. This observation is consistent with another study [8]. It is possible to determine the value of E_{BNNTs} by extrapolating the data in Figure 6.14 to zero volume fraction and this gives a value of $E_{eff} \sim 825 \pm 100$ GPa. Since it can be assumed that the BNNTs are effectively infinitely long and will become isolated as $V_{BNNTs} \rightarrow 0$, η_l can be assumed to be 1 in this case. Hence E_{BNNTs} is of the order of 825 GPa, consistent with the estimates of the intrinsic Young's modulus of MW-BNNTs (E_{BNNTs}) in the range of 0.5 - 1.2 TPa [26-28].

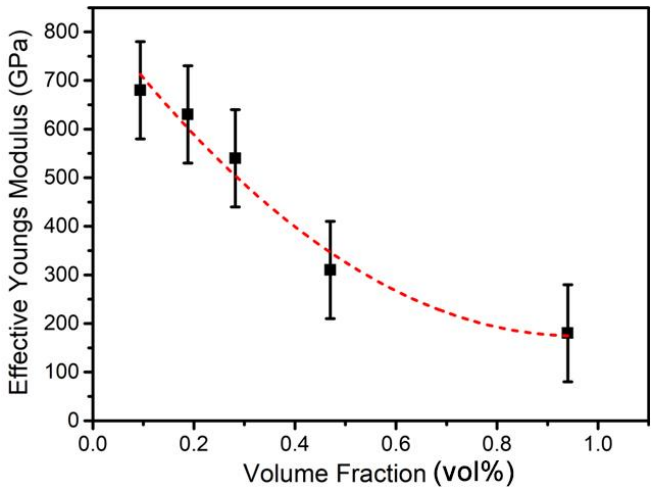

Figure 6.14 Dependence of the effective Young's modulus of the BNNTs/PVA nanocomposites upon the volume fraction of the BNNTs. The curve is an empirical fit of the data to second order polynomial function.

The value of the effective Young's modulus of the BNNTs, E_{eff} for each loading is given in Table 6.2. It can be seen that it decreases significantly as the loading of BNNTs increases and falls to a value of ~180 GPa for 1 wt% loading. This appears to result from a poor BNNTs distribution due to bundling [29] reducing the effective aspect ratio of the nanotubes [30] and leading to a large reduction in η_l. Table 6.2 also shows that the performance of the functionalized BNNTs is somewhat better, having a value E_{eff} of ~220 GPa at the same loading, implying that the OH-BNNTs have a better dispersion and stronger interfacial interaction with the PVA matrix.

It is also possible to estimate the Grüneisen parameter for the BNNTs from the stress-induced Raman band shifts. The average shift rate per percentage strain for the BNNT G band $d\omega_G/d\varepsilon$ from the three plots in Figure 6.12(c) is 2.4±1.3 cm^{-1}/% for a loading of 1 wt% in the PVA matrix. The value of E_{eff} for this loading of BNNTs is 180 GPa. Since the band shift rate would be expected to scale with the effective modulus of the nanotubes in the composite [18], this gives a band shift rate of 2.4×825/180 = 11.0±5.9 cm^{-1}/% for the as-purified BNNTs. The Grüneisen parameter can then be determined using the relationship

$$\gamma_G = \frac{\Delta\omega_G}{\omega_G^0(1-\nu)\varepsilon} \qquad (6.3)$$

where the Raman frequency of the G band is ω_G^0=1368 cm^{-1} and the Poissons ratio of the matrix ν=0.4. Setting $\Delta\omega_G/\varepsilon = d\omega_G/d\varepsilon$, then the value γ_G is calculated using this equation is 1.34±0.72. This value is similar to that determined for the BNNSs in Chapter 4 and in the middle of the range of 1.04 to 2.07 both measured experimentally and calculated for hBN nanoplatelets, reported by Androulidakis et al. [16].

6.4 Conclusions

A detailed investigation has been carried out for the microstructure and mechanical properties of PVA nanocomposites reinforced with BNNTs. The nanotubes and nanocomposites have been fully characterized. Raman mapping of the BNNT G band intensity can be employed to assess the distribution of the BNNTs in the polymer matrix. This is usually difficult since this band is relatively weak due to the lack of resonance. A method has, however, been developed of deconvoluting the band from the Raman spectrum of the matrix polymer enabling its intensity and position to be determined in the nanocomposite. It has also demonstrated that the BNNTs are

capable of producing high levels of reinforcement in the polymer-matrix nanocomposites. The effective Young's modulus of the BNNTs is found to the range from around 825 GPa at low volume fractions to the order of 180 GPa at 1 wt% loading, as a result of bundling leading to a poor dispersion in the polymer matrix at high loadings. It has also shown that the mechanical properties of the nanocomposites can be improved through –OH functionalization of the BNNTs, leading to a better dispersion, improved reinforcement and a higher effective Young's modulus. Stress transfer from the polymer matrix to the BNNTs has been followed from stress-induced shifts of the Raman G band of the BNNTs. The levels of band shift are found to be consistent with the effective Young's modulus of the BNNTs determined from mechanical testing. The stress-induced G-band shifts also enabled the Grüneisen parameter of the BNNTs to be determined that is similar to the value determined for hBN nanoplatelets. It is clear that, these BNNT materials offer considerable potential for applications in nanocomposites that need electrical insulation accompanied by high levels of stiffness and strength, along with potential good thermal stability, such as thermal management materials for electronic devices and communication equipment.

References

1. Zhi, C.; Bando, Y.; Tang, C.; Golberg, D., Boron nitride nanotubes. *Materials Science and Engineering: R: Reports* **2010,** *70* (3-6), 92-111.
2. Zhou, X.; Tang, D. M.; Mitome, M.; Bando, Y.; Sasaki, T.; Golberg, D., Intrinsic and Defect-Related Elastic Moduli of Boron Nitride Nanotubes As Revealed by in Situ Transmission Electron Microscopy. *Nano Letters* **2019,** *19* (8), 4974-4980.
3. Dresselhaus, M. S.; Dresselhaus, G.; Saito, R.; Jorio, A., Raman spectroscopy of carbon nanotubes. *Phys. Rep.* **2005,** *409* (2), 47-99.
4. Zhi, C.; Bando, Y.; Tang, C.; Honda, S.; Kuwahara, H.; Golberg, D., Boron nitride nanotubes/polystyrene composites. *J. Mater. Res.* **2006,** *21* (11), 2794-2800.
5. Zhi, C.; Bando, Y.; Terao, T.; Tang, C.; Kuwahara, H.; Golberg, D., Chemically activated boron nitride nanotubes. *Chemistry–An Asian Journal* **2009,** *4* (10), 1536-1540.
6. Thakur, V. K.; Yan, J.; Lin, M.-F.; Zhi, C.; Golberg, D.; Bando, Y.; Sim, R.; Lee, P. S., Novel polymer nanocomposites from bioinspired green aqueous functionalization of BNNTs. *Polymer Chemistry* **2012,** *3* (4), 962-969.
7. Zhou, S.-J.; Ma, C.-Y.; Meng, Y.-Y.; Su, H.-F.; Zhu, Z.; Deng, S.-L.; Xie, S.-Y., Activation of boron nitride nanotubes and their polymer composites for improving mechanical performance. *Nanotechnology* **2012,** *23* (5), 055708.
8. Guan, J.; Derdouri, A.; Ashrafi, B.; Benhalima, A.; Kim, K. S.; Daroszewska, M.; Simard, B., Boron nitride nanotubes reinforced polycarbonate nanocomposites. *Materials Today Communications* **2019,** *20*, 100586.
9. Kim, K. S.; Kingston, C. T.; Hrdina, A.; Jakubinek, M. B.; Guan, J. W.; Plunkett, M.; Simard, B., Hydrogen-catalyzed, pilot-scale production of small-diameter boron nitride nanotubes and their macroscopic assemblies. *ACS Nano* **2014,** *8* (6), 6211-6220.
10. Guan, J.; Kim, K. S.; Jakubinek, M. B.; Simard, B., pH-switchable water-soluble boron nitride nanotubes. *ChemistrySelect* **2018,** *3* (32), 9308-9312.
11. Coleman, J. N.; Lotya, M.; O'Neill, A.; Bergin, S. D.; King, P. J.; Khan, U.; Young, K.; Gaucher, A.; De, S.; Smith, R. J.; Shvets, I. V.; Arora, S. K.; Stanton, G.; Kim, H. Y.; Lee, K.; Kim, G. T.; Duesberg, G. S.; Hallam, T.; Boland, J. J.; Wang, J. J.; Donegan, J. F.; Grunlan, J. C.; Moriarty, G.; Shmeliov, A.; Nicholls, R. J.; Perkins, J. M.; Grieveson, E. M.; Theuwissen, K.; McComb, D. W.; Nellist, P. D.; Nicolosi, V., Two-dimensional nanosheets produced by liquid exfoliation of layered materials. *Science* **2011,** *331* (6017), 568-71.
12. Fang, Z.; Luo, J.; Kang, X.; Xia, H.; Wang, S.; Wen, W.; Zhou, X.; Wang, P., Facile solid-phase synthesis of the diammoniate of diborane and its thermal decomposition behavior. *Physical Chemistry Chemical Physics* **2011,** *13* (16), 7508-13.

13. Zhi, C.; Bando, Y.; Tang, C.; Honda, S.; Sato, K.; Kuwahara, H.; Golberg, D., Characteristics of boron nitride nanotube–polyaniline composites. *Angew. Chem.* **2005,** *117* (48), 8143-8146.
14. Frueh, S.; Kellett, R.; Mallery, C.; Molter, T.; Willis, W. S.; King'ondu, C.; Suib, S. L., Pyrolytic decomposition of ammonia borane to boron nitride. *Inorg. Chem.* **2010,** *50* (3), 783-792.
15. Fazen, P. J.; Remsen, E. E.; Beck, J. S.; Carroll, P. J.; McGhie, A. R.; Sneddon, L. G., Synthesis, properties, and ceramic conversion reactions of polyborazylene. A high-yield polymeric precursor to boron nitride. *Chem. Mater.* **1995,** *7* (10), 1942-1956.
16. Androulidakis, C.; Koukaras, E. N.; Poss, M.; Papagelis, K.; Galiotis, C.; Tawfick, S., Strained hexagonal boron nitride: Phonon shift and Grüneisen parameter. *Physical Review B* **2018,** *97* (24).
17. Cui, S.; Kinloch, I. A.; Young, R. J.; Noé, L.; Monthioux, M., The Effect of Stress Transfer Within Double-Walled Carbon Nanotubes Upon Their Ability to Reinforce Composites. *Adv. Mater.* **2009,** *21* (35), 3591-3595.
18. Deng, L.; Eichhorn, S. J.; Kao, C. C.; Young, R. J., The effective Young's modulus of carbon nanotubes in composites. *ACS Appl Mater Interfaces* **2011,** *3* (2), 433-40.
19. Deng, L.; Young, R. J.; van der Zwaag, S.; Picken, S., Characterization of the adhesion of single-walled carbon nanotubes in poly(p-phenylene terephthalamide) composite fibres. *Polymer* **2010,** *51* (9), 2033-2039.
20. Kannan, P.; Eichhorn, S. J.; Young, R. J., Deformation of isolated single-wall carbon nanotubes in electrospun polymer nanofibres. *Nanotechnology* **2007,** *18* (23), 235707.
21. Kannan, P.; Young, R. J.; Eichhorn, S. J., Debundling, isolation, and identification of carbon nanotubes in electrospun nanofibers. *Small* **2008,** *4* (7), 930-3.
22. Arenal, R.; Ferrari, A. C.; Reich, S.; Wirtz, L.; Mevellec, J. Y.; Lefrant, S.; Rubio, A.; Loiseau, A., Raman spectroscopy of single-wall boron nitride nanotubes. *Nano Lett.* **2006,** *6* (8), 1812-6.
23. Reich, S.; Ferrari, A. C.; Arenal, R.; Loiseau, A.; Bello, I.; Robertson, J., Resonant Raman scattering in cubic and hexagonal boron nitride. *Physical Review B* **2005,** *71* (20).
24. Zhi, C.; Bando, Y.; Tang, C.; Golberg, D., Specific heat capacity and density of multi-walled boron nitride nanotubes by chemical vapor deposition. *Solid State Commun.* **2011,** *151* (2), 183-186.
25. Liang, J.; Huang, Y.; Zhang, L.; Wang, Y.; Ma, Y.; Guo, T.; Chen, Y., Molecular-level dispersion of graphene into poly (vinyl alcohol) and effective reinforcement of their nanocomposites. *Adv. Funct. Mater.* **2009,** *19* (14), 2297-2302.
26. Chopra, N. G.; Zettl, A., Measurement of the elastic modulus of a multi-wall

boron nitride nanotube. *Solid State Commun.* **1998,** *105* (5), 297-300.

27. Suryavanshi, A. P.; Yu, M.-F.; Wen, J.; Tang, C.; Bando, Y., Elastic modulus and resonance behavior of boron nitride nanotubes. *Applied Physics Letters* **2004,** *84* (14), 2527-2529.
28. Golberg, D.; Costa, P. M. F. J.; Lourie, O.; Mitome, M.; Bai, X. D.; Kurashima, K.; Zhi, C. Y.; Tang, C. C.; Bando, Y., Direct force measurements and kinking under elastic deformation of individual multiwalled boron nitride nanotubes. *Nano Lett.* **2007,** *7* (7), 2146-2151.
29. Cronin, S.; Swan, A.; Ünlü, M.; Goldberg, B.; Dresselhaus, M.; Tinkham, M., Measuring the uniaxial strain of individual single-wall carbon nanotubes: resonance Raman spectra of atomic-force-microscope modified single-wall nanotubes. *Phys. Rev. Lett.* **2004,** *93* (16), 167401.
30. Hull, D.; Clyne, T. W., *An introduction to composite materials*. Cambridge university press: Cambridge, **1996**.

Chapter 7 Raman Spectroscopy of BNNTs in Electrospun BNNTs/PVA Nanofibres

7.1 Introduction

Electrospinning is one of the simplest methods to prepare nanofibres with diameters on the nm scale. Electrospun composite nanofibres have been attracting enormous research interest for over decades due to their versatile and adjustable properties [1-4]. A series of previous studies [5-8] on CNT/polymer electrospun nanofibres has proven that electrospinning is an effective method to disperse and orient 1D nanotubes in a polymer matrix. Both TEM [9-11], AFM [12] observations and polarized Raman characterization [5-6] have confirmed the high orientation of CNTs along the nanofibres axis. It is also found that electrospinning can effectively debundle CNTs [12], which is helpful on improving their mechanical reinforcement of the matrix.

Despite BNNTs being synthesized only 4 years after the discovery of CNTs [13-14], electrospun BNNT/polymer nanofibres have only been reported in very few studies. Terao et al. [15] first reported the preparation of BNNTs/PVA films by the stacking and hot-pressing multiple layers of electrospun composite nanofibre sheets. The BNNTs-dispersed PVA aqueous solution was spun with a high voltage and formed into nanofibres. A high-speed rotating aluminum wire drum was used to collect and orient the nanofibres. As-prepared nanofibre sheets were thus constructed using oriented nanofibres. The BNNTs in the nanofibres were found to be well aligned along the fibre axis by TEM observation. The orientation of BNNTs in the thick nanocomposites films can therefore be controlled by changing the layer stacking direction of nanofibre sheets. The authors thus prepared the films containing oriented BNNTs by stacking all nanofibre sheets into one direction and cross-linked BNNT

network by stacking sheets rotated 90 ° with respect to adjacent layers, respectively. It was found that high orientation of the BNNTs further improves the thermal conductivity of the nanocomposites film. Very recently, electrospun BNNTs/polyvinylpyrrolidone (PVP) and BNNTs/polyacrylonitrile (PAN) nanofibres were reported by Kim et al. [16] and Estevez et al. [17], respectively. However, both studies focused on the enhanced thermal conductivity of nanofibres induced by BNNTs incorporation and still used an electron microscope to prove the orientation of BNNTs. To the best of our knowledge, the orientation of BNNTs in the electrospun BNNTs/polymer nanofibres has not yet studied using Raman spectroscopy.

Different from the case of 0.04 wt% CNT/polymer nanofibres where only an individual nanofibre with ~1 μm diameter is needed to give a strong CNT Raman signals. It is found that the Raman band of MW-BNNTs in an isolated 1 wt% BNNTs/PVA electrospun nanofibre is weak and hard to distinguish. Hence in this chapter, a highly-oriented electrospun MW-BNNTs/PVA nanofibre nonwoven fabric was prepared for polarized Raman analysis. The MW-BNNT/PVA aqueous solution was prepared for nanofibre spinning. The spinning conditions were optimized to prepare composite nanofibres with a stable and appropriate diameter. A special collector consisting of two strips of conductive aluminum foils and an insulating sheet was used for collecting the uniaxially-aligned fibre fabric [18]. The orientation of BNNTs in the fabric was studied by non-resonance polarized Raman spectroscopy.

It should be noted that this chapter only contains preliminary results of a systematic project studying the orientation of BNNTs in the nanocomposites using polarized Raman spectroscopy. For future work, it is expected that the BNNTs/polymer nanocomposites containing highly-oriented BNNTs can be prepared and studied by polarized Raman spectroscopy using a VV configuration (higher accuracy), the stress transfer from the polymer matrix to the BNNTs can be studied by in-situ Raman

deformation test (See 8.2.5 in Chapter 8).

7.2 Experimental

7.2.1 Materials

The MW-BNNTs used in this work were identical with those in chapter 6, which were synthesized using a hydrogen-catalyzed induction plasma processing method [19] and purified before use [20]. The PVA (MW ~89000-98000, 99+% hydrolyzed) was purchased from Sigma Aldrich and used as received.

7.2.2 Electrospinning of BNNTs/PVA nanofibre nonwoven fabric

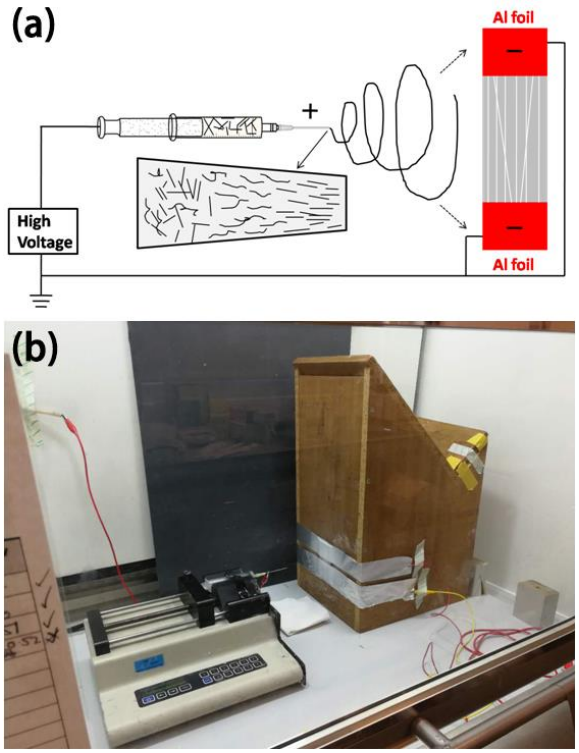

Figure 7.1 (a) Schematic diagram of electrospinning set-up for collecting oriented composite nanofibres. (b) Photograph of electrospinning set-up for collecting aligned BNNT/PVA nanofibre fabric.

The BNNT/PVA aqueous solution was prepared following the same method as described in chapter 6, the only difference being that the loading of the BNNTs was fixed at 1 wt%. Electrospinning was carried out as soon as the nanocomposites solution was prepared. A syringe of 10 ml capacity and a needle with 1.1 mm outer diameter were used and attached to the pump. The tip-to-collector was 8 cm and electric voltage was 20 kV. In order to collect well-aligned nanofibres on the collector, a PMMA sheet was used as collector of the nanofibers. A pair of parallel aluminum strips was attached on the both ends of the polymer substrate and an electric field was generated between the two aluminum electrodes thus stretched the nanofibres and made them attach uniaxiallyed on the PMMA collector (Figure 7.1(a)). To achieve a better alignment of nanofibres, a shorter distance between two aluminum strips was employed as illustrated in Figure 7.1(b).

7.2.3 Characterization

The orientation and surface morphology of electrospun nanofibres were observed using an EVO 50 SEM (Zeiss) in the secondary electron mode and a Nanowizard AFM (JPK Instruments) in the QI mode. For SEM, the nanofibre-deposited PMMA collector was stuck to the SEM stub by carbon tape, which was then sputter coated with platinum.

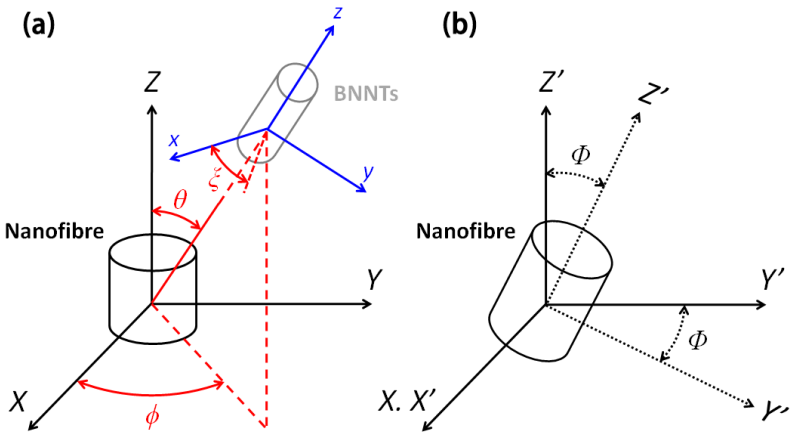

Figure 7.2 Schematic diagrams of the orientation of BNNTs in a composites nanofibre

and of the nanofibre relative to the polarized Raman spectroscopy measurement parameters. (a) Local coordinate system of the BNNTs (x, y, z) is related to that of the nanofibre (X, Y, Z) by Euler angles (θ, ϕ, ξ). (b) For polarized Raman measurement, the incident laser propagates along the X. X' axis while the polarization direction of the incident laser is changed by rotating the half-wave plate in the path of incident radiation. The scattered light was not polarized [21].

A Horiba LabRAM Evolution HR Raman spectrometer equipped with a Coherent 488 nm sapphire laser was used for the Raman measurements. The orientation of the BNNTs in the well-aligned nanofibre nonwoven fabric was determined using polarized Raman spectroscopy, in which a λ/2 (half-wave) plate was used to polarize the incident laser [21]. A VN configuration is used in this work, which meant that only the incident laser was polarized whereas the Raman scattered light was not because of the relatively weak non-resonance Raman signal from the BNNTs. The angle between polarized incident laser and the reference direction of the sample was defined as Φ and adjusted by rotating the λ/2 plate. The angle Φ was changed in steps of 10^{o} with Raman spectra collected at each step. The laser spot size was about 1-2 μm in diameter and covered many BNNTs. The principles of polarized Raman spectroscopy are illustrated in Figure 7.2.

7.3 Results and discussion

7.3.1 Nanofibre surfaces and diameter

Solution concentration, applied voltage, tip-collector distance were optimized to spin electrospun nanofibre with controllable diameter. First of all, nanofibres spun from 7 wt%, 10 wt% and 14 wt% PVA/H_2O solutions were studied using SEM as shown in Figure 7.3. A typical bead-on-string structure were observed for many nanofibres spun

from 7 wt% solution (Figure 7.3(a-b)), the number of beads gradually decreases for 10 wt% solution (Figure 7.3(c-d)) and eventually disappeared when the solution concentration reached 14 wt%.

The formation of beads in nanofibre can be explained by comparing the strength of the Coulomb force and viscoelastic force acting on the polymer jet [22]. For low viscosity solutions (7 wt%, 10 wt%), the Coulomb force is higher than viscoelastic force, which induces the overstretching of the charged polymer jet and their break-up into many small beads. When the viscosity of the solution increases (14 wt%) and eventually results in a larger viscoelastic force than coulomb force, nanofibres with smooth surface and stable diameter are obtained as the viscoelastic force is strong enough to prevent the breakup of the charged jet (Figure 7.3(e-f)).

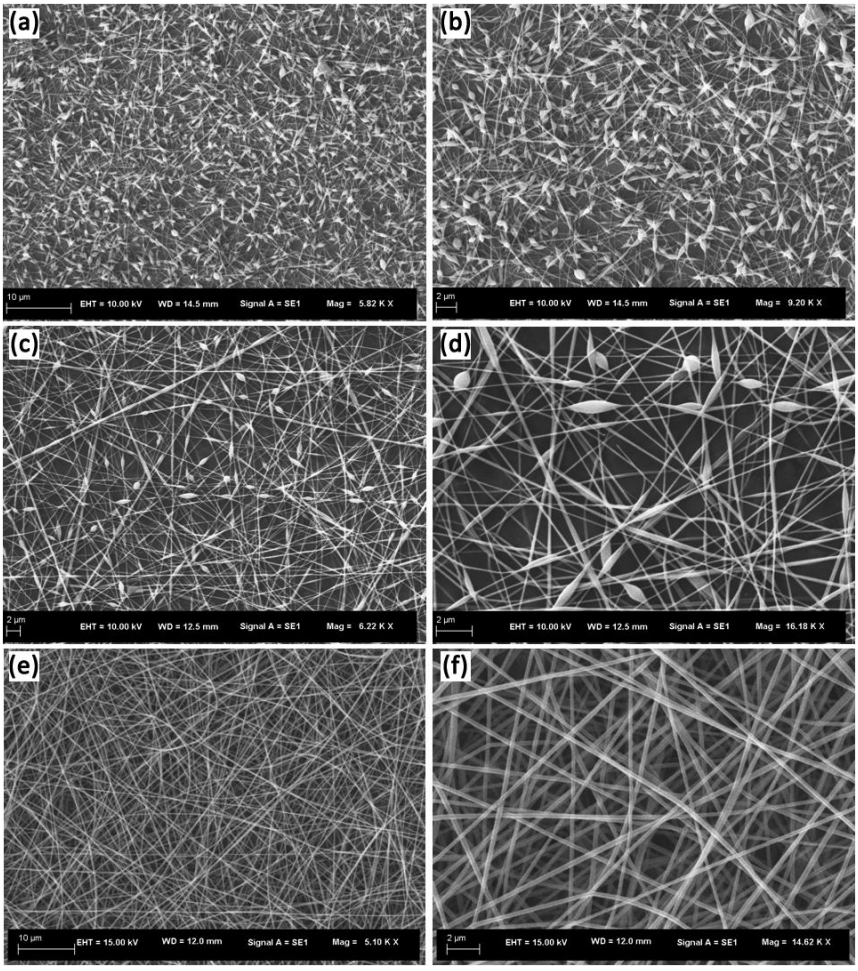

Figure 7.3 SEM images of PVA electrospun fibres with (a-b) 7 wt%, (c-d) 10 wt%, (e-f)

14 wt% polymer concentrations (tip-collector distance: 8 cm, applied voltage: 20 kV). Although it has been reported that the tip-collector distance affects the diameter of the electrospun nanofibre [23], no obvious change on both PVA and 1 wt% BNNTs/PVA nanofibre diameter was observed when the tip-collector distance increases from 4-14 cm (Figure 7.4). This suggests that the electrospun 1 wt% BNNTs/PVA nanofibres can be collected at a broad range of tip-collector distance, as in the case of electrospun CNT/PVA nanofibres [24].

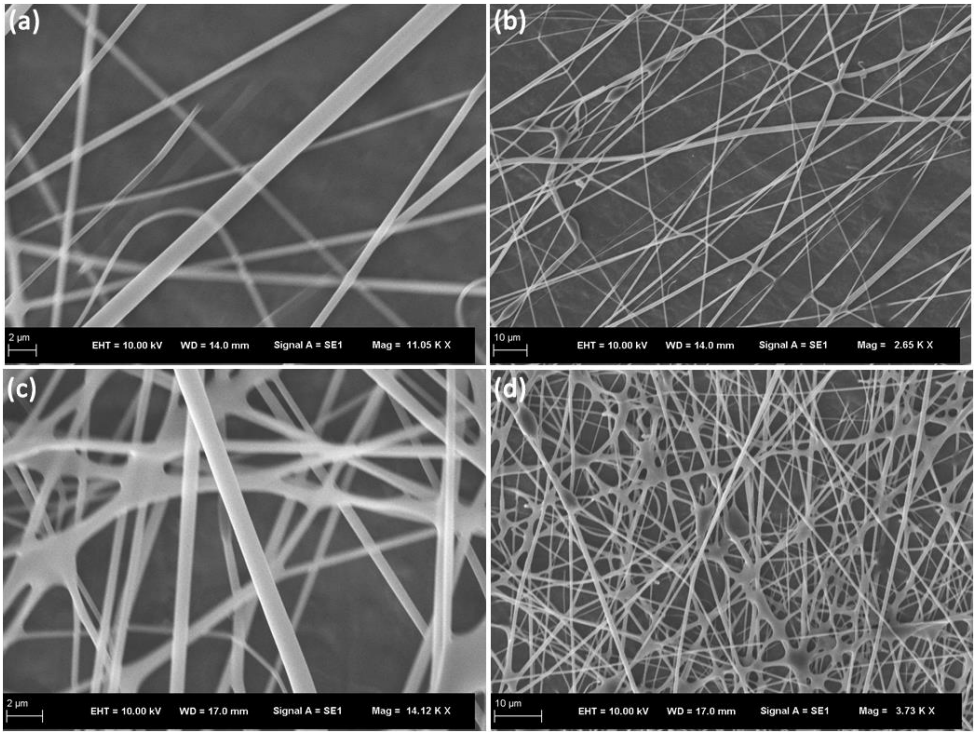

Figure 7.4 SEM images of 1 wt% BNNT/PVA electrospun fibres collected using different tip-collector distances: (a-b) 4 cm. (c-d) 8 cm (PVA concentration: 14 wt%, applied voltage: 20 kV).

It is found that the applied voltage can also massively affect the morphology of nanofibres. Figure 7.5(a) shows the SEM image of nanofibre spun at 5 kV, where a ribbon-like structure is seen. This is due to the presence of residual solvent inside the nanofibres spun at low voltage [25]. After the solvent naturally evaporates, the nanofibres on the collector collapse and become flat ribbons. When the applied voltage exceeded a certain value (15 kV), circular nanofibres were observed (Figure

7.5(b)), suggesting that the solvent evaporated fully before the nanofibres approached the collector.

Additionally, the diameter of 1 wt% BNNTs/PVA nanofibres was not as uniform as that of pure PVA nanofibres spun under identical conditions. This might indicate that the addition of 1 wt% BNNTs changes the surface tension of the PVA aqueous solution. On the other hand, insulating BNNTs further reduces the conductivity of the solution and thus reduce the charge density on the PVA jet, which consequently results in weaker charge repulsion and a weakened force to stretch and stabilize the nanofibres [26].

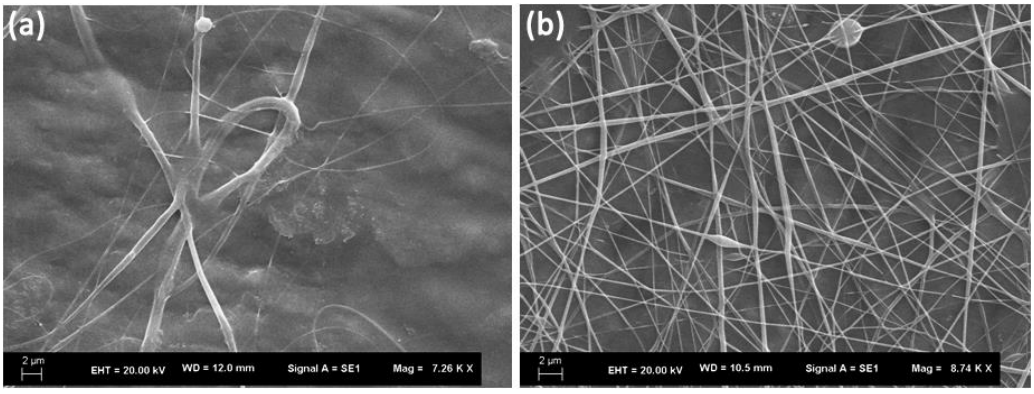

Figure 7.5 SEM images of 1 wt% BNNTs/PVA nanofibres spun at different voltage: (a) 5 kV. (b) 15kV (PVA concentration: 14 wt%, tip-collector distance: 8 cm).

7.3.2 Uniaxially-aligned nanofibres

In an attempt to massively strengthen the Raman band intensity of BNNTs/PVA nanofibre, we prepared an oriented electrospun nanofibre nonwoven fabric containing well-aligned BNNTs, based on the set-up shown in Figure 7.6. Thus multiple oriented nanofibres could be radiated by the laser spot. To verify the validity of the set-up, small numbers of nanofibres were spun on the PMMA collector and their morphology and orientation were observed. The SEM and AFM images in Figure 7.6 imply uniform orientation of most of the nanofibres along the PMMA substrate axis. AFM

height profiles of two individual oriented nanofibres in Figure 7.6(f) indicate a ~1 μm diameter of the nanofibres prepared (Note that the resolution of the AFM image is relatively low, so the shape of the profiles may not be accurate enough. A curved shape could be expected in a higher magnification micrograph).

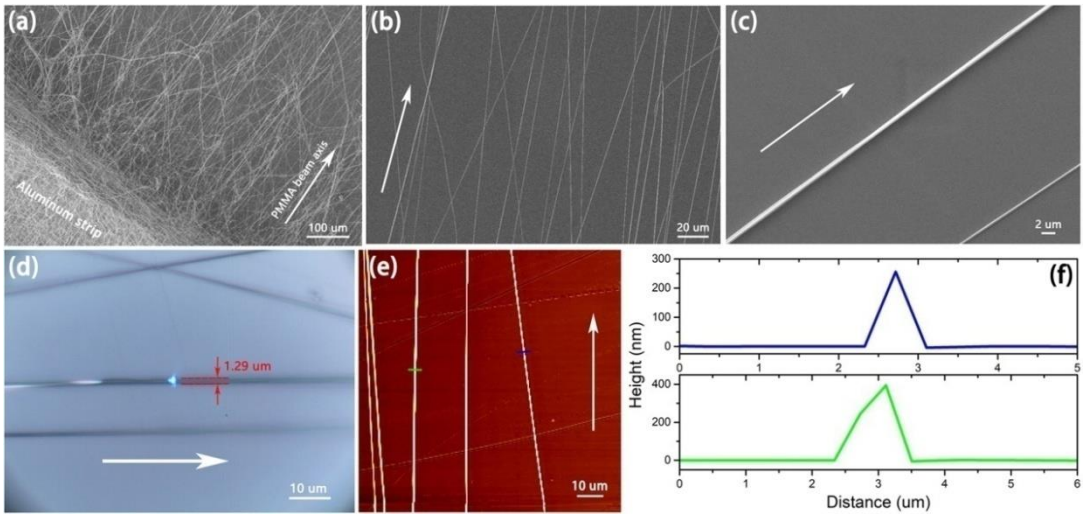

Figure 7.6 (a-c) SEM images of aligned electrospun 1 wt% BNNTs/PVA nanofibres on PMMA substrate. (d) Optical micrograph of an individual BNNTs/PVA nanofibre with ~1 μm width parallel to the axis of PMMA substrate. (e) AFM image of several BNNTs/PVA nanofibres parallel to the axis of PMMA substrate. (f) Height profiles across two nanofibres in (e).

The optical graph of the nonwoven nanofibre fabric in Figure 7.7 demonstrates that most of nanofibres are parallel to the PMMA beam axis.

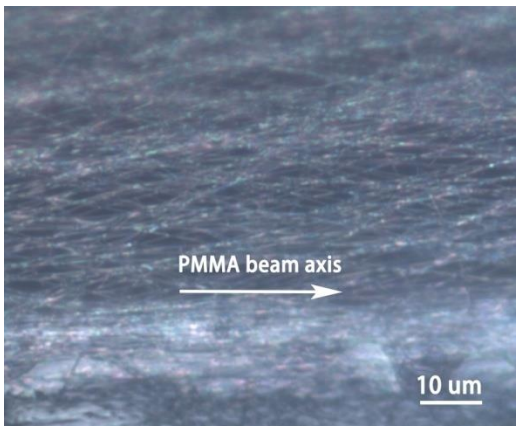

Figure 7.7 Optical micrograph of a fabric consisting of aligned 1 wt% BNNTs/PVA nanofibres.

7.3.3 Orientation of BNNTs in the nanofibre nonwoven fabric

To identify the dependence of BNNTs Raman bands intensity upon the orientation of nanotubes experimentally, we polarized the incident laser parallel to the axis of principle axis of the spectrometer by inserting a λ/2 plate between the specimen and laser source. In comparison with the aligned nanofibre nonwoven fabric (Figure 7.8(b)), the orientation of 1 wt% BNNT/PVA film (Figure 7.8(a)) prepared in chapter 6 was also studied. It can be seen from Figure 7.8(d) that the intensity of PVA peak does not change with polarization angle, which can be used as a reference. The intensity of BNNTs band at ~1366 cm^{-1} keeps almost constant in a composite film (Figure 7.8(c)), indicating a random orientation of BNNTs. In contrast, the intensity of G band in aligned nanofibre nonwoven fabric varies with angle Φ (Figure 7.8(e)). Although the BNNT peak is from the G mode, the Raman band intensity of a nanotube is still mainly contributed by the component along the direction of nanotube axis.

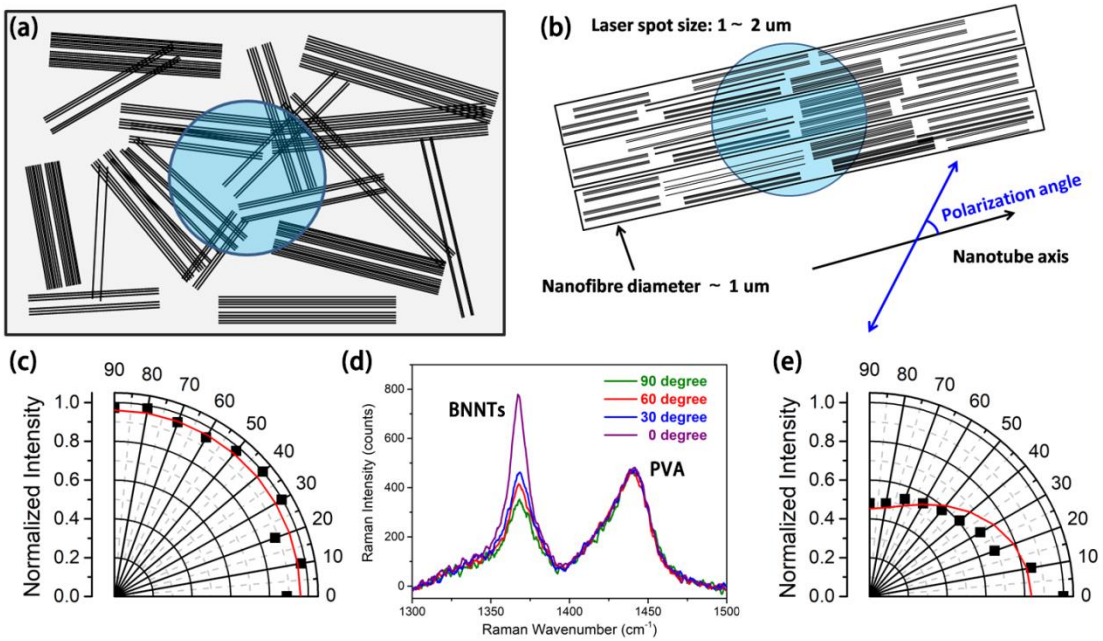

Figure 7.8 Schematics of (a) BNNTs randomly distributed into a nanocomposites film and (b) Highly-oriented BNNTs line up along the axis of electrospun nanofibres inside aligned nanofibres fabric. (c) Variation of MW-BNNTs G band intensity as a function

of the angle between incident laser and horizontal axis of the BNNT/PVA nanocomposites film (Chapter 6). (d) Raman spectra of 1 wt% BNNTs/PVA nanofibre nonwoven fabric at incremental angles between nanofibres axis and incident laser. (e) Variation of MW-BNNTs G band intensity as a function of the angle between incident laser and nanofibres axis.

Therefore, the polarizability tensor α of the BNNT can be written as [21]:

$$\alpha = \begin{bmatrix} 0 & 0 & 0 \\ 0 & 0 & 0 \\ 0 & 0 & 1 \end{bmatrix} \qquad (7.1)$$

and the intensity of Raman band can be given as [21]:

$$I \propto (\vec{e_s} \bullet \alpha \bullet \vec{e_I})^2 \qquad (7.2)$$

where I is the Raman band intensity, $\vec{e_s}$ is the tensor for scattered radiation and $\vec{e_I}$ is the tensor for incident radiation. Since the experiment was carried out with polarized incident radiation and unpolarized scattered radiation, $\vec{e_s}$ is cancelled out. Consequently, the intensity of the Raman band as the function of Φ can be expressed as [21]:

$$I_G(\Phi) = I_0 \left\{ \frac{1}{3} + \left\langle P_2(\cos\theta) \right\rangle (\cos^2 \Phi - \frac{1}{3}) \right\} \qquad (7.3)$$

where $\langle P_2(\cos\theta)\rangle = (3\langle\cos^2\theta\rangle - 1)/2$ is the second-order orientation factor, more commonly known as the Hermans' orientation factor in composite science ($0 \leq \langle P_2(\cos\theta)\rangle \leq 1$, the larger the value of $\langle P_2(\cos\theta)\rangle$, the better the orientation) [21]. Fitting the experimental results in Figure 7.8(e) using Eq7.3 gives $\langle P_2(\cos\theta)\rangle = 0.22$ and $I_0 = 1.74$, indicating that the BNNTs in the fibres are quite well oriented along the fibre direction.

Based on the value of $\langle P_2(\cos\theta)\rangle$, the orientation distribution function (ODF) of the BNNTs in the nanofibres can also be reconstructed by using [21]:

$$f(\theta) = A\exp\left[-\lambda_2 \left\langle P_2(\cos\theta)\right\rangle\right] \qquad (7.4)$$

A=0.0113783 and λ_2= -0.997918 can be obtained by solving the equations, details of these can be found in Ref [21]. On the basis of this, the ODF of BNNTs can be estimated as shown in Figure 7.9. Polarized Raman results suggest a random distribution of the BNNTs in composite film and good orientation in the nanofibres.

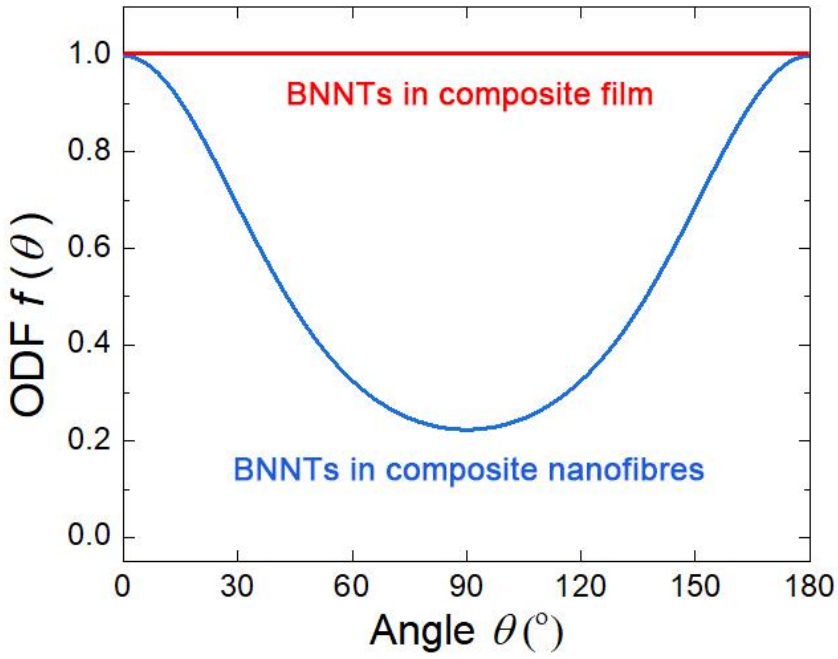

Figure 7.9 Orientation distribution function (ODF) of the BNNTs in the nanofibres and composite film.

7.4 Conclusions

Electrospun nanofibres containing BNNTs have been successfully prepared. Circular-section and smooth 1 wt% BNNTs/PVA nanofibres could be achieved by optimizing electrospinning conditions, i.e. 14 wt% PVA concentration, 15-20 kV applied voltage and 4-14 cm^{-1} tip-collector distance. A bead-on-string structure was observed for nanofibres spun from low PVA concentration solution (7 wt%-10 wt%), while low voltage (<15 kV) spun fibres demonstrate a flat ribbon structure. As-obtained nanofibres were found to have diameter varying from 0.1-1 μm. Aligned nanocomposite nanofibre nonwoven fabrics have been collected using a pair of

parallel metal electrodes sitting an insulating PMMA substrate. High orientation of BNNTs along the fibre axis has been confirmed by polarized Raman spectroscopy, in which the Raman G band intensity of BNNTs maximizes when the laser is parallel to its axis and minimizes when perpendicular. In contrast, no Raman band intensity change with laser polarization was observed for the BNNTs in nanocomposite films, suggesting a random distribution in that case.

References

1. Huang, Z.-M.; Zhang, Y.-Z.; Kotaki, M.; Ramakrishna, S., A review on polymer nanofibers by electrospinning and their applications in nanocomposites. *Compos. Sci. Technol.* **2003,** *63* (15), 2223-2253.
2. Mirjalili, M.; Zohoori, S., Review for application of electrospinning and electrospun nanofibers technology in textile industry. *Journal of Nanostructure in Chemistry* **2016,** *6* (3), 207-213.
3. Sarbatly, R.; Krishnaiah, D.; Kamin, Z., A review of polymer nanofibres by electrospinning and their application in oil–water separation for cleaning up marine oil spills. *Mar. Pollut. Bull.* **2016,** *106* (1-2), 8-16.
4. Haider, A.; Haider, S.; Kang, I.-K., A comprehensive review summarizing the effect of electrospinning parameters and potential applications of nanofibers in biomedical and biotechnology. *Arabian Journal of Chemistry* **2018,** *11* (8), 1165-1188.
5. Kannan, P.; Eichhorn, S. J.; Young, R. J., Deformation of isolated single-wall carbon nanotubes in electrospun polymer nanofibres. *Nanotechnology* **2007,** *18* (23), 235707.
6. Kannan, P.; Young, R. J.; Eichhorn, S. J., Debundling, isolation, and identification of carbon nanotubes in electrospun nanofibers. *Small* **2008,** *4* (7), 930-3.
7. Deng, L.; Young, R. J.; van der Zwaag, S.; Picken, S., Characterization of the adhesion of single-walled carbon nanotubes in poly(p-phenylene terephthalamide) composite fibres. *Polymer* **2010,** *51* (9), 2033-2039.
8. Deng, L.; Eichhorn, S. J.; Kao, C. C.; Young, R. J., The effective Young's modulus of carbon nanotubes in composites. *ACS Appl Mater Interfaces* **2011,** *3* (2), 433-40.
9. Ayutsede, J.; Gandhi, M.; Sukigara, S.; Ye, H.; Hsu, C.-m.; Gogotsi, Y.; Ko, F., Carbon nanotube reinforced Bombyx mori silk nanofibers by the electrospinning process. *Biomacromolecules* **2006,** *7* (1), 208-214.
10. Sen, R.; Zhao, B.; Perea, D.; Itkis, M. E.; Hu, H.; Love, J.; Bekyarova, E.; Haddon, R. C., Preparation of single-walled carbon nanotube reinforced polystyrene and polyurethane nanofibers and membranes by electrospinning. *Nano Lett.* **2004,** *4* (3), 459-464.
11. Dror, Y.; Salalha, W.; Khalfin, R. L.; Cohen, Y.; Yarin, A. L.; Zussman, E., Carbon nanotubes embedded in oriented polymer nanofibers by electrospinning. *Langmuir* **2003,** *19* (17), 7012-7020.
12. Gao, J.; Yu, A.; Itkis, M. E.; Bekyarova, E.; Zhao, B.; Niyogi, S.; Haddon, R. C., Large-scale fabrication of aligned single-walled carbon nanotube array and hierarchical single-walled carbon nanotube assembly. *J. Am. Chem. Soc.* **2004,** *126* (51), 16698-16699.
13. Iijima, S., Helical microtubules of graphitic carbon. *Nature* **1991,** *354* (6348), 56.

14. Chopra, N. G.; Luyken, R.; Cherrey, K.; Crespi, V. H.; Cohen, M. L.; Louie, S. G.; Zettl, A., Boron nitride nanotubes. *Science* **1995,** *269* (5226), 966-967.
15. Terao, T.; Zhi, C.; Bando, Y.; Mitome, M.; Tang, C.; Golberg, D., Alignment of boron nitride nanotubes in polymeric composite films for thermal conductivity improvement. *The Journal of Physical Chemistry C* **2010,** *114* (10), 4340-4344.
16. Kim, D.; You, M.; Seol, J. H.; Ha, S.; Kim, Y. A., Enhanced Thermal Conductivity of Individual Polymeric Nanofiber Incorporated with Boron Nitride Nanotubes. *The Journal of Physical Chemistry C* **2017,** *121* (12), 7025-7029.
17. Estevez, J. E.; Harvey, B. G.; Ostrom, G. S.; Hefley, G. H.; Yelton, C. G.; Garrison, M. D., Beyond Percolation Threshold Loading of Polyacrylonitrile Electrospun Nanofibers with Boron Nitride Nanotubes for Use in High-Temperature Composites. *ACS Applied Nano Materials* **2019,** *2* (12), 7585-7592.
18. Li, D.; Wang, Y.; Xia, Y., Electrospinning of polymeric and ceramic nanofibers as uniaxially aligned arrays. *Nano Lett.* **2003,** *3* (8), 1167-1171.
19. Kim, K. S.; Kingston, C. T.; Hrdina, A.; Jakubinek, M. B.; Guan, J. W.; Plunkett, M.; Simard, B., Hydrogen-catalyzed, pilot-scale production of small-diameter boron nitride nanotubes and their macroscopic assemblies. *ACS Nano* **2014,** *8* (6), 6211-6220.
20. Guan, J.; Kim, K. S.; Jakubinek, M. B.; Simard, B., pH-switchable water-soluble boron nitride nanotubes. *ChemistrySelect* **2018,** *3* (32), 9308-9312.
21. Li, Z.; Young, R. J.; Kinloch, I. A.; Wilson, N. R.; Marsden, A. J.; Raju, A. P. A., Quantitative determination of the spatial orientation of graphene by polarized Raman spectroscopy. *Carbon* **2015,** *88*, 215-224.
22. Mit-uppatham, C.; Nithitanakul, M.; Supaphol, P. In *Effects of Solution Concentration, Emitting Electrode Polarity, Solvent Type, and Salt Addition on Electrospun Polyamide-6 Fibers: A Preliminary Report*, Macromolecular Symposia, Wiley: New York, **2004**; pp 293-300.
23. Thompson, C.; Chase, G. G.; Yarin, A.; Reneker, D., Effects of parameters on nanofiber diameter determined from electrospinning model. *Polymer* **2007,** *48* (23), 6913-6922.
24. Deng, L. Raman Spectroscopic Studies of Carbon Nanotube Composite Fibres. PhD Thesis, The University of Manchester, **2010**.
25. Baji, A.; Mai, Y.-W.; Wong, S.-C.; Abtahi, M.; Chen, P., Electrospinning of polymer nanofibers: effects on oriented morphology, structures and tensile properties. *Compos. Sci. Technol.* **2010,** *70* (5), 703-718.
26. Lin, T.; Wang, H.; Wang, H.; Wang, X., The charge effect of cationic surfactants on the elimination of fibre beads in the electrospinning of polystyrene. *Nanotechnology* **2004,** *15* (9), 1375.

Chapter 8 Conclusions and Suggestions for Future Work

8.1 Conclusions

8.1.1 In-situ Raman deformation of few-layer BNNSs

It has been found that the G band of BNNSs linearly shifts to lower frequency under unaxial tensile strain. Different from previous report on deformed 1L-4L BNNSs [1] where the G band tends to split into two sub-bands, band broadening, rather than splitting, was observed for the case of thicker (>6 nm) few-layer BNNSs, possibly as the result of the low levels of applied strain used in this study. Measurements on the band shift of 10.0 nm, 8.8 nm and 20.0 nm thick BNNSs have shown that the shift rate drops slightly as the thickness of the BNNSs increases from 8.8 nm to 20 nm, suggesting the layer-layer interaction inside the BNNSs is much stronger than few-layer graphene. On the other hand, the band shift rate of BNNSs decreases further with an increasing number of layers eventually dropping to ~ -2 cm^{-1}/% when the thickness increased to ~100 nm (300 layers). The efficiency of internal stress transfer between the different hBN layers *k* has been found to be of the order of 99%. A value of $k = 0.99$ means that the effective Young's modulus of the BNNSs will only fall to half of the monolayer value for 100-layer BNNS ($N = 100$). Hence it appears that it is less important to achieve a high degree of exfoliation to very thin nanosheets, when using hBN in nanocomposites, than in the case of graphite and graphene whose *k* is only in the range of 0.6-0.8. Taking the reference G band shift rate to be -11 cm^{-1}/%, the Grüneisen parameter of the BNNSs has been determined to be 1.23.

Stress transfer from PMMA substrate to the BNNSs has been monitored by mapping the strain along a nanosheet of 11 μm length and 17 nm in thickness. When a low

strain (≤0.1%) was applied to PMMA substrate, the strain builds up from the two edges and becomes constant along the middle of the nanosheet where the strain in the flake equals to the applied matrix strain, suggesting good bonding between the BNNSs and PMMA substrate. The interfacial shear stress is calculated to be 9.4 MPa when applied matrix strain is 0.1%. When the applied matrix strain is increased further to 0.3%, it is found that the BNNS/polymer interface has completely failed and the interfacial shear stress for the failed interface is estimated to be 3.8 MPa. In comparison with the case of a graphene monolayer with a ~2.3 MPa maximum interfacial shear stress at well-bonded interface and a 0.3-0.8 MPa stress at failed interface, better stress transfer can be expected between BNNSs and a polymer matrix than for graphene. In summary, BNNSs should give better mechanical reinforcement than graphene in polymer-based nanocomposites as a result of good internal interlayer stress transfer within the nanosheets and better interfacial stress transfer to the polymer matrix.

8.1.2 Liquid-exfoliated BNNSs/polymer nanocomposites

Three types of BNNSs with different average flake size, thickness and aspect ratio have been prepared by liquid exfoliation and used for preparing nanocomposites. It has been found from tensile testing that M6000 with highest aspect ratio (~350) exhibits best reinforcement on polymer matrix at all different BNNSs loadings from 0.1 wt% to 1 wt%. M3000, a bigger but much thicker flake with low aspect ratio (~55) demonstrates relatively good reinforcement at low loading, but its effective modulus massively decreases at higher loading. Sigma, very small but thin BNNSs having a similar mean aspect ratio (~63) as M3000, exhibits very limited reinforcement on the PVA matrix.

The level of reinforcement is found to increase with an increasing loading of BNNSs

but the performance decrease above about 0.5 wt% of the filler. The dispersion of three types of BNNSs in the PVA matrix has been estimated by mapping the Raman BNNS E_{2g} mode (G band) intensity. Sigma and M6000 exhibit relatively homogeneous distribution even at 1 wt% loading, but some agglomerations has been seen in 1 wt% M6000/PVA film. In contrast, M3000 with much bigger flake size tends to agglomerate in polymer matrix, which has significantly damaged its reinforcement on polymer at relatively high loading. In-situ Raman deformation results are highly consistent with tensile testing results where 1 wt% M6000/PVA and 1 wt% M3000/PVA has exhibited higher Raman BNNS G band shift than 1 wt% Sigma/PVA. It has also been found that no further band shift occurred when applied matrix strain is higher than 0.3%, suggesting relatively poor interfacial adhesion between the BNNSs and polymer matrix. Hence, chemical functionalization of the BNNSs is needed for realizing a stronger BNNSs/polymer interface and better dispersion of the BNNSs in the polymer matrix.

8.1.3 BNNTs/polymer nanocomposites

The microstructure and mechanical properties of BNNTs/PVA nanocomposites have been investigated in detail. The typical multi-walled structure of the BNNTs has been confirmed by TEM and the nanocomposites have been fully characterized by non-resonance Raman spectroscopy. The distribution of BNNTs in the polymer matrix has been assessed by mapping the Raman BNNT G band intensity. Although this band is weak due to the lack of resonance, it still can be deconvoluted from the Raman spectrum of the PVA matrix, enabling its intensity and position to be determined in the nanocomposite. The BNNTs have also been found to be able to massively enhance the mechanical properties of the nanocomposites. The effective Young's modulus of the BNNTs has been found to be 825 GPa at low volume fraction but decreases to the order of 180 GPa at 1 wt% loading, due to bundling and agglomeration in the polymer

matrix at high loadings. Additionally, it has also demonstrated that hydroxylation of BNNTs can further improve the mechanical properties of the nanocomposites. -OH functionalized BNNTs exhibit a better dispersion and stronger interface with the polymer matrix, leading to a higher effective Young's modulus. Stress-induced Raman shifts of the BNNT G band have been used to study the stress transfer from the polymer matrix to both the BNNTs and functionalized BNNTs. The levels of band shift have been found to be consistent with the effective Young's modulus of the BNNTs determined from mechanical testing. A value of 1.34 ± 0.72 has been determined for the Grüneisen parameter of the BNNTs from the stress-induced Raman band shifts, very close to the value determined for the BNNSs (1.23).

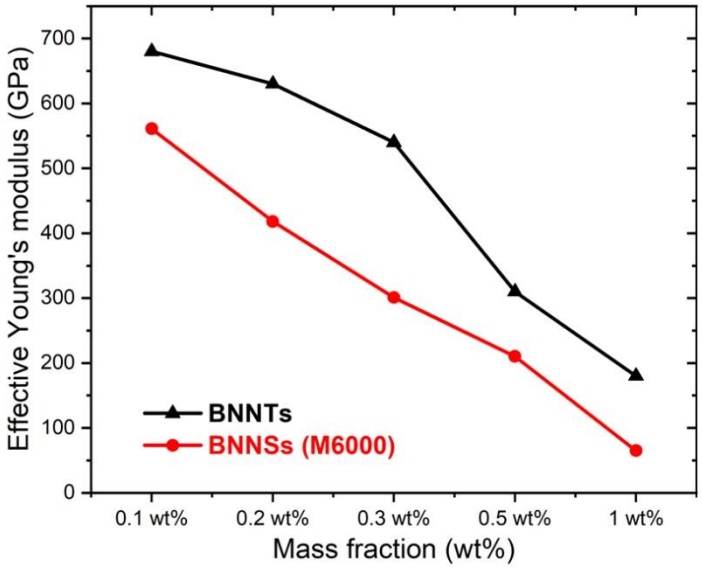

Figure 8.1 Dependence of the effective Young's modulus of the BNNSs (M6000)/PVA and BNNTs/PVA nanocomposites upon the mass fraction of the BNNSs and BNNTs.

In comparison with the M6000 BNNSs which demonstrates best reinforcement on PVA matrix, it can be observed in Figure 8.1 that 1D BNNTs shows better reinforcement than 2D BNNSs at every mass fraction, which can most likely be attributed to lower density and higher aspect ratio of BNNTs.

8.1.4 Electrospun BNNTs/polymer nanofibres

1 wt% BNNTs/PVA electrospun nanofibres with different diameters and structure have been successfully prepared. Electrospinning conditions, i.e. PVA solution concentration, voltage, tip-collector distance have been optimized as 14 wt%, 15-20 kV and 4-14 cm^{-1}, respectively, for preparing circular and smooth composite nanofibres. As-obtained nanofibres have been observed by SEM and found to have diameters varying from 0.1-1 μm. Nonwoven fabric containing highly-aligned BNNTs/PVA nanofibres has been successfully prepared by sitting a pair of parallel aluminum electrodes on insulating PMMA collector. The orientation of BNNTs inside the fabric has been investigated by polarized Raman spectroscopy with a VN configuration. It has been demonstrated that the Raman G band intensity of BNNTs maximizes when the laser is parallel to its axis and minimizes when perpendicular, indicating that the BNNTs in the fibres are quite well oriented along the fibre direction. In comparison, no Raman band intensity change with laser polarization was observed for the case of BNNTs/polymer nanocomposites film, suggesting a random distribution of the BNNTs in the polymer matrix.

8.2 Suggestions for future work

8.2.1 Deformation of a 1-4L BNNSs/polymer model composite

Although the deformation of few-layer BNNSs has been studied in chapter 4 and the strain-induced Raman band shifts of 2L-4L BNNSs have been reported by Androulidakis et al. [1], experimental measurement of the strain-induced Raman shift of 1L BNNSs, to our knowledge, still has not been realized. Furthermore, BNNSs exhibit much higher inner layer-layer bonding than graphene, the effect of this strong interlayer bonding on the deformation behaviour of BNNSs, such as the interfacial

stress transfer between polymer matrix and BNNSs with different thickness, need to be studied further.

It is reported that the thin layer of SU-8 top coating can make 4L BNNSs visible on PMMA substrate [1]. The thickness of SU-8 coating could be well controlled by adjusting the rotation speed and SU-8/thinner concentration. The thickness of SU-8 coating could be then determined by an ellipsometer.

To make 1L-3L BNNSs detectable on PMMA/SU-8 beam, an identify-transfer strategy could be designed. First of all, BNNSs could be exfoliated by standard mechanical exfoliation [2] and transferred on a Si/SiO_2 wafer with 90 nm SiO_2 coating. It is reported that the optical contrast of 1L BNNSs (~2.5%) is enough to be detected by human eye [3], so 1L-4L could be distinguished and marked by an optical microscope with a green filter. Based on the estimated ~6 μm critical length of few-layer BNNSs in this thesis, relatively large flake dimension will be needed for accurate Raman deformation testing. PMMA could be used to transfer marked 1L-4L BNNSs onto a PMMA/SU-8 beam. Hence, BNNSs will be sandwiched by PMMA coating and PMMA/SU-8 beam and as-obtained model composite could be deformed and studied by Raman in detail [4]. Theoretically, 1-3L BNNSs will become optically invisible after the transfer, but it may be possible to distinguish surrounding much thicker BNNSs or even unexfoliated bulk hBN, the location of 1L-3L BNNSs can thus be confirmed from their location on Si/SiO_2, as illustrated in Figure 8.2 [5].

The very weak Raman signal of 1L-4L BNNSs might be overcome by using a 488 nm sapphire laser and ×100 objective with appropriate grating and laser exposure time. Raman band shift of 1L-4L with big enough flake size could be studied first. Strain distribution in the BNNSs and interfacial shear stress at different applied matrix strain could be evaluated.

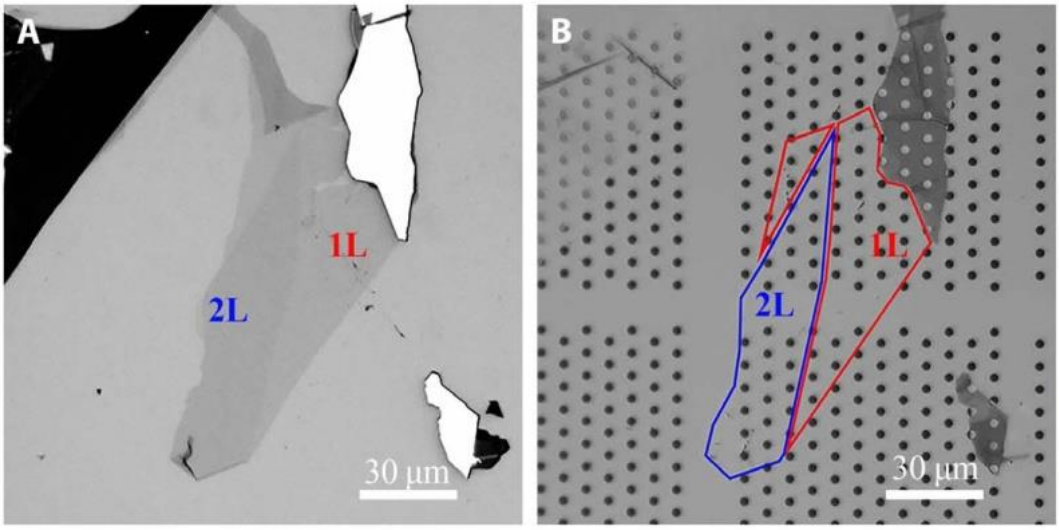

Figure 8.2 Optical images of 1L-2L BNNSs on a (a) Si/SiO_2 wafer and (b) transferred onto a TEM grid [5].

8.2.2 Deformation of wrinkled BNNSs

The deformation of wrinkled CVD graphene [6] revealed that the presence of delaminated wrinkles separate flat graphene into isolated "islands" and reduce the stress transfer inside the flake. On the contrary, Galiotis et al. [7] reported that substrate-attached wrinkles further enhanced the graphene/substrate interfacial shear stress. It is more interesting to find that these supported wrinkles massively improve the interlayer stress transfer in 2L-3L corrugated graphene, the Raman 2D band shift of 3L wrinkled graphene (-57.1 $cm^{-1}/\%$) was twice that of a 3L flat flake (-28.6 $cm^{-1}/\%$).

Different from the case of graphene, the interlayer bonding inside BNNSs has been proven to be very strong. It can be deduced that wrinkled multi-layer BNNSs will exhibit different deformation behavior from the graphene with same number of layers. In particular, the effect of delaminated wrinkles on the stress transfer across the BNNSs flake could be studied.

To make BNNSs visible, PMMA beam could be spin coated with 180 nm SU-8 photoresist. For comparison, wrinkle-free BNNSs with identical thickness could be prepared by standard mechanical exfoliation method. Both BNNSs could be transferred on PMMA/SU-8 substrate and their Raman band shifts could be studied. Strain distribution at 0.1%, 0.2%, 0.3%, 0.4%, 0.5% applied matrix strain could be monitored by Raman strain mapping.

8.2.3 Deformation of functionalized BNNSs

As shown in Chapter 4, pristine BNNSs exhibit relatively poor interfacial bonding with polymer matrix. Several review papers [8-10] have all emphasized the necessity of surface modification to realize the ideal mechanical reinforcement of BNNSs upon the polymers. Weng et al. [10] summarized different functionalization routes of BNNSs and concluded that functional groups can be attached to both in-plane and edge sites of the nanosheets. However, the effect of functionalization on the strong layer-layer bonding and AA' stacking order of BNNSs, to our knowledge, has not been investigated. Moreover, it is still a challenge to straightforwardly estimate the interfacial bonding between different types of functionalized BNNSs and different kinds of polymer matrix. This kindles our interest in studying the deformation of functionalized BNNSs by the use of the Raman deformation technique.

In this work, different kinds of functionalized BNNSs could be prepared. Pristine BNNSs could be exfoliated from bulk hBN and transferred on Si/SiO_2 wafer for gaseous functionalization. As-prepared functionalized BNNSs of variable thickness could be transferred onto a polymer beam and deformed. The change of layer-layer bonding in the functionalized BNNSs and functionalized BNNSs/polymer interfacial stress transfer could then be studied by Raman spectroscopy.

It would be particularly interesting to study the interface between some special functionalized BNNSs and polymer matrix, such as fluorinated BNNSs and fluorine-contained polymers such as polyvinylidene fluoride (PVDF), polytetrafluoroethylene (PTFE).

8.2.4 Deformation of a SW-BNNT/PVA nanocomposite film

Chapter 6 has reported the linear Raman band shift rates of MW-BNNTs, which have found to fluctuate in different areas. This can be explained by the bundling in the polymer matrix and random distribution of number of walls of the MW-BNNTs. However, the Raman band shift of SW-BNNTs, to our knowledge, has still not been studied. The preparation of SW-BNNTs is rarely reported. Arenal et al. [11] successfully synthesized SW-BNNTs using laser ablation method, but as-prepared SW-BNNTs contain many other hBN nanostructures such as nanocages and nanoplatelets [12]. Golberg et al. [13] reported the successful preparation of SW-BNNTs using hard-template method, where the SW-CNTs was used as a template reacted with B_2O_3 and nitrogen gas at >1500 ℃, to fully convert SW-CNTs into SW-BNNTs. This method is easier to realize the preparation of SW-BNNTs with relatively high purity.

In this suggestion, MW-CNTs could be used to prepare MW-BNNTs, for optimizing the experimental conditions for substitution reaction. To realize better control the reaction, ammonia gas (NH_3) could be used to prepare BNNTs at lower temperature (1100 ℃) [14]. Once the optimal parameters for the reaction are confirmed, SW-CNTs could be used to prepare SW-BNNTs. The product could be studied by different characterization technique to investigate if the single-wall structure of the CNTs is well retained after the reaction. It then could be used to prepare polymer nanocomposite films containing random distributed SW-BNNTs and oriented

SW-BNNTs (by hot pressing stacked layers of well-aligned SW-BNNTs electrospun nanofibre fabric as a film). Raman band shifts of the SW-BNNTs could be systematically studied.

8.2.5 Deformation of an oriented BNNTs/PVA nanocomposite film

Previous work on CNT/polymer nanocomposites [15] has proven that the good orientation of 1D nanotubes with high aspect ratio and excellent anisotropic properties can further improve the mechanical and other properties of the nanocomposites. Raman spectroscopy has been widely used for evaluating the CNTs/polymer interfacial stress transfer efficiency: the higher the linear Raman 2D band shift rate of CNTs, the higher the effective Young's modulus. More importantly, Wagner et al. [16-17] have demonstrated that the band shift rate is even higher if the nanotubes are parallel with the directions of maximum strain and Raman laser polarization. However, relevant Raman studies on investigating the mechanical reinforcement of oriented BNNTs upon the polymer matrix, to our knowledge, have not been reported.

Terao et al. [18] has shown that high orientation of the BNNTs improves the thermal conductivity of the nanocomposites film. Considering that nonwoven fabric containing oriented multi-walled BNNTs has been successfully prepared in Chapter 7, it may be possible to prepare BNNTs/PVA nanocomposites film contained aligned BNNTs by hot-pressing multi layers of nonwoven fabrics.

The degree of orientation of the BNNTs in the nanocomposites films could be controlled by adjusting the stacking angle between adjacent layers of nonwoven fabric. For example, if 2 layers of fabric will be needed for prepare to a nanocomposites film, film containing highly aligned BNNTs will be prepared by stacking 2 layers of fabric

along one direction; the orientation of BNNTs in the film could be gradually decreased by rotating the top layer 30, 60, 90 degree relative to the bottom layer of fabric. Hence, it may be possible to prepare nanocomposites films with oriented, partially-oriented, random BNNTs. Their mechanical properties could then be studied by mechanical testing and in-situ Raman deformation analysis.

References

1. Androulidakis, C.; Koukaras, E. N.; Poss, M.; Papagelis, K.; Galiotis, C.; Tawfick, S., Strained hexagonal boron nitride: Phonon shift and Grüneisen parameter. *Physical Review B* **2018,** *97* (24).
2. Novoselov, K. S.; Geim, A. K.; Morozov, S. V.; Jiang, D.; Zhang, Y.; Dubonos, S. V.; Grigorieva, I. V.; Firsov, A. A., Electric field effect in atomically thin carbon films. *Science* **2004,** *306* (5696), 666-669.
3. Gorbachev, R. V.; Riaz, I.; Nair, R. R.; Jalil, R.; Britnell, L.; Belle, B. D.; Hill, E. W.; Novoselov, K. S.; Watanabe, K.; Taniguchi, T.; Geim, A. K.; Blake, P., Hunting for monolayer boron nitride: optical and Raman signatures. *Small* **2011,** *7* (4), 465-8.
4. Gong, L.; Kinloch, I. A.; Young, R. J.; Riaz, I.; Jalil, R.; Novoselov, K. S., Interfacial stress transfer in a graphene monolayer nanocomposite. *Adv. Mater.* **2010,** *22* (24), 2694-2697.
5. Cai, Q.; Scullion, D.; Gan, W.; Falin, A.; Zhang, S.; Watanabe, K.; Taniguchi, T.; Chen, Y.; Santos, E. J. G.; Li, L. H., High thermal conductivity of high-quality monolayer boron nitride and its thermal expansion. *Sci Adv* **2019,** *5* (6), eaav0129.
6. Li, Z.; Kinloch, I. A.; Young, R. J.; Novoselov, K. S.; Anagnostopoulos, G.; Parthenios, J.; Galiotis, C.; Papagelis, K.; Lu, C.-Y.; Britnell, L., Deformation of wrinkled graphene. *ACS Nano* **2015,** *9* (4), 3917-3925.
7. Androulidakis, C.; Koukaras, E. N.; Rahova, J.; Sampathkumar, K.; Parthenios, J.; Papagelis, K.; Frank, O.; Galiotis, C., Wrinkled few-layer graphene as highly efficient load bearer. *ACS Appl Mater Interfaces* **2017,** *9* (31), 26593-26601.
8. Lin, Y.; Connell, J. W., Advances in 2D boron nitride nanostructures: nanosheets, nanoribbons, nanomeshes, and hybrids with graphene. *Nanoscale* **2012,** *4* (22), 6908-39.
9. Meng, W.; Huang, Y.; Fu, Y.; Wang, Z.; Zhi, C., Polymer composites of boron nitride nanotubes and nanosheets. *J. Mater. Chem. C* **2014,** *2* (47), 10049-10061.
10. Weng, Q.; Wang, X.; Wang, X.; Bando, Y.; Golberg, D., Functionalized hexagonal boron nitride nanomaterials: emerging properties and applications. *Chem. Soc. Rev.* **2016,** *45* (14), 3989-4012.
11. Arenal, R.; Stephan, O.; Cochon, J.-L.; Loiseau, A., Root-growth mechanism for single-walled boron nitride nanotubes in laser vaporization technique. *J. Am. Chem. Soc.* **2007,** *129* (51), 16183-16189.
12. Arenal, R.; Ferrari, A. C.; Reich, S.; Wirtz, L.; Mevellec, J. Y.; Lefrant, S.; Rubio, A.; Loiseau, A., Raman spectroscopy of single-wall boron nitride nanotubes. *Nano Lett.* **2006,** *6* (8), 1812-6.
13. Golberg, D.; Bando, Y.; Han, W.; Kurashima, K.; Sato, T., Single-walled B-doped carbon, B/N-doped carbon and BN nanotubes synthesized from single-walled carbon nanotubes through a substitution reaction. *Chem. Phys. Lett.* **1999,** *308*

(3-4), 337-342.

14. Han, W.-Q.; Cumings, J.; Huang, X.; Bradley, K.; Zettl, A., Synthesis of aligned BxCyNz nanotubes by a substitution-reaction route. *Chem. Phys. Lett.* **2001,** *346* (5-6), 368-372.
15. Papageorgiou, D. G.; Li, Z.; Liu, M.; Kinloch, I. A.; Young, R. J., Mechanisms of mechanical reinforcement by graphene and carbon nanotubes in polymer nanocomposites. *Nanoscale* **2020,** *12* (4), 2228-2267.
16. Frogley, M.; Zhao, Q.; Wagner, H., Polarized resonance Raman spectroscopy of single-wall carbon nanotubes within a polymer under strain. *Physical Review B* **2002,** *65* (11), 113413.
17. Wood, J.; Zhao, Q.; Wagner, H., Orientation of carbon nanotubes in polymers and its detection by Raman spectroscopy. *Composites Part A: Applied Science and Manufacturing* **2001,** *32* (3-4), 391-399.
18. Terao, T.; Zhi, C.; Bando, Y.; Mitome, M.; Tang, C.; Golberg, D., Alignment of boron nitride nanotubes in polymeric composite films for thermal conductivity improvement. *The Journal of Physical Chemistry C* **2010,** *114* (10), 4340-4344.